People's Democratic Republic of Algeria

Ministry of Higher Education and Scientific Research

Echahid Cheikh Larbi Tebessi University
- Tebessa -

Faculty of Science and Technology

Department of Electrical Engineering

LMD Doctoral Thesis

Option: Electrical Control

Presented by:

OUSSAMA BRAHMI

Theme

Advanced control structure based on the Frequency Separation Principle of a Wind Energy Conversion System (WECS)

Publicly defended on 30/06/2025 before the jury:

Djalel DIB	PROFESSOR	Echahid Cheikh Larbi Tebessi University	President
Achour BETKA	PROFESSOR	Mohamed Khider- Biskra University	Examiner
Tahar BAHI	PROFESSOR	Badji Mokhtar - Annaba University	Examiner
Abdelhamid DJARI	MCA	Echahid Cheikh Larbi Tebessi University	Examiner
Mohamed Salah Djebbar	MCA	Echahid Cheikh Larbi Tebessi University	Examiner
Amel BOUCHEMHA	MCA	Echahid Cheikh Larbi Tebessi University	Supervisor
Sami KAHLA	MRA	Research centre in Industrial Technologies	Co-Supervisor

بسم الله الرحمان الرحيم

Acknowledgments

I extend my heartfelt gratitude to God for guiding us to the successful completion of this work.

I am deeply thankful to my family for their unwavering encouragement and support, as well as the sacrifices they made throughout this journey.

I would like to express my sincere appreciation to my supervisor, ***Dr. Amel Bouchemha,*** *for her invaluable guidance and dedication in helping me complete this project.*

I am also grateful to my co-supervisor, ***Dr. Sami Kahla****, for his tremendous effort and support in navigating the challenges of this work.*

My thanks extend to all members of the discussion committee for their expertise and insights during the evaluation of my thesis.

Finally, I would like to acknowledge everyone who contributed, directly or indirectly, to the success of this endeavor. I hope they find in these acknowledgments a reflection of my gratitude.

Dedication

I dedicate this work to my beloved parents, ***Hassina Gaba*** *and* ***Boulaares Brahmi****, whose unwavering support and love have shaped my journey. To my little brother,* ***Ouail Brahmi****, and my entire family, thank you for being my foundation.*

I extend my gratitude to all my friends, whose encouragement has been invaluable. A special acknowledgment goes to my supervisor, ***Dr. Amel Bouchemha*** *, and my co-supervisor,* ***Dr. Sami Kahla****, for their guidance and mentorship throughout this process.*

To everyone who has contributed, directly or indirectly, to my journey toward becoming ***a doctor in the field of electrical control****, your influence has been profound. I also remember the teachers who inspired me during my educational journey over the past 23 years, from primary school through to university. Your dedication and wisdom have left a lasting impact.*

OUSSAMA BRAHMI

ملخص :

تتناول أطروحة الدكتوراه هذه التحديات التي تفرضها التقلبات اللحظية في الرياح وعدم خطية توربينات الرياح، والتي تعيق الاستغلال الكامل لطاقة الرياح بكفاءة وموثوقية عالية. الهدف الأساسي من هذا البحث هو اقتراح استراتيجيات تحكم مبتكرة لأنظمة تحويل طاقة الرياح (WECS) التي توازن بين تعظيم كفاءة الطاقة وتقليل الإجهاد الميكانيكي من خلال تقليل تموج عزم الدوران الكهرومغناطيسي. تستند هذه الاستراتيجيات إلى مبدأ فصل التردد، الذي يميز بين الاختلافات قصيرة المدى وطويلة المدى في ديناميكيات الرياح. يتيح هذا الفصل تطوير بنية تحكم مزدوجة الحلقة، مما يحسن كل من ديناميكيات التردد العالي والمنخفض المتأصلة في النظام. في الحلقة عالية التردد، يتم تنفيذ وحدات تحكم مختلفة، بما في ذلك وحدات التحكم LQR و H∞ ، لإدارة الديناميكيات الناجمة عن سرعة الرياح المضطربة. في حلقة التردد المنخفض، يتم استخدام وحدات تحكم متناسبة تكاملية جزئية الترتيب (FOPI) ، مع نهج متقدم يشتمل على وحدة تحكم متناسبة تكاملية جزئية الترتيب مفلترة (FOPIF) ومُحسَّنة باستخدام خوارزمية تحسين سرب الجسيمات (PSO) .تهدف وحدات التحكم هذه إلى التخفيف من تموج عزم الدوران الكهرومغناطيسي، والمعروف أيضًا باسم مشكلة الثرثرة، وضمان تتبع نقطة القدرة القصوى (MPPT) بكفاءة، وبالتالي تحسين أداء النظام في ظل ظروف الرياح المتغيرة .لا تعمل استراتيجيات التحكم المقترحة على تعظيم إنتاج الطاقة من توربينات الرياح فحسب، بل تقلل أيضًا من تموج عزم الدوران الكهرومغناطيسي، وبالتالي تقليل الإجهاد الميكانيكي، وإطالة العمر التشغيلي، وخفض تكاليف الصيانة. من خلال تحسين السلوك الديناميكي وموثوقية نظام تحويل طاقة الرياح ، يساهم هذا البحث بشكل كبير في تطوير تقنيات التحكم في أنظمة طاقة الرياح، وتعزيز نمو حلول الطاقة المتجددة الفعالة والقابلة للتطوير والمرنة. تدعم نتائج هذا العمل التحول العالمي نحو الطاقة المستدامة، وتقدم رؤى قيمة لتحسين أنظمة طاقة الرياح في ظل الظروف البيئية الصعبة.

كلمات مفتاحية :

نظام تحويل طاقة الرياح ، مبدأ فصل التردد، تتبع نقطة القدرة القصوى ، تموج عزم الدوران الكهرومغناطيسي، استراتيجيات التحكم المتقدمة، خوارزميات ميتاهيوريستية، متحكم H∞، متحكم LQR، وحدة التحكم التكاملية النسبية من الدرجة الكسرية (FOPI)، وحدة التحكم التكاملية النسبية المفلترة من الدرجة الكسرية (FOPIF)، مولد الحث.

Abstract:

This PhD thesis addresses the challenges posed by the instantaneous fluctuations in wind and the non-linearity of wind turbines, which hinder the full exploitation of wind power with high efficiency and reliability. The primary objective of this research is to propose innovative control strategies for Wind Energy Conversion Systems (WECS) that balance the maximization of energy efficiency with the minimization of mechanical stress through the reduction of electromagnetic torque ripple. These strategies are grounded in the principle of frequency separation, which distinguishes between the short-term and long-term variations in wind dynamics. This separation enables the development of a dual-loop control architecture, optimizing both the high-frequency and low-frequency dynamics inherent in the system. In the high-frequency loop, various controllers, including Linear Quadratic Regulator (LQR) and H∞ controllers, are implemented to manage the dynamics induced by turbulent wind speed. In the low-frequency loop, fractional-order proportional-integral (FOPI) controllers are employed, with an advanced approach incorporating a filtered fractional-order proportional-integral (FOPIF) controller optimized using the Particle Swarm Optimization (PSO) algorithm. These controllers aim to mitigate electromagnetic torque ripple, also known as the chattering problem, and ensure efficient Maximum Power Point Tracking (MPPT), thereby enhancing system performance under variable wind conditions. The proposed control strategies not only maximize the energy production of wind turbines but also reduce electromagnetic torque ripple, thereby minimizing mechanical stress, extending the operational lifespan, and lowering maintenance costs. By improving the dynamic behavior and reliability of the WECS, this research contributes significantly to advancing control technologies in wind energy systems, promoting the growth of efficient, scalable, and resilient renewable energy solutions. The findings of this work support the global transition toward sustainable energy, offering valuable insights into optimizing wind energy systems under challenging environmental conditions.

.

Keywords:

Wind Energy Conversion System (WECS), Frequency Separation Principle, Maximum Power Point Tracking (MPPT), Electromagnetic Torque Ripple, Advanced Control Strategies, Metaheuristic Algorithms, H∞ Control, LQR Control, Fractional-Order Proportional-Integral (FOPI) Controller, Filtered Fractional-Order Proportional-Integral (FOPIF) Controller, Induction Generator.

Résumé:

Cette thèse de Doctorat aborde les défis posés par les fluctuations instantanées du vent et la non-linéarité des éoliennes, qui entravent l'exploitation optimale de l'énergie éolienne avec une efficacité et une fiabilité élevées. L'objectif principal de cette recherche est de proposer des stratégies de commande innovantes pour les systèmes de conversion d'énergie éolienne (SCEE), équilibrant la maximisation de l'efficacité énergétique et la réduction du stress mécanique grâce à la diminution des ondulations du couple électromagnétique. Ces stratégies s'appuient sur le principe de séparation fréquentielle, qui distingue les variations dynamiques du vent à court terme et à long terme. Cette séparation permet le développement d'une architecture de contrôle à double boucle, optimisant à la fois les dynamiques haute fréquence et basse fréquence inhérentes au système. Dans la boucle haute fréquence, divers contrôleurs, notamment le contrôleur linéaire quadratique Regulator (LQR) et le contrôleur H∞, sont mis en œuvre pour gérer les dynamiques induites par les turbulences de la vitesse du vent. Dans la boucle basse fréquence, des contrôleurs proportionnels-intégrateurs d'ordre fractionnaire (FOPI) sont utilisés, avec une approche avancée incorporant un contrôleur proportionnel-intégrateur filtré d'ordre fractionnaire (FOPIF) optimisé à l'aide de l'algorithme d'optimisation par essaims particulaires (PSO). Ces contrôleurs visent à atténuer les ondulations du couple électromagnétique, également connues sous le nom de (problème de chattering), et à garantir un suivi efficace du point de puissance maximale (MPPT), améliorant ainsi les performances du système dans des conditions de vent variables. Les stratégies de commande proposées maximisent non seulement la production d'énergie des éoliennes, mais réduisent également les ondulations du couple électromagnétique, minimisant ainsi le stress mécanique, prolongeant la durée de vie opérationnelle et réduisant les coûts de maintenance. En améliorant le comportement dynamique et la fiabilité des WECS, cette recherche contribue de manière significative à l'avancement des technologies de commande dans les systèmes éoliens, favorisant le développement de solutions énergétiques renouvelables efficaces, évolutives et résilientes. Les résultats de ce travail soutiennent la transition mondiale vers une énergie durable, offrant des perspectives précieuses pour l'optimisation des systèmes éoliens dans des conditions environnementales complexes.

Mots-clés:

Système de conversion d'énergie éolienne (SCEE), principe de séparation de fréquence, suivi du point de puissance maximale (MPPT), ondulation de couple électromagnétique, stratégies de contrôle avancées, algorithmes métaheuristiques, contrôle H∞, contrôle LQR, contrôleur proportionnel-intégral d'ordre fractionnaire (FOPI), contrôleur proportionnel-intégral d'ordre fractionnaire filtré (FOPIF), générateur à induction.

Table of Contents

Acknowledgments i
Dedication ii
Table of Contents vi
Table of Figures x
List of Tables xiv
Table of symbols And Abbreviations xv
GENERAL INTRODUCTION 1
1. General Introduction 2
2. Problematic and Related Works 3
3. Thesis Objectives 4
4. Innovations and Contributions 5
5. Thesis Structure 6
CHAPTER I: Modeling And Simulation Of Wind Energy Conversion System 8
I. 1 Introduction 9
I. 2 Related Works 9
I. 3 Wind Turbine Design 11
I. 4 Wind Turbine Aerodynamics 12
I. 4.1 Wind Modeling 13
I. 4.2 Conversion of Wind Kinetic Energy 17
I. 5 Drive Train 20
I. 5.1 One-Mass Model 22
I. 5.2 Two-Mass Model 23
I. 5.3 Three-Mass Model 24
I. 6 Modeling of Squirrel Cage Induction Generator 25
I.6.1 Basic Principles of SCIG 25
I.6.2 d-q Axis Modeling of SCIG 25
I.5.2.1 Stator and Rotor Voltage Equations 25
I.6.2.2 Flux Linkage Equations 26
I.6.2.3 Mechanical Equation 27
I.6.3 State-Space Representation of SCIG 27
I.6.4 System Matrix A and Input Matrix B 28
I.7 Dynamic Modeling of Wind Energy Conversion Systems (WECS) 29
I.8 Linearization of WECS (Wind Energy Conversion Systems) 30

I.9 CONCLUSION 33
CHAPTER II: MPPT Control Strategy Of Wind Energy Conversion System 35
II. 1 Introduction 36
II. 2 Literature Review and Related Works 36
II. 2.1 Related Works 36
II. 2.2 Different MPPT Methods 37
II. 2.2.1 Indirect Power Control (IPC) Based MPPT Algorithms 40
II. 2.2.2 Direct Power Control (DPC) Based MPPT Algorithm 46
II. 2.2.3 Smart MPPT Algorithms 50
II. 3 Problem Statement 55
II. 4 Standard On-Off Controller 56
II. 4.1 Controller Design 57
II. 4.2 Simulation Results 58
II.4.2.1 Low Turbulence Stochastic Wind Speed 59
II.4.2.2 High Turbulence Stochastic Wind Speed 61
II. 5 Improved On-Off Controller 63
II. 5.1 Controller Design 63
II. 5.2 Simulation Results 64
II.5.2.1 Low Turbulence Stochastic Wind Speed 65
II.5.2.2 High Turbulence Stochastic Wind Speed 67
II. 6 Enhanced Fuzzy On-Off Controller 69
II. 6.1 Fuzzy On-Off Controller 69
II. 6.2 Enhanced Fuzzy On-Off Controller Design 70
II. 6.3 Simulation Results 72
II.6.3.1 Low Turbulence Stochastic Wind Speed 72
II.6.3.2 High Turbulence Stochastic Wind Speed 74
II. 7 Sliding Mode Controller 75
II. 7.1 Controller Design 76
II. 7.2 Simulation Results 81
II.7.2.1 Low Turbulence Stochastic Wind Speed 81
II.7.2.2 High Turbulence Stochastic Wind Speed 83
II.8 CONCLUSION 85
CHAPTER III: MPPT Control Strategy Of Wind Energy Conversion System Using Metaheuristic Algorithms 86
III. 1 Introduction 87
III. 2 Literature Review 87

III. 2.1 Hybrid MPPT Algorithms 87
III. 2.1.1 Combination of Conventional Algorithms 88
III. 2.1.2 Conventional + Smart Algorithms 88
III. 2.1.3 Conventional + Optimization Algorithms 89
III. 3 Improved On-Off Control Based On PSO 96
III. 3.1 Particle Swarm Optimization (PSO) 97
III. 3.2 Electromagnetic Torque Ripple Attenuation of WECS Using An Improved On-Off Control Based On PSO 98
III. 3.3 Simulation Results 99
III. 3.3.1 Low Turbulence Stochastic Wind Speed 100
III. 3.3.2 High Turbulence Stochastic Wind Speed 102
III. 4 Enhanced On-Off Control Based On WOA 105
III. 4.1 Whale Optimization Algorithm (WOA) 106
III. 4.2 Enhanced On-Off Control For Wind Energy Conversion System Electromagnetic Torque Ripple Minimization Based On Whale Optimization Algorithm 107
III. 4.3 Simulation Results 108
III. 4.3.1 Low Turbulence Stochastic Wind Speed 109
III. 4.3.2 High Turbulence Stochastic Wind Speed 111
III. 5 COOT Enhanced On-Off Control Based On Hysteresis Function 112
III. 5.1 COOT optimization Algorithm (COA) 114
III. 5.2 COOT Enhanced On-Off Control Based On Hysteresis Function for MPPT and Electromagnetic Torque Ripple Minimization of WECS 115
III. 5.3 Simulation Results 119
III. 5.3.1 Low Turbulence Stochastic Wind Speed 119
III. 5.3.2 High Turbulence Stochastic Wind Speed 121
III. 6 Improved On-Off Control Based On Multi Objective PSO 124
III. 6.1 Simulation Results 129
III. 6.1.1 Low Turbulence Stochastic Wind Speed 129
III. 6.1.2 High Turbulence Stochastic Wind Speed 132
III.7 CONCLUSION 135
CHAPTER IV: Advanced control structure based on the Principle of Frequency Separation of a Wind Energy Conversion System 136
IV. 1 Introduction 137
IV. 2 Control Problem Formulation 138
IV. 2.1 Steady-state optimization: tracking the optimal point 139
IV. 3 Optimal Control Structure Design Based on the Frequency Separation Principle 140
IV. 3.1 Crafting the design for the low-frequency loop 140

IV. 3.2 The High-Frequency Loop Design 142
IV. 3.2.1 The High-Frequency Loop Design based on the LQG Controller Approach 143
IV. 3.2.2 The High-Frequency Loop Design based on the H∞ Controller Approach 145
IV. 4 Results and Discussion 151
IV. 4.1 Low turbulence stochastic wind speed 151
IV. 4.2 High turbulence stochastic wind speed 156
IV. 4.3 Real Wind Model (Natural Wind Intensity Curve) 160
IV. 4.4 Robustness Test 164
IV.5 CONCLUSION 168
General Conclusions and Future Work 170
1. General Conclusions 171
2. Futures Works 172
References 174
Scientific Production 186
Appendix A 187
Appendix B 188
Biography 189

Table of Figures

CHAPTER I: Modeling And Simulation Of Wind Energy Conversion System

Figure I. 1 Types of Wind Turbines. 12
Figure I. 2 Components of a Horizontal Axis Wind Turbine. 12
Figure I. 3 Van der Hoven Wind Model. 15
Figure I. 4 Block Diagram Of Wind Speed Construction Based On Nichita Model [19]. 17
Figure I. 5 Low turbulence stochastic wind speed. 17
Figure I. 6 High turbulence stochastic wind speed. 17
Figure I. 7 Model of actuator disk interaction with wind [54]. 18
Figure I. 8 One-Mass Drive Train Model 22
Figure I. 9 Schematic Diagram Of The WECS Based SCIG. 29

CHAPTER II: MPPT Control Strategy Of Wind Energy Conversion System

Figure II. 1 WECS operating regions. 38
Figure II. 2 Characteristics of Wind Turbine Power under optimal values of λ_{opt} and CP_{opt} 38
Figure II. 3 Classification of MPPT Algorithms for WECS. 40
Figure II. 4 The Schematic Diagram of The WECS Utilizing The TSR Method. 41
Figure II. 5 The Schematic Diagram of The WECS Utilizing The PSF Method. 42
Figure II. 6 The Schematic Diagram Of The WECS Utilizing The OTC Method. 46
Figure II. 7 Decision Case For MPPT Control On The Static Power Curve Of A WECS. 56
Figure II. 8 Block Diagram Of The Standard On-Off Controller. 58
Figure II. 9 Low Turbulence Stochastic Speed. 59
Figure II. 10 Electromagnetic Torque. 59
Figure II. 11 Mechanical Speed of Generator Ωh 60
Figure II. 12 Power coefficient (CP). 60
Figure II. 13 Electrical power. 60
Figure II. 14 High turbulence stochastic wind speed. 61
Figure II. 15 Electromagnetic Torque. 61
Figure II. 16 Mechanical Speed of Generator Ωh 62
Figure II. 17 Power coefficient (CP). 62
Figure II. 18 Electrical Power. 62
Figure II. 19 Block Diagram Of The Improved On-Off Controller. 64
Figure II. 20 Electromagnetic Torque. 65
Figure II. 21 Mechanical Speed of Generator Ωh 65
Figure II. 22 Power coefficient (CP). 66
Figure II. 23 Electrical Power. 66
Figure II. 24 Electromagnetic Torque. 67
Figure II. 25 Mechanical Speed of Generator Ωh 67
Figure II. 26 Power coefficient (CP). 68
Figure II. 27 Electrical Power. 68
Figure II. 28 Block Diagram of The Fuzzy On-Off Controller. 70
Figure II. 29 Block Diagram of The Enhanced Fuzzy On-Off Controller. 71
Figure II. 30 Membership Functions Used For $\sigma, \dot{\sigma}$ and Z^f 72
Figure II. 31 Electromagnetic Torque. 72
Figure II. 32 Mechanical Speed of Generator Ωh 73

Figure II. 33 Power coefficient (CP). 73
Figure II. 34 Electrical Power. 73
Figure II. 35 Electromagnetic Torque. 74
Figure II. 36 Mechanical Speed of Generator Ωh 74
Figure II. 37 Power coefficient (CP). 75
Figure II. 38 Electrical Power. 75
Figure II. 39 Electromagnetic Torque. 81
Figure II. 40 Mechanical Speed of Generator Ωh 82
Figure II. 41 Power coefficient (CP). 82
Figure II. 42 Electrical Power. 82
Figure II. 43 Electromagnetic Torque. 83
Figure II. 44 Mechanical Speed of Generator Ωh 83
Figure II. 45 Power coefficient (CP). 84
Figure II. 46 Electrical Power. 84

CHAPTER III: MPPT Control Strategy Of Wind Energy Conversion System Using Metaheuristic Algorithms

Figure III. 1 Flow Chart Indicating Classification Of Metaheuristic Optimization Techniques. 90
Figure III. 2 PSO layout diagram block for adjustment of improved controller parameters. 97
Figure III. 3 Flowchart of the PSO approach for optimizing the Improved On-Off controller. 99
Figure III. 4 Low Turbulence Stochastic Speed. 100
Figure III. 5 Electromagnetic Torque. 101
Figure III. 6 Error $e(t)=\Gamma_{em}^{*}-\Gamma_{em}$ 101
Figure III. 7 Power coefficient (CP). 101
Figure III. 8 Mechanical Speed of Generator Ωh 102
Figure III. 9 Electrical power. 102
Figure III. 10 High turbulence stochastic wind speed. 103
Figure III. 11 Electromagnetic Torque. 103
Figure III. 12 Error $e(t)=\Gamma_{em}^{*}-\Gamma_{em}$ 104
Figure III. 13 Power coefficient (CP). 104
Figure III. 14 Mechanical Speed of Generator Ωh 104
Figure III. 15 Electrical Power. 105
Figure III. 16 WOA Layout Diagram Block For Adjustment Of Improved On-Off Controller Parameters. 106
Figure III. 17 Flowchart Of The WOA Approach For Optimizing The Improved On-Off Controller. 108
Figure III. 18 Electromagnetic Torque. 110
Figure III. 19 Electromagnetic Torque Zoom [35s-40s]. 110
Figure III. 20 Power coefficient (CP). 110
Figure III. 21 Electromagnetic Torque. 111
Figure III. 22 Electromagnetic Torque Zoom [70s-80s]. 112
Figure III. 23 Power coefficient (CP). 112
Figure III. 24 COOT Optimization Algorithm layout diagram block for adjustment of improved controller Based on Hysteresis Function parameters. 114
Figure III. 25 Flowchart of the COOT Optimization Algorithm approach for optimizing the Improved On-Off controller. 118
Figure III. 26 Power Coefficient (CP). 119
Figure III. 27 Electrical Power. 120
Figure III. 28 Electromagnetic Torque. 120

Figure III. 29 Electromagnetic Torque Zoom [67s-74s]....120
Figure III. 30 Mechanical Speed of Generator Ωh 121
Figure III. 31 Power Coefficient (CP)....122
Figure III. 32 Electrical Power....122
Figure III. 33 Electromagnetic Torque....123
Figure III. 34 Electromagnetic Torque Zoom [47s-56s]....123
Figure III. 35 Mechanical Speed of Generator Ωh 123
Figure III. 36 WECS responses (PSO Improved On-Off Controller for Electromagnetic Torque Ripple Minimization): (a) Electromagnetic Torque, (b) Power coefficient (CP)....125
Figure III. 37 WECS responses (PSO Improved On-Off Controller for Power Coefficient Maximization): (a) Electromagnetic Torque, (b) Power coefficient (CP)....125
Figure III. 38 Multi Objective PSO Layout Diagram Block For Adjustment of Improved Controller Parameters....126
Figure III. 39 Flowchart of The MOPSO Approach For Optimizing The Improved On-Off Controller....128
Figure III. 40 Electromagnetic Torque....130
Figure III. 41 Electromagnetic Torque Zoom [30s-40s]....130
Figure III. 42 Power Coefficient (CP)....130
Figure III. 43 Mechanical Speed of Generator Ωh 131
Figure III. 44 Electrical Power....131
Figure III. 45 Electromagnetic Torque....133
Figure III. 46 Electromagnetic Torque Zoom [30s-40s]....133
Figure III. 47 Power Coefficient (CP)....133
Figure III. 48 Mechanical Speed of Generator Ωh 134
Figure III. 49 Electrical power....134

CHAPTER IV: Advanced control structure based on the Principle of Frequency Separation of a Wind Energy Conversion System

Figure IV. 1 Frequency Separation Principle....139
Figure IV. 2 The correlation between the power coefficient and the tip speed....140
Figure IV. 3 Low-Frequency loop based on FOPI/PSO-FOPIF Controller....141
Figure IV. 4 Block Diagram of the Controllers and Their Transfer Functions....141
Figure IV. 5 Block Diagram of the PSO-FOPIF Controller....142
Figure IV. 6 The Optimal High-Frequency Loop....143
Figure IV. 7 General control configuration....148
Figure IV. 8 Low turbulence stochastic wind speed....152
Figure IV. 9 Power Coefficient (CP)....152
Figure IV. 10 Power Coefficient (CP) Zoom [0s-8s]....152
Figure IV. 11 Electrical Power....153
Figure IV. 12 Electromagnetic Torque....153
Figure IV. 13 Electromagnetic Torque Zoom [70s-75s]....153
Figure IV. 14 Mechanical Speed of Generator ωh 154
Figure IV. 15 High turbulence stochastic wind speed....156
Figure IV. 16 Power Coefficient (CP)....156
Figure IV. 17 Power coefficient (CP) Zoom [0s-8s]....157
Figure IV. 18 Electrical power....157
Figure IV. 19 Electromagnetic Torque....157
Figure IV. 20 Electromagnetic Torque Zoom [8s-11s]....158
Figure IV. 21 Mechanical Speed of Generator ωh 158

Figure IV. 22 Extracting the natural wind intensity curve using an anemometer [The Renewable Energy Laboratory at the College of Engineering at the University of Sharjah]. 160
Figure IV. 23 Real Wind Model (Natural Wind Intensity Curve). 161
Figure IV. 24 Power coefficient (CP). 161
Figure IV. 25 Power coefficient (CP) Zoom [0s-8s]. 161
Figure IV. 26 Electrical power. 162
Figure IV. 27 Electromagnetic Torque. 162
Figure IV. 28 Electromagnetic Torque Zoom [0s-10s]. 162
Figure IV. 29 Mechanical Speed of Generator ωh 163
Figure IV. 30 Total High Speed Shaft Inertia. 165
Figure IV. 31 Power coefficient (CP). 166
Figure IV. 32 Power coefficient (CP) Zoom [44s-51s]. 166
Figure IV. 33 Electromagnetic Torque. 166
Figure IV. 34 Electromagnetic Torque Zoom [44s-51s]. 167

List of Tables

CHAPTER II: MPPT Control Strategy Of Wind Energy Conversion System

Table II. 1 Comparison of IPC based MPPT Algorithms for WECS. 40
Table II. 2 Comparison of DPC based MPPT Algorithms for WECS. 46
Table II. 3 Comparison of Smart MPPT Algorithms for WECS. 50
Table II. 4 MPPT Control Logic. 55
Table II. 5 Fuzzy Rules. 71

CHAPTER III: MPPT Control Strategy Of Wind Energy Conversion System Using Metaheuristic Algorithms

Table III. 1 Summary of Hybrid-Conventional MPPT Algorithms for WECS. 88
Table III. 2 Summary of hybrid methods (conventional MPPT and Smart Algorithms) for WECS. 88
Table III. 3 Summary of Reviewed Swarm-Based Metaheuristic Optimization Techniques. 96
Table III. 4 PSO Parameters. 98
Table III. 5 Parameters of The Improved ON-OFF Control Using Low Turbulence Stochastic Wind Speed. 100
Table III. 6 Parameters of The Improved ON-OFF Control Using High Turbulence Stochastic Wind Speed. 103
Table III. 7 WOA Parameters. 109
Table III. 8 Parameters of The Enhanced ON-OFF Control Using Low Turbulence Stochastic Wind Speed. 109
Table III. 9 Parameters of The Improved ON-OFF Control Using High Turbulence Stochastic Wind Speed. 111
Table III. 10 COOT Parameters. 117
Table III. 11 Parameters of the Different Controllers using low turbulence stochastic wind speed. 119
Table III. 12 Parameters Of The Different Controllers Using High Turbulence Stochastic Wind. 122
Table III. 13 MOPSO Parameters. 129
Table III. 14 Parameters of The Different Controllers Using Low Turbulence Stochastic Wind Speed. 129
Table III. 15 Parameters of The Different Controllers Using High Turbulence Stochastic Wind. 132

CHAPTER IV: Advanced control structure based on the Principle of Frequency Separation of a Wind Energy Conversion System

Table IV. 1 Comparison of Different Control Strategies Under Low-Turbulence Wind Conditions. 155
Table IV. 2 Comparison of Different Control Strategies Under High-Turbulence Wind Conditions. 159
Table IV. 3 Comparison of Different Control Strategies Under Real Wind Model. 164
Table IV. 4 The Values of The Inertias Parameters. 165
Table IV. 5 Comparison of Different Control Strategies Under Varying Internal System Parameters. 167

Appendix A

Table A. 1 Parameters of The Low Turbulence Stochastic Wind Speed 187
Table A. 2 Parameters of The High Turbulence Stochastic Wind Speed. 187

Appendix B

Table B. 1 Parameters of The Low-Power Rigid-Drive-Train SCIG-Based WECS. 188

Table of symbols And Abbreviations

Symbols		**Symbols**	
P_{wt}	Aerodynamic power.	J_h	The Inertia rendered in HSS (the high-speed shaft).
C_P	The Power Coefficient.	T_G	The Electromagnetic torque subsystem time constant.
CP_{max}	The Optimal Power Coefficient.	Ω_h	Mechanical Speed of Generator.
$C_\Gamma(\lambda)$	The Torque coefficient.	G	Gearbox ratio.
λ	The Tip-Speed Ratio.	T_f	Filtering time constant.
R	The Radius of the wind turbine blades.	K_f	Gain.
ρ	The Air density.	η	Efficiency.
v	Wind speed.	Rr	Rotor Resistance.
Ω_t	The Turbine Speed.	Rs	Stator Resistance.
Γ_{wt}	The Aerodynamic torque	Lr	Rotor inductance.
Γ_G	The Electromagnetic torque .	Ls	Stator inductance.
Γ_G^*	The Electromagnetic torque reference.	Lm	Magnetizing inductance.
Abbreviations			
WECS	Wind Energy Conversion System		
MPPT	Maximum Power Point Tracking		
SCIG	Squirrel Cage Induction Generator		
WTGs	Wind Turbine Generators		
LQG	Linear Quadratic Gaussian Control		
LQR	Linear Quadratic Regulator		
FOPI	Fractional-Order Proportional-Integral Controller		
CP	The Power Coefficient.		
ORC	The Optimal Regimes Characteristic		
HSS	High-Speed Shaft		
HAWT	horizontal axis wind turbine		
WWEA	The World Wind Energy Association		
GWEC	The Global Wind Energy Council		
Std	Standard deviation of Electromagnetic Torque		

GENERAL INTRODUCTION

1. General Introduction

The context of the ongoing technological and industrial renaissance, the insatiable human appetite for energy has reached unprecedented levels. This surge in energy consumption is driven by individual needs and the broader requirements of societies and nations. Consequently, renewable energy sources have emerged as a crucial and unavoidable reality, representing an urgent necessity for global sustainability. This imperative transcends national boundaries, emphasizing the need for alternative energy sources to mitigate reliance on fossil fuels, which are not only depleting but also contributing significantly to environmental challenges. The environmental impact of fossil fuel consumption, characterized by greenhouse gas emissions, has become a pressing concern as it exacerbates climate change [1-136].

The significance of renewable energy lies in its cleaner and less polluting nature compared to traditional methods of energy production. Renewable energy sources, particularly wind energy, offer a promising alternative that avoids the detrimental consequences associated with fossil fuel consumption, such as heightened global warming and the environmental hazards posed by nuclear reactor waste. Wind energy, characterized by the horizontal movement of air masses across the atmosphere, is driven by variations in atmospheric pressure between different regions. This results in a consistent flow of wind from areas of high pressure to those with lower pressure [1,137]. Historically, wind power was harnessed to perform mechanical tasks, such as grinding grains through windmills. However, recent advancements have enabled the transformation of wind energy into electrical energy, marking a significant evolution spurred by human innovation.

The integration of wind energy into contemporary energy portfolios signifies a pivotal shift towards sustainability. However, this transition comes with new challenges, particularly in terms of environmental impact and technological efficiency. The last few decades have witnessed remarkable advancements in wind energy harvesting, driven by technological innovations that have significantly enhanced its feasibility and cost-effectiveness. Modern wind turbines, engineering marvels in their own right, have grown substantially in size and capacity, allowing for more efficient capture of the kinetic energy of the wind. This progress is further supported by improvements in energy storage solutions, which are crucial for managing the intermittent nature of wind power and ensuring a consistent energy supply.

The global capacity for installed wind power has seen impressive growth, from 748.6 GW in 2018 to 1201.7 GW in 2024, according to The World Wind Energy Association (WWEA) [2]. Forecasts from the Global Wind Energy Council (GWEC) predict a potential increase in wind energy production to 2,750 GW by 2030 [3], underscoring the sector's vast potential and its integral role in the

broader landscape of sustainable energy. The efficiency of wind turbines is predominantly contingent upon the performance of the electrical generators embedded within them, the efficacy of the control systems employed, and the integration of power electronics for grid connection. Various generator types are utilized in wind energy systems [45,73], including the doubly-fed induction generator (DFIG), the permanent magnet synchronous generator (PMSG), and the squirrel cage induction generator (SCIG). Among these, squirrel cage induction generators are increasingly favored due to their straightforward modeling, high reliability, and ability to optimize power output [4].

2. Problematic and Related Works

Wind turbine control has garnered extensive research attention, particularly in the domain of electromagnetic torque control within wind energy conversion systems. Among the commonly explored approaches, the Standard On-Off controller has been widely studied [5,80]. However, its reliance on a sign function introduces significant challenges, most notably the chattering phenomenon. Chattering induces high-frequency oscillations that jeopardize system stability, degrade performance, and accelerate wear, thereby increasing maintenance demands. To mitigate these issues, various studies have proposed enhancements to the Standard On-Off controller. A notable solution, introduced in [6], incorporates a first-order filter into the controller's discontinuous segment, effectively reducing chattering, though not eradicating it entirely. Building on this, the researchers in [7] have leveraged Metaheuristic algorithms, such as particle swarm optimization (PSO), to fine-tune the parameters of the improved On-Off controller. This optimization further mitigates electromagnetic torque ripple and enhances overall performance. While the PSO-optimized controller significantly alleviated chattering, it revealed a critical trade-off: a substantial reduction in the power coefficient (CP), leading to decreased electrical power generation. Further advancements in controller design focused on modifying the internal structure of the improved On-Off controller by replacing the sign function with a hysteresis function [6]. This adjustment notably reduced electromagnetic torque ripple but at the cost of imperfect maximum power point tracking, which hindered the turbine's ability to generate peak power. To address these limitations, researchers in [8] explored the COOT optimization algorithm (COA) to enhance the Improved On-Off controller based on hysteresis function. This approach aimed to optimize controller parameters for superior power tracking and electrical output. Although the proposed controller successfully tracked the maximum power point, it failed to maintain a low torque ripple. These findings underscore a persistent inverse relationship between minimizing electromagnetic torque ripple and maximizing power generation. This trade-off presents a significant challenge for wind power producers. While reducing torque ripple enhances system durability and lowers maintenance costs, it often compromises power output. Conversely, maximizing electrical power generation tends to amplify torque ripple, complicating control strategies. In response to these

complexities, researchers have turned to advanced control frameworks. One promising approach employs the frequency separation principle to establish a dual-loop control architecture for variable-speed wind turbines [9,53]. This method seeks to balance power maximization with mechanical stress reduction. The proposed architecture integrates two distinct controllers: a Linear Quadratic Gaussian (LQG) controller to attenuate torque ripple and a classical Proportional-Integral (PI) controller to optimize power conversion [10,12,53]. Preliminary evaluations demonstrate significant improvements in turbine performance, including higher power output and reduced mechanical stress. Despite these advances, there remains considerable scope for refinement. By further enhancing the frequency separation-based framework and integrating supplementary control strategies, future developments may achieve an optimal balance between power generation and torque ripple mitigation, advancing the efficiency and reliability of wind energy systems.

3. Thesis Objectives

Wind energy systems have been emerging as a highly significant solution to the problem of limited traditional energy sources. In this thesis, control methodologies adapted to wind energy systems are topically modelised, reviewed and analysed. The proposed research addresses the challenges posed by instantaneous wind fluctuations and the non-linearity of wind turbines, which prevent the full exploitation of wind energy with high efficiency and reliability. More specifically, the main objective of this work is to suggest a new optimal control structure for the wind Energy conversion system (WECS), which guarantees a compromise between maximizing energy efficiency and minimizing input control effort.

To achieve this, first, we explored and improved various controllers using metaheuristic algorithms for single and multi-objective optimization, based on fuzzy logic and sliding-mode controllers. The obtained results from the various experiments showed that while significant performance gains have been achieved, persistent problems such as continuous chattering and sub-optimal maximum power point tracking (MPPT) remain unsolved challenges. Next, to improve conversion chain performance, we proposed and analyzed a control structure based on the principle of frequency separation, which enables WECS dynamics to be analyzed on two distinct time scales. In this approach, WECS dynamics are divided into low-frequency dynamics caused by slower wind speed components and high-frequency dynamics resulting from turbulent wind speed variations. This dual dynamic framework provides a more nuanced understanding of system behavior, allowing more precise control strategies that respond to varying operational conditions. The proposed control structure aims to enhance wind power point tracking while while simultaneously reducing mechanical loads, thus facilitating operation of the conversion system at its optimum point. By adopting this

innovative control strategy, the research seeks to address the inherent trade-offs between maximizing energy output and minimizing maintenance costs associated with wind turbines. This is particularly important given the non-linear characteristics of wind turbines, which can complicate the control strategies employed. The complexity of the turbine dynamics necessitates advanced control techniques that can adapt to real-time changes in wind conditions while ensuring optimal performance.

4. Innovations and Contributions

The innovative approach outlined in this thesis extends to the development of advanced control algorithms, including H∞ control [11] and Fractional-Order Proportional-Integral (FOPI) control and Filtred Fractional-Order Proportional-Integral (FOPIF) control tuned by PSO [12]. The H∞ control method offers robust performance in the presence of uncertainties and disturbances, making it suitable for managing the variable nature of wind energy. The FOPI controller, on the other hand, leverages the advantages of fractional calculus to enhance system responsiveness and improve tracking accuracy, addressing some of the limitations associated with traditional integer-order controllers. These advancements are particularly significant in the context of the electromagnetic torque ripple, commonly referred to as the chattering problem, which can negatively impact turbine performance and longevity.

The challenges associated with wind energy conversion systems are multifaceted. One of the primary issues is the inherent variability of wind. Wind speeds are subject to fluctuations due to meteorological conditions, leading to inconsistent energy production. Traditional control systems often struggle to keep pace with these rapid changes, resulting in suboptimal performance. The proposed control strategies in this research aim to counteract these challenges by utilizing advanced algorithms that can adapt to real-time wind conditions, ensuring that the system operates efficiently despite the variable nature of wind resources. This adaptability is crucial for maximizing the power coefficient of the turbines, which is a key indicator of the efficiency of wind energy conversion.

Moreover, the advancement of power electronics has played a pivotal role in the evolution of wind energy systems. The integration of sophisticated power converters enables better control of the output power, facilitating grid connection and improving the overall efficiency of the system. These converters allow for the optimization of the power extracted from the wind, reducing losses associated with the conversion process. As a result, they significantly contribute to the effectiveness of the proposed control strategies by ensuring that the generated energy is transmitted to the grid with minimal losses.

The research presented in this thesis is underpinned by a thorough literature review that highlights the evolution of wind energy technologies and the associated control strategies. This review encompasses various methodologies that have been employed over the years, including classical control approaches and modern optimization techniques. The literature indicates a clear trend towards the adoption of Metaheuristic algorithms for optimizing control parameters in wind energy systems. Techniques such as Particle Swarm Optimization (PSO) [13] and COOT Optimization Algorithm (COA) [14,15] have garnered attention for their effectiveness in fine-tuning control parameters to enhance performance. By building upon this existing body of knowledge, this research aims to introduce innovative control strategies that leverage these optimization techniques to improve the overall performance of wind energy conversion systems.

5. Thesis Structure

In light of these advancements, the thesis is structured into several chapters, each designed to systematically explore the intricacies of WECS and the proposed control strategies. The first chapter begins with an exploration of the modeling and simulation of wind energy conversion systems, providing a foundational understanding of wind turbine design, aerodynamics, and the dynamics of squirrel cage induction generators. It concludes with an overview of the linearization of WECS, laying the groundwork for the subsequent chapters. This initial chapter is critical as it establishes the baseline upon which the rest of the research is built, ensuring that the subsequent discussions are grounded in a solid understanding of the underlying principles governing wind energy systems.

The second chapter shifts focus to various maximum power point tracking (MPPT) control strategies employed in wind energy conversion systems. This chapter includes a literature review of existing control methodologies, detailing the design and simulation results of traditional and improved controllers, such as Standard On-Off, Improved On-Off, Enhanced Fuzzy On-Off and Sliding Mode controllers, highlighting their strengths and limitations. The discussion delves into the mechanisms by which these controllers operate, examining how they respond to changes in wind conditions and the challenges they face in maintaining optimal performance. The literature review also underscores the importance of real-time data acquisition and monitoring systems that can facilitate responsive control strategies.

The third chapter delves into the application of Metaheuristic algorithms in optimizing the control of WECS. It covers a range of techniques, including Particle Swarm Optimization (PSO), Whale Optimization Algorithm (WOA) [16], COOT Optimization Algorithm (COA) and other contemporary algorithms aimed at minimizing electromagnetic torque ripple while maximizing power output. By employing these algorithms, the research aims to enhance the performance of the improved

On-Off controller, addressing the inherent trade-offs between energy efficiency and mechanical stress. The integration of Metaheuristic optimization methods is particularly valuable as it allows for a more systematic exploration of the parameter space, leading to the identification of optimal control settings that enhance overall system performance.

The fourth chapter presents an advanced control structure grounded in the frequency separation principle for wind energy conversion systems (WECS). This chapter introduces novel approaches, including the integration of Linear Quadratic Regulator (LQR) and H∞ control strategies within the proposed dual-loop control architecture, showcasing their efficacy in improving system performance under diverse operational scenarios. The dual-loop control design effectively addresses high-frequency fluctuations caused by turbulent wind conditions and low-frequency dynamics resulting from gradual wind speed variations. This strategic separation of dynamics is pivotal for achieving optimal maximum power point tracking (MPPT) while simultaneously minimizing mechanical stress on turbine components.

The thesis concludes with a comprehensive synthesis of the findings and offers recommendations for future research, underscoring the potential benefits of the proposed control strategies for wind energy producers. The contributions of this research are multifaceted, aiming to make a significant impact on the field of wind energy conversion systems. By proposing an innovative control architecture founded on the frequency separation principle, the study tackles critical challenges related to the integration of renewable energy into existing energy infrastructures. Furthermore, it establishes a robust framework for optimizing energy output and reducing maintenance costs, both of which are essential for the long-term sustainability of wind energy as a viable power source.

Ultimately, this research endeavors to enrich the growing body of knowledge on wind energy conversion systems and their control strategies. By addressing the complexities inherent in these systems, it aspires to contribute meaningfully to the global transition toward a more sustainable and resilient energy future.

CHAPTER I: Modeling And Simulation Of Wind Energy Conversion System

I. 1 Introduction

This chapter explores the intricate processes and advanced technologies integral to converting wind energy into electrical power, which is central to modern sustainable energy systems. Wind Energy Conversion Systems (WECS) are crucial in harnessing the kinetic energy of the wind. These systems convert wind energy first into mechanical energy using rotor blades, and subsequently into electrical energy via generators. Effective design and operation of WECS require a deep understanding of both fundamental principles and the sophisticated technologies that ensure efficient and reliable energy conversion. The chapter begins with a comprehensive overview of WECS, setting the stage for a detailed exploration of the technologies driving wind turbines. It includes a comparative analysis of horizontal and vertical axis turbines, highlighting their unique characteristics and applications. The discussion also emphasizes the critical role of modeling and simulation in optimizing turbine performance and reliability. Central to the wind energy conversion process is the role of wind speed, which significantly influences power output. This chapter examines the relationships between wind speed and power capture, providing insights into how power can be adjusted through pitch angle modifications or generator torque and speed control. Such power control methods are essential for maximizing energy output over a range of wind speeds while ensuring the system's reliability and protecting against damage from strong gusts. By integrating fundamental principles with advanced technological insights, this chapter contributes to a deeper understanding of WECS, advancing knowledge and supporting the ongoing development and integration of wind energy systems into broader energy infrastructures.

I. 2 Related Works

Extensive research has been conducted on wind turbine design, delving into various techniques, components, and critical aspects of wind power generation. These studies aim to address the engineering challenges inherent in wind energy conversion systems. Quarton [17] examines the evolution of analytical methods for wind turbine design over the past two decades. The field has transitioned from relying on basic calculations informed by engineering intuition to the widespread use of sophisticated computer-based analyses. This progression reflects a shift towards more rigorous and accurate methodologies. The work also explores the factors driving this transformation, evaluates the current state of the art, identifies unresolved uncertainties, and predicts future developments in wind turbine calculation techniques. Similarly, Tong [18] provides a comprehensive resource on wind turbine design, incorporating recent developments and practical approaches for engineers and researchers in the wind energy sector. Covering fundamental principles, design techniques, primary

component development, and critical issues in wind power generation, the text serves as a foundational reference. It integrates insights from leading manufacturers, national laboratories, and academic institutions, offering an invaluable resource for both practitioners and students.

A critical aspect of understanding wind energy conversion systems lies in modeling and simulating wind behavior. Accurate wind models are necessary for realistic experimental simulations. Nichita et al. [19] propose methodologies for simulating wind speed applicable to wind turbine simulators in both standalone and hybrid systems. Their approach decomposes wind speed into medium- and long-term components defined by site-specific power spectra and a turbulence component influenced by the larger-scale wind speed evolution. The turbulence component, treated as a nonstationary process, is simulated using rational and nonrational filters. These models, characterized by parameters derived experimentally or estimated a priori, address practical implementation considerations, providing a robust framework for wind speed simulation.

The drive train is a pivotal component in wind energy conversion systems, serving as the primary link between the turbine and the generator. Its performance significantly influences the overall efficiency and reliability of the system. Numerous studies have focused on optimizing the drive train to enhance system performance. Struggl, Berbyuk, and Johansson [20] review investigations into drive train systems for wind turbines, highlighting the critical role of gearboxes in system maintenance. Issues such as gear tooth damage and bearing faults are identified as leading causes of downtime. Their research emphasizes the need for detailed models that capture complex phenomena, including backlash and gear transmission errors, while avoiding oversimplifications. These models are essential for designing lightweight, durable components capable of faultless operation over a 20-year lifespan. Peeters [21] contributes further by developing a consistent modeling approach to describe the dynamic behavior of wind turbine drive trains, focusing particularly on gearboxes. This work addresses limitations in traditional design codes that treat drive train components quasi-statically, providing insufficient insight into load variations and stress distribution. The research introduces three multibody system modeling approaches. The first examines torsional vibrations, while the second offers a detailed representation of bearings and gears, applicable to various configurations, including helical and spur gears in parallel and planetary gear stages. The third approach extends this analysis to incorporate elastic deformations in drive train components, alongside their rigid-body motion. These methodologies are applied to analyze individual gear stages, complete gearboxes, and entire drive trains, considering interactions with the rotor, tower, and generator. By focusing on low- and mid-frequency ranges, the research identifies potential resonances within the drive train. Validation is achieved through comparison with data from a measurement campaign conducted on a modern multi-megawatt wind turbine, underscoring the practical relevance of the proposed models. This body of

work collectively advances the understanding and design of wind energy systems, addressing key challenges and contributing to the optimization of turbine components and system performance.

I. 3 Wind Turbine Design

Wind turbine design is a multidisciplinary field that integrates principles from aerodynamics, mechanical engineering, electrical engineering, and environmental science to create efficient systems for converting wind energy into electrical power. The two main types of wind turbines, as shown in Figure I.1, are Horizontal Axis Wind Turbines (HAWTs)—the most common type, with components illustrated in Figure I.2—and Vertical Axis Wind Turbines (VAWTs), which are less common but capable of capturing wind from any direction [1,22]. The aerodynamics of wind turbines are crucial, with the blades designed to maximize lift and minimize drag as they interact with the wind. These blades, typically shaped like an airfoil, are engineered to optimize the lift-to-drag ratio, improving the turbine's efficiency [23]. The rotor, which includes the blades and hub, converts the wind's kinetic energy into rotational energy. Mechanical design elements such as the gearbox, yaw mechanism, and tower are also vital. The gearbox adjusts the rotor speed to match the generator's optimal speed, while the yaw mechanism ensures the rotor is always aligned with the wind. The tower's height is essential, as wind speed increases with altitude, and the materials used in construction, like fiberglass-reinforced plastic for blades and steel for towers, are chosen for their strength and durability [22, 24]. On the electrical side, the generator converts the rotational energy into electrical energy. Power electronics, including converters and inverters, regulate the electrical output to ensure compatibility with the grid. Advanced control systems, like pitch, yaw, and torque controls, optimize turbine performance and protect the system under various conditions [25, 26]. Structural integrity and material selection are vital for withstanding the stresses and fatigue from environmental conditions over the turbine's lifespan. Composite materials are used for blades, and towers are usually constructed from steel [22, 28]. Environmental and site considerations include wind resource assessment, where locations with optimal wind speeds are identified, and environmental impact assessments, which consider noise, visual impact, wildlife, and land use [3,24]. Finally, wind turbine design must comply with international standards, such as those provided by the International Electrotechnical Commission (IEC), and meet specific grid connection requirements to ensure power quality and safety [24]. In summary, wind turbine design integrates complex principles across several fields to create systems capable of efficiently harnessing wind energy while considering environmental impacts, economic viability, and regulatory compliance.

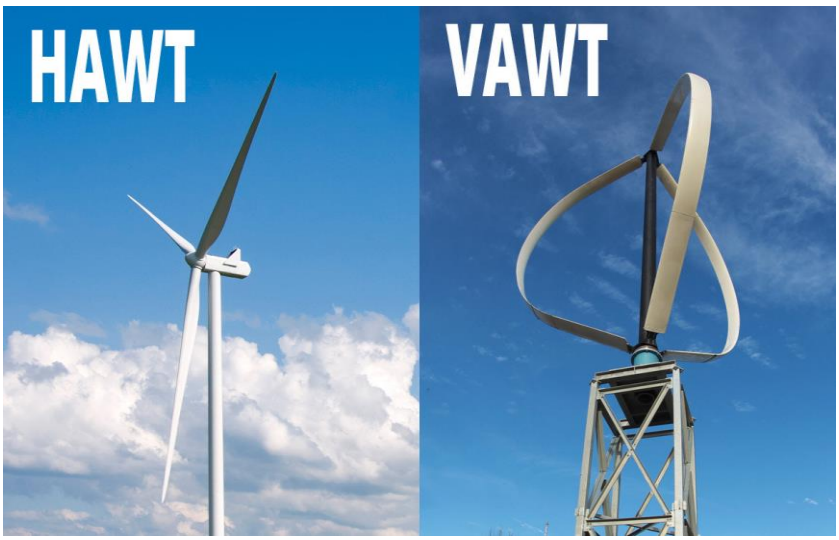


Figure I. 1 Types of Wind Turbines.

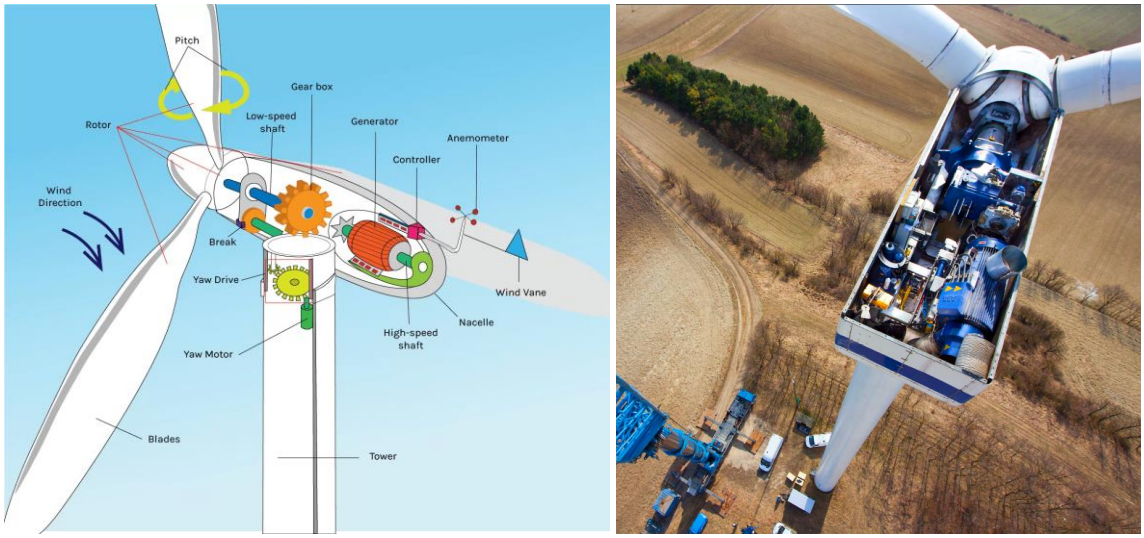


Figure I. 2 Components of a Horizontal Axis Wind Turbine.

I. 4 Wind Turbine Aerodynamics

The aerodynamic design of wind turbine blades is a critical factor in optimizing the efficiency of energy capture from wind resources. The design process must incorporate strategies to regulate power output and limit the rotational speed of the turbine rotor under wind conditions that exceed the rated or nominal wind speed. This is necessary to prevent excessive mechanical loads and to ensure that the generator operates within its specified power limits, thereby maintaining the structural integrity and longevity of the system. For large-scale wind turbines, these considerations are particularly imperative due to their inherently narrower safety margins, which are constrained by economic and size-related factors. Consequently, advanced aerodynamic design techniques, including blade pitch control and active load management, must be employed to mitigate the risks associated with high wind speeds and to optimize the overall performance and reliability of the turbine system.

I. 4.1 Wind Modeling

Wind is a complex and highly variable natural phenomenon, shaped by numerous factors, including geographic location, altitude, temperature, and atmospheric pressure. As one of the most rapidly expanding renewable energy sources globally, the effective utilization of wind energy necessitates precise wind modeling, which is critical for the analysis, design, and optimization of Wind Energy Conversion Systems (WECS). Accurate wind models are essential for predicting the behavior of wind turbines across a range of environmental conditions, thereby enhancing the performance, reliability, and efficiency of these systems. The ability to model wind accurately is crucial for capturing its inherent variability over both time and space, a key requirement in the design of effective WECS. This modeling process facilitates the prediction of wind turbine power output, enabling engineers to optimize energy generation based on anticipated wind conditions. Moreover, it supports the development of control strategies aimed at maximizing turbine performance through the application of advanced control mechanisms. Wind modeling also allows for the simulation of various wind scenarios, which is vital for stress testing turbines to assess their resilience under different conditions. Furthermore, understanding the impact of wind on turbine loads and structural dynamics is integral to ensuring the durability and longevity of these systems. Thus, wind modeling is indispensable in advancing the technology and reliability of wind energy systems. At the simplest level, wind can be modeled as a constant speed over time. This approach is often used for preliminary analysis and basic design calculations. However, constant speed models do not capture the inherent variability of wind, limiting their usefulness for dynamic simulations. A more refined approach is the steady wind model, which assumes a constant mean wind speed but can incorporate gradual changes over time. While still an oversimplification, it provides a better foundation for understanding wind behavior over longer periods.

To capture the statistical nature of wind, distribution models are employed. These models describe how wind speed varies over time at a given location.

- **Weibull Distribution:** The Weibull distribution was promoted by the Swedish physicist Weibull [27]. The Weibull distribution is the most commonly used model in wind energy studies. It is defined by two parameters: the shape parameter (k) and the scale parameter (c) . The shape parameter indicates how peaked the distribution is, while the scale parameter reflects the wind speed. A higher k -value suggests less variability in wind speeds, while a lower value indicates more variability. The Weibull probability density function for wind model is given by [28]:

$$f(v) = k.c^{-k}.v^{k-1}e^{-\left(\frac{v}{c}\right)^k} \quad \text{(I.1)}$$

Where the probability density $f(v)$ is the frequency distribution of the measured speeds, v is the wind speed.

The two Weibull parameters k and c are used to calculate the mean wind speed $\bar{v}$. We use the following expression [28]:

$$\bar{v} = c.\Gamma\left(1+\frac{1}{k}\right) \tag{I.2}$$

Where Γ is the gamma function.

- **Hybrid Weibull distribution:** The Hybrid Weibull distribution [29] is particularly significant in wind energy studies, where real wind speed data often display complexities that a single Weibull distribution may not adequately capture. Factors such as varying wind regimes, turbulence, and seasonal changes contribute to these complexities. To address these challenges, the Hybrid Weibull distribution integrates the Weibull distribution with another probability distribution, enabling a more accurate representation of wind speed data. This hybrid approach is more effective in modeling the diverse wind conditions observed across different periods or locations, as it better captures tail behavior, multiple peaks, and variations in wind speed [29,30]. The hybrid Weibull distribution is used when the quiet frequency is greater than or equal to 15% [54]. In general, this proportion cannot be neglected and must be taken into account when characterizing the site in terms of wind. This distribution is as follows [54]:

$$f(v) = (1-ff_0).\left(\frac{k}{c}\right).\left(\frac{v}{c}\right)^{k-1} e^{-\left(\frac{v}{c}\right)^k} \qquad \text{For} \quad v>0 \tag{I.3}$$

$$f(v) = ff_0 \qquad \text{For} \quad v<0 \tag{I.4}$$

Where ff_0 is the quiet frequency, which is determined from the wind data [30].

- **Rayleigh Distribution:** This is a special case of the Weibull distribution with a shape parameter (k) of 2 [54]. It is commonly employed in situations where detailed wind speed data is not available, and only the mean wind speed is known. Due to its simplicity and reasonable accuracy, the Rayleigh distribution is often considered suitable for various wind energy applications. The probability density function for this distribution is given by:

$$f(v) = 2.\frac{v}{c^2}.e^{-\left(\frac{v}{c}\right)^2} \tag{I.5}$$

Compared to the Weibull distribution, the Rayleigh distribution contains only one parameter, making it more convenient to use and its parameters easier to estimate.

However, the Rayleigh distribution is based on the assumption that the long-term mean wind vector is zero.

Wind dynamics arise from the interplay between meteorological conditions and the specific attributes of a particular wind site. Consequently, wind speed is represented in the literature as a non-stationary random process, formed by the superposition of two components [19,31,32].

$$v(t) = \bar{v}(t) + \Delta v(t) \tag{I.6}$$

In this context, $\bar{v}(t)$ represents the low-frequency component, which accounts for long-term, low-frequency variations, while $\Delta v(t)$ corresponds to the turbulence component, associated with rapid, high-frequency variations. These two components are also recognized in the Van der Hoven wideband model (Figure I.3). The spectral pause around 0.5 MHz permits the turbulence component to be modeled as a zero-mean random process. The low-frequency component reflects very gradual changes in wind speed and provides an energetic characterization of the wind site. This component can be described using a Rayleigh distribution (Equation I.5). Although this component influences the amplitude of turbulence, its progression is not critical for the short- and medium-term dynamic behavior of the WECS.

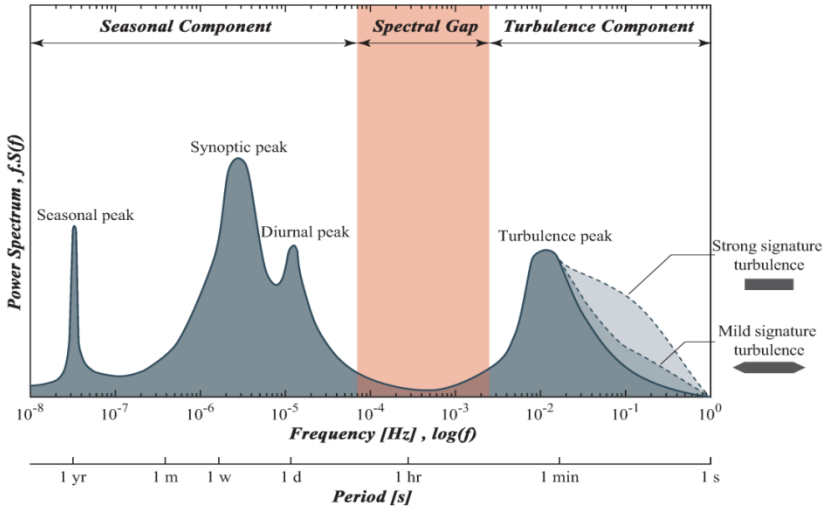


Figure I. 3 Van der Hoven Wind Model.

- **Nichita Model for Wind Speed**

Modeling wind turbines necessitates an understanding of how wind speed varies over time. However, wind speed remains an unpredictable and challenging variable to replicate at a specific site. One model, among many others, was introduced by C. Nichita in [19]. This method involves generating the temporal profile of wind from white noise, to which a transfer function of the non-

rational Von Karman filter is applied. The parameters of this function are determined by the site's characteristics and the nature of the wind [33]. The transfer function is approximated by:

$$\hat{H}_F(s) = K_F \frac{(m_1 T_F s + 1)}{(T_F s + 1)(m_2 T_F s + 1)} \tag{I.7}$$

Here, (m_1, m_2) represents Nichita parameters. The mathematical parameters TF and KF are calculated according to the following expressions:

$$T_F = \frac{L_F}{V} \tag{I.8}$$

$$K_F = \sqrt{\frac{\pi}{T_s \Delta\omega S_F}} \tag{I.9}$$

Where, L_F is the wind turbulence length scale (This value depends on the characteristics of the site, and varies from 100 at sea to 500 in turbulent areas), V is the average wind speed, which varies based on the wind's intensity (weak, medium, or strong), T_s is the sampling period, $\Delta\omega = 0.002 \text{rad/s}$

and

$$S_F = \sum_{k=0}^{\frac{\pi}{T_s \Delta\omega}} \frac{(m_1 T_F K \Delta\omega)^2 + 1}{\left[(T_F K \Delta\omega)^2 + 1\right]\left[(m_2 T_F K \Delta\omega)^2 + 1\right]} \tag{I.10}$$

The expression $v_0(t)$ of the wind speed at a fixed point can be represented by the following equation [34]:

$$v_0(t) = V + v_t(t) \tag{I.11}$$

The component representing turbulence, $v_t(t)$, is defined by the scale length L_F and the standard deviation σ_v of the turbulence, which is dependent on the mean wind speed V according to the relation I.12:

$$\sigma_v = \kappa_\sigma V \tag{I.12}$$

Where κ_σ is the turbulence intensity. The value of this coefficient varies from 0.1 at sea to 0.25 in a turbulent zone.

Thus, the wind speed is constructed according to the block diagram of Figure I.4.

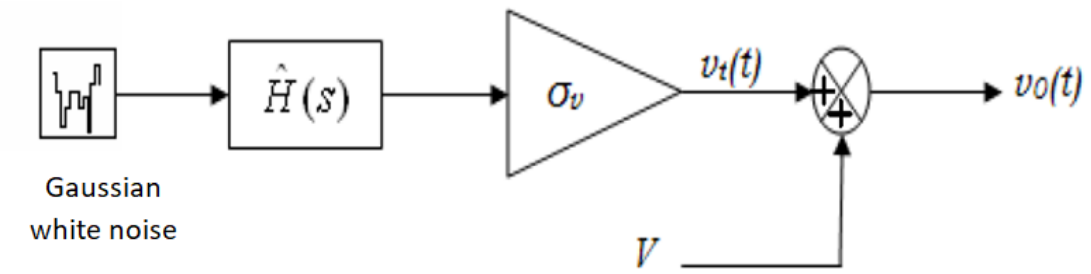


Figure I. 4 Block Diagram Of Wind Speed Construction Based On Nichita Model [19].

In our work, using the model from Figure I.4 in Matlab Simulink with the parameters listed in Appendix A, the following curves are obtained (See Figure I.5 and Figure I.6).

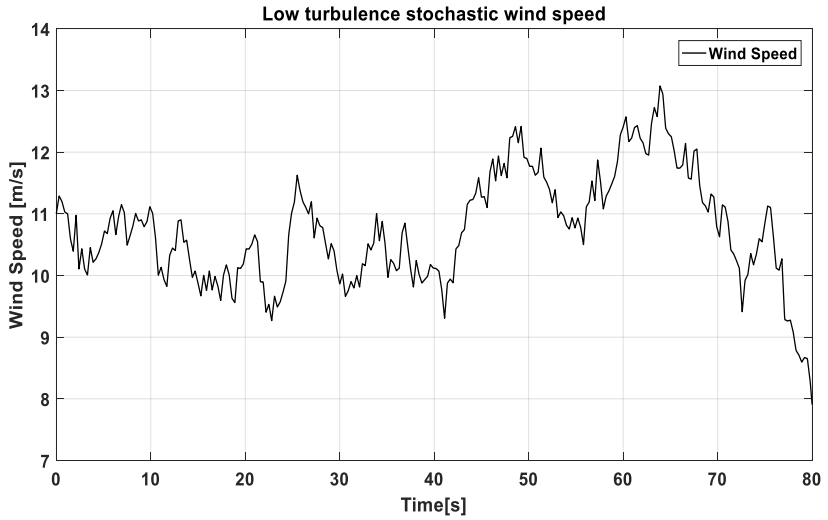


Figure I. 5 Low turbulence stochastic wind speed.

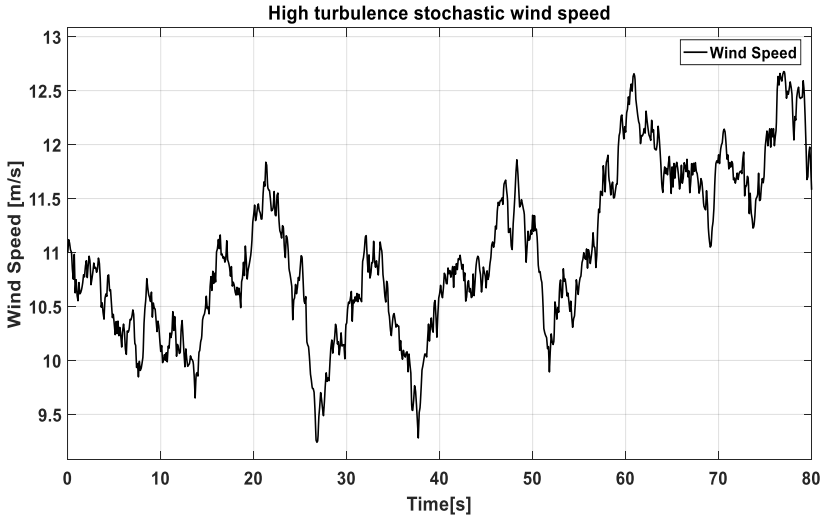


Figure I. 6 High turbulence stochastic wind speed.

I. 4.2 Conversion of Wind Kinetic Energy

The aerodynamic behavior of wind turbines is essential for understanding their performance and efficiency. An effective approach to this analysis involves the use of the actuator disk model, which simplifies the wind turbine to an idealized disk through which the wind flows [22]. This model

enables the examination of how wind kinetic energy is converted into mechanical energy by the turbine.

In this model, an actuator disk is positioned within a uniform wind flow, as depicted in Figure I.7. The disk interacts with the wind in three distinct regions: upstream (u) , at the disk (0) , and downstream (ω) . The conditions in these regions are characterized by their respective velocities and pressures [1]. The momentum theory serves as a fundamental framework for analyzing the forces and power generated by the wind turbine. The momentum H imparted to the disk by the air mass m flowing through the disk area A can be expressed as

$$H = m\left(v_u - v_\omega\right) \tag{I.13}$$

Where v_u represents the upstream wind velocity and v_ω denotes the downstream wind velocity. The momentum H imparted to the disk by the air mass m passing through the area A generates a force, which can be expressed as:

$$T = \frac{\Delta H}{\Delta t} = \frac{\Delta m\left(v_u - v_\omega\right)}{\Delta t} = \frac{\rho A v_0 \Delta t\left(v_u - v_\omega\right)}{\Delta t} = \rho A v_0\left(v_u - v_\omega\right) = A\left(p_0^+ - p_0^-\right) \tag{I.14}$$

With ρ being the air density [35].

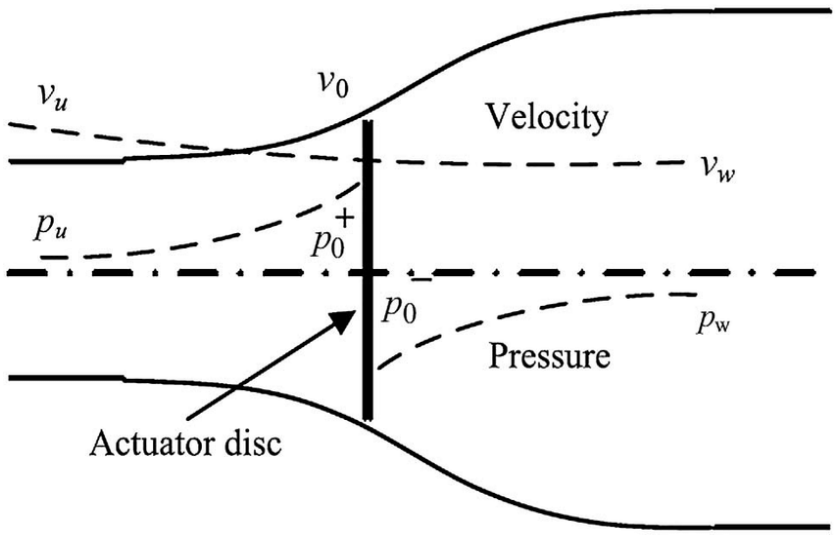


Figure I. 7 Model of actuator disk interaction with wind [54].

Applying Bernoulli's equation [54], the pressure difference is

$$p_0^+ - p_0^- = \frac{1}{2}\rho\left(v_u^2 - v_\omega^2\right) \tag{I.15}$$

Substituting equation (I.15) into equation (I.14), we get

$$T = \frac{1}{2}\rho A\left(v_u^2 - v_\omega^2\right) \tag{I.16}$$

From equations (I.14) and (I.16), we obtain

$$v_0 = \frac{1}{2}\left(v_u + v_\omega\right) \Rightarrow v_u - v_\omega = 2\left(v_u - v_0\right) \tag{I.17}$$

The mass flow rate $\dot{m}$ is given by

$$\dot{m} = \rho A v_u \tag{I.18}$$

By substituting $\dot{m}$ into the momentum equation, the expression for momentum becomes

$$H = \rho A v_u \left(v_u - v_\omega\right) \tag{I.19}$$

The primary goal of a wind turbine is to convert the kinetic energy of the wind into mechanical energy. The kinetic energy per unit mass of the wind before and after passing through the disk is given by $E_{k_u} = \frac{1}{2}v_u^2$ for the upstream flow and $E_{k_\omega} = \frac{1}{2}v_\omega^2$ for the downstream flow. The kinetic energy of an air mass moving at speed v is given by:

$$E_k = \frac{1}{2}mv^2 \tag{I.20}$$

The power P extracted by the turbine is determined by the difference in kinetic energy flux between the upstream and downstream flows. This can be computed as

$$P = \frac{1}{2}\dot{m}\left(v_u^2 - v_\omega^2\right) \tag{I.21}$$

Substituting $\dot{m}$ into this equation yields

$$P = \frac{1}{2}\rho A v_u \left(v_u^2 - v_\omega^2\right) \tag{I.22}$$

The efficiency of the wind turbine is characterized by the power coefficient C_p, which represents the fraction of the wind's kinetic energy converted into mechanical energy. The theoretical

maximum value of C_p is known as the Betz limit [36, 37], which is approximately 0.593. This limit is derived from the principles of mass and momentum conservation. The force F exerted on the actuator disk is given by

$$\mathrm{F} = \rho A v_u \left(v_u - v_\omega\right) \tag{I.23}$$

Consequently, the power extracted by the turbine is

$$P = \mathrm{F} v_\omega = \rho A v_u \left(v_u - v_\omega\right) v_\omega \tag{I.24}$$

Using the continuity equation $A v_u = A v_\omega + A\left(v_u - v_\omega\right)$, the power coefficient C_p is expressed as

$$C_p = \frac{P}{\frac{1}{2}\rho A v_u^3} \tag{I.25}$$

Substituting the power P into this equation, we get

$$C_p = \frac{\rho A v_u \left(v_u - v_\omega\right) v_\omega}{\frac{1}{2}\rho A v_u^3} = \frac{2\left(v_u - v_\omega\right) v_\omega}{v_u^2} \tag{I.26}$$

By maximizing C_p with respect to v_ω, the Betz limit is obtained as

$$C_{p,max} = \frac{4}{27} \approx 0.593 \tag{I.27}$$

In practical applications, the performance of wind turbines is influenced by various factors, including the design of the blades, operational conditions, and control strategies employed. While the Betz limit provides an upper bound on efficiency, real-world turbines achieve efficiencies close to this limit but rarely exceed it. Ongoing advancements in control techniques and aerodynamic optimizations continue to enhance turbine performance and efficiency.

I. 5 Drive Train

The drive train in wind energy conversion systems (WECS) plays a crucial role in the overall efficiency and functionality of the system. It acts as the mechanical connection between the wind turbine's rotor and the generator, enabling the conversion of wind's kinetic energy into electrical power. A thorough understanding of the drive train's components, design factors, and associated challenges is key to enhancing the performance and reliability of wind turbines.

The drive train typically comprises several key components: the main shaft, gearbox, coupling, and generator. The main shaft connects directly to the rotor, transmitting the rotational motion induced by wind forces. Depending on the turbine design, this shaft may be a low-speed or high-speed shaft. In most conventional wind turbines, the low-speed main shaft is coupled to a gearbox, which steps up the rotational speed to match the operational requirements of the generator. The gearbox is a critical component, as it must withstand significant mechanical stresses while efficiently converting the slow rotational speed of the rotor into the higher speed needed for electricity generation [38].

The gearbox design is influenced by the need to balance efficiency, durability, and weight [21]. It usually consists of multiple stages, with each stage employing different gear ratios to incrementally increase the rotational speed. However, gearboxes are also one of the most failure-prone components in wind turbines, primarily due to the variable and harsh operating conditions they endure. Failures can arise from factors such as misalignment, improper lubrication, material fatigue, and excessive loads caused by gusty winds or grid disturbances [39]. These challenges necessitate robust design practices, including the use of high-quality materials, advanced manufacturing techniques, and comprehensive testing. To mitigate some of the challenges associated with gearboxes, some modern wind turbines employ direct-drive systems. In these systems, the rotor is directly coupled to the generator, eliminating the need for a gearbox. This design reduces mechanical complexity, enhances reliability, and lowers maintenance requirements [40]. However, direct-drive systems require large, low-speed generators, which can be more expensive and heavier than traditional generator designs. Despite these trade-offs, direct-drive turbines are gaining popularity, particularly in offshore wind farms where maintenance access is more difficult. Another critical aspect of the drive train is the coupling mechanism, which connects the gearbox (or rotor in direct-drive systems) to the generator. The coupling must accommodate misalignments, vibrations, and thermal expansions while transmitting torque effectively. Various types of couplings are used, including rigid, flexible, and fluid couplings, each offering different advantages depending on the specific application and operating conditions [41].

The generator, as the final component in the drive train, converts the mechanical energy from the rotating shaft into electrical energy. The choice of generator type—typically synchronous or asynchronous—depends on factors such as cost, efficiency, and grid connection requirements. Synchronous generators are often preferred for their ability to operate at a constant speed, which simplifies grid integration. Asynchronous (induction) generators, on the other hand, are more robust and can tolerate variable speeds, making them suitable for turbines that operate in fluctuating wind conditions [42].

The overall performance of the drive train is influenced by various factors, including the aerodynamic efficiency of the rotor, the mechanical efficiency of the gearbox, and the electrical efficiency of the generator. Therefore, optimizing the drive train requires a holistic approach, considering the interactions between all components and their impact on the system's energy conversion efficiency.

The dynamics of a drive train in wind energy conversion systems (WECS) can be modeled using different levels of complexity, commonly referred to as the one-mass, two-mass, and three-mass models. These models help capture the behavior of the drive train, including the interaction between the rotor, gearbox, generator, and sometimes other components. The choice of model depends on the level of detail required for the analysis.

I. 5.1 One-Mass Model

The one-mass model is the simplest representation of the drive train, as depicted in Figure I.8. In this model, the entire drive train is considered as a single rigid mass. This approach assumes that the rotor, gearbox, and generator are all rigidly connected without any flexibility or compliance between them. The one-mass model is typically used for basic analysis where the detailed dynamics of the drive train are not critical, such as in steady-state or basic dynamic studies [1,25]. This model is governed by a single equation of motion that relates the total inertia of the drive train to the applied torque and rotational speed.

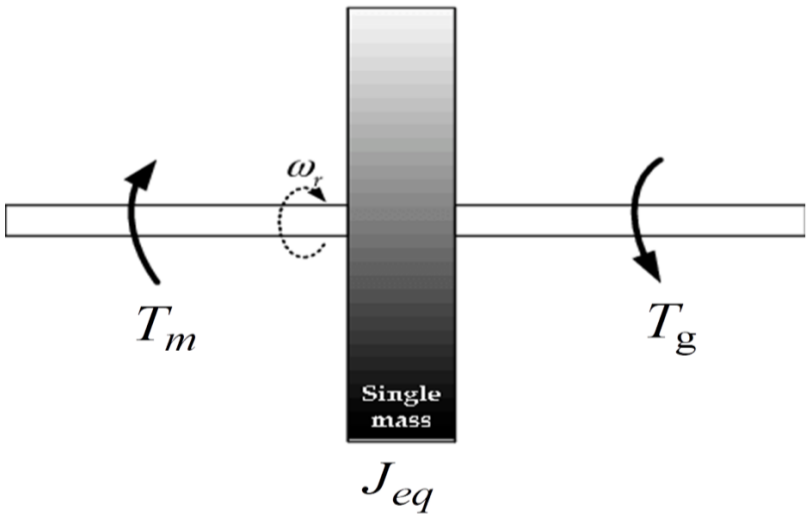


Figure I. 8 One-Mass Drive Train Model

In this model, the equation of motion is:

$$J_{eq}\frac{d\omega_r}{dt} = T_m - T_g \tag{I.28}$$

Where:

- J_{eq} represents the equivalent inertia of the entire drive train, encompassing the rotor, gearbox, and generator.
- ω_r is the angular velocity of the rotor (and the entire drive train, since they are treated as one mass).
- T_m is the mechanical torque generated by the wind turbine blades due to wind energy.
- T_g is the electromagnetic torque exerted by the generator as it converts mechanical energy into electrical energy.

This model assumes that the components are perfectly rigidly connected, meaning there is no flexibility or compliance in the drive train. The one-mass model is sufficient for scenarios where a broad overview of system performance is needed, such as initial design considerations or in control strategies where high-frequency dynamics are not critical.

I. 5.2 Two-Mass Model

The two-mass model adds more complexity by considering the rotor and generator as separate masses connected by a flexible shaft, usually representing the gearbox. This model accounts for the torsional flexibility of the shaft, which introduces the possibility of torsional oscillations between the rotor and generator. The two-mass model is governed by two coupled differential equations—one for the rotor and one for the generator [25,44]. The flexibility between the two masses allows for a more accurate representation of the drive train dynamics, especially when considering transient responses, such as those caused by wind gusts or changes in load [43].

The dynamics are described by two coupled differential equations:

$$J_r \frac{d\omega_r}{dt} = T_m - K_s\left(\theta_r - \theta_g\right) - D_s\left(\omega_r - \omega_g\right) \tag{I.29}$$

$$J_g \frac{d\omega_g}{dt} = K_s\left(\theta_r - \theta_g\right) + D_s\left(\omega_r - \omega_g\right) - T_g \tag{I.30}$$

Where:

- J_r is the inertia of the rotor, and J_g is the inertia of the generator.
- ω_r and ω_g are the angular velocities of the rotor and generator, respectively.
- θ_r and θ_g are the angular displacements of the rotor and generator, respectively.

- K_s represents the stiffness of the shaft connecting the rotor and generator, and D_s represents the damping effect of the shaft.
- T_m and T_g remain the mechanical and electromagnetic torques, respectively.

The inclusion of shaft stiffness and damping introduces the possibility of oscillations and resonance phenomena between the rotor and generator, which are essential to consider for accurate dynamic analysis and for designing effective control systems. This model is widely used in the analysis of wind turbine drive trains, especially in the context of control strategy development and load analysis.

I. 5.3 Three-Mass Model

The three-mass model further increases the complexity by introducing an additional mass, typically representing the gearbox or other intermediate components in the drive train. In this model, the rotor, gearbox, and generator are each considered as separate masses, connected by flexible shafts. This model captures even more detailed dynamics, including the interaction between different components and the potential for complex oscillatory behavior [1,47]. The three-mass model is governed by three coupled differential equations, making it the most detailed and accurate representation of the drive train dynamics. This model is particularly useful for analyzing the effects of control strategies, mechanical resonances, and other dynamic phenomena in the drive train [45,48].

The equations governing the three-mass model are:

$$J_r \frac{d\omega_r}{dt} = T_m - K_{s1}\left(\theta_r - \theta_{gb}\right) - D_{s1}\left(\omega_r - \omega_{gb}\right) \tag{I.31}$$

$$J_{gb} \frac{d\omega_{gb}}{dt} = K_{s1}\left(\theta_r - \theta_{gb}\right) + D_{s1}\left(\omega_r - \omega_{gb}\right) - K_{s2}\left(\theta_{gb} - \theta_g\right) - D_{s2}\left(\omega_{gb} - \omega_g\right) \tag{I.32}$$

$$J_g \frac{d\omega_g}{dt} = K_{s2}\left(\theta_{gb} - \theta_g\right) + D_{s2}\left(\omega_{gb} - \omega_g\right) - T_g \tag{I.33}$$

Where:

- J_{gb} is the inertia of the gearbox.
- ω_{gb} is the angular velocity of the gearbox.
- θ_{gb} is the angular displacement of the gearbox.

- K_{s1} and K_{s2} are the shaft stiffnesses between the rotor-gearbox and gearbox-generator, respectively.
- D_{s1} and D_{s2} are the corresponding damping coefficients.

These equations form the basis for analyzing the dynamics of wind turbine drive trains. The three-mass model is particularly useful for advanced control design, where precise modeling of the system dynamics is required to ensure stability and performance under various operating conditions.

In summary, the choice between a one-mass, two-mass, or three-mass model depends on the required accuracy and the specific aspects of the drive train dynamics that are of interest. The one-mass model offers simplicity, while the two-mass and three-mass models provide increasingly detailed insights into the dynamic behavior of the drive train [25,43,45].

I. 6 Modeling of Squirrel Cage Induction Generator

The Squirrel Cage Induction Generator (SCIG) is widely used in wind energy conversion systems due to its robustness, simplicity, and cost-effectiveness [54]. Modeling the SCIG is essential for analyzing its dynamic behavior and designing control strategies. The state-space model of the SCIG provides a mathematical representation that captures its dynamics under different operating conditions. This model is based on the d-q axis theory, which simplifies the analysis by transforming three-phase quantities into two-phase quantities.

I.6.1 Basic Principles of SCIG

The SCIG operates on the same principle as an induction motor but functions as a generator when the rotor is driven above the synchronous speed. In this mode, it converts mechanical energy into electrical energy. The Squirrel Cage rotor consists of short-circuited bars, which makes the machine robust but also means that it lacks the ability to control rotor currents directly, unlike wound rotor machines.

I.6.2 d-q Axis Modeling of SCIG

The d-q axis modeling is a standard approach for representing the SCIG in a reference frame that rotates synchronously with the stator magnetic field. This approach leads to the following set of differential equations that describe the electrical and mechanical dynamics of the SCIG.

I.5.2.1 Stator and Rotor Voltage Equations

The stator and rotor voltage equations in the d-q reference frame are derived from Faraday's Law and are given by:

$$\begin{cases} V_{ds} = R_s \mathrm{I}_{ds} + \dfrac{d\Phi_{ds}}{dt} - \omega\Phi_{qs} \\ V_{qs} = R_s \mathrm{I}_{qs} + \dfrac{d\Phi_{qs}}{dt} + \omega\Phi_{ds} \\ 0 = R_{\mathrm{r}} \mathrm{I}_{dr} + \dfrac{d\Phi_{dr}}{dt} - (\omega - \omega_{\mathrm{r}})\Phi_{qr} \\ 0 = R_{\mathrm{r}} \mathrm{I}_{qr} + \dfrac{d\Phi_{qr}}{dt} + (\omega - \omega_{\mathrm{r}})\Phi_{dr} \end{cases} \quad \text{(I.34)}$$

Where:

- $\mathrm{V}_{ds}, \mathrm{V}_{qs}$ are the d-axis and q-axis stator voltages.
- $\mathrm{I}_{ds}, \mathrm{I}_{qs}$ are the d-axis and q-axis stator currents.
- R_s is the stator resistance.
- Φ_{ds}, Φ_{qs} are the d-axis and q-axis stator flux linkages.
- ω is the synchronous angular velocity.
- ω_{r} is the rotor angular velocity.
- R_{r} is the rotor resistance.
- Φ_{dr}, Φ_{qr} are the d-axis and q-axis rotor flux linkages.

I.6.2.2 Flux Linkage Equations

The flux linkages are related to the currents by the following equations, considering the mutual inductance between the stator and rotor:

$$\begin{cases} \Phi_{ds} = \mathrm{L}_s \mathrm{I}_{ds} + \mathrm{L}_{\mathrm{m}} \mathrm{I}_{dr} \\ \Phi_{qs} = \mathrm{L}_s \mathrm{I}_{qs} + \mathrm{L}_{\mathrm{m}} \mathrm{I}_{qr} \\ \Phi_{dr} = \mathrm{L}_{\mathrm{m}} \mathrm{I}_{ds} + \mathrm{L}_{\mathrm{r}} \mathrm{I}_{dr} \\ \Phi_{qr} = \mathrm{L}_{\mathrm{m}} \mathrm{I}_{qs} + \mathrm{L}_{\mathrm{r}} \mathrm{I}_{qr} \end{cases} \quad \text{(I.35)}$$

Where:

- L_s is the stator inductance.
- L_{r} is the rotor inductance.
- L_{m} is the mutual inductance between the stator and rotor.

I.6.2.3 Mechanical Equation

The mechanical dynamics of the SCIG are governed by the following equation, which represents the balance of torques on the rotor:

$$J\frac{dW_r}{dt} = T_m - T_e - F_r \mathrm{W}_r \tag{I.36}$$

Where:

- J is the moment of inertia of the rotor.
- T_m is the mechanical torque applied to the rotor.
- T_e is the electromagnetic torque generated by the machine.
- F_r is the damping coefficient representing friction and windage losses.

The Electromagnetic torque T_e is given by:

$$T_e = \frac{3}{2}P\left(\Phi_{ds}I_{qs} - \Phi_{qs}I_{ds}\right) \tag{I.37}$$

Where P is the number of pole pairs.

I.6.3 State-Space Representation of SCIG

To derive the state-space model of the SCIG [54], the equations are rearranged to express the time derivatives of the state variables (currents and rotor speed) as a function of the state variables themselves and the inputs (voltages and mechanical torque).

Let the state vector x be defined as:

$$\mathrm{x} = \begin{bmatrix} \mathrm{I}_{ds} \\ \mathrm{I}_{qs} \\ \mathrm{I}_{dr} \\ \mathrm{I}_{qr} \\ \omega_{\mathrm{r}} \end{bmatrix} \tag{I.38}$$

The state-space model can be expressed in the form:

$$\frac{d\mathrm{x}}{dt} = A(\omega)\mathrm{x} + Bu \tag{I.39}$$

Where:

- A is the system matrix that encapsulates the dynamics of the SCIG.
- B is the input matrix.
- $u = \begin{bmatrix} V_{ds} \\ V_{qs} \\ T_m \end{bmatrix}$ is the input vector.

I.6.4 System Matrix A and Input Matrix B

The matrices A and B are derived from the stator and rotor voltage equations, flux linkage equations, and the mechanical equation.

The matrix A is given by:

$$A = \begin{bmatrix} -\frac{R_s}{L_s} & \omega & 0 & \frac{-L_m}{L_s} & 0 \\ -\omega & -\frac{R_s}{L_s} & \frac{-L_m}{L_s} & 0 & 0 \\ 0 & \frac{-L_m}{L_r} & -\frac{R_r}{L_r} & (\omega - \omega_r) & 0 \\ \frac{-L_m}{L_r} & 0 & -(\omega - \omega_r) & -\frac{R_r}{L_r} & 0 \\ 0 & 0 & 0 & 0 & \frac{1}{J} \end{bmatrix} \quad \text{(I.40)}$$

The matrix B is given by:

$$B = \begin{bmatrix} \frac{1}{L_s} & 0 & 0 \\ 0 & \frac{1}{L_s} & 0 \\ 0 & 0 & 0 \\ 0 & 0 & 0 \\ 0 & 0 & -1 \end{bmatrix} \quad \text{(I.41)}$$

The Nonlinear state-space model of the SCIG is given by [54]:

$$\begin{cases} \dot{x} = A(\Omega_h).x + B.u \\ y \equiv T_{em} = \frac{3pL_m}{2}(x_2x_3 - x_1x_4) \end{cases} \quad \text{(I.42)}$$

The state-space model of the SCIG provides a comprehensive mathematical framework for analyzing and controlling the generator's behavior. This model is essential for the design of advanced

control strategies in applications like wind energy conversion systems, where the ability to manage the dynamic response of the generator directly impacts the efficiency and stability of the overall system.

I.7 Dynamic Modeling of Wind Energy Conversion Systems (WECS)

The rotation of the turbine blades is caused by the wind. In Figure I.9, the high speed shaft is connected to the gearbox. The gearbox then converts the turbine's slow, high-torque rotation into a more suitable rotation speed for the generator. The generator's rotor is linked to the gearbox through a second shaft called the high speed shaft. This arrangement produces aerodynamic power known as P_{wt}. Equation (I.42) describes this power, where C_P represents the power coefficient that corresponds to the maximum kinetic energy extractable from the wind. According to Betz' theory, this extraction is limited to 59.3% [49]. Additionally, ρ denotes the air density, R stands for the radius of the wind turbine blades, and v represents the wind speed.

$$P_{wt} = 0.5\rho\pi R^2 v^3 C_p(\lambda,\beta) \tag{I.43}$$

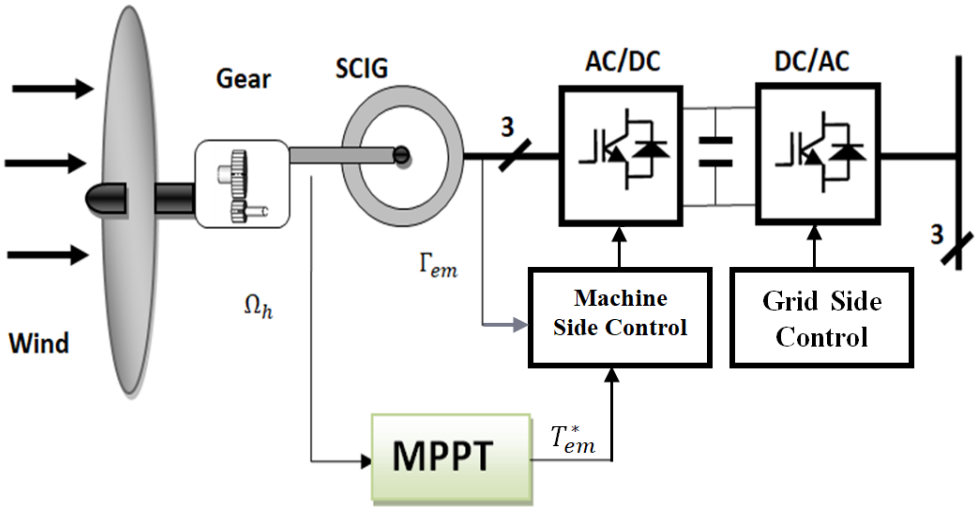


Figure I. 9 Schematic Diagram Of The WECS Based SCIG.

The power coefficient is defined by [6,8]

$$C_p(\lambda) = C_\Gamma(\lambda) * \lambda \tag{I.44}$$

The torque coefficient $C_\Gamma(\lambda)$ can be described by a polynomial function of the Tip-Speed Ratio λ [6,54]

$$C_\Gamma(\lambda) = a_6\lambda^6 + a_5\lambda^5 + a_4\lambda^4 + a_3\lambda^3 + a_2\lambda^2 + a_1\lambda + a_0 \tag{I.45}$$

The tip-speed ratio is defined by

$$\lambda = \frac{\omega_t R}{v} \tag{I.46}$$

Where R is the blade radius and ω_t is the Turbine Speed. The expression of the aerodynamic torque as a function of the wind speed v is defined by [50]:

$$\Gamma_{wt} = 0.5\rho\pi R^3 v^2 C_\Gamma(\lambda,\beta) \tag{I.47}$$

The dynamics of the WECS can be expressed rendered as the high-speed shaft (HSS):

$$J_h \frac{d\Omega_h}{dt} = \frac{\eta}{G}.\Gamma_{wt} - \Gamma_{em} \tag{I.48}$$

Where Γ_{wt} is the aerodynamic torque, parameterized by the wind speed.

Γ_{em} is the electromagnetic torque . J_h is inertia rendered in the high-speed shaft (HSS) [51].

The expression of electromagnetic torque as a function of the electromagnetic torque reference:

$$\frac{d}{dt}\Gamma_{em} = -\frac{\Gamma_{em}}{T_G} + \frac{u}{T_G} \tag{I.49}$$

With $u = \Gamma_{em}^*$ and $T_G = 0.02$ is the electromagnetic torque subsystem time constant.

I.8 Linearization of WECS (Wind Energy Conversion Systems)

Dynamic linearization of nonlinear systems is a very common practice. It consists in linearizing the nonlinear state model locally around a nominal operating point, in order to obtain a locally valid linear model under the assumptions of small deviations around the operating point [52].

Wind Energy Conversion Systems (WECS) are inherently nonlinear due to the complex interactions between their various components, including the wind turbine, gearbox, and generator. These nonlinearities predominantly stem from aerodynamic forces acting on the turbine blades, the variable power coefficient, and the fluctuations in wind speed. For the application of linear control techniques, it is essential to linearize the WECS around a specified operating point to simplify the analysis and design process [52].

This subsection is dedicated to presenting the linearized models of various WECS configurations. These models are derived by integrating the primary components: aerodynamics, drivetrain, and electrical generator. The linearization process involves approximating the nonlinear system dynamics by a linear model around a particular equilibrium point, which facilitates the application of linear control methods. In the context of grid-connected WECS, the critical inputs

include the wind speed, stator voltages, and, depending on the generator type and control strategy, rotor voltages. These inputs are crucial for the regulation of power output and maintaining synchronization with the electrical grid. The control strategies for grid-connected systems often involve advanced techniques such as Maximum Power Point Tracking (MPPT) to ensure optimal performance and grid stability. Conversely, stand-alone WECS, which operate independently of the grid, rely on the load as a primary input. The load affects the system's power balance and stability, requiring precise management to maintain efficient operation. In these systems, control strategies may focus on load matching and storage solutions to stabilize the energy output and ensure continuous operation.

By analyzing the linearized models of these different configurations, we gain a deeper understanding of the dynamic behavior and performance characteristics of WECS. This insight is crucial for developing and implementing effective control strategies tailored to various operational scenarios, such as optimizing power output and managing standalone system performance.

The intended method strives to stabilize a fixed operational state aligned with the peak power coefficient while concurrently optimizing a performance metric amid variations around this point. Consequently, it is imperative to derive the linearized model of the system centered on this specific operational point. It's essential to note that λ_{opt} represents the tip speed value at which the maximum energy conversion efficiency is achieved. Subsequently, in the context of a variable x within the model, the subsequent notations are employed:

$$\overline{x} = x\big|_{optimal\ operating\ point}\ ; \Delta x = x - \overline{x}\ ; \overline{\Delta x} = \frac{\Delta x}{\overline{x}} \tag{I.50}$$

The linear model of the turbine is derived from the nonlinear characteristics (I.46) using Taylor Series Expansion Method, as described in [52]. Simplified linear approximations of the power (I.42) and torque (I.46) functions are crucial in the analysis of the basic process performance and in controller synthesis. The aerodynamic torque can be expressed in terms of the $C_p(\lambda)$ function [52]:

$$T_{wt} = \frac{\pi \rho R^2 v^3(t)}{2\omega_{\mathrm{T}}(t)} C_p(\lambda) \tag{I.51}$$

Using the definition (I.45) of λ, we can determine the partial derivative with respect to turbine speed at the operating point (OP) as follows:

$$\left.\frac{\partial T_{wt}}{\partial \omega_{\mathrm{T}}}\right|_{o.p.} = \frac{\pi \rho R^2 v_0^3}{2}\left(\frac{C_p'(\lambda_0).\mathrm{R}}{\omega_{\mathrm{T}0}.v_0} - \frac{C_p(\lambda_0)}{\omega_{T0}^2}\right) \tag{I.52}$$

$$\left.\frac{\partial T_{wt}}{\partial \omega_{\mathrm{T}}}\right|_{o.p.} = \frac{\pi \rho R^2 v_0^3}{2.\omega_{T0}^2}\left(C_p^{'}(\lambda_0).\lambda_0 - C_p(\lambda_0)\right) \tag{I.53}$$

Where
$$C_p^{'}(\lambda_0) = \left.\frac{dC_p(\lambda)}{d\lambda}\right|_{o.p.} \tag{I.54}$$

The partial derivative with respect to wind speed is derived in the same manner, it equals

$$\left.\frac{\partial T}{\partial \omega}\right|_{o.p.} = \frac{\pi \rho R^2 v_0^2}{2.\omega_0}\left(3C_p(\lambda_0) - C_p^{'}(\lambda_0).\lambda_0\right) \tag{I.55}$$

Normalizing the variables with respect to the operating point, denoted by the bars on top, simplifies the linearized torque model to:

$$\overline{\Delta T_{wt}}(t) = \gamma \overline{\Delta \omega_T}(t) + (2-\gamma)\overline{\Delta v}(t) \tag{I.56}$$

Where $\overline{\Delta T_{wt}} = \Delta T_{wt} / \overline{\mathrm{T}_{\mathrm{wt}}}$, $\overline{\Delta v} = \Delta v / \bar{v}$ and γ depends on the chosen operating point:

$$\gamma = \frac{C_p^{'}(\lambda_0).\lambda_0 - C_p(\lambda_0)}{C_p(\lambda_0)} \tag{I.57}$$

With $C_p^{'}(\lambda) = \mathrm{d}\,C_p(\lambda) / \mathrm{d}\,\lambda$ (in our case, $\bar{\lambda} = \lambda_{opt}$).

The parameter γ is contingent on the operating point's $C_p(\lambda)$ function and is known as the torque parameter. The aerodynamic power, represented as $P_{wt} = T_{wt}.\omega_T$, is derived from this:

$$\overline{\Delta P_{wt}}(t) = \overline{\Delta T_{wt}}(t) + \overline{\Delta \omega_T}(t) = (1+\gamma)\overline{\Delta \omega_T}(t) + (2-\gamma)\overline{\Delta v}(t) \tag{I.58}$$

These equations are valid for all points where the power coefficient $C_p(\lambda)$ is defined and differentiable. In the stall region, γ is positive, leading to an unstable system. Determining the torque parameter can be numerically challenging at low tip speed ratios, as it requires dividing small $C_p(\lambda)$ values.

It has been proposed that the turbulence in wind speed arises from filtering a white noise signal, denoted as $e(t)$, through a low-pass filter. This conceptualization yields the wind model as follows:

$$\dot{\overline{\Delta v}}(t) = -\frac{1}{T_w}\overline{\Delta v}(t) + \frac{1}{T_w}e(t) = \frac{1}{T_w}\left(e(t) - \overline{\Delta v}(t)\right) \tag{I.59}$$

Where $T_w = L / \bar{v}$, is the time constant of a first-order shaping filter , computed as [31-53]. With L being the turbulence length, which depends of the site roughness.

Linearizing the equation that describes the dynamics of the interaction between the Electromechanical subsystem and the turbine rotation through the drive train given by

$$J_t \frac{d\omega}{dt} = T_{wt} - T_{em} \tag{I.60}$$

, we can derive the following equation:

$$J_T \overline{\Delta\omega} = \overline{\Delta T_{wt}} - \overline{\Delta T_{em}} \tag{I.61}$$

Where $$J_T = \overline{\omega}.J_t / \overline{T_{wt}} \tag{I.62}$$

represents the mechanical time constant. Equation (I.55), when differentiated with respect to time and combined with equations (I.58) and (I.60), gives

$$\overline{\Delta T_{wt}}(t) = \frac{\gamma}{J_T}\left(\overline{\Delta T_{wt}}(t) - \overline{\Delta T_{em}}(t)\right) + \frac{(2-\gamma)}{T_w}\left(e(t) - \overline{\Delta v}(t)\right) \tag{I.63}$$

This, along with equation (I.60), forms the state-space matrix equation:

$$\dot{x}(t) = A.x(t) + B.u(t) + L.e(t) \tag{I.64}$$

Where $x(t) = \left[\overline{\Delta\omega}(t) \quad \overline{\Delta T_{wt}}(t)\right]^T$ is the state vector, $u(t) = \overline{\Delta T_{em}}$ is the control input and

$$A = \begin{bmatrix} 0 & \frac{1}{J_T} \\ \frac{\gamma}{T_w} & \frac{\gamma}{J_T} - \frac{1}{T_w} \end{bmatrix}, B = \begin{bmatrix} -\frac{1}{J_T} \\ -\frac{\gamma}{J_T} \end{bmatrix}, L = \begin{bmatrix} 0 \\ \frac{(2-\gamma)}{T_w} \end{bmatrix} \tag{I.65}$$

The output (measurement) variable is characterized as the normalized change in the tip speed ratio: $\overline{\Delta\lambda}(t) = \Delta\lambda / \overline{\lambda}$. Therefore, the output equation is

$$y(t) = C.x(t) \tag{I.66}$$

Where $$C = \begin{bmatrix} \frac{2}{(2-\gamma)} & -\frac{1}{(2-\gamma)} \end{bmatrix} \tag{I.67}$$

Equations (I.64) and (I.66) depict the linearized model of the wind power system.

I.9 CONCLUSION

This chapter has presented a comprehensive modeling of the wind energy conversion chain. We began with an overview of wind turbine designs, detailing the components and their respective

roles. This was followed by an exploration of wind turbine aerodynamics, including the modeling of wind itself, which serves as the foundation for simulating the control methods discussed in subsequent chapters. Next, we examined how the kinetic energy of the wind is converted into electrical energy within wind energy conversion systems. We also provided a detailed analysis of the drive train, modeling all its variants. The squirrel cage induction generator was then selected, defined, and modeled, as it forms the basis of the wind energy conversion system studied in this thesis. Finally, recognizing the need to apply linear control techniques, we linearized the wind energy conversion system around a specific operating point to facilitate the analysis and design process. In the next chapter, we will analyze the dynamic behavior of the wind energy conversion system, aiming to maximize captured energy through the implementation of five different controllers: the standard On-Off controller, the improved On-Off controller, the improved fuzzy On-Off controller, and the sliding mode controller.

CHAPTER II: MPPT Control Strategy Of Wind Energy Conversion System

II. 1 Introduction

The pursuit of renewable energy sources has intensified in recent years, driven by the imperative to address the challenges of climate change and the need for sustainable energy solutions. Among these sources, wind energy has emerged as a prominent contender due to its abundance and low environmental impact. To harness this energy efficiently, wind energy conversion systems (WECS) have been developed, with a critical focus on optimizing their performance through various control strategies. One of the most effective methods employed is the Maximum Power Point Tracking (MPPT) control strategy, which plays a pivotal role in maximizing the energy output from wind turbines under varying operational conditions. MPPT control strategies are designed to extract the maximum available power from wind by dynamically adjusting the operational parameters of the turbine in response to fluctuations in wind speed. This chapter delves into the principles and methodologies underlying MPPT control strategies in WECS, examining their significance in enhancing energy capture and overall system efficiency. It begins by exploring the theoretical foundations of MPPT. The discussion will highlight the advantages and limitations of each approach, emphasizing the necessity of selecting an appropriate MPPT strategy based on specific environmental conditions and system configurations. Furthermore, this chapter will analyze recent advancements in MPPT technologies, integrating insights from both simulation studies and practical implementations. By evaluating the effectiveness of these strategies, we aim to contribute to the ongoing discourse on optimizing wind energy conversion, ultimately fostering the transition towards more efficient and sustainable energy systems.

II. 2 Literature Review and Related Works

II. 2.1 Related Works

In recent years, there has been significant progress in the development of Maximum Power Point Tracking (MPPT) techniques for wind energy conversion systems (WECS). These techniques are crucial for optimizing energy capture under varying wind conditions and improving the overall efficiency of wind turbines. Among various optimization algorithms, particle swarm optimization (PSO) has gained prominence due to its effectiveness in addressing multiple objectives, including maximizing power output and minimizing mechanical stress. A notable contribution in this field is the work by Coello et al. [75], who proposed a PSO variant that integrates Pareto dominance alongside a secondary particle repository and a specialized mutation operator to enhance the exploration capabilities of the algorithm. In a similar vein, Sierra and Coello [76] developed a multi-objective PSO approach that employs Pareto dominance combined with a crowding factor for leader selection. These advancements aim to refine control strategies in WECS, specifically targeting the reduction of torque

ripple—a common issue that can lead to performance degradation. Chen and Chen [77] introduced a modified power control strategy that employs current control methods to effectively reduce shaft torque ripple, with experimental validation conducted on a 1.2 kW WECS. Additionally, Erfort et al. [78] optimized a vertical axis wind turbine model utilizing genetic and gradient-based methods to minimize torque ripple, finding that sinusoidal blade pitching plays a critical role in diminishing torque variations. In their research, Brahmi et al. [7] proposed an Improved On-Off control strategy based on a hysteresis function, optimized through PSO to effectively track the maximum power point while simultaneously minimizing chattering and mechanical stress in WECS. Kahla et al. [79] introduced a fuzzy sliding mode controller optimized with multi-objective grey wolf optimization (MOGWO), focusing on enhancing power capture and reducing load stress. Furthermore, Hannachi et al. [80] compared the performance of Artificial Bee Colony (ABC) and Ant Colony Optimization (ACO) algorithms in tuning an On-Off controller, demonstrating that ABC outperformed ACO in maximizing power output and minimizing performance metrics such as Integral Absolute Error (IAE). Hannachi et al. [81] also optimized a permanent magnet synchronous generator (PMSG) within WECS using PSO for effective MPPT, achieving efficient operation across varying wind speeds. A comparative study investigated four MPPT techniques—Perturbation and Observation (P&O), Optimal Torque (OT), On-Off control, and Tip Speed Ratio (TSR)—highlighting the OT technique as particularly effective in maximizing power extraction. Additionally, an innovative Advanced Torque Ripple Unit (ATRU) was introduced by Gupta et al. [82], along with a modified power control strategy, with experimental results confirming its effectiveness in mitigating torque ripple. Emerging techniques, such as the variable-step perturb and observe (VS-PO) method proposed by Youssef et al. [83], have shown promise in enhancing MPPT efficiency. This approach segments the operating region into sectors and dynamically adjusts step sizes, validated on large-scale grid-tied WECS. Moreover, AI-based methods, including Artificial Intelligence based Adaptive P&O (AIAPO), have reported substantial improvements in MPPT efficiency, achieving a power output increase of 37.93% compared to conventional methods [84]. Other innovative strategies, such as the integration of the trapezoidal rule with the P&O algorithm, have also been proposed, demonstrating superior results in voltage stability and overall power output [85]. The continuous advancement of MPPT techniques and optimization algorithms, encompassing PSO, fuzzy logic, and AI-based approaches, is essential for enhancing power extraction and minimizing torque ripple in WECS, thereby driving forward the evolution of wind energy technology.

II. 2.2 Different MPPT Methods

Maximum Power Point Tracking (MPPT) is crucial for optimizing the efficiency of Wind Energy Conversion Systems (WECS) by ensuring operation at the optimal point to extract maximum

power under varying wind conditions. WECS operate in distinct regions based on power generation capabilities, as illustrated in Figure II.1. The cut-in wind speed (V_{cut-in}) represents the minimum velocity required to initiate power generation, while the rated wind speed (V_{rated}) defines the point at which the turbine reaches its nominal power capacity. MPPT algorithms primarily operate in the intermediate region between V_{cut-in} and V_{rated}, where power extraction is maximized, as shown in Figure II.2 . Various control strategies are implemented in this region to optimize performance by adjusting turbine speed, voltage, and duty cycle.

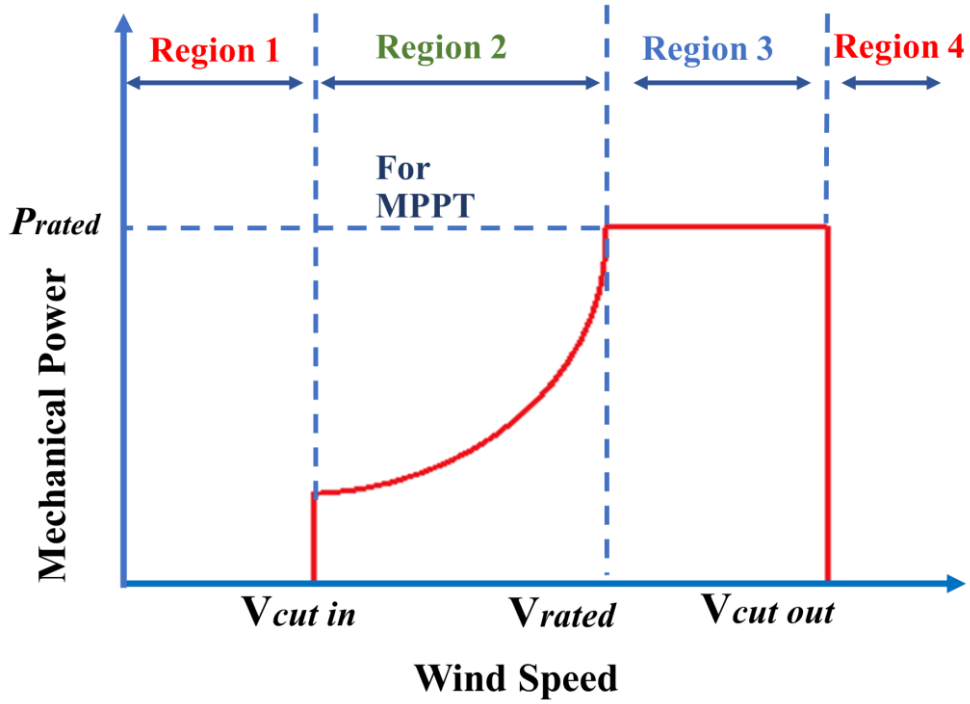


Figure II. 1 WECS operating regions.

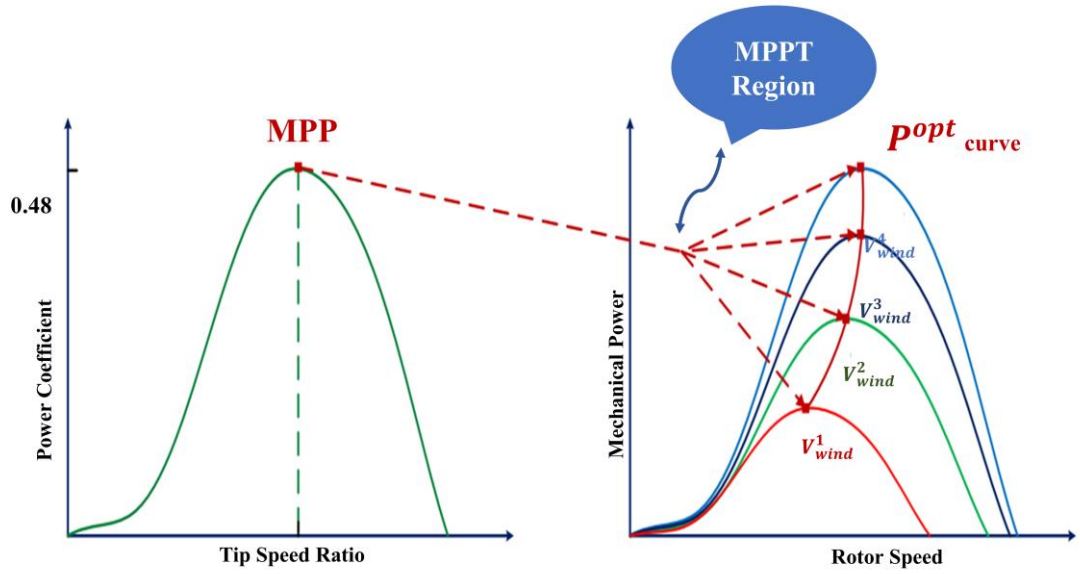


Figure II. 2 Characteristics of Wind Turbine Power under optimal values of λ_{opt} and CP_{opt} .

MPPT techniques can be categorized based on their dependency on wind speed sensors, as categorized in Figure II.3. Speed sensor-based methods rely on direct wind speed measurements, typically using anemometers, to optimize turbine performance. Examples include Tip Speed Ratio (TSR) control [59], which maintains an optimal ratio between blade tip speed and wind speed, and Power Signal Feedback (PSF) control [60], which adjusts turbine parameters based on predefined power curves. Sensorless methods eliminate the need for wind speed sensors, reducing system complexity and cost. These include Perturb and Observe (P&O) [61], which iteratively perturbs operating points and observes power output changes, Incremental Conductance (INC), which adjusts turbine operation based on real-time power variations, and Optimal Relation-Based (ORB) control, which utilizes predefined power-speed relationships to track the optimal point.

Hybrid approaches combine multiple techniques to enhance robustness and adaptability, overcoming the limitations of conventional MPPT methods. Intelligent control strategies such as Fuzzy Logic Control (FLC) [63] and Neural Networks (NN) provide adaptive decision-making and predictive capabilities. Additionally, Metaheuristic optimization techniques, including Genetic Algorithm (GA) [64] and Particle Swarm Optimization (PSO) [13], further improve tracking efficiency by optimizing the search for the maximum power point.

MPPT algorithms can also be classified into Direct Power Control (DPC) and Indirect Power Control (IPC) approaches. DPC methods directly regulate electrical power output (P_{ele}) by continuously adjusting turbine parameters, with examples such as P&O, INC, and ORB. IPC methods rely on precomputed wind speed-power curves to optimize mechanical power (P_{wind}), incorporating strategies like TSR and PSF control.

Recent research has introduced modifications to conventional MPPT methods, such as adaptive step-size P&O, which enhances tracking speed and stability. Hybrid techniques that integrate heuristic optimization with conventional MPPT methods demonstrate improved performance under dynamic wind conditions. Smart MPPT controllers, including FLC and NN-based approaches, offer superior adaptability by learning from historical data and real-time environmental variations. Comprehensive studies have highlighted the continuous evolution of MPPT strategies, underscoring their critical role in maximizing energy extraction from WECS. As renewable energy systems advance, the integration of intelligent and hybrid MPPT techniques is expected to drive further improvements in wind energy harvesting.

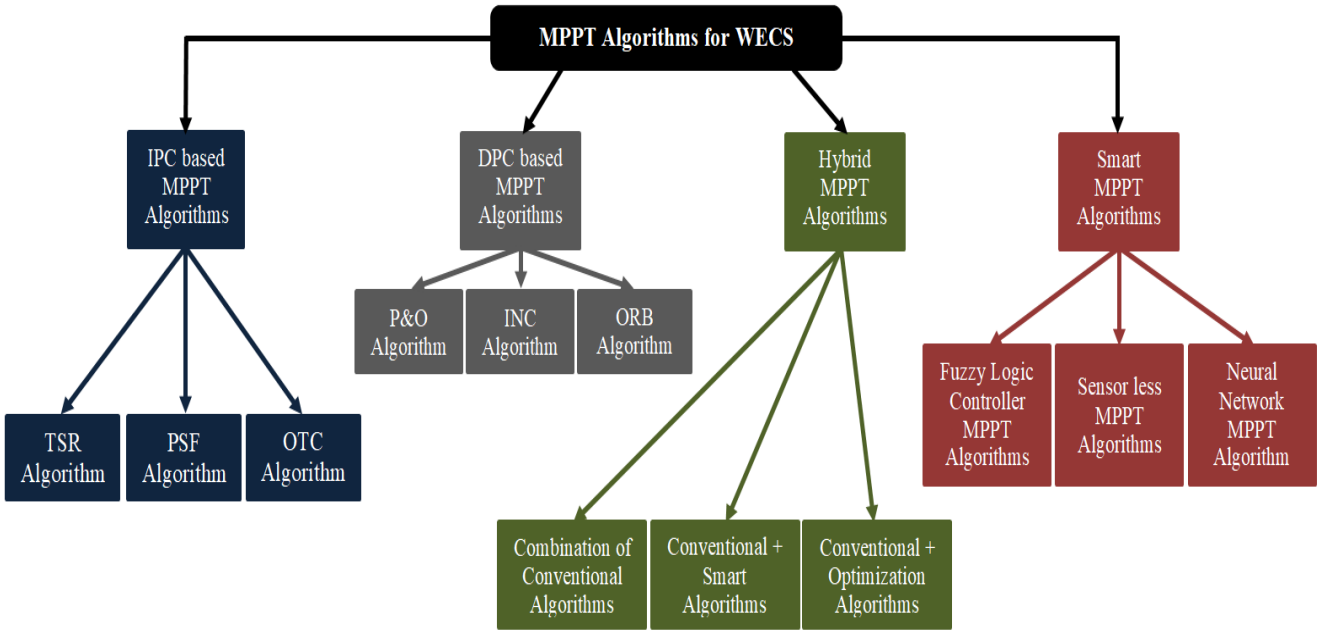


Figure II. 3 Classification of MPPT Algorithms for WECS.

II. 2.2.1 Indirect Power Control (IPC) Based MPPT Algorithms

Indirect Power Control (IPC)-based Maximum Power Point Tracking (MPPT) algorithms are widely employed in renewable energy systems, particularly in wind energy conversion systems, to maximize power extraction. Unlike conventional MPPT methods that directly regulate the system's power output, IPC-based approaches adjust specific system parameters that indirectly influence power generation. This strategy enhances the efficiency of maximum power point tracking. A comparison of various IPC-based techniques is provided in Table II.1.

Features of the MPPT Algorithm	**TSR**	**PSF**	**OTC**
Efficiency	High efficiency	Moderate efficiency	High efficiency
Complexity	Less	Less	Less
Convergence Speed	Higher	Higher	Higher
Oscillations at MPP	No	No	No
Prior knowledge	Not needed	Needed	Needed
Memory requirement	No	Yes	No
Sensors for wind speed measurement	Yes	Yes	No
Parameter Sensitivity	Yes	Yes	Yes
Cost	Very High	Moderate	Moderate
Online Updating	No	No	No
Performance under fluctuating wind speed	Moderately Fair	Moderately Fair	Moderately Fair

Table II. 1 Comparison of IPC based MPPT Algorithms for WECS [91].

II. 2.2.1.1 Tip Speed Ratio (TSR) Control

Tip Speed Ratio (TSR) control [65] is a fundamental strategy in the operation of wind energy conversion systems (WECS). The TSR is defined as the ratio between the tangential speed of the wind turbine blade tips and the wind speed. Mathematically, it is expressed as:

$$TSR = \frac{\omega_1 R}{v} \tag{II.1}$$

where ω_1 is the rotational speed of the turbine, R is the radius of the rotor, and v is the wind speed. Maintaining an optimal TSR is crucial for maximizing the aerodynamic efficiency of the wind turbine, as it ensures that the turbine operates at its maximum power coefficient $\left(C_{p_{max}}\right)$, thereby extracting the maximum possible energy from the wind [1,66].

In practice, TSR control involves adjusting the rotational speed of the turbine to match the variations in wind speed. This is typically achieved by controlling the generator torque, blade pitch angle, or both [22]. When the wind speed increases, the rotational speed must be increased proportionally to maintain the optimal TSR, and vice versa. TSR control is especially important in variable speed wind turbines, where it allows the system to adapt to changing wind conditions, thereby optimizing energy capture and reducing mechanical stresses on the turbine [1,67]. However, the implementation of TSR control requires precise measurements of wind speed and turbine rotational speed, as well as an accurate model of the turbine's aerodynamic characteristics [68]. Advanced control algorithms, such as those based on optimization techniques, are often employed to fine-tune the TSR control strategy, improving the overall performance and reliability of the WECS [67].

Figure II.4 illustrates the schematic diagram of the Wind Energy Conversion System (WECS) utilizing the Tip-Speed Ratio (TSR) method.

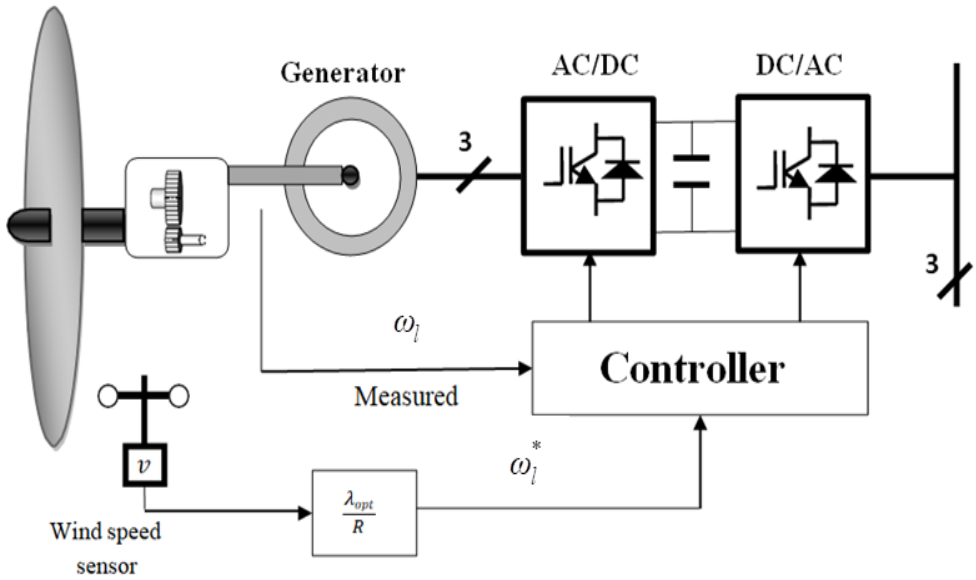


Figure II. 4 The Schematic Diagram of The WECS Utilizing The TSR Method.

II. 2.2.1.2 Power Signal Feedback (PSF) Control

Power Signal Feedback (PSF) Control is a method used in wind energy conversion systems to optimize energy extraction by maintaining the wind turbine's rotor speed near its optimal value, regardless of fluctuating wind conditions. The approach centers on a pre-determined reference power curve, which indicates the ideal power output of the turbine at various wind speeds. This curve, derived from the turbine's characteristics, serves as a benchmark for desired performance.

PSF control operates through a feedback loop that continuously monitors the actual power output and compares it with the reference power. When a discrepancy is detected, the control system adjusts the rotor speed through mechanisms such as pitch control or generator torque modification, thus bringing the turbine back to its optimal operating condition. A crucial element of PSF control is the accurate estimation of wind speed. Since direct measurement at the rotor plane is difficult, various techniques, including sensor fusion and indirect measurements, are employed to estimate wind speed effectively. This estimation informs the control system's adjustments, ensuring alignment with the reference power curve. The control strategy in PSF involves dynamically modulating control inputs based on the deviation between actual and reference power. This allows the system to maintain optimal performance across varying wind conditions, maximizing efficiency and energy capture [69]. PSF control is particularly advantageous in its simplicity and effectiveness, making it a popular choice in wind energy systems. It can also be integrated with other control strategies, such as Maximum Power Point Tracking (MPPT), to further improve performance [70]. By maintaining the power coefficient at its peak value, PSF ensures that the turbine operates efficiently, maximizing the energy extracted from the wind and enhancing overall system performance. Figure II.5 illustrates the schematic diagram of the Wind Energy Conversion System (WECS) utilizing the Power Signal Feedback (PSF) method.

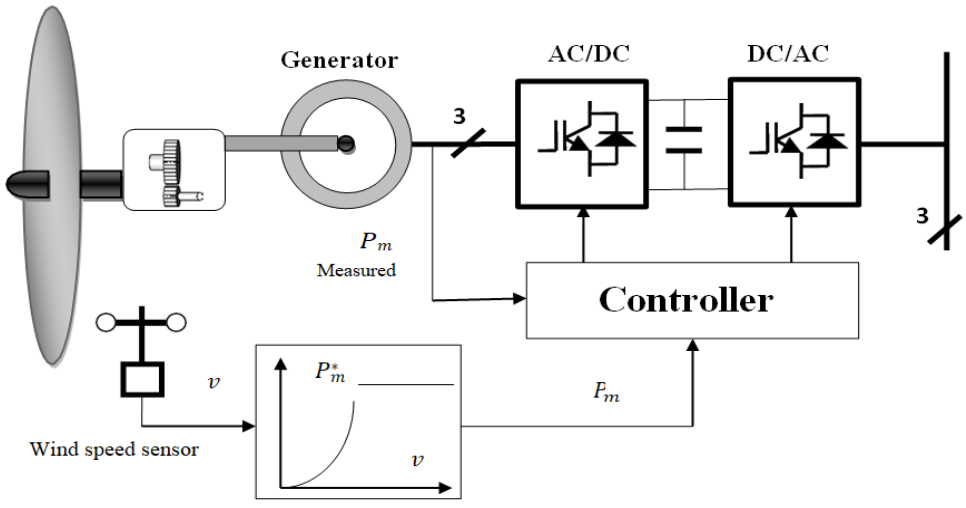


Figure II. 5 The Schematic Diagram of The WECS Utilizing The PSF Method.

II. 2.2.1.3 Optimal torque control - OTC

Optimal Torque Control (OTC) is a sophisticated control strategy employed in variable-speed Wind Energy Conversion Systems (WECS) to optimize the amount of energy extracted from the wind. The core objective of OTC is to ensure that the wind turbine operates at its optimal tip-speed ratio (λ_{opt}), thereby maximizing the aerodynamic efficiency of the turbine, which is represented by the power coefficient (C_p). By adjusting the generator torque (T_g) in relation to the rotor speed (ω_r), OTC ensures that the turbine operates at the maximum power point (MPP) under varying wind conditions [73].

The amount of power extracted from the wind can be expressed by the equation:

$$P_m = \frac{1}{2}\rho A C_p(\lambda) v^3 \tag{II.2}$$

Where P_m denotes the mechanical power extracted from the wind, ρ is the air density, A is the swept area of the turbine blades, $C_p(\lambda)$ represents the power coefficient, and V is the wind speed. The swept area A can be calculated as πR^2, with R being the rotor radius. The power coefficient C_p is a function of the tip-speed ratio (λ), which needs to be optimized to maximize the extracted power.

The tip-speed ratio (λ) is defined as:

$$\lambda = \frac{\omega_r R}{v} \tag{II.3}$$

Where $\omega_r = \omega_l$ is the rotor speed and v is the wind speed. For the turbine to operate at its most efficient point, the rotor speed must be adjusted to maintain the optimal tip-speed ratio, λ_{opt} ,which corresponds to the maximum value of C_p [74]. This relationship ensures that the turbine extracts the maximum amount of energy from the wind.

The mechanical power produced by the wind turbine is related to the generator torque (T_g) and the rotor speed (ω_r) by the equation:

$$P_m = T_g.\omega_r \tag{II.4}$$

Substituting the expression for the mechanical power extracted from the wind into this equation, we get:

$$T_g.\omega_r = \frac{1}{2}\rho A C_p(\lambda) v^3 \quad \text{(II.5)}$$

At the optimal tip-speed ratio (λ_{opt}), the power coefficient $C_p(\lambda_{opt})$ is maximized. To derive the optimal control law for generator torque, we first express the wind speed v in terms of rotor speed and tip-speed ratio:

$$v = \frac{\omega_r R}{\lambda_{opt}} \quad \text{(II.6)}$$

Substituting this expression into the power equation:

$$P_m = \frac{1}{2}\rho A C_p(\lambda_{opt})\left(\frac{\omega_r R}{\lambda_{opt}}\right)^3 \quad \text{(II.7)}$$

This simplifies to:

$$P_m = \frac{1}{2}\rho A C_p(\lambda_{opt})\frac{R^3}{\lambda_{opt}^{\ 3}}\omega_r^{\ 3} \quad \text{(II.8)}$$

Since P_m is also given by $T_g.\omega_r$, we can solve for the generator torque T_g:

$$T_g = \frac{1}{2}\rho A C_p(\lambda_{opt})\frac{R^3}{\lambda_{opt}^{\ 3}}\omega_r^{\ 2} \quad \text{(II.9)}$$

The constant k, which encapsulates the turbine's physical characteristics, is defined as:

$$k = \frac{1}{2}\rho A C_p(\lambda_{opt})\frac{R^3}{\lambda_{opt}^{\ 3}} = \frac{1}{2}\frac{C_p(\lambda_{opt})}{\lambda_{opt}^{\ 3}}\rho\pi R^5 \quad \text{(II.10)}$$

Thus, the optimal torque control law can be written as:

$$T_g = T_{em} = k.\omega_r^{\ 2} \quad \text{(II.11)}$$

In the absence of wind speed measurements, the goal of maximizing conversion efficiency can be attained by generating an optimal torque reference through equation (II.12), which depends solely

on a limited set of turbine parameters and basic measurements of generator speed Ω_h, as illustrated in Figure II.6.

$$T_g^* = T_{em}^* = k_{opt}.\Omega_{h_opt}^2 \tag{II.12}$$

With

$$k_{opt} = \frac{1}{2}\frac{C_{p_opt}(\Omega_h)}{\lambda_{opt}^3(\Omega_h).G^3}\rho\pi R^5 \tag{II.13}$$

$$\omega_{r_opt} = \frac{v.\lambda_{opt}}{R} \tag{II.14}$$

$$\omega_r = \omega_l = \frac{\Omega_h}{G} \tag{II.15}$$

Where G is the Multiplier ratio.

Also, the mechanical power law can be written as:

$$P_m = P_m^* = k.\omega_r^3 \tag{II.16}$$

In practice, the OTC strategy requires real-time adjustments based on rotor speed measurements. The control system continuously monitors the rotor speed and calculates the corresponding generator torque to ensure the turbine operates at the optimal tip-speed ratio. The generator torque is modulated via power electronic converters, which adjust the current supplied to the generator to achieve the desired torque. These converters are crucial for precise control, particularly in variable-speed systems using generators like squirrel cage induction generators, doubly-fed induction generators (DFIG) or permanent magnet synchronous generators (PMSG). Advanced control techniques may also be integrated with OTC to handle system dynamics and time delays, ensuring stable and efficient operation of the wind turbine. By maintaining the optimal torque-speed relationship, OTC maximizes energy capture, improves system efficiency, and reduces mechanical stress on the turbine components [73,74].

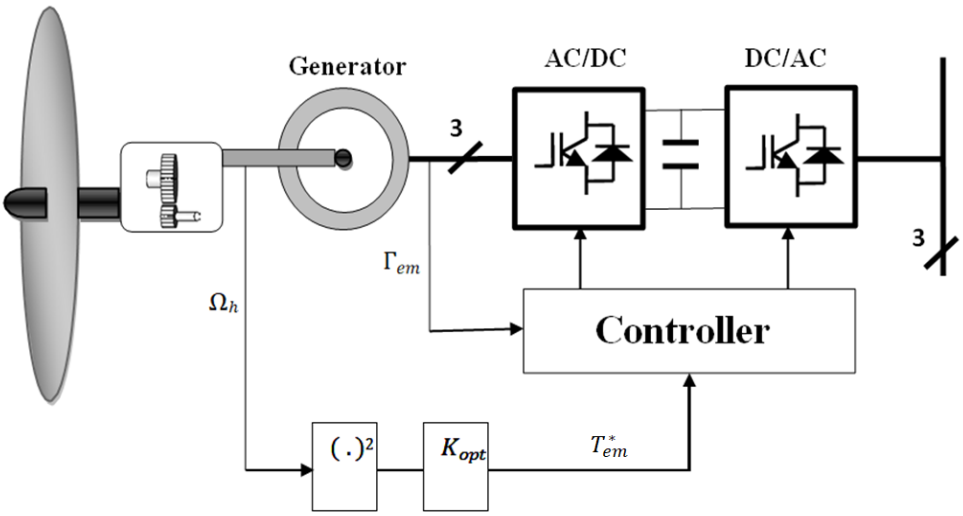


Figure II. 6 The Schematic Diagram Of The WECS Utilizing The OTC Method.

II. 2.2.2 Direct Power Control (DPC) Based MPPT Algorithm

Direct Power Control (DPC)-based MPPT strategies are widely used in Wind Energy Conversion Systems (WECS) for their ability to regulate power directly without relying on complex wind speed measurements. These strategies primarily include Incremental Conductance (INC), Perturb and Observe (P&O), and Optimal Rotor Blade (ORB) MPPT algorithms. Unlike traditional methods that track voltage or current, DPC adjusts the switching states of the power converter to control active and reactive power. This approach enhances dynamic response and maximizes power extraction efficiency from the wind turbine. A comparison of the DPC-based techniques is presented in Table II.2.

Features of the MPPT Algorithm	**P&O**	**INC**	**ORB**
Efficiency	Low	Low	Moderate
Complexity	Simple	Simple	Simple
Convergence Speed	Slow	Slow	Medium
Oscillations at MPP	Yes	Yes	No
Prior knowledge	Not needed	Not Needed	Not Needed
Memory requirement	No	No	Yes
Need of Sensors for measuring wind speed	Not Needed	Not Needed	No Needed
Parameter Sensitivity	No	No	Yes
Cost	Moderate	Moderate	High
Online Updating	Yes	Yes	No
Performance under fluctuating wind speed	Moderately Fair	Moderately Fair	Moderately Fair

Table II. 2 Comparison of DPC based MPPT Algorithms for WECS [91].

II. 2.2.2.1 Perturb and Observe (P&O) Control

The Perturb and Observe (P&O) control [61,71] method is commonly employed in wind energy conversion systems (WECS) to achieve maximum power point tracking (MPPT). This method operates by iteratively perturbing the system variables, such as rotor speed or duty cycle, and observing the resulting changes in the output power. If the power increases after a perturbation, the

control system continues adjusting the variable in the same direction; otherwise, it reverses the direction of perturbation [71,72]. In the context of wind energy, the P&O algorithm attempts to maximize the power extracted from the wind by adjusting the rotor speed toward the optimal tip speed ratio (TSR), which corresponds to the point at which the wind turbine achieves maximum aerodynamic efficiency. This iterative process allows the turbine to continually adjust to varying wind speeds and maintain optimal energy capture.

While P&O is straightforward to implement and computationally efficient, it has some limitations, particularly under rapidly changing wind conditions. The algorithm can cause oscillations around the maximum power point (MPP) because of the continuous perturbations, which may reduce system efficiency. Moreover, in cases of large wind speed fluctuations, the algorithm can become slow in tracking the new MPP, thus affecting the overall performance of the wind turbine [71,72]. To mitigate these drawbacks, more sophisticated variants of P&O, or alternative control strategies such as Incremental Conductance (INC) or optimization-based methods, may be employed to enhance tracking precision and reduce power losses associated with oscillations.

II. 2.2.2.2 Hill Climb Search (HCS)

In wind energy conversion systems (WECS), Hill Climb Search (HCS) [62] shares similarities with the Perturb and Observe (P&O) method , particularly in their use of iterative search processes to optimize performance. P&O is commonly used in Maximum Power Point Tracking (MPPT) algorithms for both photovoltaic systems and wind energy systems, where it iteratively perturbs the operating point (such as rotor speed or generator torque) and observes the resulting change in power output [72]. In the context of WECS, P&O works by slightly adjusting the control parameters, such as the generator's speed, and measuring the change in power. If an increase in power is observed, the perturbation continues in the same direction. If the power decreases, the direction of the perturbation is reversed. This process continues until the maximum power point is reached, analogous to the goal of Hill Climb Search.

The Hill Climb Search algorithm operates in a similar fashion but focuses on broader control variable adjustments. It evaluates neighboring solutions to find the best local performance, whether in terms of maximizing power or minimizing torque ripple. However, like P&O, HCS can suffer from the issue of getting trapped in local optima, especially in nonlinear systems like WECS, where the power curve may have multiple peaks. To enhance the performance of both P&O and HCS, hybrid approaches are often explored. These may involve combining HCS with global optimization techniques like Particle Swarm Optimization (PSO) or Multi-Objective Particle Swarm Optimization

(MOPSO) to overcome the limitations of local search and find better solutions in complex and dynamic wind energy systems.

II. 2.2.2.3 Incremental Conductance (INC) Algorithm

The Incremental Conductance (INC) algorithm is an effective Maximum Power Point Tracking (MPPT) technique for wind energy conversion systems (WECS) [86], ensuring optimal power extraction by dynamically adjusting the system's operating point in response to variations in wind speed. The core principle of the INC algorithm is based on the derivative of power with respect to voltage, which determines whether the system operates at, below, or above the Maximum Power Point (MPP). At the MPP, the power derivative is zero, meaning that no further adjustment is needed. Mathematically, this condition is expressed as

$$\frac{dP}{dV} = 0 \tag{II.17}$$

Where P represents the power generated, and V denotes the terminal voltage of the generator. By applying the chain rule, this derivative expands to

$$\frac{dP}{dV} = I + V\frac{dI}{dV} \tag{II.18}$$

Where I is the current. Based on this equation, the algorithm evaluates the power variation and determines the appropriate control action.

If $\frac{dI}{dV} > -I/V$, the system operates below the MPP, requiring an increase in the duty cycle of the power converter. Conversely, if $\frac{dI}{dV} < -I/V$, the operating point is beyond the MPP, necessitating a decrease in the duty cycle. When $\frac{dI}{dV} = -I/V$, the MPP is reached, and the control action is maintained.

The implementation of the INC algorithm in a wind energy system involves continuous monitoring of voltage and current, computing incremental conductance, and dynamically adjusting the power converter's duty cycle. This process ensures that the system adapts efficiently to variations in wind speed, maintaining operation at the optimal power point. The real-time decision-making capability of the INC method allows it to respond effectively to rapid wind fluctuations, enhancing energy capture and overall system efficiency. Additionally, by accurately determining the slope of the

power curve, the algorithm minimizes unnecessary oscillations around the MPP, leading to stable and efficient operation.

One of the key advantages of the INC algorithm is its ability to improve power extraction under variable wind conditions. Since wind speed changes frequently, the system must continuously track the optimal operating point to ensure maximum efficiency. The INC method achieves this by evaluating small variations in voltage and current and making precise adjustments accordingly. This results in enhanced energy yield and improved performance of the wind turbine-generator system. Furthermore, the method reduces steady-state oscillations around the MPP, contributing to the stability and reliability of the overall system.

Despite its benefits, the INC algorithm presents certain challenges that must be addressed for optimal implementation. The computational complexity of the method is higher compared to simpler MPPT techniques, as it requires differentiation operations and real-time calculations. This necessitates the use of a fast and efficient microcontroller capable of handling the processing requirements. Additionally, the accuracy of the algorithm is highly dependent on the precision of voltage and current measurements. Small sensor inaccuracies or noise in the measurements can lead to incorrect decisions, affecting the overall tracking efficiency. To mitigate these issues, advanced filtering techniques and proper calibration of sensors are essential.

In practical applications, the INC algorithm demonstrates strong adaptability to dynamic wind conditions, making it a suitable choice for modern wind energy conversion systems. By continuously optimizing power extraction, it enhances the efficiency of wind turbines and contributes to improved energy generation. Its ability to quickly detect and adjust the operating point ensures reliable performance even in fluctuating environmental conditions. Proper tuning of the control parameters further enhances the responsiveness of the system, allowing for smooth and efficient operation. The Incremental Conductance algorithm remains a valuable MPPT technique, ensuring optimal utilization of wind energy resources while maintaining stability and efficiency in wind energy conversion systems.

II. 2.2.2.4 Optimal Relation-Based (ORB) control

The Optimal Relation-Based (ORB) control is a mature MPPT strategy in which wind speed measurement is not required and the response to wind speed change is fast [87]. ORB control ensures MPPT using a precalculated look-up table which is structured with the aid of knowledge of optimum relationships among various system parameters [88]; for instance, the power versus shaft speed , the power versus torque, the power versus rectified dc-link voltage and the dc-link voltage and dc-side current. The ORB control is simple to implement, has good dynamic response, requires no wind speed

sensor, can produce smoother output power when compared with the other strategies and is widely used in commercial WECSs [89]. The main drawback of ORB control is that system pre-knowledge is a requisite, which varies from one system to the other and may even change with the system aging [87]. Furthermore, ORB control may require lots of memory space [90].

II. 2.2.3 Smart MPPT Algorithms

Intelligent controllers such as neural networks (NN) and fuzzy logic controllers (FLC), along with various soft computing-based algorithms [91], have been widely explored in the literature. These approaches are particularly attractive for wind energy conversion system (WECS) applications, as they do not require detailed mathematical modeling of the system. However, their accuracy in optimizing control variables remains somewhat limited. Additionally, numerous adaptive algorithms, which operate without mechanical sensors, have been developed to handle system uncertainties under optimal conditions. This section provides a brief overview of FLC, NN, and sensorless MPPT algorithms. A comparative analysis of smart MPPT algorithms for WECS is presented in Table II.3.

Features of the MPPT Algorithm	FLC	NN	Sensorless
Efficiency	Higher	Higher	Moderate
Complexity	Higher	Higher	Higher
Speed of Convergence	Medium	Medium	Medium
Oscillations at MPP	Do not occur	Do not occur	Depends
Prior knowledge	Needed	Needed	Not Needed
Memory	Required	Required	Required
Need of Sensors for wind speed measurement	Depends	Depends	Not Needed
Parameter Sensitivity	Depends	Depends	Not found
Cost	Higher	Higher	Lower
Online Updating	Required	Required	Depends
Performance under fluctuating wind speed	Higher	Higher	Higher

Table II. 3 Comparison of Smart MPPT Algorithms for WECS [91].

II. 2.2.3.1 Fuzzy Logic Controller (FLC) Based MPPT Algorithm

A Fuzzy Logic Controller (FLC)-Based MPPT Algorithm [91] is an intelligent control strategy used to optimize the performance of Wind Energy Conversion Systems (WECS). Unlike traditional MPPT (Maximum Power Point Tracking) methods such as Perturb and Observe (P&O) or Incremental Conductance (INC), which rely on fixed algorithms, FLC provides a more adaptive and robust approach by effectively handling nonlinearities and uncertainties in the system.

Fuzzy Logic Control (FLC) operates based on linguistic rules rather than precise mathematical models, making it particularly suitable for dynamic and unpredictable environments like wind energy systems. The FLC structure used in MPPT consists of three main stages. The first stage is fuzzification, where numerical inputs are converted into fuzzy linguistic variables. These variables represent qualitative states such as "low," "medium," or "high," which help define the system's

behavior under different conditions. The second stage is the inference engine, which applies a predefined set of fuzzy rules in the form of IF-THEN statements to determine the appropriate control action. These rules are formulated based on expert knowledge of the system's response to wind variations. The final stage is defuzzification, where the fuzzy output is converted into a crisp numerical control signal that can be used to adjust the system's operating point toward the maximum power point (MPP). The input variables of the fuzzy controller are typically the error $(\boldsymbol{E})$ and the change in error $(\boldsymbol{\Delta E})$. The output of the FLC is a control variable that adjusts the generator speed or the electomagnetic torque or duty cycle of the power converter to track the MPP efficiently. By continuously adjusting the control action based on these input variables, FLC ensures that the wind turbine operates at the optimal power coefficient, even under varying wind speeds.

The effectiveness of the FLC-based MPPT algorithm depends on the fuzzy rule base, which defines the system's response to different conditions. The rule base typically consists of a matrix where each combination of error and change in error values corresponds to a specific control action. For example, if both the error and change in error are negative, the controller may increase the duty cycle significantly to extract more power. Conversely, if both values are positive, the system reduces the duty cycle to avoid overshooting the MPP. A well-optimized rule base ensures that the system moves toward the maximum power point smoothly without excessive oscillations. One of the main advantages of the FLC-based MPPT algorithm is its adaptability to varying wind conditions. Unlike conventional MPPT techniques that rely on fixed-step perturbations, FLC dynamically adjusts its control strategy based on real-time conditions. This makes it highly effective in dealing with the nonlinear characteristics of wind turbines and power converters. Another significant benefit is that FLC does not require an explicit mathematical model of the wind energy system, making it easier to implement in systems where modeling is complex or impractical. Furthermore, FLC offers robust performance in the presence of system noise and parameter variations, making it a reliable choice for real-world applications.

Despite its advantages, FLC-based MPPT also presents some challenges. One of the primary difficulties is the computational complexity associated with real-time processing. Since FLC involves multiple fuzzy rules and inference calculations, it requires a microcontroller or digital signal processor (DSP) with sufficient processing power. Additionally, designing an efficient fuzzy rule base requires expertise and experimentation to ensure optimal performance across different operating conditions. Another limitation is the defuzzification process, which can introduce computational overhead, especially if a large number of fuzzy sets and rules are used.

The FLC-based MPPT algorithm provides a powerful and flexible approach for maximizing wind power extraction in WECS. Its ability to handle nonlinearities and uncertain conditions makes it a promising alternative to conventional MPPT methods. However, its successful implementation requires careful tuning of fuzzy rules, appropriate selection of membership functions, and adequate computational resources to handle real-time processing demands. When designed and optimized correctly, an FLC-based MPPT controller can significantly improve the efficiency and reliability of wind energy systems, making it a valuable tool for modern renewable energy applications.

II. 2.2.3.2 Neural Network (NN) Based MPPT Algorithm

Neural networks have emerged as a powerful tool for optimizing the performance of wind energy conversion systems [135], particularly in the field of maximum power point tracking (MPPT). Traditional MPPT algorithms, such as perturb and observe (P&O) or incremental conductance (INC), rely on iterative searching methods that introduce oscillations and slow convergence when tracking the optimal power point. In contrast, neural network (NN)-based MPPT algorithms provide a fast and accurate approach by leveraging machine learning to model the nonlinear relationship between wind speed, rotor speed, and power output.

The neural network-based MPPT algorithm is designed to estimate the optimal control parameters for the wind energy system based on input variables such as wind speed, rotor speed, generator voltage, and output power. The neural network consists of three main layers: the input layer, hidden layers, and output layer. The input layer receives real-time sensor data from the wind turbine system, while the hidden layers process this information through activation functions such as ReLU, Sigmoid, or Tanh. These hidden layers extract complex relationships between the input variables and enable accurate predictions of the optimal operating conditions. Finally, the output layer generates the control signal, which may correspond to the optimal power coefficient, the duty cycle of the converter, or the reference torque setpoint. To develop a robust NN-based MPPT algorithm, the neural network undergoes a training process using historical or simulated wind turbine data. This training phase involves collecting data that maps different wind conditions to corresponding MPPT setpoints. The network is trained using optimization techniques such as backpropagation and gradient descent, minimizing the error between predicted and actual power output. Once trained, the neural network is validated through testing under various wind speed scenarios to ensure its accuracy and generalization capability. After successful validation, the trained model is deployed in real-time control, where it continuously updates MPPT control signals based on real-world operating conditions.

One of the key advantages of NN-based MPPT algorithms is their ability to achieve fast convergence without the oscillations observed in traditional MPPT methods. Since the neural network

predicts the optimal setpoint directly rather than iteratively searching for it, the system responds rapidly to changes in wind speed, thereby improving the overall efficiency of power extraction. Additionally, neural networks provide adaptive control by learning from variations in the wind profile, generator characteristics, and environmental factors. Unlike conventional methods, which may struggle with abrupt wind speed changes, NN-based MPPT can dynamically adjust to varying conditions, ensuring continuous operation at the maximum power point.

Despite their advantages, neural network-based MPPT algorithms come with certain challenges. The quality of training data is a crucial factor influencing the network's performance. Poor or insufficient data can lead to inaccurate predictions, reducing the effectiveness of the MPPT control. Furthermore, implementing neural networks in real-time control requires computational resources, as the inference process can be more complex compared to traditional MPPT techniques. Advanced microcontrollers, field-programmable gate arrays (FPGAs), or digital signal processors (DSPs) may be needed to handle the real-time execution of the NN-based MPPT algorithm. Additionally, ensuring the generalization of the trained model across different wind turbines and environmental conditions remains an ongoing research challenge. Compared to conventional MPPT techniques, neural network-based MPPT offers superior performance in terms of tracking speed, accuracy, and adaptability. While perturb and observe (P&O) and incremental conductance (IC) methods rely on step-based searching, which results in power fluctuations, NN-based MPPT provides a smoother and more precise control strategy. Fuzzy logic-based MPPT techniques offer similar adaptability but require extensive rule-based tuning, whereas neural networks can automatically learn the optimal control strategy through data-driven training. Due to these advantages, NN-based MPPT is increasingly being adopted in advanced wind energy systems, particularly in smart wind farms where artificial intelligence-driven control is essential for maximizing energy yield.

The application of neural network-based MPPT extends beyond standalone wind turbines to hybrid renewable energy systems, where optimizing power extraction is crucial for ensuring system stability. Offshore and remote wind farms, where maintenance is challenging, also benefit from NN-based MPPT, as it reduces mechanical stress on turbine components by minimizing unnecessary fluctuations in generator torque. As machine learning and artificial intelligence continue to advance, NN-based MPPT algorithms are expected to evolve further, incorporating deep learning techniques and reinforcement learning to enhance their adaptability and efficiency. Future developments may also include the integration of neural networks with predictive maintenance strategies, allowing wind energy systems to not only maximize power output but also extend the lifespan of turbine components through intelligent control.

II. 2.2.3.3 Smart Sensorless MPPT Algorithms

Smart sensorless Maximum Power Point Tracking (MPPT) algorithms for Wind Energy Conversion Systems (WECS) have garnered significant attention due to their ability to optimize power extraction without relying on mechanical sensors [91]. Traditional MPPT methods depend on wind speed sensors, anemometers, or rotary encoders to determine the optimal operating point of the wind turbine. However, these sensors increase costs, require frequent maintenance, and are prone to reliability issues in harsh environmental conditions. Sensorless MPPT techniques overcome these challenges by leveraging electrical measurements, such as voltage and current, to estimate critical system parameters, ensuring efficient and robust power optimization.

These algorithms utilize estimation techniques and advanced control strategies to track the optimal power point without direct mechanical measurements. Among them, Artificial Intelligence (AI)-based sensorless MPPT techniques have emerged as promising solutions for WECS. Reinforcement Learning (RL) algorithms, in particular, continuously learn and refine MPPT strategies through real-time interaction with the system, enhancing adaptability and performance in highly variable wind conditions.

Sliding Mode Observers (SMO) are widely used in sensorless MPPT implementations due to their robustness against system uncertainties. By analyzing electrical signals, SMO-based MPPT techniques estimate rotor and wind speeds with high accuracy and noise resistance, making them particularly suitable for environments where sensor failures could compromise performance. Another advanced approach, Model Predictive Control (MPC), predicts future system behavior based on past and present measurements. By dynamically adjusting control parameters, MPC ensures maximum power extraction while accounting for system constraints and disturbances, achieving fast and efficient optimization without mechanical sensors.

Additionally, smart sensorless MPPT algorithms employ Extended Kalman Filters (EKF) and adaptive observers to estimate unmeasured states such as wind speed, rotor position, and torque. These advanced filtering techniques process electrical measurements in real time, compensating for modeling inaccuracies and measurement noise. The resulting improved state estimation enhances MPPT precision and stability, particularly in fluctuating wind conditions.

The advantages of smart sensorless MPPT algorithms in WECS are substantial. By eliminating mechanical sensors, they reduce system complexity, maintenance costs, and failure risks while improving reliability through robust state estimation and control strategies. Furthermore, these techniques enable real-time adaptation to rapidly changing wind conditions, enhancing power tracking efficiency. As technology advances, the integration of AI, machine learning, and predictive control in

sensorless MPPT algorithms is expected to further enhance the efficiency and resilience of wind energy systems, making them increasingly viable for large-scale renewable energy deployment.

II. 3 Problem Statement

For a low-power horizontal-axis WECS operating in the partial load region [54], the control problem focuses on maximizing the energy extracted from the wind. Let's assume that the aerodynamic and drive train models are not fully available, and only a limited set of constructive parameters is known. Additionally, only the high-speed shaft variables, generator variables, and wind speed can be measured. The problem of maximizing captured energy can be addressed using linear methods to determine the control law. However, their real-world performance depends heavily on the accuracy of the system parameters used in control, as well as on intrinsic nonlinearities and parametric variations. As a result, nonlinear methods are often preferred. These approaches typically employ simple and robust control laws that minimize the sensitivity of the controlled system to WECS parameters and unmodeled dynamics. Given that key WECS parameters, such as the optimal specific speed and maximum aerodynamic efficiency, are unknown, MPPT algorithms generally aim to maintain the optimal operating point by ensuring that $\Delta P_a / \Delta \omega_{ls}$ equals zero, where P_a represents the aerodynamic power and ω_{ls} is the angular velocity of the low-speed shaft. The control input, which defines the wind turbine's speed reference, is therefore dependent on the position of the operating point and its directional shift, as indicated by the sign of $\Delta P_a / \Delta \omega_{ls}$ (refer to Figure II.7 and Table II.4). Since the rotor power cannot be directly measured, an estimated value, derived from the measurement of active power, is used to identify the operating point, resulting in a static approach. Furthermore, the generator speed is measured to estimate the angular velocity of the low-speed shaft.

$\frac{dP_a}{dt}$ / $\frac{d\omega_{ls}}{dt}$	< 0	> 0
< 0	$\omega_{ls} \nearrow$ - Case I	$\omega_{ls} \searrow$ - Case II
> 0	$\omega_{ls} \searrow$ - Case III	$\omega_{ls} \nearrow$ - Case IV

Table II. 4 MPPT Control Logic.

In this approach, the rotational speed is controlled according to the position of the operating point on the power curve, steering it towards the maximum available power. However, the search for

maximum power, influenced by wind speed fluctuations and the high inertia of the turbine, presents several drawbacks. The most notable are significant estimation errors and the occurrence of high-frequency power variations, which negatively impact the system's overall reliability.

To address the first drawback, heuristic methods have been employed, which estimate wind speed and identify the characteristics of the power coefficient [55,56]. For the second issue, certain extensions of MPPT algorithms, developed through fuzzy control techniques [57,58], have proven effective. These lead to more advanced and flexible controllers. The rule base is designed to maintain the operating point at a low value of $\Delta P_a / \Delta \omega_{ls}$, representing an extension of the control logic outlined in Table II.4. The variation in rotational speed, $\Delta \omega_0$, occurs in steps and is adjusted based on the distance from the optimal operating point, as well as its direction of movement and speed.

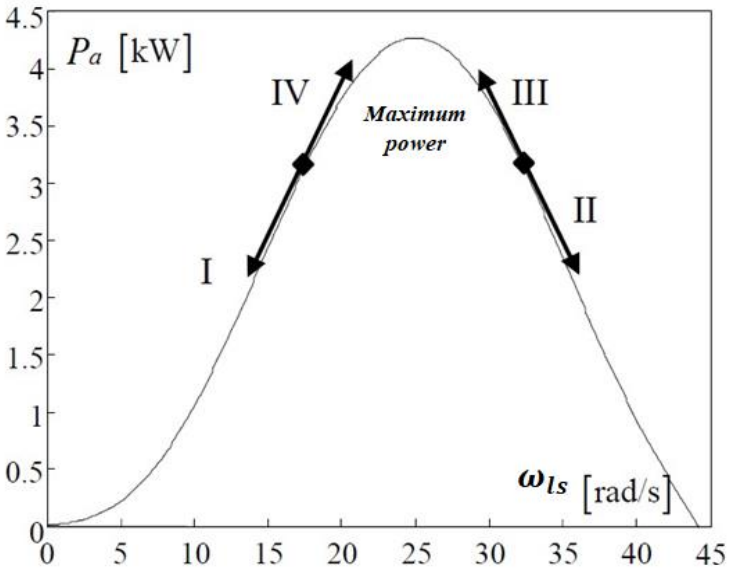


Figure II. 7 Decision Case For MPPT Control On The Static Power Curve Of A WECS.

II. 4 Standard On-Off Controller

Standard On-Off control is a robust technique used in wind energy conversion systems (WECS) with a squirrel cage induction generator (SCIG) connected to the grid [5]. Its primary function is to maximize the power extracted from wind energy by controlling the system's operation near its optimal point. This method achieves efficiency by dynamically adjusting the generator's electromagnetic torque in response to varying wind conditions. Through continuous monitoring, it ensures the torque closely aligns with the optimal value, promoting effective power capture. The approach minimizes energy losses, enhancing system reliability and performance under fluctuating wind speeds.

II. 4.1 Controller Design

This method operates on the premise that the WECS is capable of promptly adapting to low-frequency fluctuations in wind speed, which is particularly true for systems with lower power ratings. Therefore, to optimize energy conversion, it suffices to apply the torque control value corresponding to the system's steady-state operating point. For this purpose, a framework utilizing the Standard On-Off controller can be implemented to eliminate the error $e(t) = \lambda_{opt} - \bar{\lambda}(t)$, where $\bar{\lambda}(t)$ is derived from the low-frequency component of the wind speed v_s.

$$\bar{\lambda} = \frac{\omega_l R}{v_s} \tag{II.19}$$

The structure illustrated in Figure II.8 is chosen for its robustness in managing the parametric uncertainties characteristic of any WECS [92,93]. The control law associated with this diagram generates the steady-state torque reference T_{em}^*, which is composed of two components:

$$\Gamma_{em}^* = u^{eq} + u^n \tag{II.20}$$

Where the equivalent command, u^{eq} is a component corresponding to the optimal operating point (at λ_{opt}), and proportionally depends on the squared low-frequency wind speed, v_s^2 :

$$u^{eq} = 0.5\pi.\rho.R^3.v_s^2.\frac{C_p\left(\lambda_{opt}\right)}{G.\lambda opt} = \frac{\Gamma_{wt}\left(\omega_{lopt}, v_s\right)}{G} \tag{II.21}$$

As the control loop is imposed to operate in self-oscillations, u^n is a high-frequency alternating component, which switches between two values, $+\beta$ and $-\beta$ with $\beta > 0$.

$$u^n = \beta.sign(\sigma) \tag{II.22}$$

(Figure II.8) shows a schematic diagram of the standard On-Off controller.

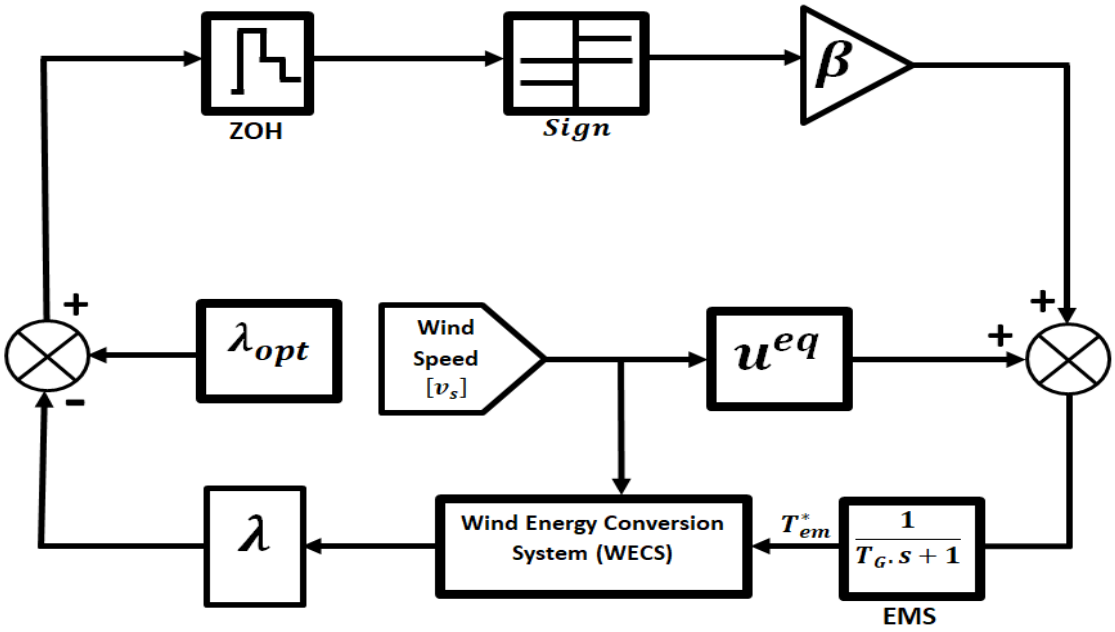


Figure II. 8 Block Diagram Of The Standard On-Off Controller.

The component u^{eq} is designed to guide the system toward the optimal operating point, while u^{n} plays a crucial role in stabilizing the system's behavior once it reaches that point. The control input in this scenario spans a broad frequency range, which means that the time constant T_G of the electromagnetic subsystem (EMS) can no longer be overlooked. To address this, a zero-order hold (ZOH) was introduced to constrain the switching frequency of the control loop. When this frequency becomes excessively high, the EMS dynamics accelerate beyond the loop's ability to control it effectively. Additionally, the introduction of ZOH increases the system's order, enabling stabilization through the phenomenon of self-oscillation [92].

II. 4.2 Simulation Results

The evaluation of the On-Off Control's effectiveness was carried out by simulating the wind energy conversion system and applying the proposed control strategy within the MATLAB/Simulink framework. The parameters governing the WECS, provided in Table B.1 of Appendix B., were used to configure the system. The simulation spanned a duration of 80 seconds, during which the wind profile had an average velocity of approximately 11 m/s. Furthermore, the analysis considered two distinct levels of turbulence intensity—low and high—both generated in accordance with the von Karman turbulence model, as prescribed by the standards of the International Electrotechnical Commission (IEC).

II.4.2.1 Low Turbulence Stochastic Wind Speed

To obtain a more accurate evaluation of the on-off controller's performance, a low-turbulence stochastic wind model was employed. Specifically, the wind model proposed by C. Nichita [19] was used for simulation purposes, with detailed modeling provided in Chapter I, Section 3.1. This model generates a time-varying wind profile derived from white noise, which is then processed through the transfer function of the von Karman irrational filter. The parameters of this filter depend on the characteristics of the site and the inherent properties of the wind, as shown in Figure II.9.

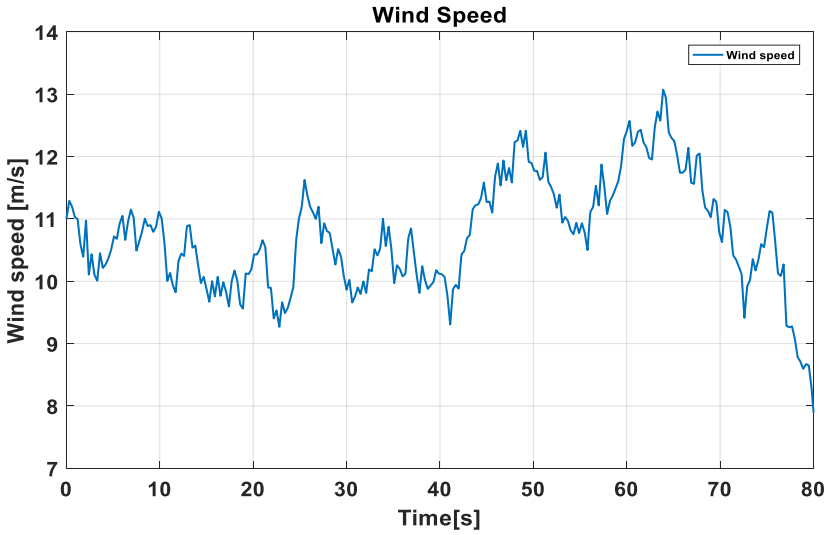


Figure II. 9 Low Turbulence Stochastic Speed.

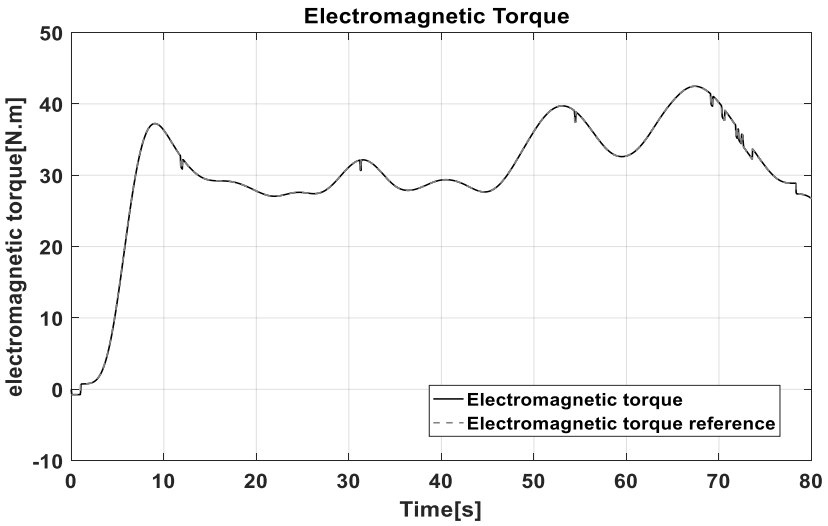


Figure II. 10 Electromagnetic Torque.

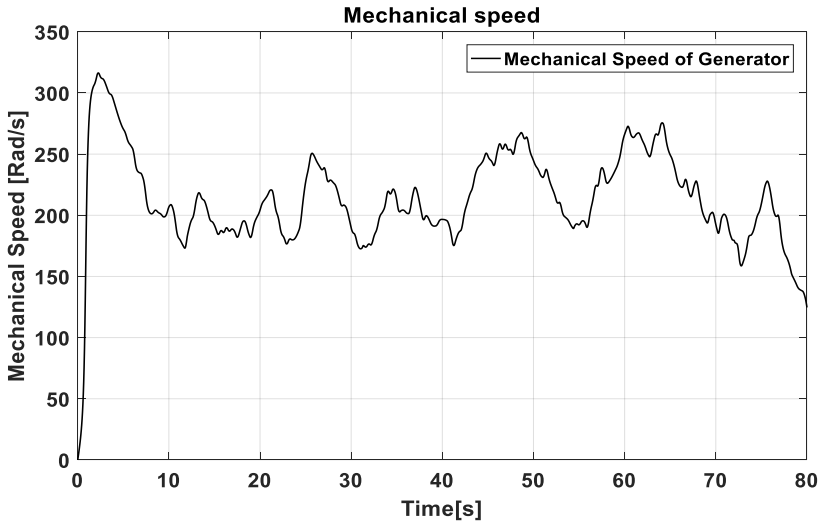


Figure II. 11 Mechanical Speed of Generator Ω_h .

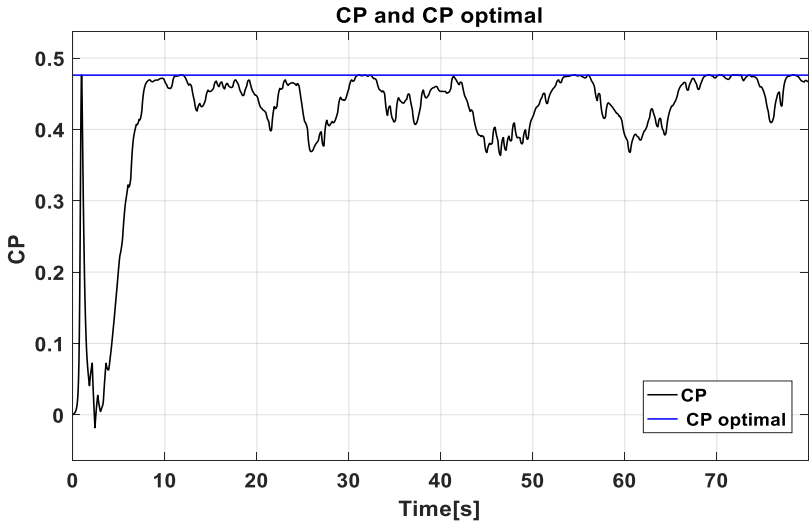


Figure II. 12 Power coefficient (CP).

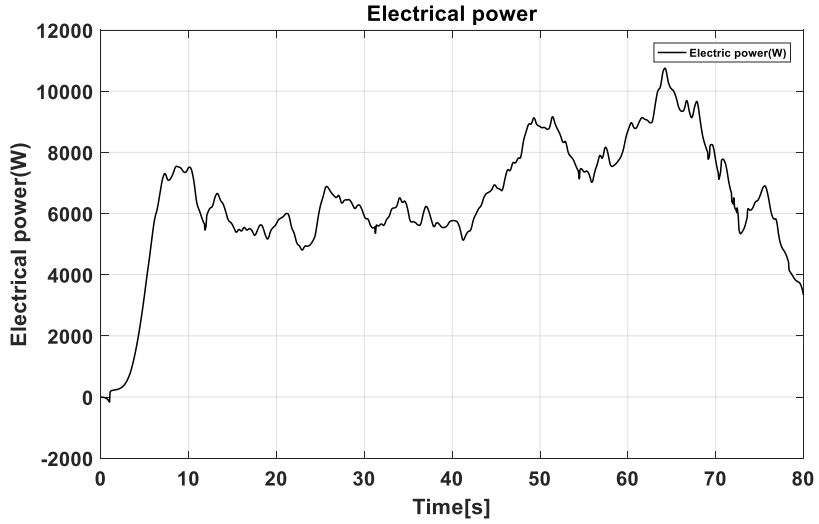


Figure II. 13 Electrical power.

By analyzing the performance of the standard On-Off controller using the low-turbulence stochastic wind speed model (Figure II.9), it became apparent that the inclusion of the sign function in

the control law generated a pronounced chattering effect, which was clearly reflected in the electromagnetic torque curve (Figure II.10). This chattering resulted in considerable vibrations and fluctuations in the generator's mechanical speed curve (Figure II.11). Moreover, although the standard On-Off controller succeeded in tracking the optimal power coefficient (CP), it did so inconsistently, struggling to maintain stable and continuous tracking of the maximum power point (Figure II.12). The corresponding electrical power curve (Figure II.13) indicates that the controller reached a peak power output of 10.9 kW under optimal wind conditions, particularly when the wind speed attained its highest value.

II.4.2.2 High Turbulence Stochastic Wind Speed

To evaluate the resilience of the On-Off controller, it was crucial to analyze its performance under various operational conditions. Thus, simulations were performed utilizing a high-turbulence wind model to investigate the controller's behavior in challenging environments. Figure II.14 illustrates the highly turbulent stochastic wind model employed in the simulations.

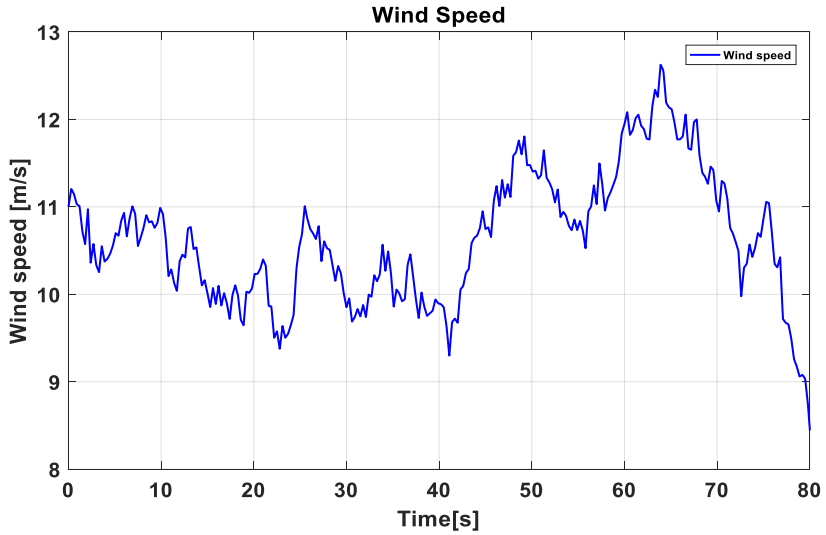


Figure II. 14 High turbulence stochastic wind speed.

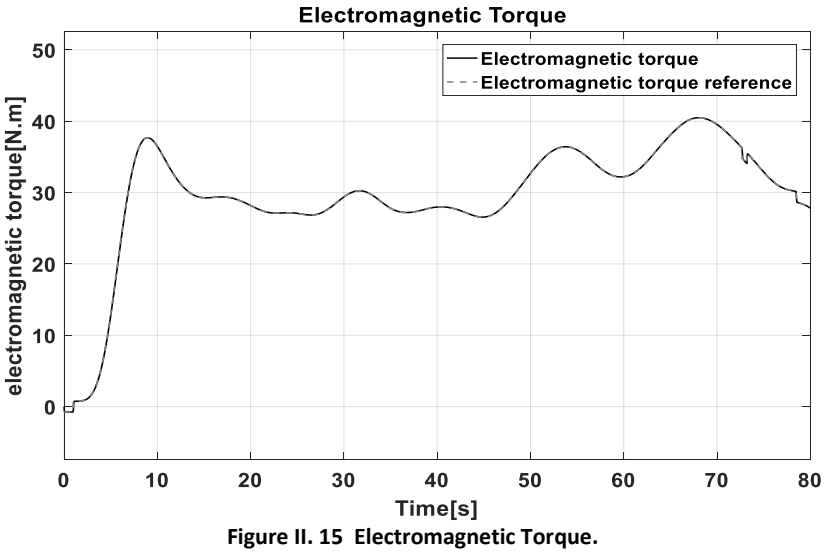


Figure II. 15 Electromagnetic Torque.

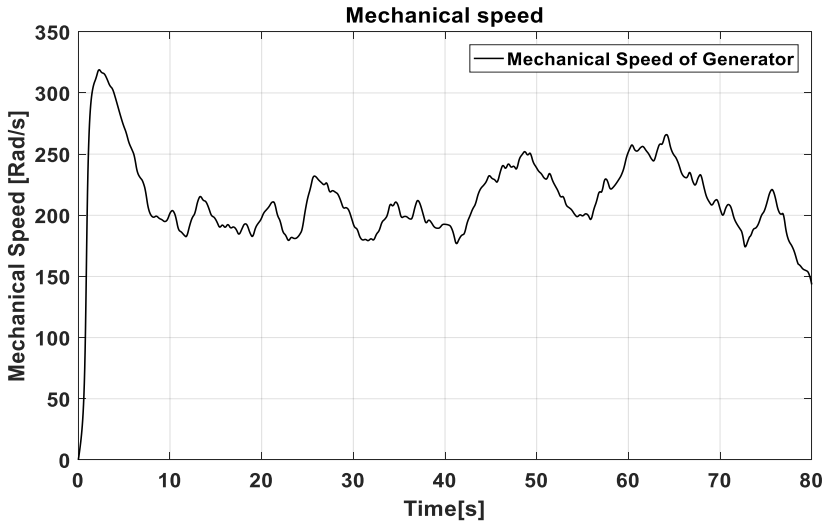


Figure II. 16 Mechanical Speed of Generator Ω_h .

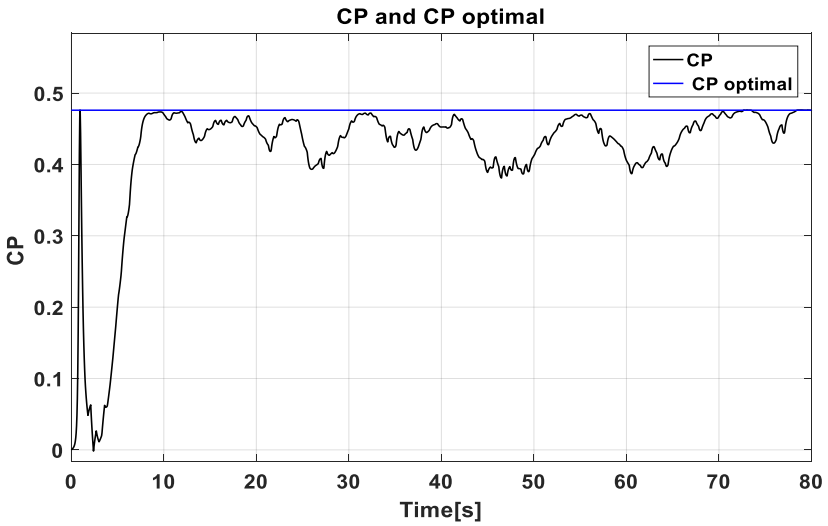


Figure II. 17 Power coefficient (CP).

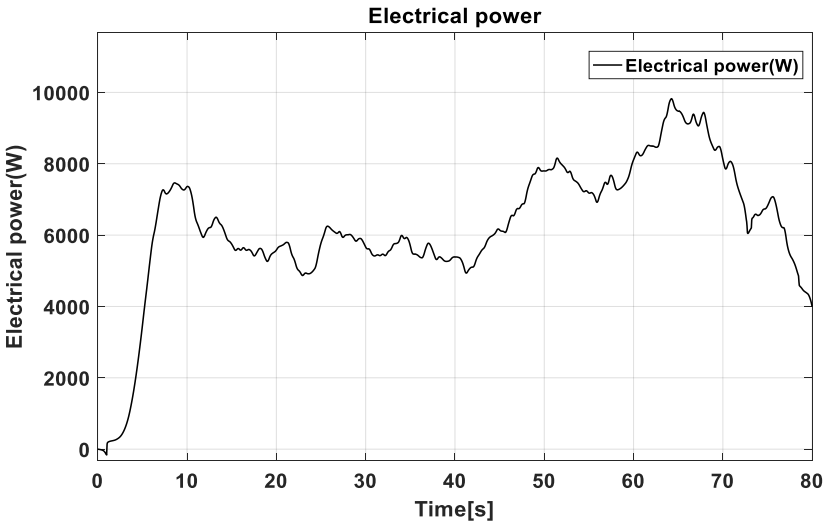


Figure II. 18 Electrical Power.

By analyzing the performance of the standard on-off controller under different conditions using a high-turbulence stochastic wind speed model (Figure II.14), it became clear that the inclusion of the sign function in the control law introduces a pronounced chattering effect, which is clearly visible in

the electromagnetic torque curve (Figure II.15). This chattering results in large oscillations and fluctuations in the mechanical speed curve of the generator as well as its decreasing due to the effect of high-turbulence wind speed (Figure II.16). Furthermore, although the standard on-off controller successfully tracked the optimum power coefficient (CP), it did so inconsistently and with poor performance under high-turbulence wind conditions, where it struggled to maintain a stable and continuous tracking of the maximum power point (Figure II.17). The corresponding electrical power curve (Figure II.18) indicates that the controller, due to the high turbulence winds that slowed the generator speed, significantly decreased the electrical power output, reaching a peak power output of 9.8 kW under optimum wind conditions, especially when the wind speed reached its highest value.

II. 5 Improved On-Off Controller

Following the analysis of the results of the on-off controller discussed in the previous section, several drawbacks have surfaced, primarily due to the presence of the sign function in the control law. The most critical of these is the chattering phenomenon, which can excite high-frequency oscillations, potentially leading to system damage. To address this issue, numerous methods have been proposed in the literature. In this section, we propose an improved on-off controller as a solution to the chattering problem by integrating a first-order filter into the discontinuous part of the control.

II. 5.1 Controller Design

To mitigate the torque fluctuations caused by the control input, a modified control law, derived from Equation (II.22) [93], is proposed. This revised controller not only offers robustness against parametric uncertainties but also helps to reduce torque variations resulting from the switched control component. The block diagram of this improved controller is illustrated in Figure II.19.

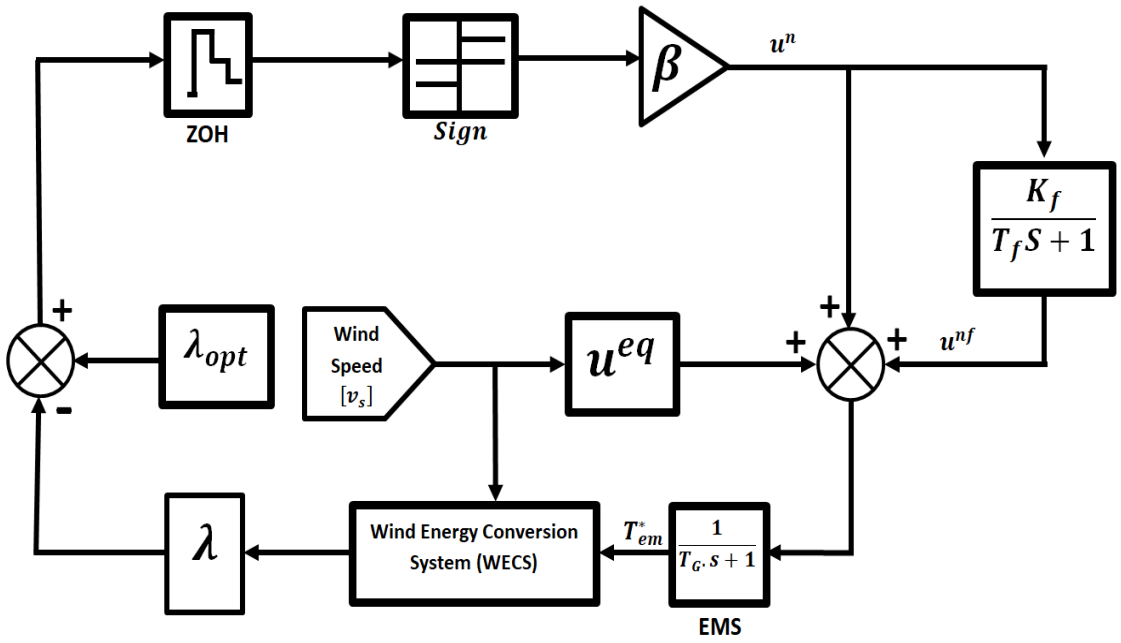


Figure II. 19 Block Diagram Of The Improved On-Off Controller.

The modified control law, u^{mod}, contains an additional low frequency component, denoted u^{nf}, obtained by filtering the alternate component, u^n (Figure II.19):

$$u^{\text{mod}} = u^{eq} + u^n + u^{nf} \tag{II.23}$$

Where:

$$u^{nf} = u^n . \frac{K_f}{T_f s + 1} \tag{II.24}$$

The filtering time constant T_f, results in imposing a maximum allowable ripple for u^{nf}; regarding the gain K_f, a sufficient value may be $K_f = \Delta u^{eqmax} . \omega_0 T/\beta$, where Δu^{eqmax} represents the maximum expected value of the difference Δu^{eq} and ω_0 represents the cutoff frequency.

II. 5.2 Simulation Results

To guarantee a fair comparison between the Standard On-Off control and the Improved On-Off control, the same low-turbulence and high-turbulence stochastic wind models from the previous section were employed. This comparative study involved simulating a wind energy conversion system and applying the corresponding control strategies within the MATLAB/Simulink environment. The control parameters for the WECS, as specified in Table B.1 of Appendix B., were utilized to set up the system. The simulation was conducted over a period of 80 seconds, during which the average wind speed was approximately 11 m/s.

II.5.2.1 Low Turbulence Stochastic Wind Speed

As mentioned earlier and as in the previous chapter which studies the Standard on-off controller in detail, to obtain a more accurate evaluation of the performance of the improved on-off controller, a low-turbulence stochastic wind model was used. Figure II.9 shows the wind model used in the simulation.

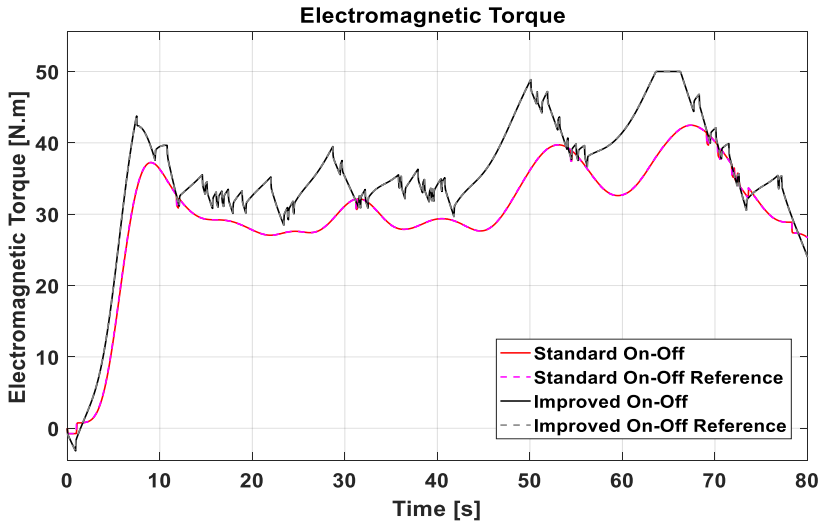


Figure II. 20 Electromagnetic Torque.

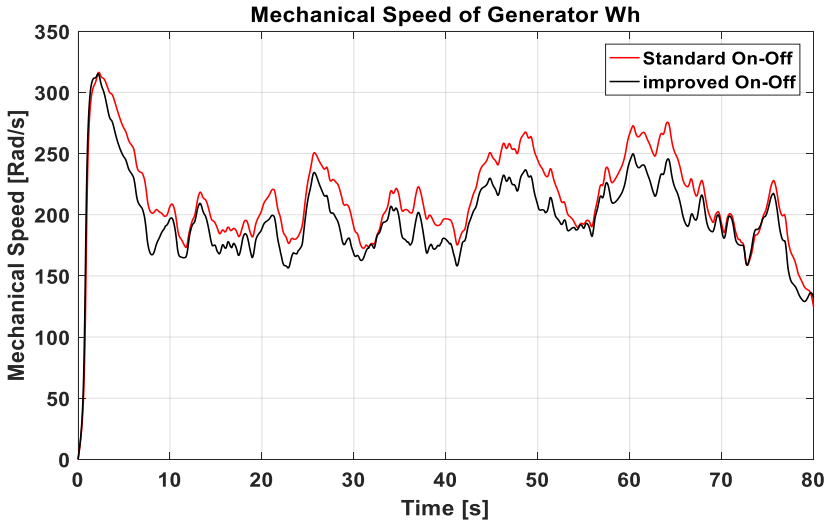


Figure II. 21 Mechanical Speed of Generator Ω_h .

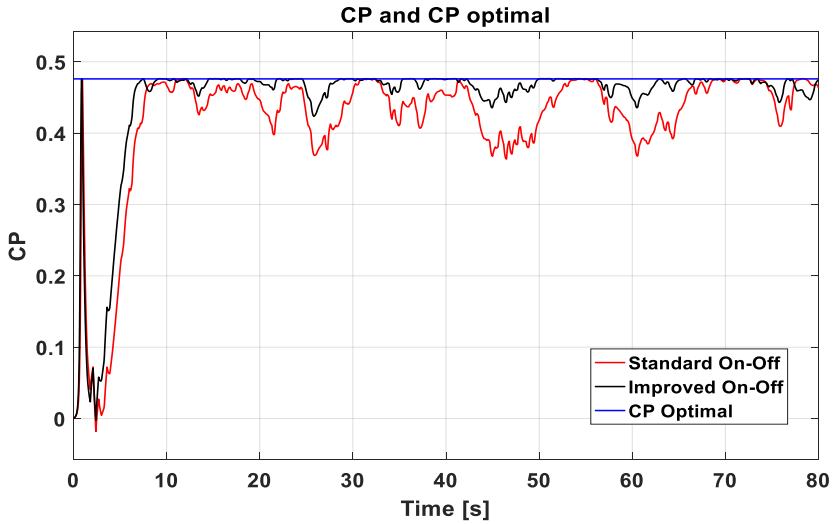


Figure II. 22 Power coefficient (CP).

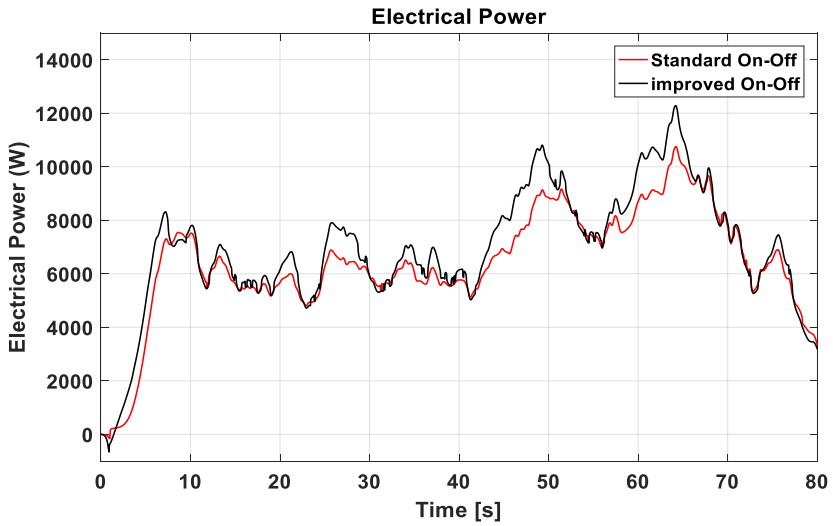


Figure II. 23 Electrical Power.

By comparing the performance of the Improved On-Off controller with that of the Standard On-Off controller using a low-turbulence stochastic wind speed model (Figure II.9), we found that the standard controller was more effective in reducing the chattering issue, albeit not completely. In contrast, the improved On-Off controller resulted in a notable increase in electromagnetic torque ripple (Figure II.20), which escalated due to the lower generator speed compared to the standard controller (Figure II.21). However, the improved On-Off controller demonstrated superior tracking of the optimal power coefficient (CP) relative to its standard counterpart (Figure II.22). This capability explains the significant increase in electrical power produced by the improved controller compared to the standard one (Figure II.23). The electrical power curve (Figure II.23) shows that the improved On-Off controller achieved a peak output of 12.2 kW under optimal wind conditions, particularly at the highest wind speeds.

II.5.2.2 High Turbulence Stochastic Wind Speed

As mentioned earlier, evaluating the adaptability of the Improved On-Off controller required a thorough analysis of its performance across diverse operating conditions, alongside a comparison with a Standard On-Off controller under the same scenarios. To achieve this, simulations were performed using a high-turbulence wind model to investigate the controller's behavior in challenging environments. Figure II.14 presents the high-turbulence random wind model utilized in these simulations.

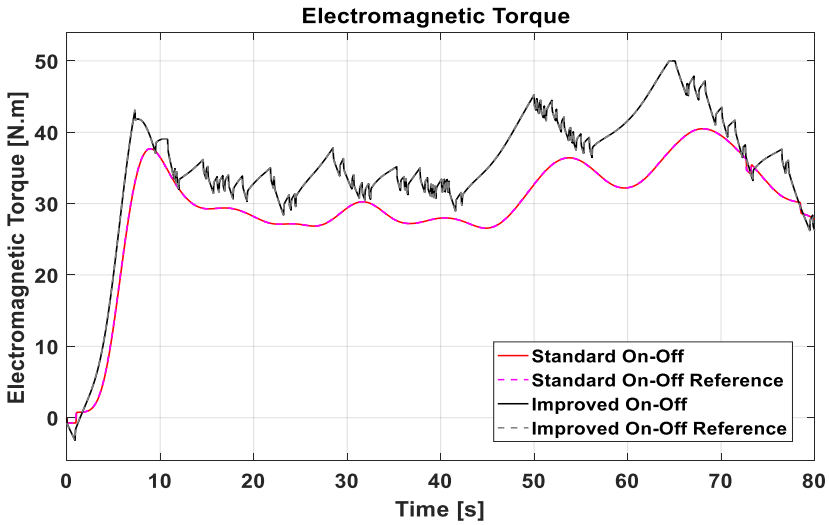


Figure II. 24 Electromagnetic Torque.

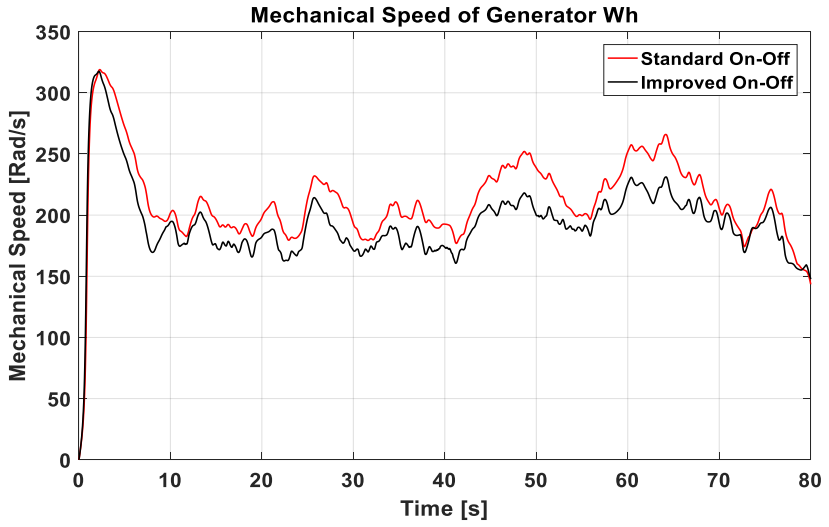


Figure II. 25 Mechanical Speed of Generator Ω_h .

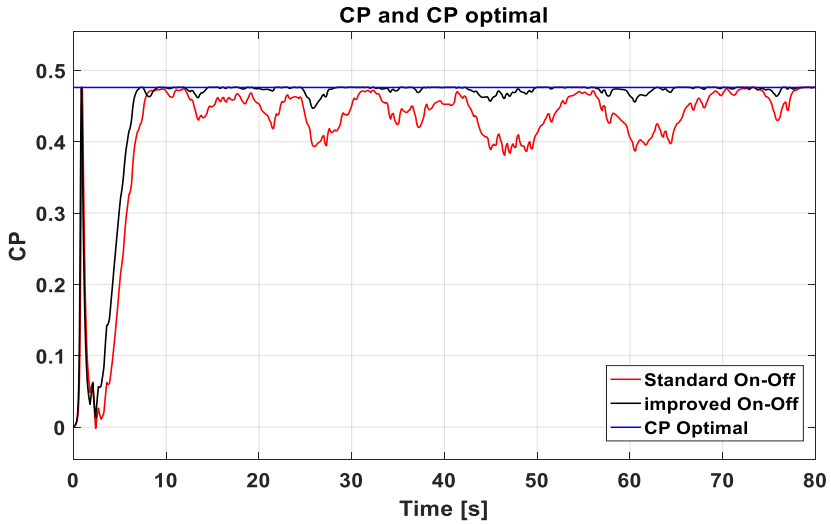


Figure II. 26 Power coefficient (CP).

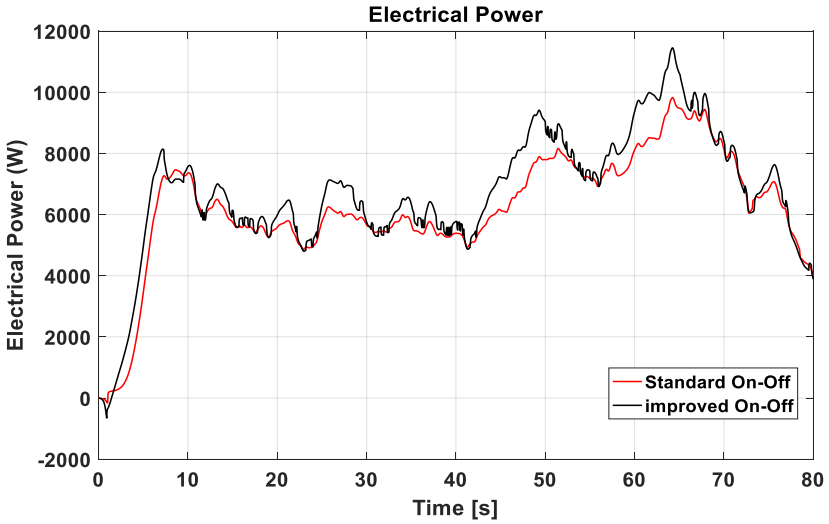


Figure II. 27 Electrical Power.

By comparing the performance of the improved ON-OFF controller with that of the standard ON-OFF controller using a high-turbulence stochastic wind speed model (Figure II.14), it becomes evident that the improved ON-OFF controller excels in enhancing power output by more effectively tracking the maximum power point. The results derived from testing under various operating conditions using this high-turbulence wind model confirm the effectiveness of the improved ON-OFF controller in significantly increasing electrical power production compared to the standard controller. While the standard controller offers better mitigation of vibration issues, it does not completely resolve them. In contrast, the improved ON-OFF controller, despite achieving superior power tracking, introduces a noticeable increase in electromagnetic torque ripple (Figure II.24), partly due to the higher reduction in generator speed caused by vibrations compared to the standard controller (Figure II.25). Nevertheless, the improved controller demonstrates significantly better tracking of the optimal power coefficient (CP), as illustrated in Figure II.26. This capability accounts for the substantial increase in electrical power output observed with the improved controller, as reflected in (Figure II.27). The

electrical power curve further reveals that the improved ON-OFF controller reaches a peak output of 11.8 kW under optimal wind conditions, particularly at higher wind speeds.

II. 6 Enhanced Fuzzy On-Off Controller

As outlined in the previous sections, the standard on-off controller for electromagnetic torque regulation suffers from a significant drawback—chattering—which adversely impacts the operational lifespan of wind turbines. To address this issue, various methods have been explored in the literature. In a prior study [50,54], a Fuzzy On–Off Synthesis Controller was introduced to enhance energy extraction and eliminate chattering induced by mechanical stress. While this approach effectively reduced chattering, it exhibited limitations in tracking the maximum power point. The primary goal of this section is to design and evaluate an Enhanced Fuzzy On-Off Controller aimed at optimizing energy harvesting. This improvement is realized by integrating a first-order filter into the discontinuous portion of the control. To validate the effectiveness of the Enhanced Fuzzy On-Off Controller in maximizing wind energy production and improving maximum power point tracking, its simulation results are compared with those obtained from the Fuzzy On–Off Synthesis Controller.

II. 6.1 Fuzzy On-Off Controller

As previously discussed in this chapter, it is important to recall that the control component u^{eq} ensures the system operates at its optimal point, while the component u^{n} plays a critical role in stabilizing the system's dynamic response once this point is reached. The chattering phenomenon, which emerges due to the term $sign(\sigma)$ in Equation (II.22), can be mitigated by substituting the high-frequency component u^{n} with the fuzzy control law u^{f} . This adjustment significantly reduces chattering, thereby resolving the issue and yielding the following new control law for the fuzzy on-off controller [50,54]:

$$\Gamma_{em}^{*} = u = u^{eq} + u^{f} \tag{II.25}$$

The equation below denotes the fuzzy control law u^{f} .

$$u^{f} = \beta . Z^{f} = \beta . \frac{\sum_{i=1}^{49} \left(\theta^{i} \mu_{\sigma i} \mu_{\dot{\sigma} i} \right)}{\sum_{i=1}^{49} \left(\mu_{\sigma i} \mu_{\dot{\sigma} i} \right)} \tag{II.26}$$

In this context, θ^{i} denotes the singular control in the i_{th} rule, whereas $\mu_{\sigma i}$ and $\mu_{\dot{\sigma} i}$ represent the membership functions of σ and $\dot{\sigma}$ in the i_{th} rule.

Figure II.28 shows a schematic diagram of the Fuzzy On-Off controller.

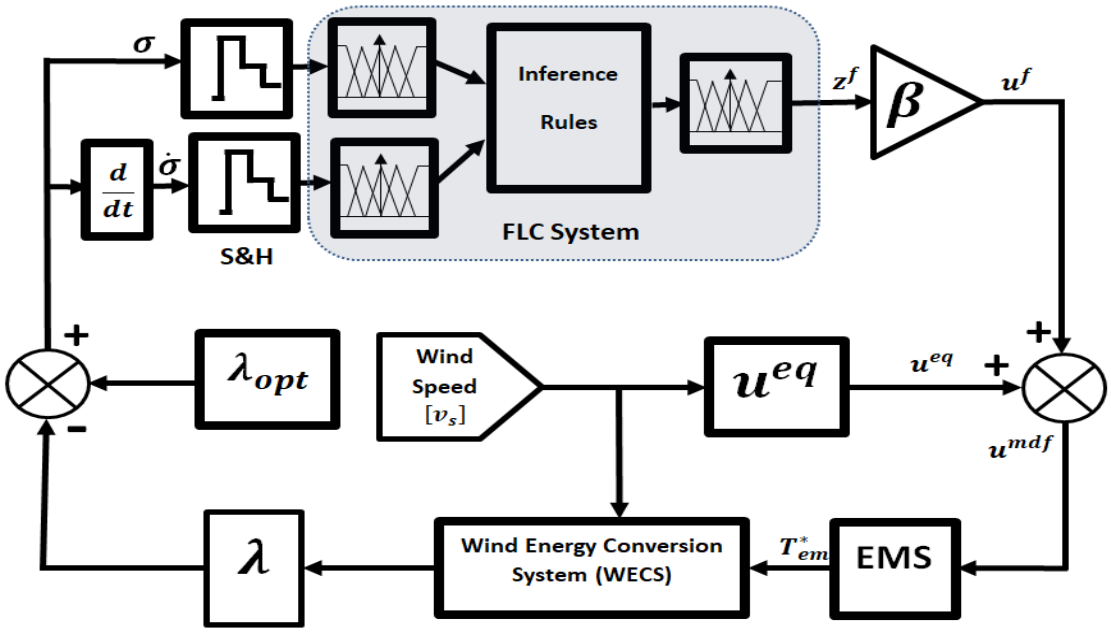


Figure II. 28 Block Diagram of The Fuzzy On-Off Controller.

II. 6.2 Enhanced Fuzzy On-Off Controller Design

While the Fuzzy On-Off controller proves effective in mitigating the chattering issue that could otherwise shorten wind turbine lifespan, as compared to the standard On-Off controller [5], additional improvements are required to achieve optimal tracking of the maximum power point, thus maximizing wind energy production. To this end, we propose an enhancement to the Fuzzy On-Off controller by incorporating a first-order filter into its internal structure. This modification is intended to enhance the controller's capability to more accurately track the maximum power point. The updated control law for the Enhanced Fuzzy On-Off Controller is presented in Equation II.27.

$$u_{new} = u^{eq} + u^{f} + u^{nf} \tag{II.27}$$

u^{nf} Represents a new component in the internal structure of the Fuzzy On-Off controller, as depicted in Equation II.28.

$$u^{nf} = u^{f} \frac{K_f}{T_f s + 1} \tag{II.28}$$

By incorporating a first-order filter, the detailed overall equation that results in the Enhanced fuzzy on-off controller becomes as follows:

$$u_{new} = \left(\frac{1}{2} \pi R^3 \frac{C_P\left(\lambda_{opt}\right)}{\lambda_{opt}.G} \right) + \beta . \frac{\sum_{i=1}^{49} \left(\theta^i \mu_{\sigma i} \mu_{\dot{\sigma} i} \right)}{\sum_{i=1}^{49} \left(\mu_{\sigma i} \mu_{\dot{\sigma} i} \right)} + u^{f} \frac{K_f}{T_f s + 1} \tag{II.29}$$

Figure II.29 depicts a schematic diagram of the Fuzzy On-Off controller.

In Table II.5, the fuzzy sets used are as follows: NB for negative big, NM for negative medium, NS for negative small, ZR for zero, PS for positive small, PM for positive medium, and PB for positive big. The fuzzy rules for the output variable Z^f are detailed in Table II.5, aiming to maintain system stability around the operating point by selecting a control law that keeps $\sigma = 0$. Enhanced Fuzzy On-Off Control utilizes fuzzy logic to address system uncertainty and minimize chattering effects. The process of formulating fuzzy rules is similar to applying a saturation function, with the control gain adjusting continuously along the on-off surface. For instance, to avoid chattering, when σ is PB and $\dot{\sigma}$ is PB, the control permits the PB value of Z^f. The required fuzzy control law is defined by equation II.26.

Z^f		$\dot{\sigma}$						
		NB	NM	NS	ZR	PS	PM	PB
σ	NB	NB	NB	NB	NB	NM	NS	ZR
	NM	NB	NB	NB	NM	NS	ZR	PS
	NS	NB	NB	NM	NS	ZR	PS	PM
	ZR	NB	NM	NS	ZR	PS	PM	PB
	PS	NM	NS	ZR	PS	PM	PB	PB
	PM	NS	ZR	PS	PM	PB	PB	PB
	PB	ZR	PS	PM	PB	PB	PB	PB

Table II. 5 Fuzzy Rules.

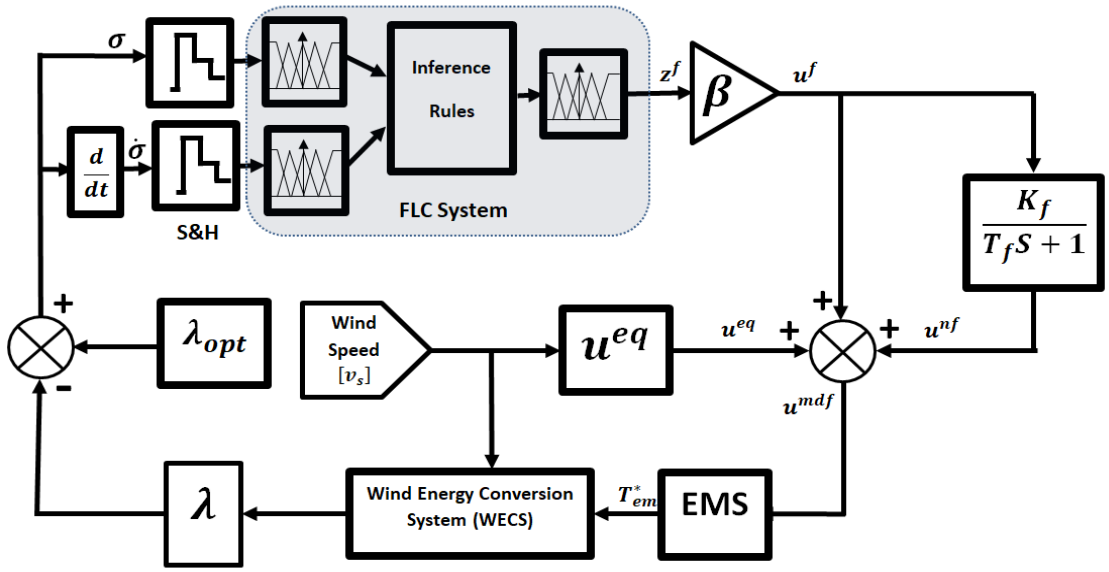


Figure II. 29 Block Diagram of The Enhanced Fuzzy On-Off Controller.

Figure II.30 visually presents the linguistic values for σ , $\dot{\sigma}$ and Z^f. We establish seven triangular membership functions spread across the interval $[-1, 1]$. These functions are employed to formulate 49 rules, as outlined in Table II.5 , and are utilized in the simulation.

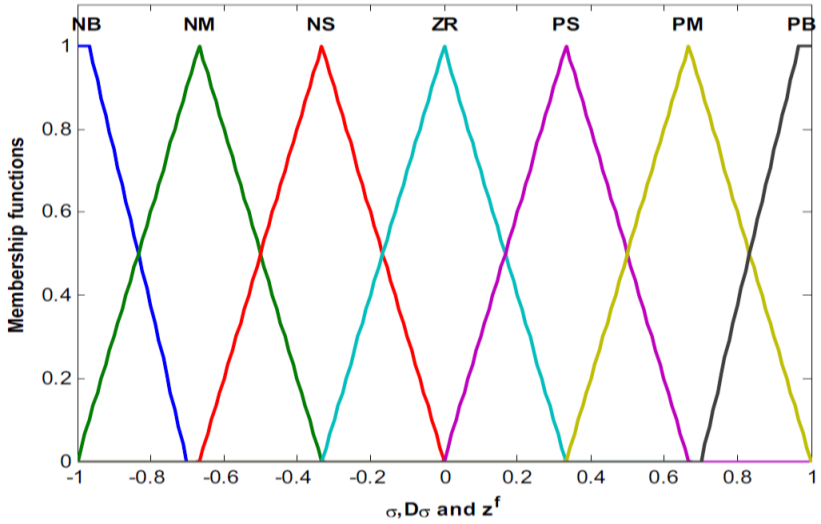


Figure II. 30 Membership Functions Used For $\sigma, \dot{\sigma}$ and Z^f .

II. 6.3 Simulation Results

To evaluate the effectiveness of the Enhanced Fuzzy On-Off control, the Wind Energy Conversion System (WECS) and its control strategy were modeled and implemented in a MATLAB/Simulink environment, with the results compared against those of the standard Fuzzy On-Off control. The simulations used the WECS parameters provided in Table B.1 of Appendix B and were conducted across two turbulence categories: low and high turbulence intensity, to assess performance under diverse operating conditions. The simulations ran for 80 seconds, with an average wind speed of around 11 m/s.

II.6.3.1 Low Turbulence Stochastic Wind Speed

Initially, the low-turbulence stochastic wind model depicted in Figure II.9 was employed to compare the performance of the Enhanced Fuzzy On-Off Controller with that of the Fuzzy On-Off Controller.

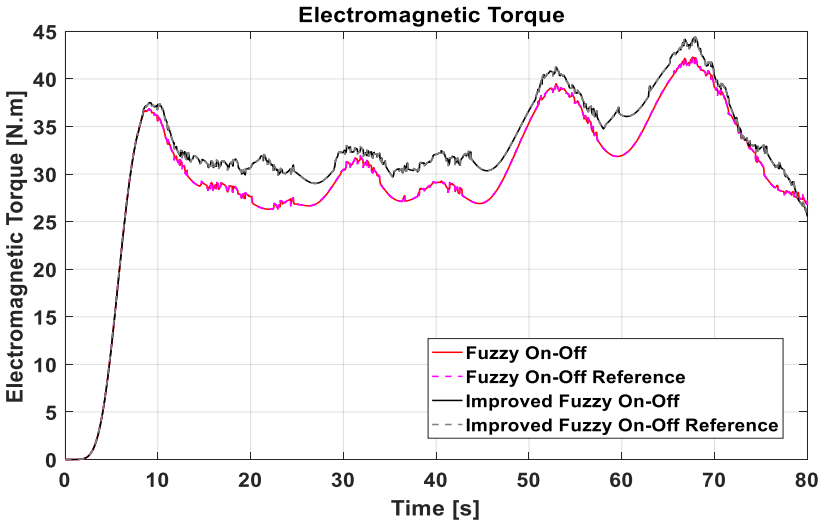


Figure II. 31 Electromagnetic Torque.

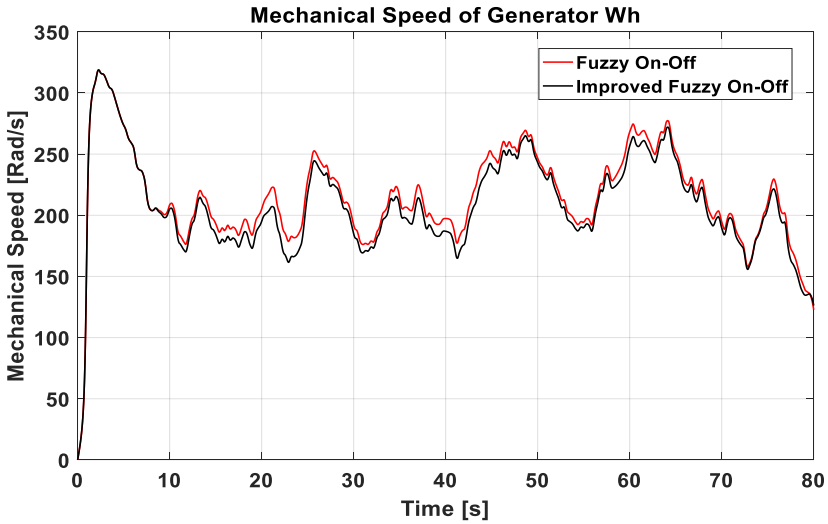


Figure II. 32 Mechanical Speed of Generator Ω_h .

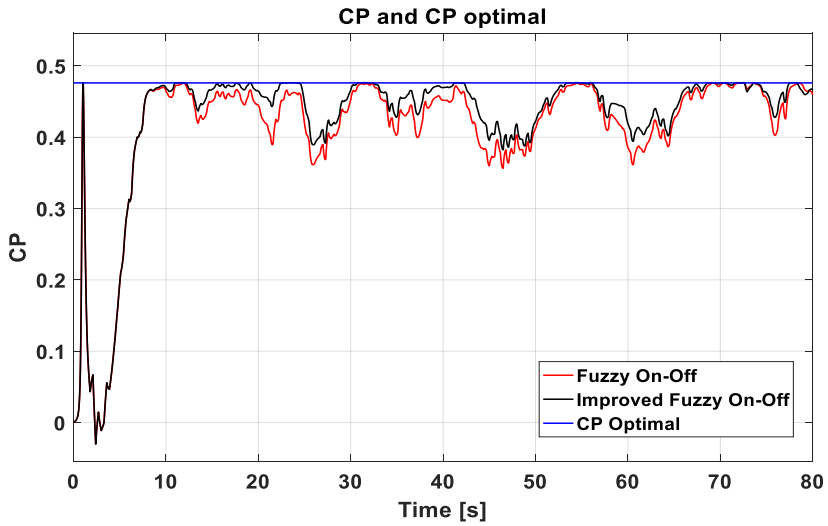


Figure II. 33 Power coefficient (CP).

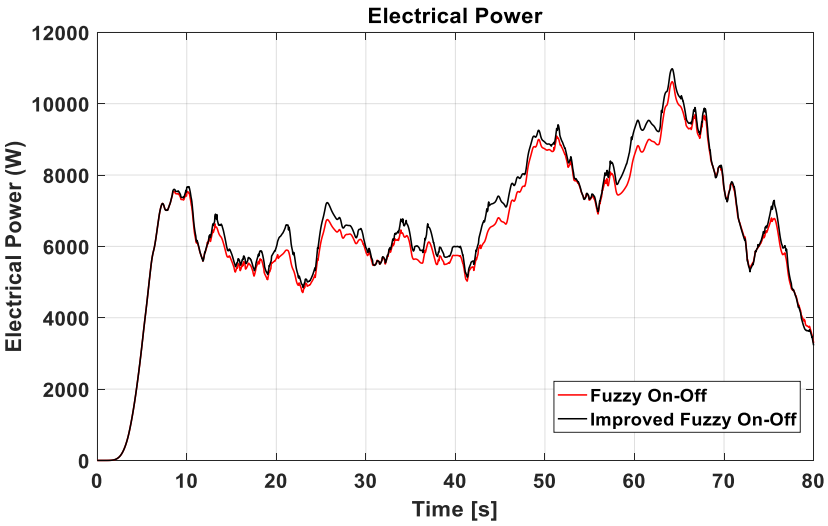


Figure II. 34 Electrical Power.

Upon reviewing the simulation results with low-turbulence stochastic wind speeds, several critical observations emerge. First, the comparison of the results in Figure II.31 reveals that, under low-turbulence wind conditions (Figure II.9), the Fuzzy On-Off controller is more effective in

reducing electromagnetic torque than the Enhanced Fuzzy On-Off controller. This reduction plays a key role in extending the operational lifespan of wind turbines. However, when it comes to tracking the maximum power point by following the optimal power coefficient (CP), the Enhanced Fuzzy On-Off controller exhibits superior performance over the Fuzzy On-Off controller, as demonstrated in Figure II.33. Consequently, the Enhanced Fuzzy On-Off controller offers a distinct advantage in maximizing power production, as shown in Figure II.34.

II.6.3.2 High Turbulence Stochastic Wind Speed

To validate the efficiency and robustness of the proposed controller, the high-turbulence stochastic wind model depicted in Figure II.14 was employed to compare the performance of the Enhanced Fuzzy On-Off Controller against that of the standard Fuzzy On-Off Controller.

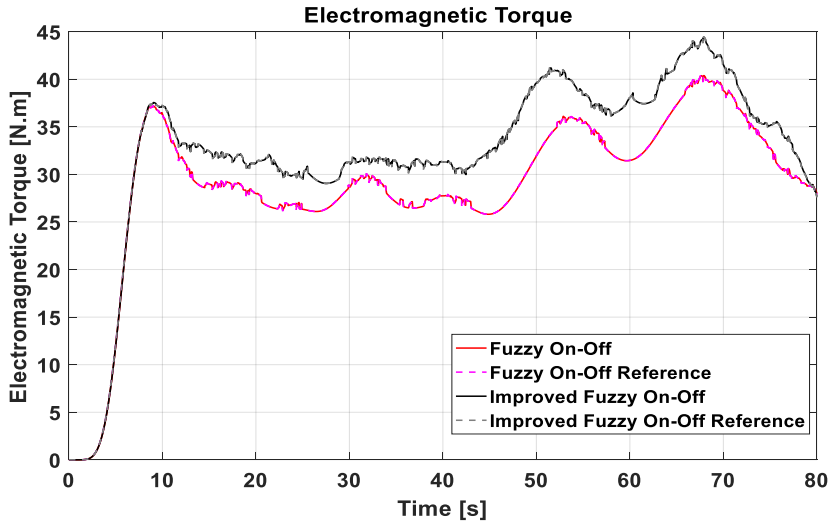


Figure II. 35 Electromagnetic Torque.

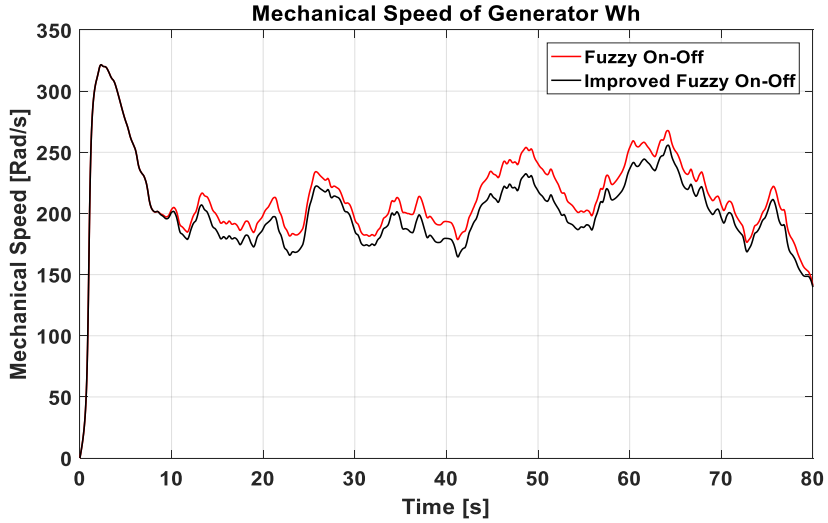


Figure II. 36 Mechanical Speed of Generator Ω_h .

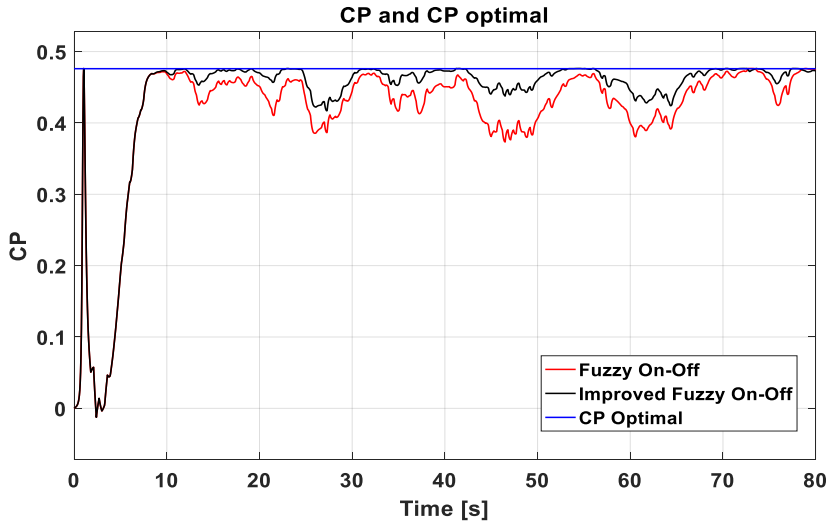


Figure II. 37 Power coefficient (CP).

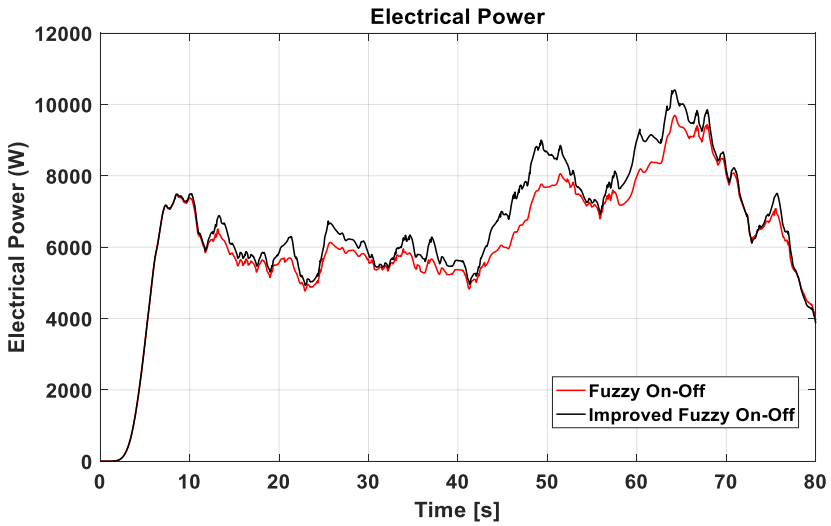


Figure II. 38 Electrical Power.

When comparing the plots in (Figure II.37) and (Figure II.38), and in simulations with highly turbulent wind speeds (Figure II.14), the Enhanced Fuzzy On-Off controller demonstrates superior performance over the Fuzzy On-Off controller in tracking the maximum power point, as depicted in (Fig II.37). This highlights its effectiveness in maximizing power output, as demonstrated in (Figure II.38). Conversely, it is important to note that in scenarios with highly turbulent wind speeds (Figure II.14), the Fuzzy On-Off controller exhibits better performance in reducing electromagnetic torque ripple compared to the Enhanced Fuzzy On-Off controller, as shown in (Figure II.35). However, it is worth mentioning that both controllers exhibit noticeable chattering issues under these conditions.

II. 7 Sliding Mode Controller

Sliding Mode Control (SMC) [94,95,96] is a robust variable-structure control technique widely used in wind energy conversion systems due to its capacity to manage system uncertainties, nonlinearities, and external disturbances, such as fluctuating wind conditions. This method operates by

driving the system's state trajectory toward a defined surface, known as the sliding or switching surface, and ensuring the system evolves along this surface until reaching equilibrium. The dynamics of the system in this ideal sliding regime are fully governed by the parameters that define the surface, resulting in a reduction of system order and rendering the system insensitive to disturbances in the same direction as the inputs. SMC's robustness is crucial for maintaining performance despite parameter variations or model mismatches, making it well-suited for dynamic environments like wind energy systems. The ability of SMC to reject disturbances effectively ensures high tracking accuracy and system stability, even in unpredictable and constantly changing wind conditions. However, a common challenge associated with SMC is the chattering effect, characterized by high-frequency oscillations near the sliding surface due to the control law's switching nature. In wind energy applications, this can cause mechanical wear or noise, particularly affecting components such as the generator and drivetrain. Despite this drawback, the primary objective of SMC in wind energy systems is to optimize the capture of wind power while minimizing mechanical stress and energy losses.

II. 7.1 Controller Design

Les Variable Structure Control (VSC) through Sliding Mode Control (SMC) was initially proposed and developed in the Soviet Union during the early 1950s by Emelyanov, along with researchers such as Utkin and Itkis [97]. Over recent decades, VSC and SMC have attracted considerable attention from the System Control and Automation research community. SMC has been employed not only for nonlinear systems but also for multi-input multi-output (MIMO) systems, discrete-time models, large-scale and infinite-dimensional systems, and stochastic systems. Its most notable characteristic is its complete robustness against parametric uncertainties and external disturbances during sliding mode operation [98]. At its core, variable structure control utilizes a high-frequency switching control law to direct the system's state trajectory toward a predefined surface in the state space, referred to as the sliding or switching surface [99].

SMC presents two key advantages: the system's dynamic behavior can be precisely shaped through the appropriate selection of the switching function, and the closed-loop system becomes entirely insensitive to a specific class of uncertainties. Additionally, the ability to define performance parameters directly enhances the appeal of SMC from a design standpoint.

Designing SMC involves two critical steps. The first step is to define a sliding surface such that the system, once restricted to this surface, exhibits the desired behavior. This entails constraining the state variables to satisfy a set of equations that define the switching surface. The second step involves constructing a state feedback gain capable of driving the system's state trajectory onto this sliding surface. These structures are grounded in the generalized Lyapunov stability theory [100].

The sliding mode approach can also be used for tracking the energy optimum of a variable-speed Wind Energy Conversion System (WECS). The sliding surface is systematically derived by imposing a desired reduced-order dynamic, thus allowing the wind turbine to operate more or less along the Maximum Power Point Tracking (MPPT) trajectory, depending on a trade-off imposed between torque ripple (control input) and optimal path tracking. In this way, by controlling the generator torque, a multi-functional optimization (energy-reliability) is effectively achieved.

The modeling is done under the assumption of a single-mass model and within the limited frequency range of wind speed [101]. The power coefficient curve is considered to be known, and the structural dynamics are negligible. The electric generator is ideal, meaning it has constant parameters. Power losses result in constant efficiency for the wind speed range. From the equation of motion of the high-speed shaft, the system equations are written as follows:

$$\begin{cases} \dot{\Omega}_h(t) = \dfrac{T_t(G.\Omega_h, v)}{(G.J_t)} - \dfrac{T_{em}}{T_G} \\ \dot{T}_{em}(t) = -\dfrac{T_{em}}{T_G} + \dfrac{u}{T_G} \end{cases} \tag{II.30}$$

Given that J_t represents the inertia of the high-speed shaft (expressed as $J_t = J_{wt} / \mathrm{G}^2$, where J_{wt} is the rotor inertia), and u denotes the reference for the electromagnetic torque, $u = T_{\mathrm{em}}^*$, the goal is to design a sliding surface that enables the Wind Energy Conversion System (WECS) to operate near the Maximum Power Point Tracking (MPPT) trajectory. For this to occur, the desired surface must be wind speed-dependent, ensuring that its projection in the $(\omega_1, \mathrm{P_e})$ plane intersects the MPPT trajectory at each wind speed.

The state equations (Equation II..31) can thus be reformulated as:

$$\dot{\boldsymbol{x}} = f(\boldsymbol{x}, t) + B(\boldsymbol{x}, t).u \tag{II.31}$$

Where:

$$f(\boldsymbol{x}, t) = \begin{bmatrix} \dfrac{T_t}{(J_t.G)} - \dfrac{T_{em}}{J_t} \\ -\dfrac{T_{em}}{T_G} \end{bmatrix} \tag{II.32}$$

$$B(\boldsymbol{x}, t) = \begin{bmatrix} 0 \\ \dfrac{1}{T_G} \end{bmatrix} \tag{II.33}$$

The state equation is already presented in regular form [102]. As a result, the reduced-order dynamic is represented by the following first equation:

$$\begin{bmatrix} \dot{\Omega}_h \\ \dot{T}_{em} \end{bmatrix} = \begin{bmatrix} \frac{T_t}{(J_t.G)} - \frac{T_{em}}{J_t} \\ -\frac{T_{em}}{T_G} \end{bmatrix} + \begin{bmatrix} 0 \\ \frac{1}{T_G} \end{bmatrix}.u \tag{II.34}$$

Let $\sigma(x,u,t)$ represent the sliding surface. Equation (II.34) and the condition $\frac{\partial \sigma}{\partial x}.B(x,t) \neq 0$, which ensures the existence of the equivalent control [96,103], impose that $\frac{\partial \sigma}{\partial T_{em}} \neq 0$. For simplicity, this is denoted as $\frac{\partial \sigma}{\partial T_{em}} = a_3 \neq 0$. Therefore, a preliminary expression for the switching surface can be formulated as:

$$\sigma(\Omega_h, T_{em}) = \sigma_1(\Omega_h) + a_3.T_{em} \tag{II.35}$$

The equation $\sigma(\Omega_h, T_{em}) = 0$ implies that $\sigma_1(\Omega_h) + a_3.T_{em} = 0$, which simplifies to:

$$\sigma_1(\Omega_h) = -a_3.T_{em} \tag{II.36}$$

This equation shows that the function $\sigma_1(\Omega_h)$, related to the high-speed shaft angular velocity, is directly proportional to the negative of the electromagnetic torque T_{em}, with a_3 acting as the proportionality constant.

The behavior of the system on the sliding mode (i.e., on the sliding surface) can be represented as equivalent to specific dynamics. By using relation (II.34), we can derive:

$$\dot{\Omega}_h = \frac{\left(\frac{T_t}{G} - T_{em}\right)}{J_h} \equiv \begin{bmatrix} a_1 & a_2 \end{bmatrix}.\begin{bmatrix} \Omega_h & T_{em} \end{bmatrix}^T \tag{II.37}$$

Where a_1 and a_2 represent the first-order dynamics on the sliding surface. From equation (II.37), it follows that:

$$T_{em} = \frac{1}{1 + a_2.J_h}.\left(\frac{T_t}{G} - a_1.J_h.\Omega_h\right) \tag{II.38}$$

For simplification, let $a_3 = 1 + a_2.J_h$. Combining relations (II.36) and (II.38) with equation (II.35) provides the expression for the sliding surface:

$$a_1 = -\frac{1}{T_{sm}} \tag{II.39}$$

$$a_2 = -\frac{a_1.\Omega_{hopt}}{T_{emopt}} \tag{II.40}$$

Here, J_h denotes the equivalent inertia assigned to the high speed shaft, and T_{sm} represents a time constant. The parameter a_1 characterizes the time constant of the sliding mode dynamics. Steady-state conditions are achieved by adjusting a_2, thus defining the equilibrium on the sliding surface. In this scenario, where energy optimization is crucial, the equilibrium point is set to the optimum (i.e., on the Optimal operating characteristic). Consequently, the switching surface depends on the derivative of a state variable (the rotational speed), which presents a challenge for real-time implementation. To address this, a first-order high-pass filter with the transfer function $\frac{s}{T_f.s+1}$, where $T_f = 0.1s$, can be employed to approximate this derivative.

To determine the equivalent control, the following relation is used:

$$u^{eq} = -\left[\frac{\partial \sigma}{\partial x}.B\right]^{-1}.\left[\frac{\partial \sigma}{\partial t} + \frac{\partial \sigma}{\partial x}.f(x,t)\right] \tag{II.41}$$

Next, the relevant expressions are calculated as follows:

$$\frac{\partial \sigma}{\partial x}.B = \left[\frac{\partial \sigma}{\partial \Omega_h} \quad \frac{\partial \sigma}{\partial T_{em}}\right].\begin{bmatrix} 0 \\ \frac{1}{T_G} \end{bmatrix} = \frac{1}{T_G}.\frac{\partial \sigma}{\partial T_{em}} \tag{II.42}$$

The partial derivatives of the sliding surface with respect to the electromagnetic torque and the rotor speed are expressed as follows:

$$\frac{\partial \sigma}{\partial T_{em}} = 1 + a_2.J_h \tag{II.43}$$

$$\frac{\partial \sigma}{\partial \Omega_h} = a_1.J_h - \frac{1}{G}.\frac{\partial T_t}{\partial \Omega_h} \tag{II.44}$$

According to equation (I.46), the partial derivative of the wind torque with respect to the rotor speed is expressed as:

$$\frac{\partial T_t}{\partial \Omega_h} = 0.5\rho.\pi.R^3.v^2\frac{\partial C_\Gamma(\lambda)}{\partial \Omega_h} = \frac{Kv^2R}{G}\left(\frac{\dot{C_P}(\lambda).\lambda - C_P(\lambda)}{\lambda^2}\right) \tag{II.45}$$

With $K = 0.5\rho\pi R^2$, where $\dot{C}_P(\lambda)$ represents the derivative of the power coefficient with respect to λ , equation (II.39) can be reformulated as follows:

$$\frac{\partial \sigma}{\partial \Omega_h} = \mathrm{a}_1 . J_h - \mathrm{A}(\lambda, v) \tag{II.46}$$

$$\mathrm{A}(\lambda, v) = K.\mathrm{R}^2.v.\left(\frac{\dot{\mathrm{C}}_\mathrm{P}(\lambda).\lambda - \mathrm{C}_\mathrm{P}(\lambda)}{\lambda^2.\mathrm{G}^2} \right) \tag{II.47}$$

Thus, the expression for the equivalent control u^{eq} is given by:

$$u^{eq} = T_{em} - \frac{\mathrm{T_G}}{1 + \mathrm{a}_2 J_h} \left(\mathrm{a}_1 . J_h . \Omega_h + \mathrm{a}_2 . J_h . T_{em} \right) (\mathrm{a}_1 - \mathrm{A}(\lambda, v)) \tag{II.48}$$

The parameter a_2 in equation (II.40) can be dynamically adjusted using the following expression:

$$\mathrm{a}_2 = -\mathrm{a}_1 \frac{\Omega_{hopt}}{T_{emopt} \left(1 + k . \dfrac{\Omega_h - \Omega_{hopt}}{\Omega_{hopt}} \right)} \tag{II.49}$$

With $k \geq 0$.

The fluctuations of the operating point around the optimal operating point can be minimized. Expression (II.49) is only valid near the optimal operating point (OOP); otherwise, the parameter a_2 may increase significantly, causing the system to exit the normal operating regime. In the following section, we demonstrate that as the value of k increases, the system more effectively achieves the optimal equilibrium state $\left(\Omega_{hopt}, T_{emopt} \right)$, resulting in improved tracking accuracy of the optimal regime characteristic (ORC). Consequently, the system more precisely adheres to the control objective, which is energy optimization. However, this also leads to greater control variations, which can impact system reliability. This parameter regulates the control effort and can be used to balance the trade-off between energy optimization and reliability. The on-off component of the sliding control law u^{n} is derived by selecting the square of the sliding surface as the Lyapunov (energy) function. Therefore, we can conclude:

$$u^n = -\beta . sign_h(\sigma) \tag{II.50}$$

Where $sign_h(.)$ represents a hysteretic sign function with a width h .

The overall sliding mode control law is the combination of the equivalent control component and the on-off control component, given by:

$$u = u^{eq} + u^{n} \tag{II.51}$$

II. 7.2 Simulation Results

To rigorously evaluate the effectiveness of Sliding Mode Control, the Wind Energy Conversion System (WECS) and its associated control strategy were thoroughly modeled and simulated within a MATLAB/Simulink environment. The WECS parameters, detailed in Table B.1 of Appendix B, served as the foundation for the simulations, which were conducted under two distinct turbulence intensities: low and high. This approach aimed to examine the controller's performance across a range of operational conditions. Each simulation was executed over a duration of 80 seconds, with the wind speed averaging around 11 m/s.

II.7.2.1 Low Turbulence Stochastic Wind Speed

As with the earlier controller experiments detailed in the previous sections of this chapter, the analysis of the Sliding Mode Controller (SMC) performance initially employed the low-turbulence stochastic wind model depicted in Figure II.9.

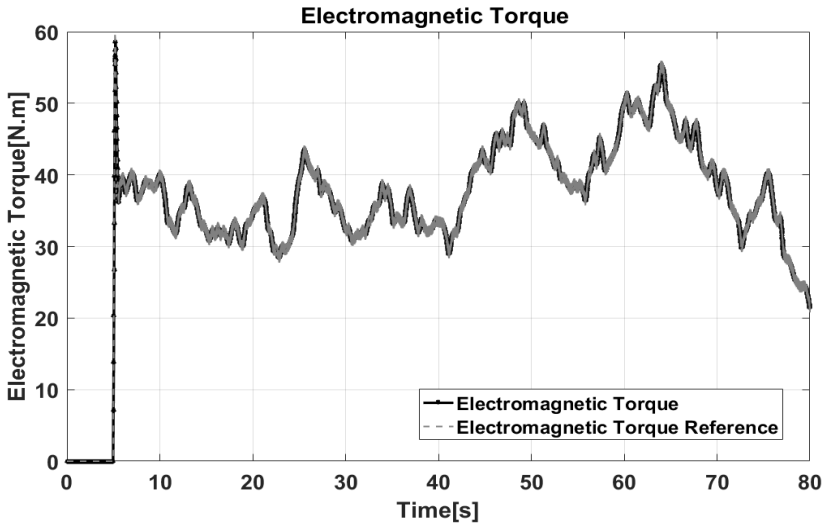


Figure II. 39 Electromagnetic Torque.

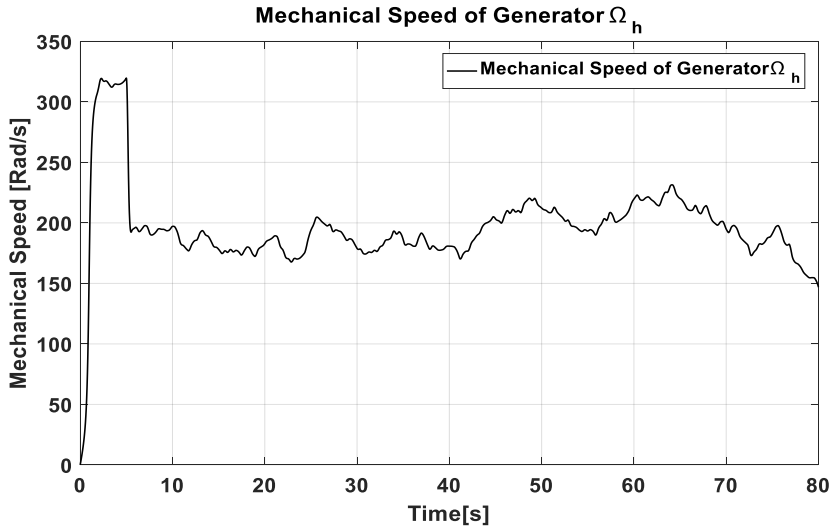


Figure II. 40 Mechanical Speed of Generator Ω_h .

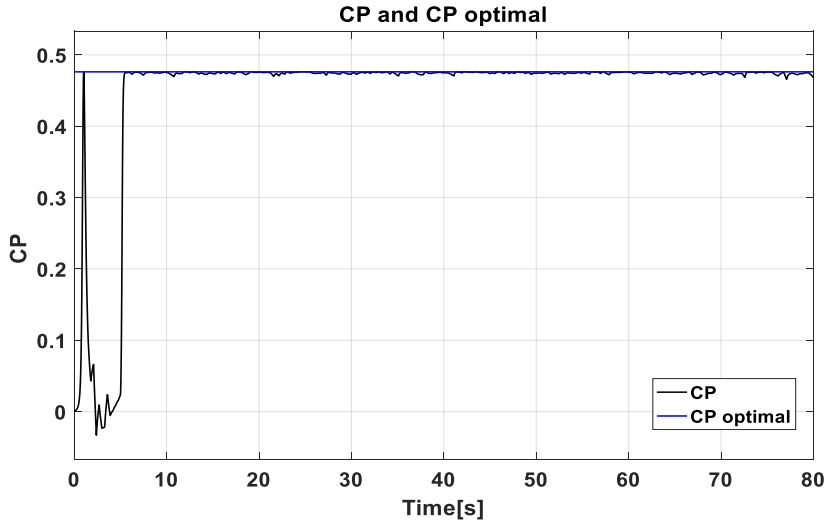


Figure II. 41 Power coefficient (CP).

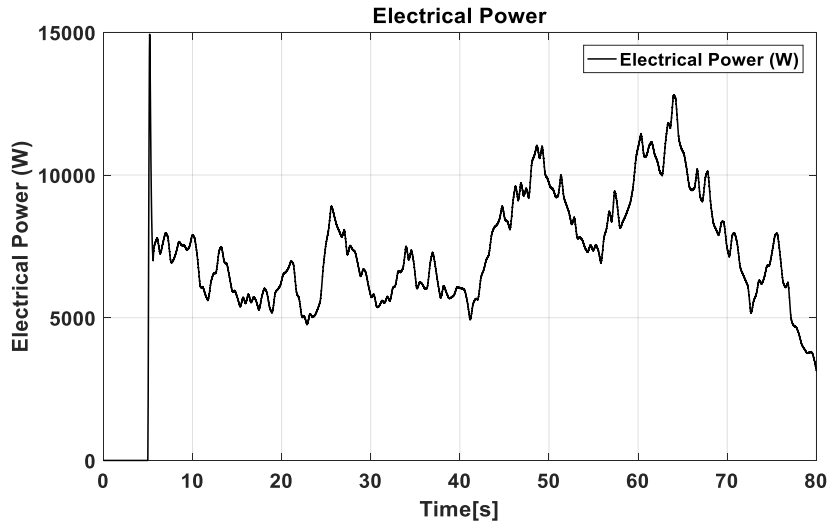


Figure II. 42 Electrical Power.

The results obtained from using the sliding mode controller (SMC) to regulate the wind energy conversion system, based on the low-turbulence stochastic wind speed model (Figure II.9), reveal a significant ripple in the electromagnetic torque (Figure II.39). This ripple introduces considerable

mechanical stress, which accelerates wear and reduces the lifespan of the wind turbine due to the chattering phenomenon. The chattering induced large vibrations and fluctuations in the generator's mechanical speed (Figure II.40). Despite this limitation, the SMC demonstrated its effectiveness in tracking the maximum power point by consistently maintaining a stable and continuous tracking of the optimal power coefficient (Figure II.41). This performance resulted in the generation of desirable electrical power, as shown in (Figure II.42), where the SMC achieved peak electrical power output of 13 kW under optimal wind conditions, particularly when the wind speed reached its highest value.

II.7.2.2 High Turbulence Stochastic Wind Speed

Consistent with the previous control experiments outlined in earlier sections of this chapter, validating the robustness of the Sliding Mode Controller (SMC) performance necessitated testing under varying conditions; thus, the high-turbulence stochastic wind model presented in Figure II.14 was utilized.

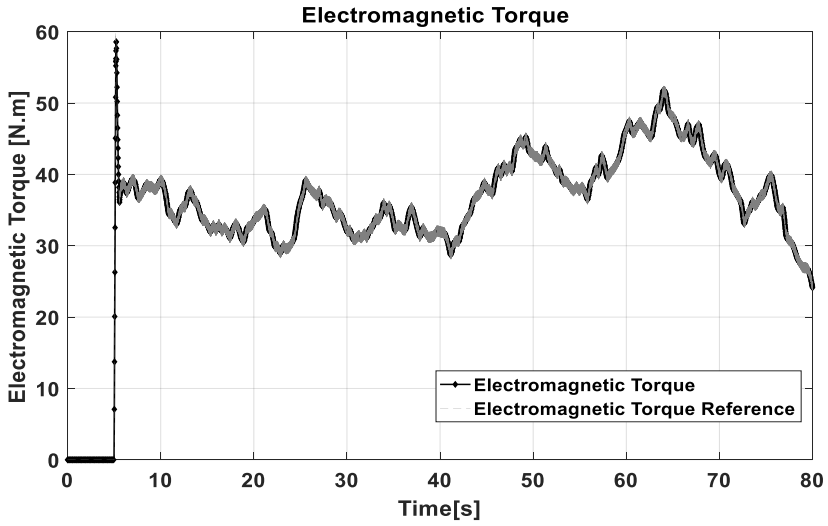


Figure II. 43 Electromagnetic Torque.

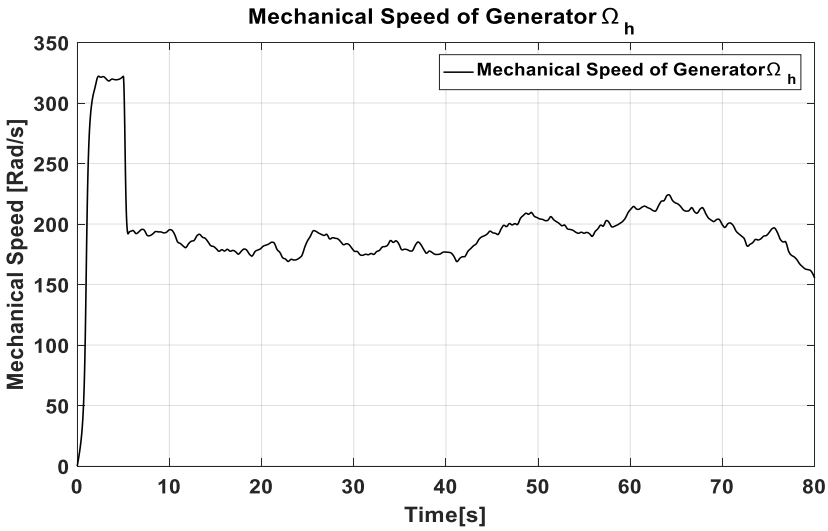


Figure II. 44 Mechanical Speed of Generator Ω_h .

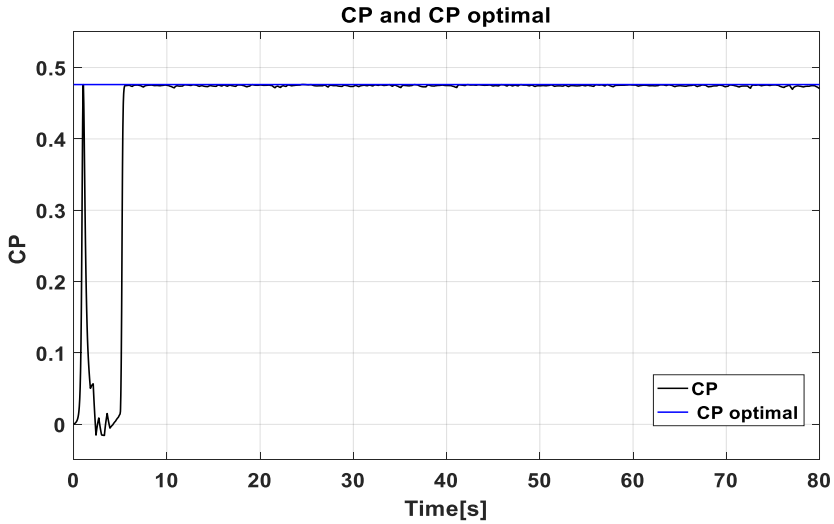


Figure II. 45 Power coefficient (CP).

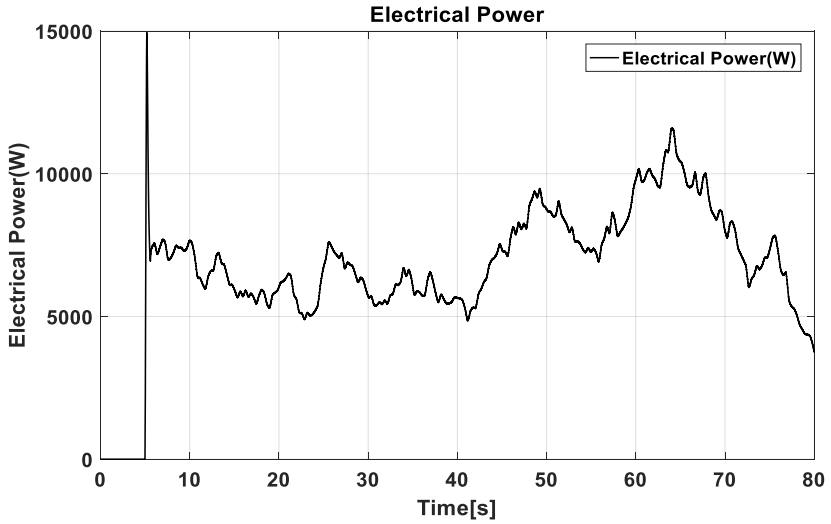


Figure II. 46 Electrical Power.

The results obtained from using the sliding mode controller (SMC) to regulate the wind energy conversion system (WECS), based on the high-turbulence stochastic wind speed model (Fig. II.14), reveal an increase in the electromagnetic torque ripple due to high disturbances in the applied wind speed (Fig. II.43). This ripple introduces greater mechanical stress, which accelerates wear and reduces the lifespan of the wind turbine due to the chattering phenomenon. Chattering causes large vibrations and fluctuations in the mechanical speed of the generator, which are reduced by high disturbances in the wind speed (Fig. II.44). Despite this limitation, the sliding mode controller has proven its robustness under varying operational conditions in tracking the maximum power point by consistently maintaining a stable and continuous tracking of the optimum power coefficient (CP) (Fig. II.45). This performance resulted in good electrical power generation as shown in (Figure II.46), although the value of the generated electrical power decreased, SMC reached a peak electrical power output of 12.3 kW under optimal wind conditions, especially when the wind speed reached its highest value.

II.8 CONCLUSION

In this chapter, we explored various control strategies for tracking the maximum power point (MPPT) of wind energy conversion systems. After addressing the problem statement, we provided a detailed explanation of different MPPT methods. A literature review followed, focusing on various strategies for tracking the maximum power point. The standard on-off controller was introduced, but its performance was hindered by a slight chattering issue due to the use of the sign function in the control law. Additionally, it failed to consistently track the maximum power point, which necessitated further improvements. To address this, an improved on-off controller was proposed by adding a first-order filter to its internal structure. This enhancement led to more accurate MPPT tracking, improving electrical power generation, but it also caused a notable increase in electromagnetic torque ripple, which creates high oscillations that negatively impact the longevity of wind turbines. To address the chattering issue, the literature proposed a fuzzy on-off controller, replacing the sign function with a fuzzy logic controller. This approach proved effective in reducing torque ripple but introduced instability in tracking the maximum power point, leading to incomplete MPPT tracking. Motivated by these findings, an enhanced fuzzy on-off controller was proposed, with the addition of a first-order filter to its internal structure. This solution improved tracking of the power coefficient (CP) and power generation, although stability in tracking the maximum power point still required improvement. Additionally, the comparison revealed that the fuzzy on-off controller outperformed in mitigating the chattering problem. Analyzing the results of the previous controllers, it became evident that there exists an inverse relationship between reducing electromagnetic torque ripple and maximizing power production. Efforts to enhance power output resulted in increased chattering, which negatively affects the turbine's lifespan. Conversely, reducing chattering to preserve the turbine's lifespan and minimize maintenance costs led to a decrease in MPPT accuracy and, consequently, reduced energy production. In the final section, a sliding mode controller (SMC) was explored, which demonstrated strong performance in tracking the maximum power point and maximizing electrical energy production. However, it too suffered from an undesirable level of chattering, further affecting wind turbine durability. Through an analysis of all the controllers discussed, it was concluded that producers must navigate a trade-off: either reduce maintenance costs and extend turbine lifespan by choosing a controller that minimizes the chattering problem or prioritize maximum energy production while accepting the associated maintenance costs. This chapter sets the foundation for addressing this challenge, and in the next chapter, we will investigate metaheuristic methods to improve controllers performance, aiming to simultaneously reduce electromagnetic torque ripple and maximize energy production.

CHAPTER III: MPPT Control Strategy Of Wind Energy Conversion System Using Metaheuristic Algorithms

III. 1 Introduction

Building on the previous chapter's discussion of the improved on-off controller, it is evident that while performance enhancements have been achieved, the persistent chattering issue and suboptimal tracking of the maximum power point (MPPT) remain unresolved challenges. This chapter aims to address these issues by investigating various approaches to enhancing the performance of wind energy conversion systems, particularly in terms of MPPT accuracy and the reduction of electromagnetic torque ripple. A central focus of this chapter is the application of Metaheuristic algorithms to optimize the parameters of the improved on-off controller. In the subsequent section, an in-depth review of the evolution and application of metaheuristic algorithms is provided. Following this, the third section examines the application of the single-objective particle swarm optimization (PSO) algorithm, a well-established and reliable method, to refine the improved on-off controller with the goal of reducing electromagnetic torque ripple. The fourth section introduces a more contemporary approach, employing the whale optimization algorithm to fine-tune the parameters of the improved on-off controller, with the aim of mitigating the chattering and vibration issues. As the chapter progresses, the fifth section addresses the shortcomings identified in the previous sections, which necessitated a revision of the controller's internal structure. To ensure optimal energy efficiency, the COOT algorithm is employed to identify the most effective parameters for this newly proposed controller. In the sixth section, a multi-objective particle swarm optimization (MOPSO) algorithm is applied to simultaneously enhance MPPT accuracy and minimize electromagnetic torque ripple, providing a comprehensive solution to the challenges identified. The chapter concludes with a synthesis of the findings, summarizing the outcomes and insights gained from the various methodologies and experiments discussed throughout.

III. 2 Literature Review

III. 2.1 Hybrid MPPT Algorithms

This approach combines different conventional MPPT techniques or integrates smart-based algorithms into the MPPT method to enhance the tracking of the maximum power point in a WECS. Accordingly, hybrid MPPT methods can be classified as combinations of conventional algorithms, conventional algorithms augmented with smart techniques, or conventional algorithms enhanced with optimization methods. The following sections discuss various hybrid MPPT algorithms developed in recent years to improve the performance of conventional MPPT techniques.

III. 2.1.1 Combination of Conventional Algorithms

The combination of conventional algorithms, also known as hybrid conventional MPPT algorithms, integrates multiple traditional MPPT techniques to enhance maximum power point tracking. This approach offers greater robustness compared to standalone algorithms and contributes to improved overall system performance. Table III.1 presents a summary of hybrid MPPT algorithms based on Conventional techniques that have been explored and applied in WECS.

Type of MPPT Algorithms	Remarks	Reference
P&O + PSF	Improvement in power efficiency tracking was achieved with the hybrid MPPT.	[129]
ORB + P&O	Combines ORB with a self-rotating P&O-based controller that improves the tracking speed of the hybrid MPPT.	[130]
P&O+OTC	The OTC was employed to detect power peak point and reduce the perturbation step size of the P&O algorithm to reach MPP.	[131]

Table III. 1 Summary of Hybrid-Conventional MPPT Algorithms for WECS.

III. 2.1.2 Conventional + Smart Algorithms

Due to their intelligent capability in solving complex problems, smart-based algorithms have been developed and integrated with conventional MPPT methods, as shown in Table III.2. This integration enhances the robustness of the technique while reducing its dependence on the machine's characteristics. According to the literature, these combinations effectively overcome the limitations of traditional methods, improving reliability and efficiency. Additionally, they enhance tracking speed and increase accuracy.

Hybrid MPPT Name	Description	Algorithm Performance Evaluation	Reference
P&O + FLC	Fuzzy logic controller (FLC) has been integrated into the adaptive P&O MPPT method which increased the computational speed of the MPPT controller. Furtherly, the new hybrid method successfully eliminated the drawbacks of both the standalone conventional adaptive P&O MPPT and the FLC.	The proposed controller yielded a power increase of 37.93% compared to the P&O method and 17.65% compared to the FLC controller. Additionally, 110 W more power was generated with the proposed controller than with the P&O method and 60 W more than the FLC controller [45]. Moreover, 36.38% of energy yield was recorded with the new controller in [46].	[132-133-134]
P&O + ANN	By integrating ANN into the traditional P&O algorithm, an increase in accuracy was achieved.	The new approach effectively monitored the power coefficient at the optimal level of 0.35 and the nominal power generation of 3 MW.	[135]

Table III. 2 Summary of hybrid methods (conventional MPPT and Smart Algorithms) for WECS.

III. 2.1.3 Conventional + Optimization Algorithms

A hybrid approach that combines conventional Maximum Power Point Tracking (MPPT) algorithms with metaheuristic optimization techniques, such as Particle Swarm Optimization (PSO), has been proposed to overcome the limitations inherent in traditional MPPT methods. Metaheuristic optimization techniques, known for their problem-independent nature, have gained significant traction in addressing complex engineering challenges. This popularity can be attributed to their simplicity, flexibility, and ability to efficiently solve intricate problems. These techniques, grounded in the principles of randomness, seek optimal solutions through two key processes: diversification, which explores the entire search space, and intensification, which refines the search within a specific area of the space [43]. Drawing inspiration from various natural phenomena—such as the human body, the laws of physics, and animal behavior—metaheuristic optimization methods enable the development of robust mathematical models that accurately replicate nature-based occurrences, thereby providing optimal solutions to engineering problems [44]. An example of such a hybrid approach is the integration of the ORB algorithm with PSO, as presented in [153]. This methodology follows a two-phase process: initially, PSO is employed to determine the optimal coefficient, and subsequently, the ORB MPPT algorithm is applied. This combination enhances system efficiency while eliminating the need for sensors or prior knowledge of system parameters. In the following sections, we will explore various control strategies that leverage this hybrid approach, illustrating its potential for improving the performance of MPPT systems. Metaheuristic optimization techniques can typically be classified into four main categories, as illustrated in Figure III.1. While this classification is not exhaustive, it covers most of the currently implemented techniques. The adaptability and efficiency of these methods make them a powerful tool in the optimization of MPPT systems and other complex engineering applications.

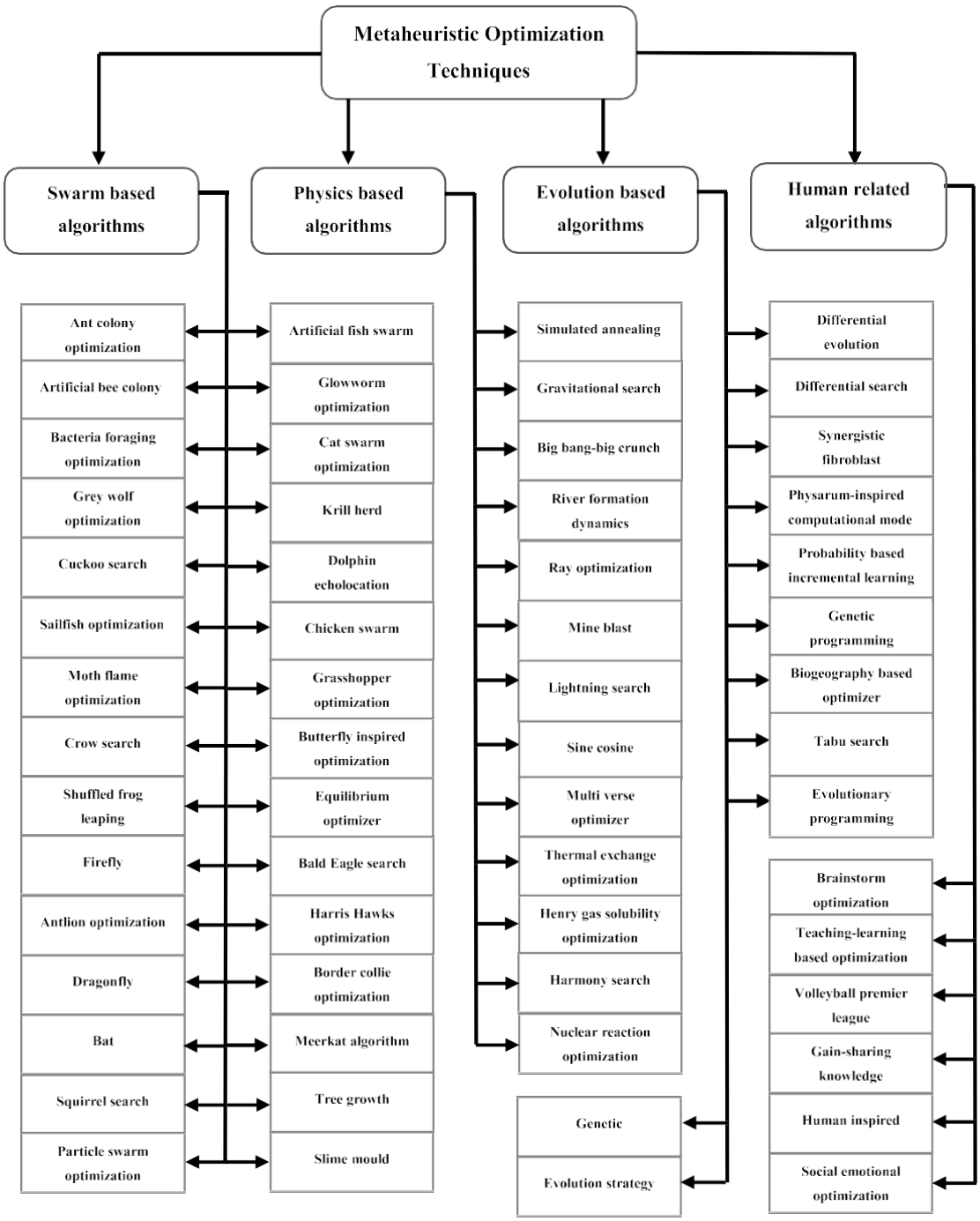


Figure III. 1 Flow Chart Indicating Classification Of Metaheuristic Optimization Techniques.

III. 2.1.3.1 History of Metaheuristic Algorithms

Metaheuristic algorithms, also known as Optimization algorithms, have become essential tools for solving complex optimization problems, particularly those that are non-linear, non-convex, and high-dimensional, where traditional deterministic methods often fail. The development of these algorithms stems from the need to efficiently find near-optimal solutions to real-world problems across various fields, such as engineering, economics, logistics, and artificial intelligence. The evolution of metaheuristics is characterized by a blend of natural inspiration, interdisciplinary approaches, and continuous innovation.

The conceptual foundation of Metaheuristics can be traced back to the 1950s with the development of **the Monte Carlo method**. This method [104], named after the Monte Carlo Casino in Monaco due to its reliance on randomness and statistical sampling, was one of the earliest approaches to tackle complex mathematical problems using stochastic processes. While not a metaheuristic in the strictest sense, the Monte Carlo method introduced key principles that would later be central to metaheuristics, such as the use of randomization to explore the solution space and approximate solutions for intractable problems. The 1960s saw the emergence of other significant developments that laid the groundwork for metaheuristics, including random search methods explored as a means of solving optimization problems where the search space is too large or complex to be handled by exhaustive methods. These early techniques highlighted the potential of using randomness and iterative improvement in finding solutions to difficult optimization problems.

The 1980s marked the true beginning of metaheuristics as a distinct class of optimization algorithms, with Simulated Annealing (SA) being one of the earliest and most influential examples. Introduced by **Scott Kirkpatrick, C. Daniel Gelatt, and Mario P. Vecchi** in 1982 [105], SA was inspired by the physical process of annealing in metallurgy, where a material is heated to a high temperature and then slowly cooled to reduce defects and achieve a more stable structure. In optimization, SA mimics this process by allowing the algorithm to explore the solution space in a manner that can occasionally accept worse solutions early on (analogous to the high-temperature phase), helping the algorithm avoid becoming trapped in local minima. As the algorithm progresses, the probability of accepting worse solutions decreases, effectively "cooling" the search and guiding it toward a global optimum. Simulated Annealing quickly became popular due to its simplicity and effectiveness in solving a wide range of optimization problems, including the Traveling Salesman Problem (TSP), scheduling, and network design. Simultaneously, another groundbreaking metaheuristic was being developed: Genetic Algorithms (GAs), pioneered by **John Holland** in the 1970s and further refined in the 1980s by Holland and his students, including **David E. Goldberg** [106,107]. GAs are based on the principles of natural selection and genetics as described by Charles Darwin. GAs work by evolving a population of candidate solutions (often represented as binary strings or chromosomes) over several generations. The process begins with an initial population of randomly generated solutions, each evaluated using a fitness function that measures its quality or closeness to the optimal solution. The fittest solutions are selected for reproduction, where genetic operators such as crossover (recombination of parts of two solutions) and mutation (random alteration of parts of a solution) are applied to create new solutions. Over time, the population evolves, with successive generations converging toward better solutions. GAs were initially applied to problems in biology and

engineering, but their versatility and robustness quickly made them popular in fields ranging from economics to artificial intelligence.

The 1990s saw the rapid expansion of metaheuristics, particularly those that employ population-based approaches. These algorithms leverage the collective behavior of a population of agents (solutions) to explore the search space more effectively than single-solution approaches like Simulated Annealing. One of the most influential population-based algorithms introduced during this time was Particle Swarm Optimization (PSO) [13], developed by **James Kennedy** and **Russell Eberhart** in 1995. PSO is inspired by the social behavior of birds flocking or fish schooling. In PSO, a population of candidate solutions, known as particles, moves through the search space, adjusting their positions based on their own experience and the experience of neighboring particles, following simple rules inspired by social interactions. The movement of the particles is influenced by two main components: the cognitive component, which pulls the particle toward its own best-known position, and the social component, which pulls it toward the best-known position of the entire swarm. This dual influence allows the swarm to effectively balance exploration (searching new areas) and exploitation (refining known good areas), leading to robust and efficient optimization. Another significant contribution to the field during the 1990s was Ant Colony Optimization (ACO), introduced by **Marco Dorigo** and his collaborators [108]. ACO is inspired by the foraging behavior of ants, particularly how they find the shortest path between their colony and food sources. In nature, ants communicate via pheromones, leaving chemical trails that guide other ants. The more ants follow a particular path, the more pheromones are deposited, reinforcing that path and making it more attractive to other ants. In ACO, artificial ants construct solutions to combinatorial optimization problems by simulating this behavior. Solutions that yield better results leave stronger pheromone trails, encouraging the algorithm to explore those paths further. ACO has been particularly successful in solving combinatorial problems like the Traveling Salesman Problem, vehicle routing, and network optimization.

As the 1990s drew to a close, new metaheuristics continued to emerge, each bringing unique strategies and applications to the optimization landscape. Differential Evolution (DE), introduced by **Rainer Storn** and **Kenneth Price** in 1997 [109], is an evolutionary algorithm that emphasizes simplicity and effectiveness in handling continuous optimization problems. DE operates on a population of candidate solutions, similar to Genetic Algorithms, but uses the differences between randomly selected pairs of solutions to generate new candidate solutions. This process, known as differential mutation, is followed by a selection step where the new candidate solution competes with the existing one, and the better of the two is retained for the next generation. DE has proven particularly effective in optimization problems with complex, multi-modal landscapes. Another innovative metaheuristic from this period is the Harmony Search (HS) algorithm, proposed by **Zong**

Woo Geem, **Joong Hoon Kim**, and **G.V. Loganathan** in 2001 [110]. HS is inspired by the process of musical improvisation, where musicians aim to find a harmonious state by adjusting the pitch of their instruments. In HS, a population of candidate solutions, analogous to musical notes, is adjusted iteratively to find an optimal harmony. Each solution is generated by considering whether to pick a value from the current solution (exploitation), introduce a new random value (exploration), or make a slight adjustment to an existing value (mutation). HS is particularly well-suited for continuous optimization problems and has been successfully applied in various fields, including structural design, water resource management, and machine learning.

The 21st century has seen a proliferation of new metaheuristics, many of which are bio-inspired, drawing on increasingly diverse aspects of nature for inspiration. These algorithms often blend the principles of earlier metaheuristics with new ideas derived from the study of biological systems, animal behavior, and other natural phenomena. The Firefly Algorithm (FA) [111], introduced by **Xin-She Yang** in 2009, is one such bio-inspired algorithm. FA is based on the flashing behavior of fireflies, where the attractiveness of a firefly is determined by its brightness, which in turn is associated with the quality of the solution it represents. The algorithm assumes that all fireflies are unisex and can attract each other regardless of gender. The attractiveness between two fireflies decreases as the distance between them increases, which encourages fireflies to move toward brighter (better) solutions. This movement helps the algorithm to explore the search space more effectively. FA has been applied successfully in a wide range of optimization problems, including engineering design, image processing, and feature selection. Another notable bio-inspired metaheuristic is the Bat Algorithm (BA) [112], also proposed by **Xin-She Yang** in 2010. BA is inspired by the echolocation behavior of bats, which use sound waves and their echoes to navigate and locate prey. In the algorithm, bats are represented as agents that fly through the search space, adjusting their velocity and position based on the intensity of the echoes they receive. The loudness and pulse emission rate of each bat are adjusted dynamically as the search progresses, balancing exploration and exploitation. BA has been particularly effective in solving both continuous and discrete optimization problems, including engineering design and signal processing. Whale Optimization Algorithm (WOA) [16], developed by **Seyedali Mirjalili** and his team in 2016, is another bio-inspired metaheuristic that has gained attention for its effectiveness in handling complex optimization problems. WOA is inspired by the bubble-net hunting strategy of humpback whales, where whales create a spiral-shaped bubble net to encircle prey. The algorithm simulates this behavior by having agents (whales) search the solution space in a spiral pattern, encircling and converging toward the best-known solution. WOA has demonstrated strong performance in a variety of optimization tasks, including feature selection, clustering, and engineering design.

As metaheuristics have matured, researchers have increasingly explored hybrid approaches that combine the strengths of multiple algorithms to create more powerful and versatile optimization tools. Hybrid metaheuristics often integrate different strategies, such as combining the global search capabilities of Genetic Algorithms with the local search strengths of Simulated Annealing, or merging swarm-based algorithms like PSO with evolutionary techniques like Differential Evolution. These hybrid approaches aim to overcome the limitations of individual algorithms, such as premature convergence or slow convergence speed, and have been applied successfully in areas such as multi-objective optimization, machine learning, and complex system design. Looking to the future, metaheuristics are expected to play an even more significant role in tackling the optimization challenges posed by emerging technologies, such as big data, artificial intelligence, and autonomous systems. Advances in computational power, coupled with the growing availability of large datasets, are likely to drive the development of new metaheuristic algorithms that can efficiently handle high-dimensional, dynamic, and uncertain optimization problems. Moreover, the integration of machine learning techniques into metaheuristics, allowing algorithms to learn and adapt their strategies based on past experiences, is an exciting area of ongoing research. Overall, the history of metaheuristic algorithms is a testament to the power of interdisciplinary thinking and the potential of nature-inspired approaches in solving some of the most challenging optimization problems. From their early beginnings in randomized search methods to the sophisticated bio-inspired algorithms of today, metaheuristics have continually evolved, offering robust and flexible solutions that have transformed the way we approach optimization in science, engineering, and beyond. As the field continues to grow, it is poised to make even greater contributions to the advancement of technology and our understanding of complex systems.

Table III.3 summarizes some of metaheuristic optimization techniques, providing an overview of their inspiration, working mechanisms, and common applications. It also highlights each technique's advantages and limitations.

Algorithm	Inspiration	Mechanism	Key Features	Applications	Merits	Demerits
Particle Swarm Optimization (PSO)	Flock of birds, fish schools	Particles move through the search space based on personal and global best positions.	Simplicity, ease of implementation, requires tuning.	Continuous optimization, machine learning, engineering design.	Fast convergence, simple to implement, good global search.	Sensitive to parameter settings, may get stuck in local optima.
Ant Colony	Ants	Simulated	Good for	Traveling	Effective	Slower

Optimization (ACO)	foraging for food	ants lay pheromones to find optimal paths. Pheromone strength guides others.	combinatorial problems, adaptable.	salesman problem (TSP), routing, network design.	for combinatorial problems, good memory of solutions.	convergence, high computational cost, sensitive to pheromone decay.
Artificial Bee Colony (ABC)	Honeybee foraging behavior	Bees search for food (solutions) and share information with the colony.	Balance between exploration and exploitation.	Continuous optimization, machine learning, engineering problems.	Simple, efficient, and robust for continuous optimization.	May suffer from slow convergence, sensitive to parameter tuning.
Cuckoo Search (CS)	Cuckoo bird parasitism	Cuckoos lay eggs in other birds' nests; solutions are replaced with better ones.	Random and greedy search, balance between exploration and exploitation.	Engineering design, continuous optimization.	Fast convergence, good balance between exploration and exploitation.	May get stuck in local optima, requires proper parameter tuning.
Firefly Algorithm (FA)	Flashing of fireflies	Fireflies move towards brighter ones, representing better solutions.	Light intensity guides search, balance between exploration and exploitation.	Continuous/discrete optimization, image processing, feature selection.	Simple, efficient, good for both exploration and exploitation.	Can get trapped in local optima, may require parameter fine-tuning.
Bat Algorithm (BA)	Echolocation of bats	Bats search for prey using echolocation and adjust their flight based on solution quality.	Balance between exploration and exploitation.	Function optimization, signal processing, image reconstruction.	Good for continuous optimization, high solution quality.	Requires tuning of parameters, may converge slowly.
Gravitational Search Algorithm (GSA)	Gravitational attraction in space	Agents are attracted to more massive ones based on gravitationa	Focus on cooperation and gravitational interaction.	Continuous optimization, engineering design, control systems.	Good exploration, easy to implement.	Computationally expensive, slow convergence in some cases.

		l forces.				
Seagull Optimization Algorithm (SOA)	Hunting and searching behavior of seagulls	Seagulls explore the solution space, balancing exploration and exploitation.	Hybrid exploration - exploitation, adaptable to various tasks.	Continuous and combinatorial optimization.	Efficient balance of exploration and exploitation.	May require parameter tuning, can get stuck in local optima.
Wolf Pack Algorithm (WPA)	Wolf pack hunting strategies	Wolves cooperate to find prey, with a leader-following mechanism for optimization.	Cooperative search, leader-following.	Continuous optimization, machine learning.	Effective for global search, robust to local optima.	May require a large number of iterations, sensitivity to parameters.
Whale Optimization Algorithm (WOA)	Humpback whale hunting strategies	Mimics bubble-net feeding behavior of whales. Whales search for prey and adjust their movements to improve solutions.	Exploits both global search and local refinement.	Engineering problems, image segmentation, function optimization.	Good exploration and exploitation, easy to implement.	May be slow to converge, sensitive to parameters.
Multi-Objective PSO (MOPSO)	Flock of birds, with focus on multiple objectives	A variant of PSO that handles multiple conflicting objectives. It uses Pareto dominance to guide the search.	Multi-objective optimization, handles trade-offs between conflicting goals.	Multi-objective optimization in engineering, scheduling problems.	Handles multiple objectives efficiently, good for complex problems.	Requires advanced techniques for balancing objectives, sensitive to parameter settings.

Table III. 3 Summary of Reviewed Swarm-Based Metaheuristic Optimization Techniques.

III. 3 Improved On-Off Control Based On PSO

Despite the efficiency of the improved On-Off controller, after experiments, it was noticed that the problem of chattering did not disappear completely, and therefore the performance must be improved more by modifying some of the parameters of the controller to get better performance.

To improve the performance of the improved on-off control, we use the particle swarm optimization algorithm (PSO) to obtain the best values of u^{nf} (equation II.24) by searching for the best value for the filtering time constant T_f , the gain K_f and β (Figure III.2).

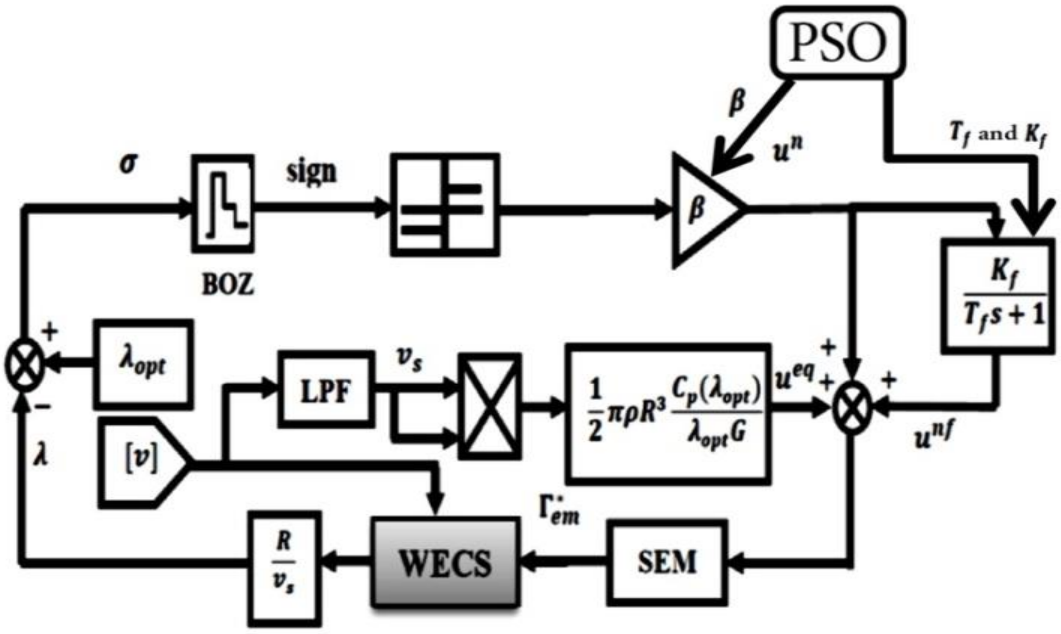


Figure III. 2 PSO layout diagram block for adjustment of improved controller parameters.

III. 3.1 Particle Swarm Optimization (PSO)

Particle Swarm Optimization (PSO) is an evolutionary computation technique developed by Kennedy and Eberhart in 1995 [13]. It draws inspiration from the collective behavior observed in nature, such as bird flocking, fish schooling, and the swarming behavior of insects. PSO belongs to the category of population-based stochastic optimization techniques, where a population of potential solutions, referred to as particles, explores the search space simultaneously in pursuit of an optimal or near-optimal solution. There is a perception that members of a group seem to be sharing information among themselves, thereby increasing the effectiveness of the group.

An individual in a swarm comes close to the optimum by his current velocity, previous experience, and the experience of his neighbors. The iteration is defined by the following two equations in this review :

$$\begin{cases} V_{iD}^{t+1} = k.\left(V_{iD}^{t} + c_1.r_1\left(P_{iD}^{t} - X_{iD}^{t}\right) + c_2.r_2\left(g_i^{t} - X_{iD}^{t}\right)\right) \\ X_{iD}^{t+1} = P_{iD}^{t} + X_{iD}^{t} \end{cases} \quad \text{(III.1)}$$

Where, i = 1, ..., n and n is the size of the swarm, D is dimension of the problem space, C_1 and C_2 are positive constants, k is the momentum or inertia, r_1 and r_2 are random numbers which are

uniformly distributed in [0, 1], t determines the iteration number, p_i represents the best previous position (the position giving the best fitness value) of the ith particle, and g represents the best particle among all the particles in the swarm.

III. 3.2 Electromagnetic Torque Ripple Attenuation of WECS Using An Improved On-Off Control Based On PSO

To determine the optimal values, previous experiments and studies were consulted to establish the most effective ranges for T_f , K_f and β. The PSO algorithm then randomly selects initial values from within these intervals. To obtain a more accurate solution within minimal computation time, the best solution is identified by minimizing a specific criterion, the Mean Integrated Squared Error (MISE), which is calculated using the following equation:

$$\text{MISE} = \text{Fit} = \int \left(e(t)^2 \right) dt \tag{III.2}$$

$$\text{Subject to} \quad \begin{cases} \beta_{\min} \le \beta \le \beta_{\max} \\ K_{f\min} \le K_f \le K_{f\max} \\ T_f \le T_f \le T_{f\max} \end{cases} \tag{III.3}$$

Where: $e(t) = \Gamma^*_{em} - \Gamma_{em}$ is the difference between value of the electromagnetic torque reference and the value of the electromagnetic torque under Improved On-Off control.

As shown in Figure III.3, after setting the initial values such as swarm size and the initial velocity of particles, PSO calculates the parameters of the improved On-Off controller for each particle and records the corresponding MISE. Based on the MISE, the best position of each particle is identified, and the optimal particle among the entire population is selected. This process is repeated until the number of iterations reaches the maximum iteration count, at which point the best particle is selected. The best particle represents the optimal parameters for the improved On-Off controller, corresponding to the minimum value of the objective function, MISE. The PSO parameters utilized to determine the optimal values for the improved On-Off Controller are listed in Table III.4.

Parameters	Values
Number of Particles	10
Number of variables	3
Max Iteration	40
Inertia Weight Factor (W)	0.9
Confidence Coefficient	$C_1 = 0.12$ and $C_2 = 1.2$

Table III. 4 PSO Parameters.

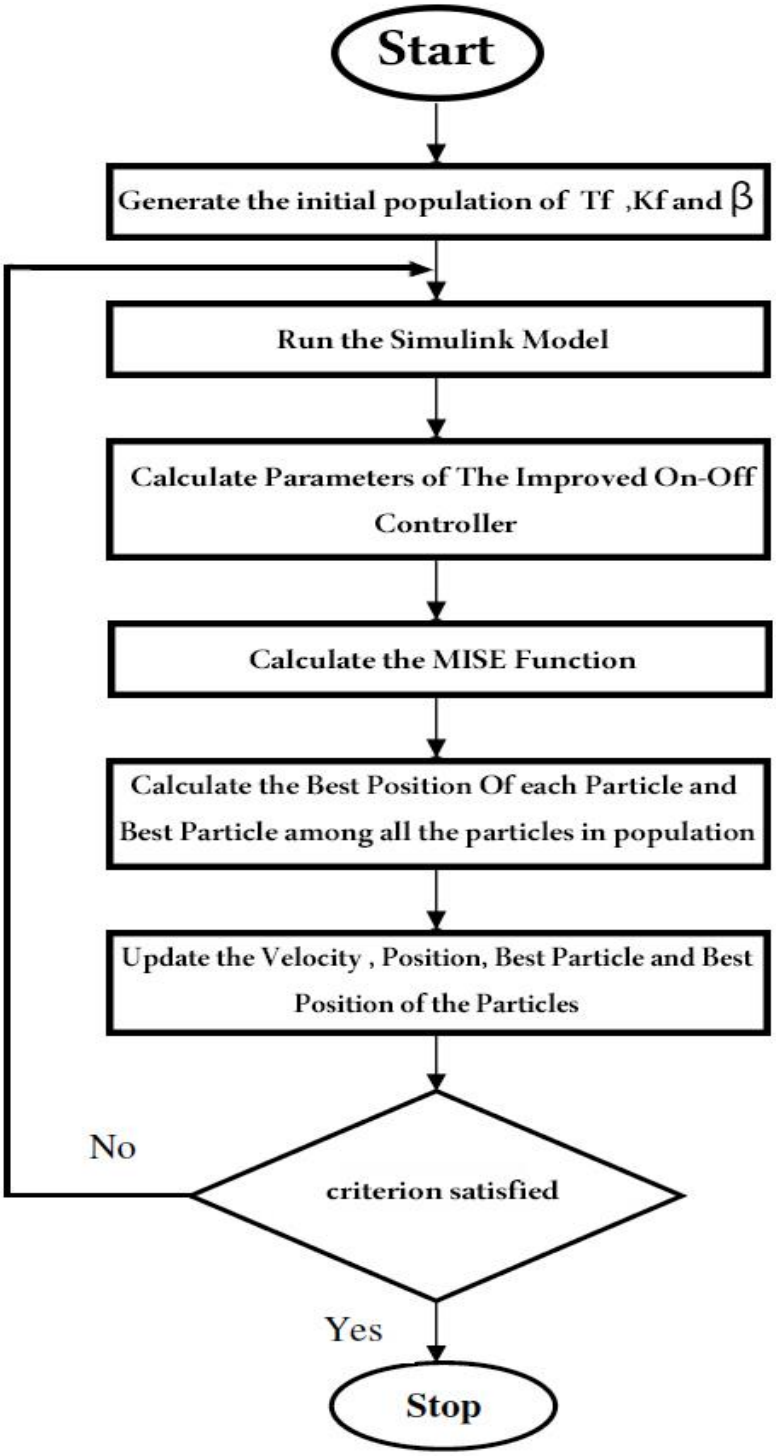


Figure III. 3 Flowchart of the PSO approach for optimizing the Improved On-Off controller.

III. 3.3 Simulation Results

To assess the performance of the Improved On-Off Control based on PSO, the wind energy conversion system and the proposed control strategy were implemented in the MATLAB/Simulink environment, with WECS parameters detailed in Table B.1 of Appendix B. Simulations were conducted for 80 seconds using a wind sequence with an average speed of approximately 11 m/s. The

study included two classes of turbulence intensity—low and high—derived using the von Karman spectrum as specified in the International Electrotechnical Commission (IEC) standard.

III. 3.3.1 Low Turbulence Stochastic Wind Speed

To achieve a more realistic comparison between the results from the Improved On-Off Controller and the PSO-Improved On-Off Controller, a wind model proposed by C. Nichita is utilized for simulation [19]. Detailed modeling information is provided in Chapter I, Section 3.1. This model generates the temporal wind profile from white noise, which is then processed through a Von Karman non-rational filter transfer function. The parameters of this filter are dependent on site characteristics and wind nature, as illustrated in Figure III.4.

The parameters T_f , K_f and β of the improved On-Off Controller using low turbulence stochastic wind speed are presented in Table III.5.

Parameters	Values	
	PSO Improved ON-OFF Control	Improved ON-OFF Control
K_f	1	20
T_f	2.68	5
β	0.1	0.75

Table III. 5 Parameters of The Improved ON-OFF Control Using Low Turbulence Stochastic Wind Speed.

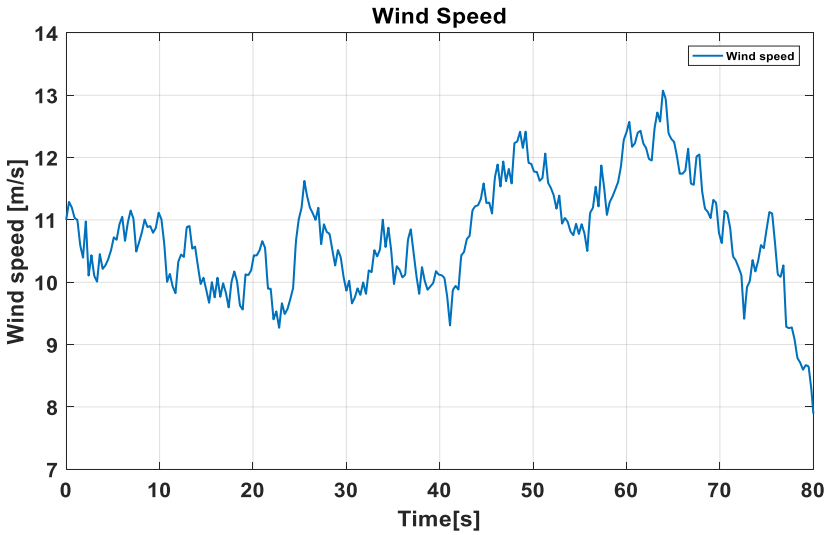


Figure III. 4 Low Turbulence Stochastic Speed.

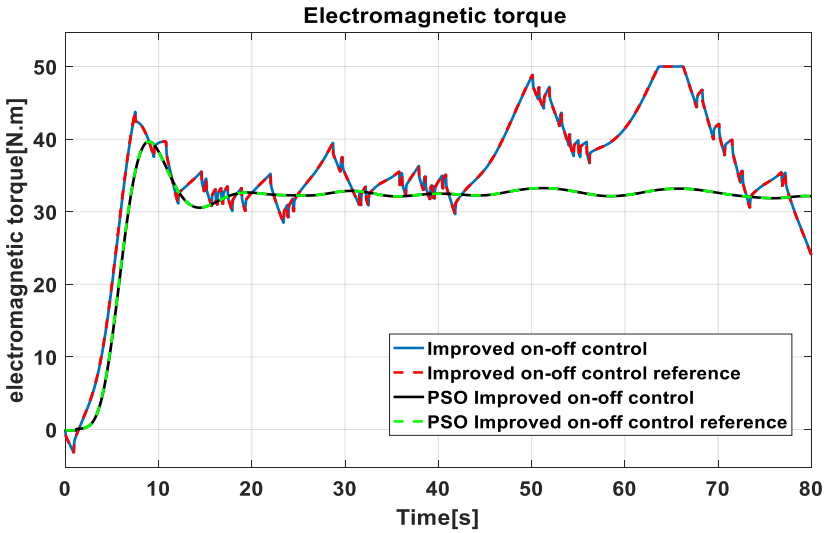


Figure III. 5 Electromagnetic Torque.

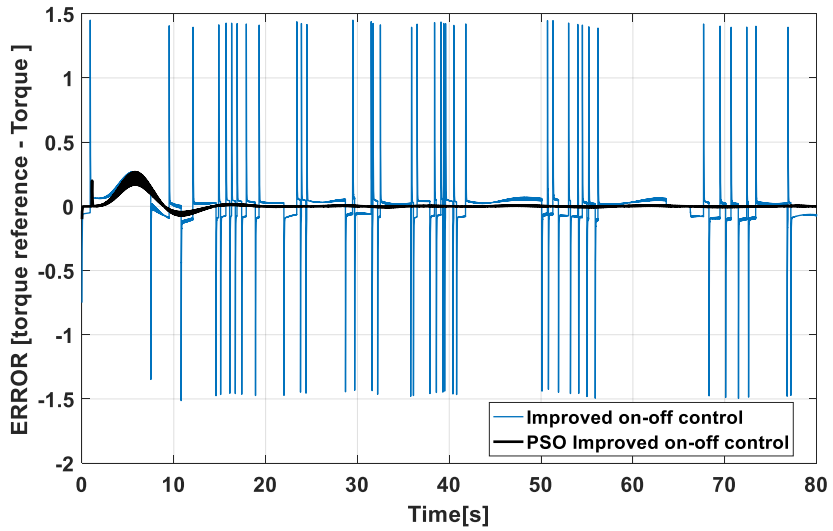


Figure III. 6 Error $e(t) = \Gamma_{em}^{*} - \Gamma_{em}$

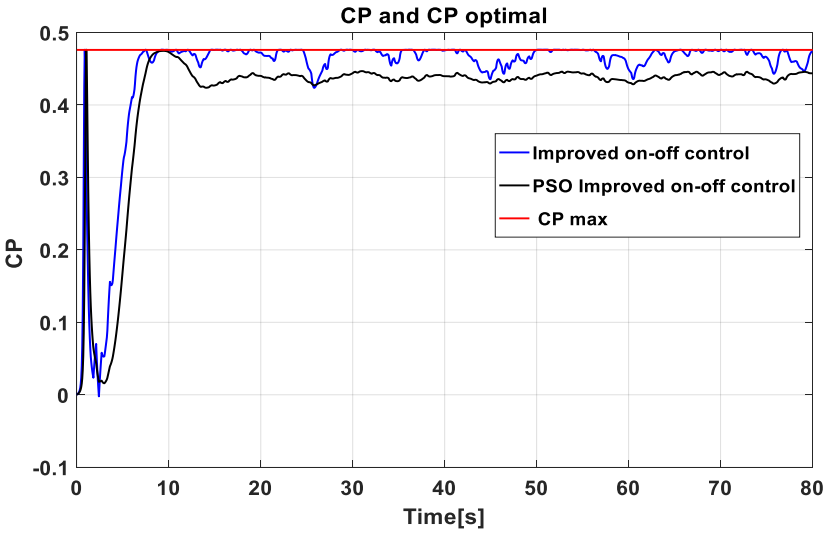


Figure III. 7 Power coefficient (CP).

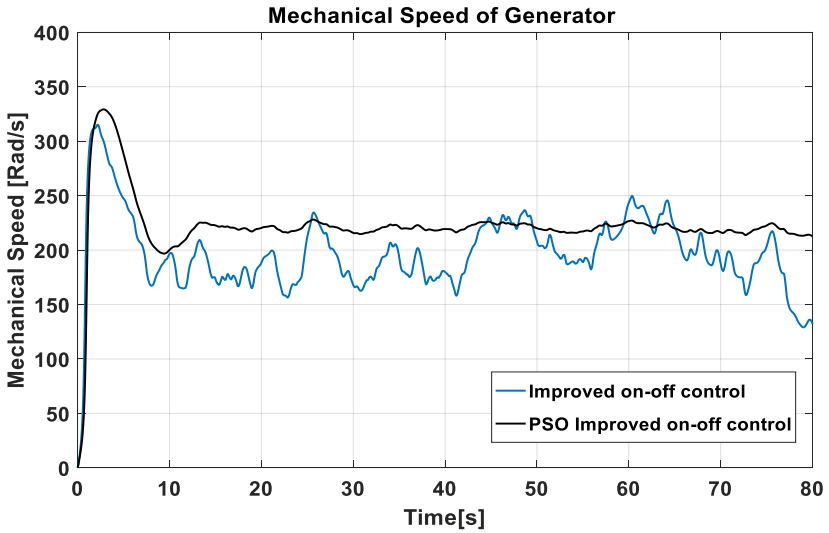


Figure III. 8 Mechanical Speed of Generator Ω_h .

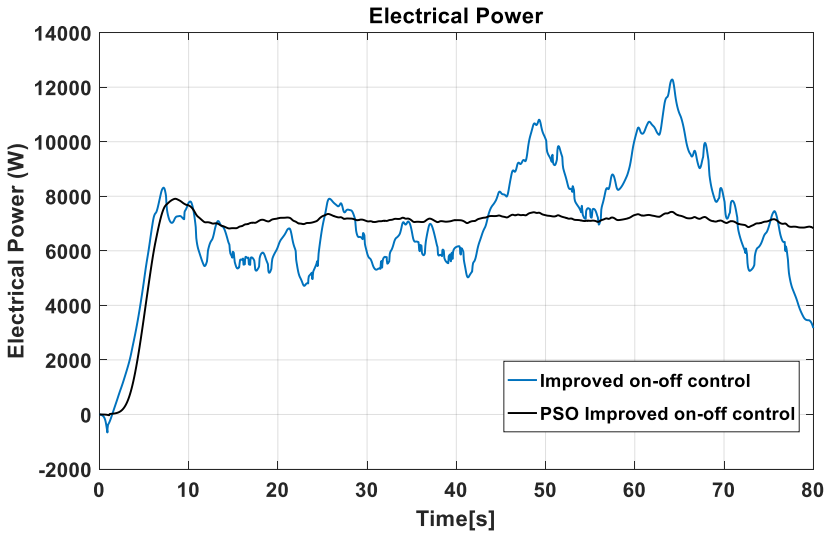


Figure III. 9 Electrical power.

When analyzing the results obtained using a low turbulence stochastic wind profile, it becomes apparent that the chattering issue observed in the electromagnetic torque with the improved On-Off control, as tuned by PSO, has been entirely mitigated (refer to Figures III.5 and III.6). Nevertheless, the resolution of the chattering problem has given rise to a new challenge: the tracking of the maximum power point has been adversely affected, leading to a decrease in energy production (see Figures III.7 and III.9). This is despite an observed increase in generator speed, attributable to the reduction in mechanical loads following the elimination of the chattering issue (as illustrated in Figure III.8).

III. 3.3.2 High Turbulence Stochastic Wind Speed

To assess the robustness of the proposed controller, it was essential to evaluate its performance under varying conditions. Consequently, we simulated the controller using a high turbulence wind model.

The parameters T_f , K_f and β of the improved On-Off Controller using high turbulence stochastic wind speed are presented in Table III.6.

Parameters	Values	
	PSO Improved ON-OFF Control	Improved ON-OFF Control
K_f	1	20
T_f	4.29	5
β	0.1	0.75

Table III. 6 Parameters of The Improved ON-OFF Control Using High Turbulence Stochastic Wind Speed.

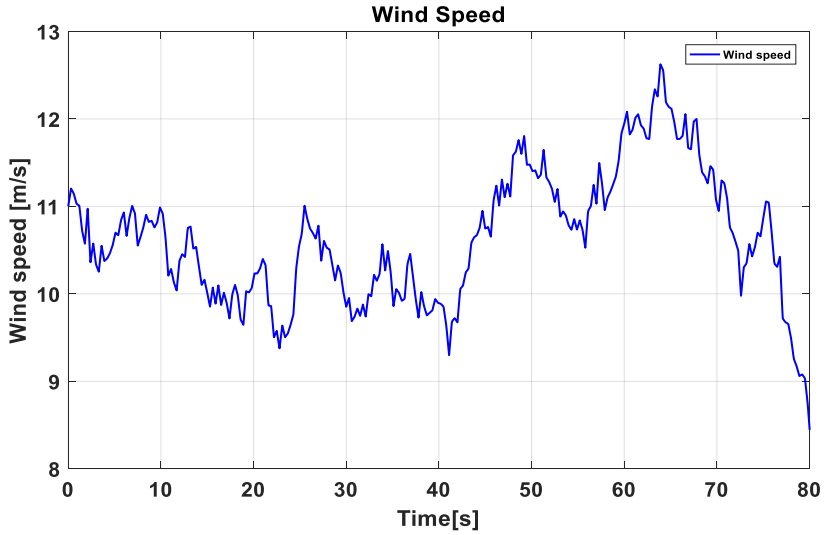


Figure III. 10 High turbulence stochastic wind speed.

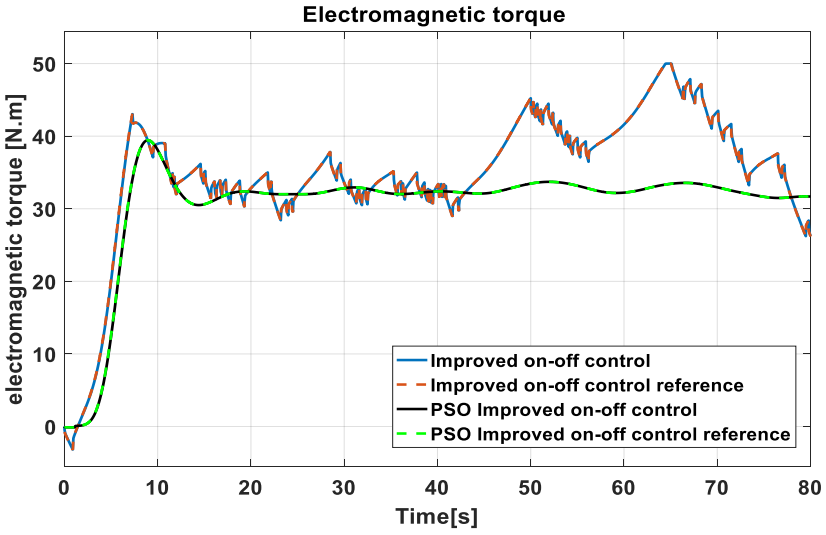


Figure III. 11 Electromagnetic Torque.

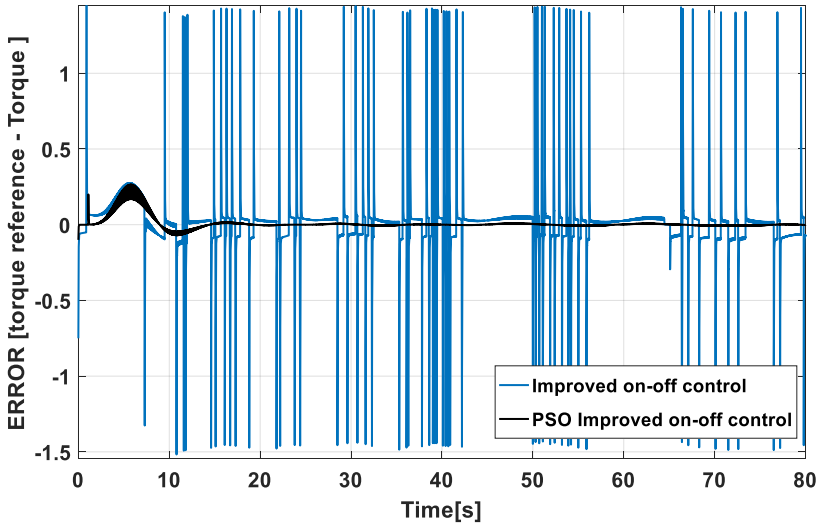


Figure III. 12 Error $e(t) = \Gamma_{em}^{*} - \Gamma_{em}$

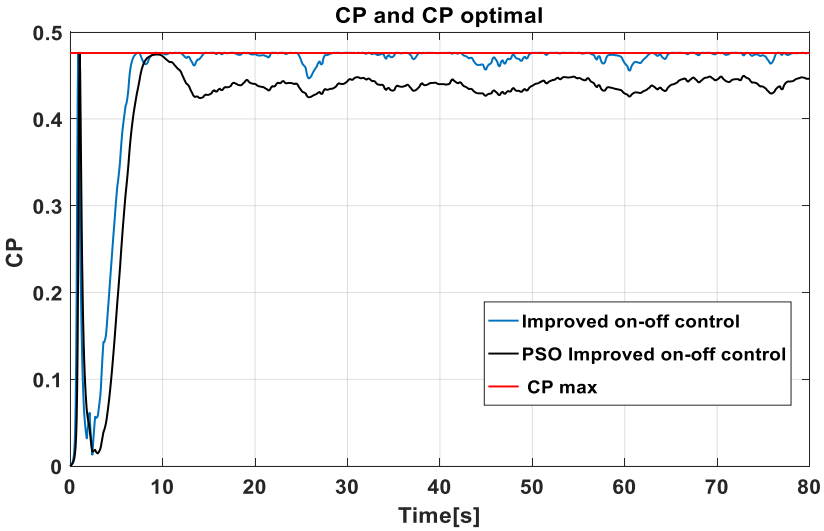


Figure III. 13 Power coefficient (CP).

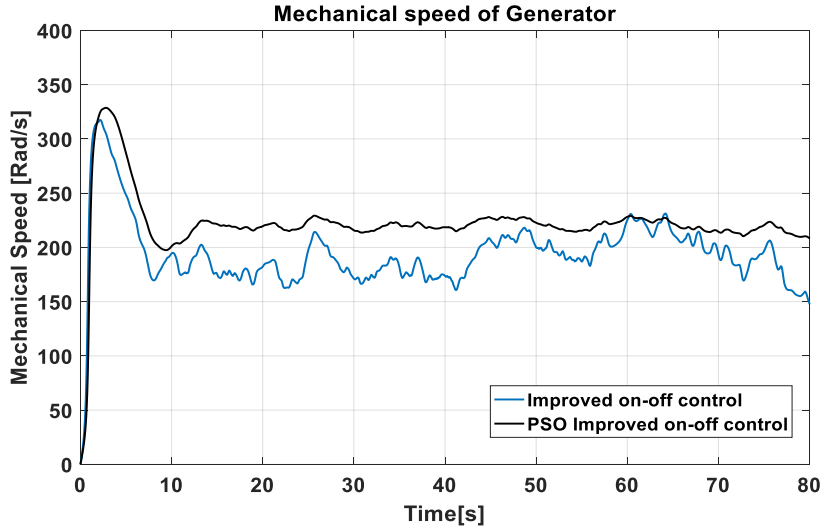


Figure III. 14 Mechanical Speed of Generator Ω_h .

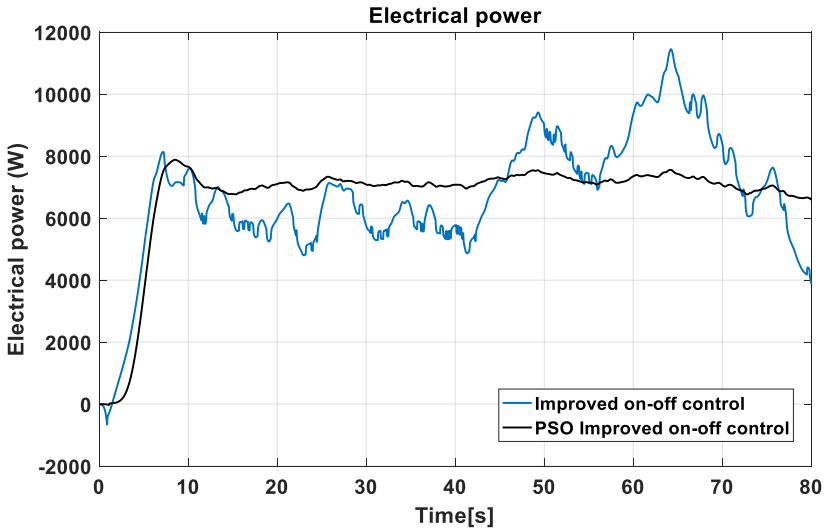


Figure III. 15 Electrical Power.

Comparing the curves shown in Figure III.11 and Figure III.12, it is clear that the results obtained with the improved On- Off controller optimized by PSO are clearly better, especially from the point of view of an alleviate the chattering problem in the electromagnetic torque input, at the same time, we can observe the good tracking of the improved On-Off controller (Figure III.13) and the good energy production (Figure III.15). Figure III.14 show the generator speed obtained by using two different control methods. These results confirm that the disturbance of the wind speed variation is strongly deflecting the generator speed to its optimal trajectory. This deviation has obvious consequences for the capture of wind energy; counter to the improved On-Off control based PSO, which manages to assure the optimal speed tracking.

III. 4 Enhanced On-Off Control Based On WOA

Despite the demonstrated efficiency of the improved On-Off controller [6], experimental findings have shown that the chattering issue persists to some degree. Therefore, further refinements are necessary to enhance the controller's performance [113]. To achieve this, the Whale Optimization Algorithm (WOA) is employed to identify the optimal values of u^{nf} (as defined in Equation II.24). The focus of the algorithm is on optimizing the filtering time constant T_f, gain K_f, and parameter β, as illustrated in Figure III.16. By fine-tuning these parameters, the controller's performance is expected to be significantly improved.

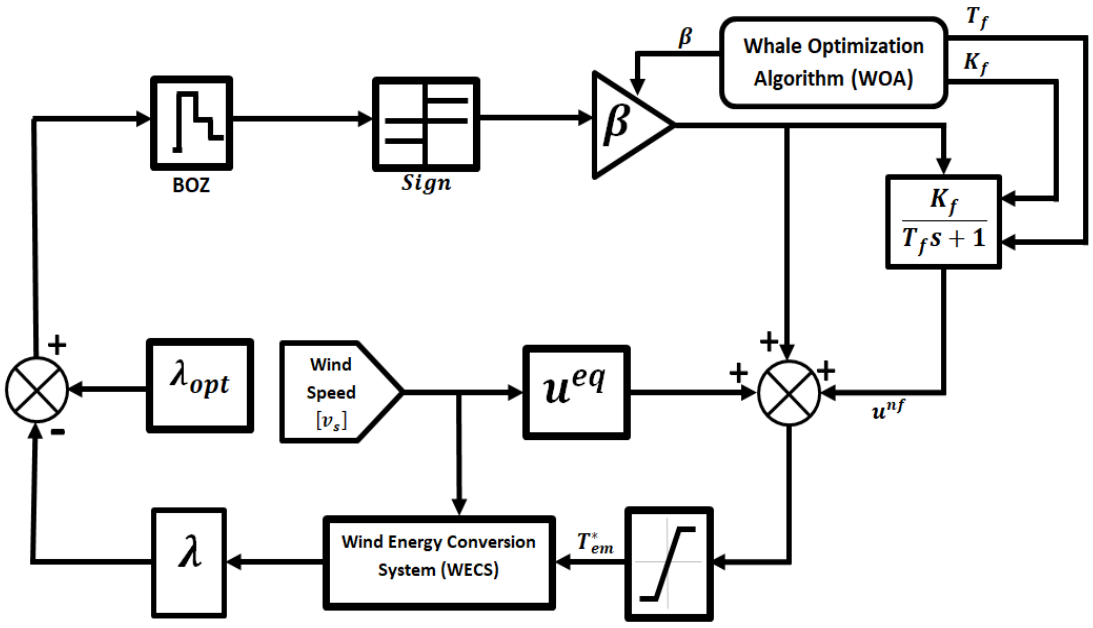


Figure III. 16 WOA Layout Diagram Block For Adjustment Of Improved On-Off Controller Parameters.

III. 4.1 Whale Optimization Algorithm (WOA)

WOA, introduced in 2016 (Mirjalili & Lewis, 2016) [16], is a population-based algorithm that draws inspiration from the social behavior of humpback whales. Like other population-based algorithms, WOA operates with a group of random candidate solutions known as the population. The algorithm employs three rules to update and enhance the position of candidate solutions in each iteration. These rules are encircling prey, spiral updating position, and search for prey. Let's delve into each of these rules:

1. Encircling Prey: This rule mimics the behavior of humpback whales encircling their prey. It involves adjusting the positions of candidate solutions towards a selected target solution.

   If $\left(p<0.5 \text{ and } |A|<1\right)$

   The position of the candidate solution, $\vec{X}(t+1)$, is updated according to eqations (III.4) and (III.5):

$$\vec{D}=\left|\vec{C}.\overrightarrow{X^*}-\vec{X}(t)\right| \quad \text{(III.4)}$$

$$\vec{X}(t+1)=\left|\overrightarrow{X^*}(t)-\vec{A}.\vec{D}\right| \quad \text{(III.5)}$$

   Where $p\in[0.1]$ and $\overrightarrow{X^*}$ is the best candidate solution in current generation. $\vec{A}$ and $\vec{C}$ are calculated as equations (III.6) and (III.7):

$$\vec{A}=\left|2\vec{a}.\vec{r}-\vec{a}\right| \quad \text{(III.6)}$$

$$\vec{C} = 2.\vec{r} \tag{III.7}$$

Where $\vec{a}$ is linearly decreased from 2 to 0 and $\vec{r}$ is randomly vector in [0,1].

2. Search for Prey: This rule involves exploration and exploitation of the search space. It enables the candidate solutions to search for better positions by moving randomly.

   If $\left(p < 0.5 \text{ and } |A| < 1\right)$

   Searching for prey is very similar to encircling prey, but in contrast to it, in searching for prey instead of using $\overrightarrow{X^*}$, a randomly candidate solution, $\overrightarrow{X_{rand}}$, is selected. Eqautions (III.8) and (III.9) describe the process.

$$\vec{D} = \left|\vec{C}.\overrightarrow{X_{rand}} - \vec{X}(t)\right| \tag{III.8}$$

$$\vec{X}(t+1) = \left|\overrightarrow{X_{rand}}(t) - \vec{A}.\vec{D}\right| \tag{III.9}$$

   Searching for prey is used during the exploration phase and enables WOA to perform global search.

3. Spiral Updating Position: In this rule, the candidate solutions update their positions by following a spiral pattern. This behavior is analogous to the spiraling motion of humpback whales as they approach their prey.

   If $p \geq 0.5$

   The spiral updating position method involves altering the positions of individuals according to Equation (III.10):

$$\vec{X}(t+1) = \overrightarrow{D^t}.e^{bl}.\cos(2\pi l) + \overrightarrow{X^*}(t) \tag{III.10}$$

   Where $\overrightarrow{D} = \left|\overrightarrow{X^*}(t) - \vec{X}(t)\right|$ which is the distance between ith candidate solution and the best solution in the current generation. b is a constant and $l \in [-1,1]$.

By employing these rules, WOA aims to optimize the candidate solutions and improve the overall performance of the algorithm.

III. 4.2 Enhanced On-Off Control For Wind Energy Conversion System Electromagnetic Torque Ripple Minimization Based On Whale Optimization Algorithm

To identify the optimal values for K_f, T_f and β, the Whale Optimization Algorithm (WOA) selects random initial values within predetermined intervals, as defined by Equation III.3. These intervals are established based on previous experiments and studies to facilitate an efficient search for the best values. To achieve an improved solution with minimal computation time and high precision,

the Mean Integrated Squared Error (MISE) is used as the objective function, calculated according to Equation III.2.

(Figure III.17) illustrates the process of utilizing the whale optimization algorithm (WOA) to enhance the performance of the improved on-off controller [113].

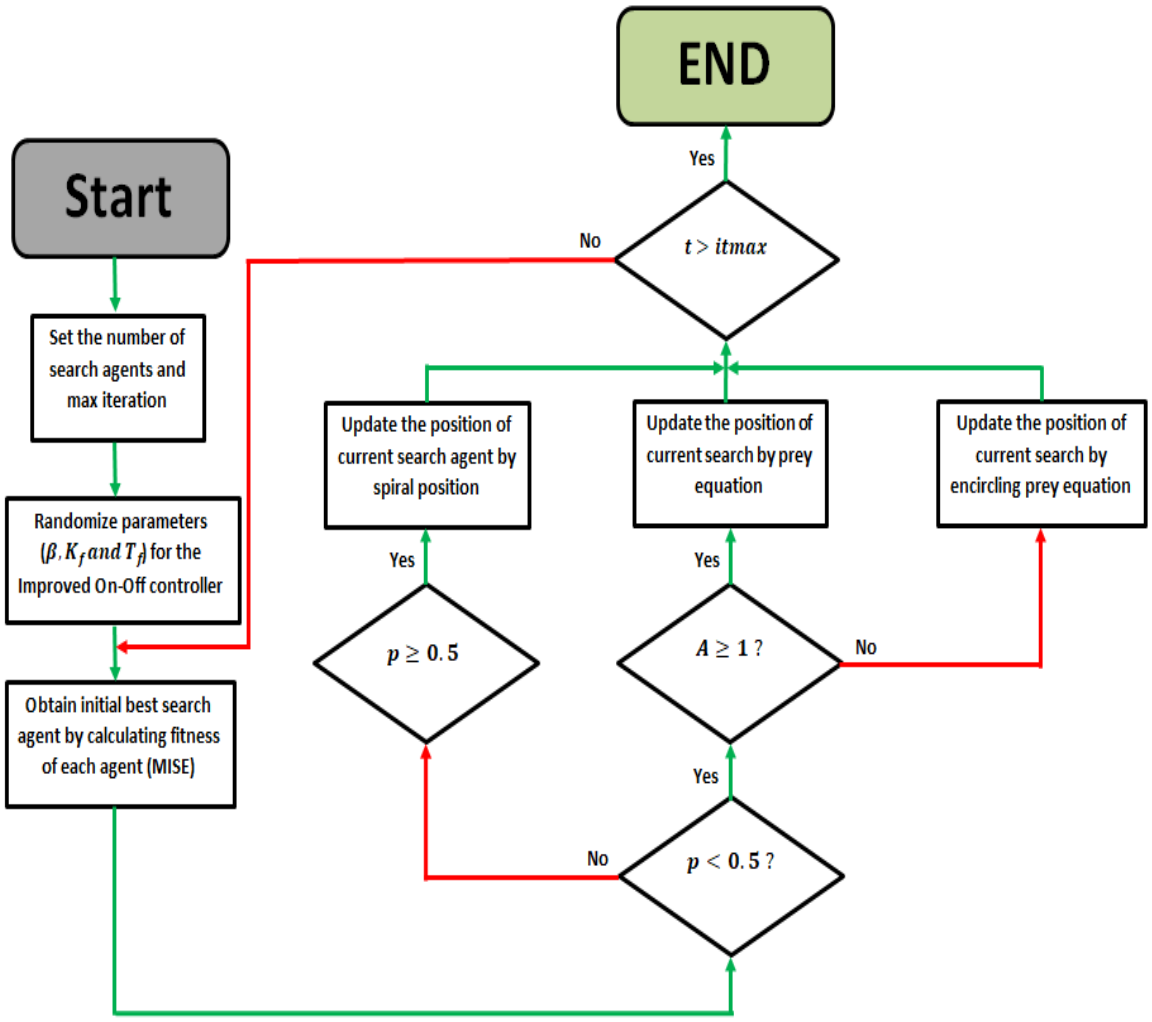


Figure III. 17 Flowchart Of The WOA Approach For Optimizing The Improved On-Off Controller.

III. 4.3 Simulation Results

To rigorously assess the effectiveness of the proposed control methodology, the wind energy conversion system, along with the corresponding control strategy, was implemented within the MATLAB/Simulink environment. The WECS parameters, as specified in Table B.1 of Appendix B, were employed in the simulations. These simulations were conducted over a duration of 80 seconds, utilizing the wind sequence outlined in Chapter I, Section 3.1. The analysis encompassed two distinct turbulence intensity categories—low and high—generated in accordance with the von Karman spectrum, as prescribed by the International Electrotechnical Commission (IEC) standard.

Numerous experiments were conducted to optimize the performance of the whale optimization algorithm. These experiments involved testing different maximum iteration values and subsequently comparing the results to determine the most suitable value for the simulation, ensuring optimal performance. After analyzing the results, it was observed that the optimal maximum iteration value for our experiments is 30. This value will be utilized to evaluate the performance of the WOA Enhanced ON-OFF Controller.

Table III.7 displays the WOA parameters utilized for determining the optimal values of the Enhanced On-Off Controller parameters.

Parameters	Values
Number of Search Agents	10
Max Iterations	30
a	[2,0]
α^2	[2, 1]
b	1

Table III. 7 WOA Parameters.

III. 4.3.1 Low Turbulence Stochastic Wind Speed

To facilitate a realistic comparison between the results produced by the improved ON-OFF controller and the WOA-enhanced ON-OFF controller, a low-turbulence stochastic wind model is employed in the initial stage, as depicted in Figure III.3 of Section 3.3.1 of this chapter. Notably, this wind model, proposed by C. Nichita for simulation purposes [19], is comprehensively detailed in Chapter I, Section 3.1.

For the Enhanced ON-OFF Controller, the parameters K_f , T_f and β are tuned using the WOA algorithm with the aid of low turbulence stochastic wind speed. The specific values of these parameters for the WOA Enhanced on-off controller are provided in Table III.8.

Parameters	Values	
	Improved ON-OFF Control	WOA Enhanced ON-OFF Control
K_f	20	10
T_f	5	400
β	0.75	0.1

Table III. 8 Parameters of The Enhanced ON-OFF Control Using Low Turbulence Stochastic Wind Speed.

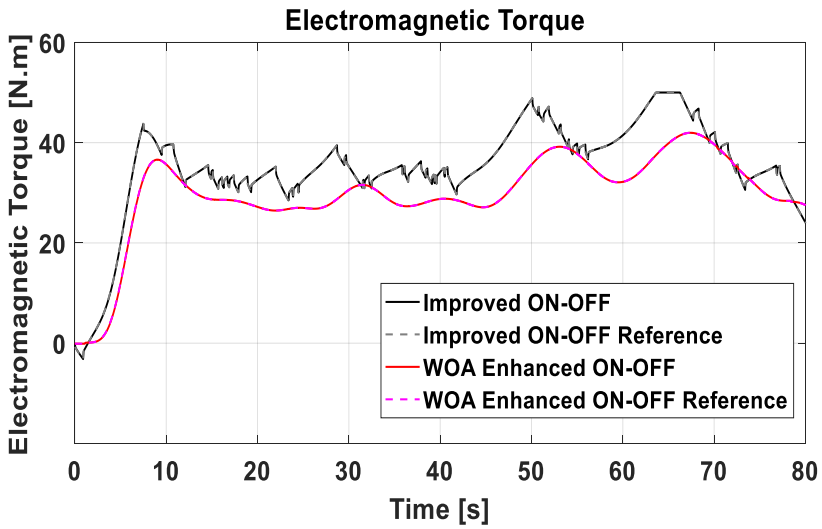


Figure III. 18 Electromagnetic Torque.

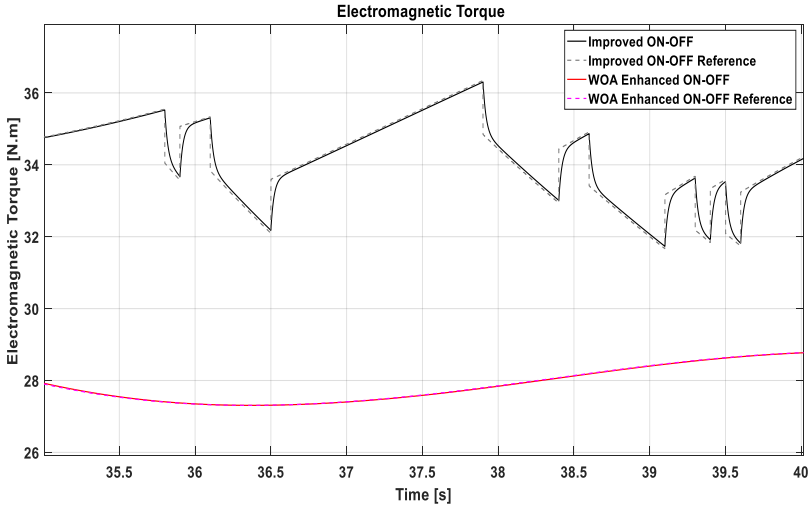


Figure III. 19 Electromagnetic Torque Zoom [35s-40s].

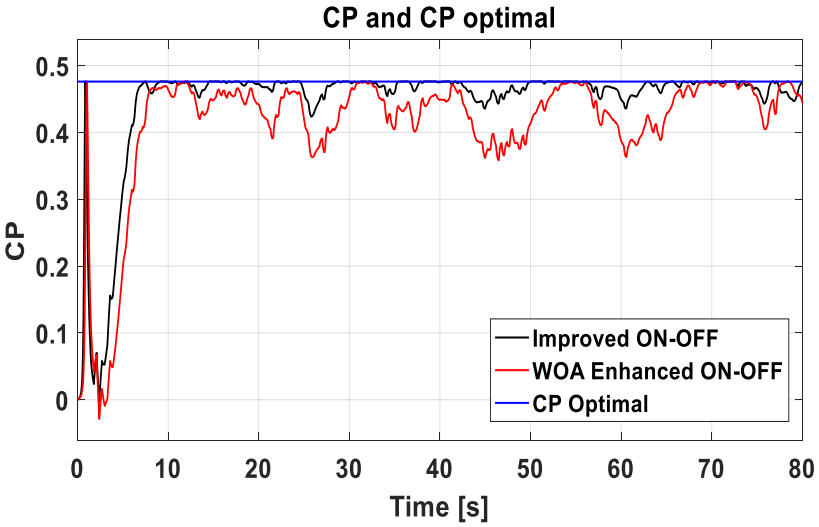


Figure III. 20 Power coefficient (CP).

Upon a thorough comparison of the simulation results derived from a low turbulence stochastic wind speed, several critical insights can be drawn. Firstly, the chattering phenomenon previously observed in the electromagnetic torque with the improved ON-OFF control has been completely

eradicated when employing the WOA-enhanced ON-OFF control, as illustrated in Figures III.18 and III.19. Additionally, a notable decrease in the magnitude of the electromagnetic torque is observed, as depicted in Figure III.18. Nevertheless, while the resolution of the chattering issue represents a significant improvement, a new challenge has emerged regarding the accurate tracking of the maximum power point, as demonstrated in Figure III.20. This issue directly impacts the overall efficiency of energy production.

III. 4.3.2 High Turbulence Stochastic Wind Speed

To assess the robustness of the proposed controller, it was crucial to test its performance under various conditions. As a result, we conducted simulations using a high turbulence wind model (Figure III.10). In these simulations, the parameters K_f ,T_f and β of the Enhanced On-Off Controller were tuned using the WOA algorithm with the assistance of a high turbulence stochastic wind speed. The specific values of these parameters for the Enhanced controller can be found in Table III.9.

Parameters	Values	
	Improved ON-OFF Control	WOA Enhanced ON-OFF Control
K_f	20	10
T_f	5	400
β	0.75	0.1

Table III. 9 Parameters of The Improved ON-OFF Control Using High Turbulence Stochastic Wind Speed.

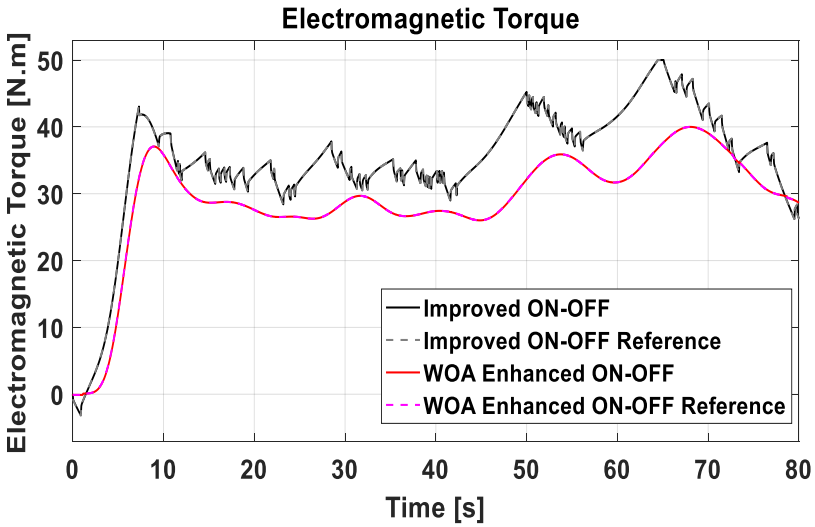


Figure III. 21 Electromagnetic Torque.

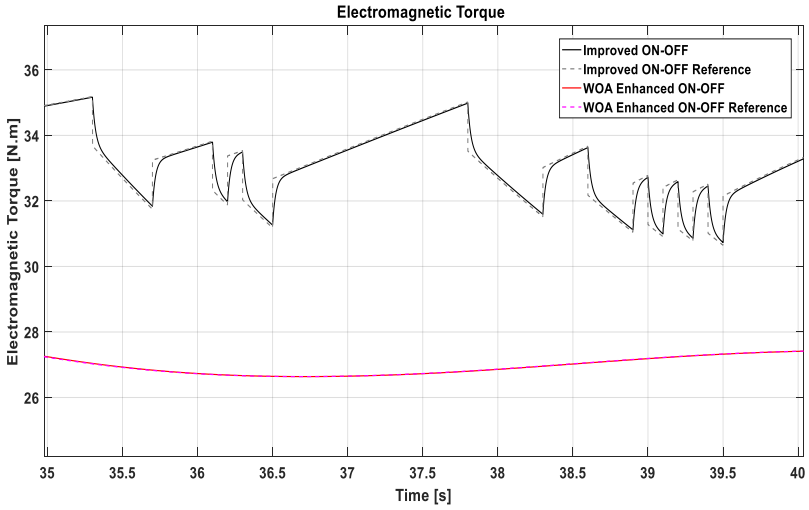


Figure III. 22 Electromagnetic Torque Zoom [70s-80s].

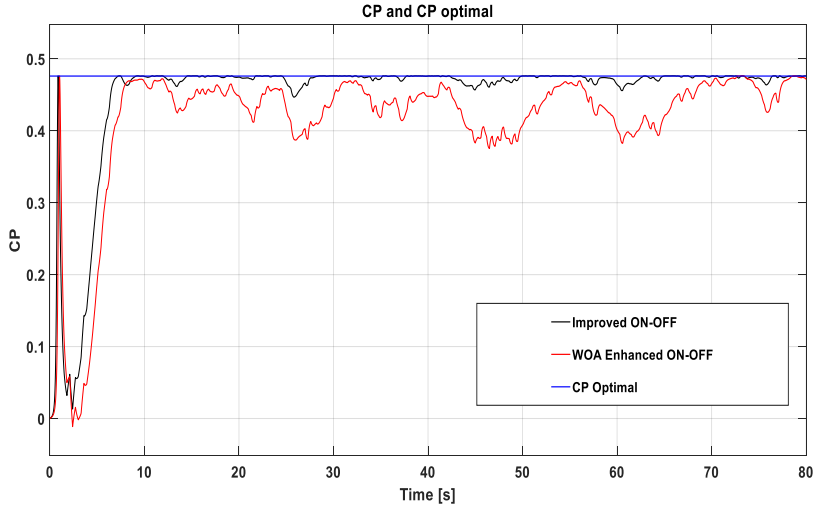


Figure III. 23 Power coefficient (CP).

Upon examining the curves presented in Figures III.21 and III.22, it is evident that the results obtained with the WOA Enhanced ON-OFF controller demonstrate substantial improvements. Notably, there is a significant reduction in the chattering problem related to the electromagnetic torque, which underscores the effectiveness of the WOA Enhanced ON-OFF controller in addressing this issue. This improvement not only enhances the longevity of the wind turbine but also reduces maintenance requirements. Conversely, in terms of tracking the maximum power point to optimize energy production, the improved ON-OFF controller exhibits superior performance, as illustrated in Figure III.23.

III. 5 COOT Enhanced On-Off Control Based On Hysteresis Function

The comparative analysis of the previous controllers, namely the "Improved On-Off Control Based on PSO" and the "Enhanced On-Off Control Based on WAO," revealed a critical trade-off. Specifically, while aiming to reduce torque ripple through metaheuristic approaches, the controllers

tend to deviate from the ideal trajectory necessary for maximum power point tracking (MPPT), resulting in suboptimal power generation. To address this issue, we propose the utilization of the COOT Optimization Algorithm (COA). This algorithm will be employed to optimize the gain K_f ,the filter time constant T_f and β. The objective is to enhance the performance of the improved on-off controller, ensuring more precise MPPT, as illustrated in Figure III.24.

Moreover, to further mitigate the chattering effect often encountered in on-off control systems, we suggest a modification to the internal structure of the controller. Specifically, we propose replacing the conventional sign function "$\text{sign}\ (\sigma)$" with a hysteresis function. This modification is expected to significantly enhance the robustness and efficiency of the controller, as depicted in the following formulation.

$$u^n = \beta.Hyst(\sigma(t)) \tag{III.11}$$

With:

$$Hyst(\sigma) = \begin{cases} \dfrac{d\sigma}{dt} = g_1(u,\sigma)\left(\dfrac{du}{dt}\right)^+ - g_2(u,\sigma)\left(\dfrac{du}{dt}\right)^- & \text{in [0,T]} \\ \sigma(0) = \sigma^0 \end{cases} \tag{III.12}$$

Here g_1 and g_2 are prescribed nonnegative functions, and are assumed to be so regular that the Cauchy problem (III.12) has one and only one solution [114].

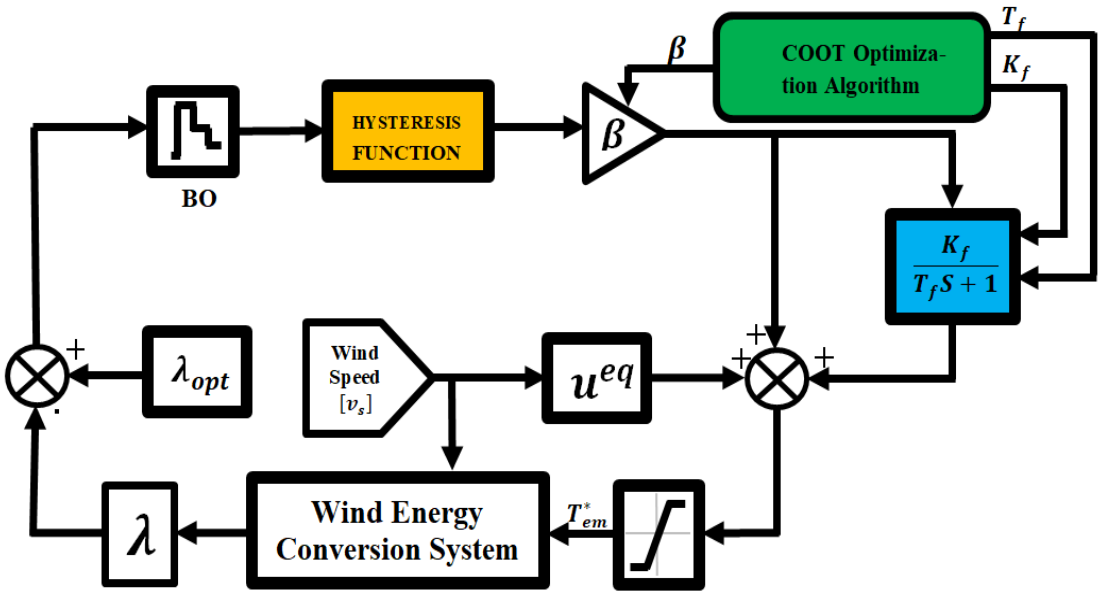


Figure III. 24 COOT Optimization Algorithm layout diagram block for adjustment of improved controller Based on Hysteresis Function parameters.

III. 5.1 COOT optimization Algorithm (COA)

The COOT Optimization Algorithm (COA), a recently developed meta-heuristic approach by Naruei and Keynia (2021) [14] and Mostafa et al. (2022) [15], is inspired by the movement behaviors of American coot birds in aquatic environments like lakes and seas. These birds utilize four distinct movement strategies: random walk, forming chains, moving toward the positions of group leaders, or taking the lead in guiding the group. The algorithm begins by randomly generating the initial population, as defined by Equations (III.12) and (III.13).

$$\mathrm{CootPos}(i) = \mathrm{rand}(1,d).*(ub - lb) + lb \tag{III.12}$$

$$lb = [lb_1, lb_2, \ldots, lb_d], ub = [ub_1, ub_2, \ldots, ub_d] \tag{III.13}$$

Here, CootPos represents the position of the i-th coot, and d refers to the dimension number. The variables ub and lb denote the upper and lower boundaries, respectively, while 'rand' represents a random vector within the range of [0, 1]. When coots move randomly, they transition towards a randomly selected position Q , which is calculated using Equation (III.14).

$$Q = \mathrm{rand}(1,d).*(ub - lb) + lb \tag{III.14}$$

To avoid getting trapped in local optimal regions, coots will apply Equation (III.15) if they become stuck in a local region.

$$CootPos(i) = CootPos(i) + A \times R2 \times (Q - CootPos(i)) \quad \text{(III.15)}$$

Where $R2 \in [0,1]$ and A can be calculated using Equation (III.16)

$$A = 1 - L \times \left(\frac{1}{I_{ter}} \right) \quad \text{(III.16)}$$

Where L is current iteration, I_{ter} is maximum iteration.

Equation (III.17) is used to mathematically represent the movement during the chain phase.

$$\mathrm{CootPos(i)} = 0.5 \times (\mathrm{CootPos(i-1)} + \mathrm{CootPos(i)}) \quad \text{(III.17)}$$

When a coot's movement aims to align its position with that of the leader, Equation (III.18) is employed.

$$k = 1 + (iMODNL) \quad \text{(III.18)}$$

During the update process, Equation (III.19) is used, where "i" represents the total number of coots, "NL" denotes the number of leaders, and "k" refers to a specific leader.

$$CootPos(i) = LeaderPos(k) + 2 \times RI \times Cos(2R\pi) \times (LeaderPos(k) - CootPos(i)) \quad \text{(III.19)}$$

In the final stage, leaders will use Equation (III.20) to update their positions.

$$LeaderPos(i) = \begin{cases} B \times R3 \times Cos(2\mathrm{R}\pi) \times (gBest - LeaderPos(i)) + gBest & if\ R4 < 0.5 \\ B \times R3 \times Cos(2\mathrm{R}\pi) \times (gBest - LeaderPos(i)) - gBest & if\ R4 \geq 0.5 \end{cases} \quad \text{(III.20)}$$

Where gBest is the best position, $\mathrm{R} \in [-1,1]$, both $\mathrm{R3\,\&\,R4} \in [0,1]$, B can be calculated using Equation (III.21).

$$B = 2 - L \times \left(\frac{1}{I_{ter}} \right) \quad \text{(III.21)}$$

III. 5.2 COOT Enhanced On-Off Control Based On Hysteresis Function for MPPT and Electromagnetic Torque Ripple Minimization of WECS

In Figure III.25, an illustrative diagram is presented that demonstrates how the COOT optimization algorithm enhances the performance of the improved ON-OFF controller based on the Hysteresis function. The primary objective is to maximize power generation by accurately tracking the

maximum power point, a process achieved through the use of the MISE objective function, as defined in Equation III.2.

The COOT Optimization Algorithm begins with an initialization phase, where an initial population of candidate solutions is generated randomly within the search space. During this phase, algorithm parameters—such as population size, number of iterations, and other specific COOT-related parameters—are established. Following initialization, the algorithm proceeds to the fitness evaluation step, where the fitness of each candidate solution is assessed using a predefined fitness function. This function is pivotal as it measures how well a candidate solution aligns with the optimization objectives, including maximizing power point tracking and minimizing energy loss. Once the fitness values are determined, the candidate solutions are ranked from best to worst based on their fitness scores, facilitating the identification of the most promising solutions to guide the subsequent search process. The algorithm then generates a new population by employing both exploration and exploitation strategies. During the exploration phase, new candidate solutions are created by broadly searching the space, which may involve random mutations or perturbations of existing solutions. In contrast, the exploitation phase focuses on generating new solutions by combining or crossing over the best solutions identified earlier, thereby intensifying the search in promising areas. After the new population is generated, it replaces the old one, and the algorithm checks for convergence to determine if the stopping criteria have been met—such as reaching the maximum number of iterations or observing convergence in fitness values. If the criteria are met, the algorithm terminates and outputs the best solution; otherwise, the process repeats from the fitness evaluation step. The output of the COOT Optimization Algorithm is the best candidate solution identified during the optimization process, representing the optimized K_f , T_f and β parameters for the Improved ON-OFF controller.

Several critical aspects of this approach warrant attention. The initialization phase is crucial, as the selection of an appropriate initial population and parameters sets a strong foundation for the optimization process. The fitness function must accurately capture the objectives of the optimization problem to effectively guide the search. A balanced interplay between exploration and exploitation is vital for the algorithm's success, ensuring that the search space is thoroughly explored while focusing on the most promising solutions. Lastly, well-defined stopping criteria are essential to prevent unnecessary computations and ensure the timely conclusion of the algorithm. This structured methodology allows the COOT Optimization Algorithm to iteratively refine candidate solutions, steering the search towards an optimal solution for the Improved ON-OFF controller.

Table III.10 details the parameters used in the COOT Optimization Algorithm to determine the optimal settings for the Improved ON-OFF Controller, aimed at maximizing the Power Coefficient.

Parameters	Values
Population Number N_{pop}	10
Leaders Number N_L	1
COOT Number N_c	9
Max Iteration	40

Table III. 10 COOT Parameters.

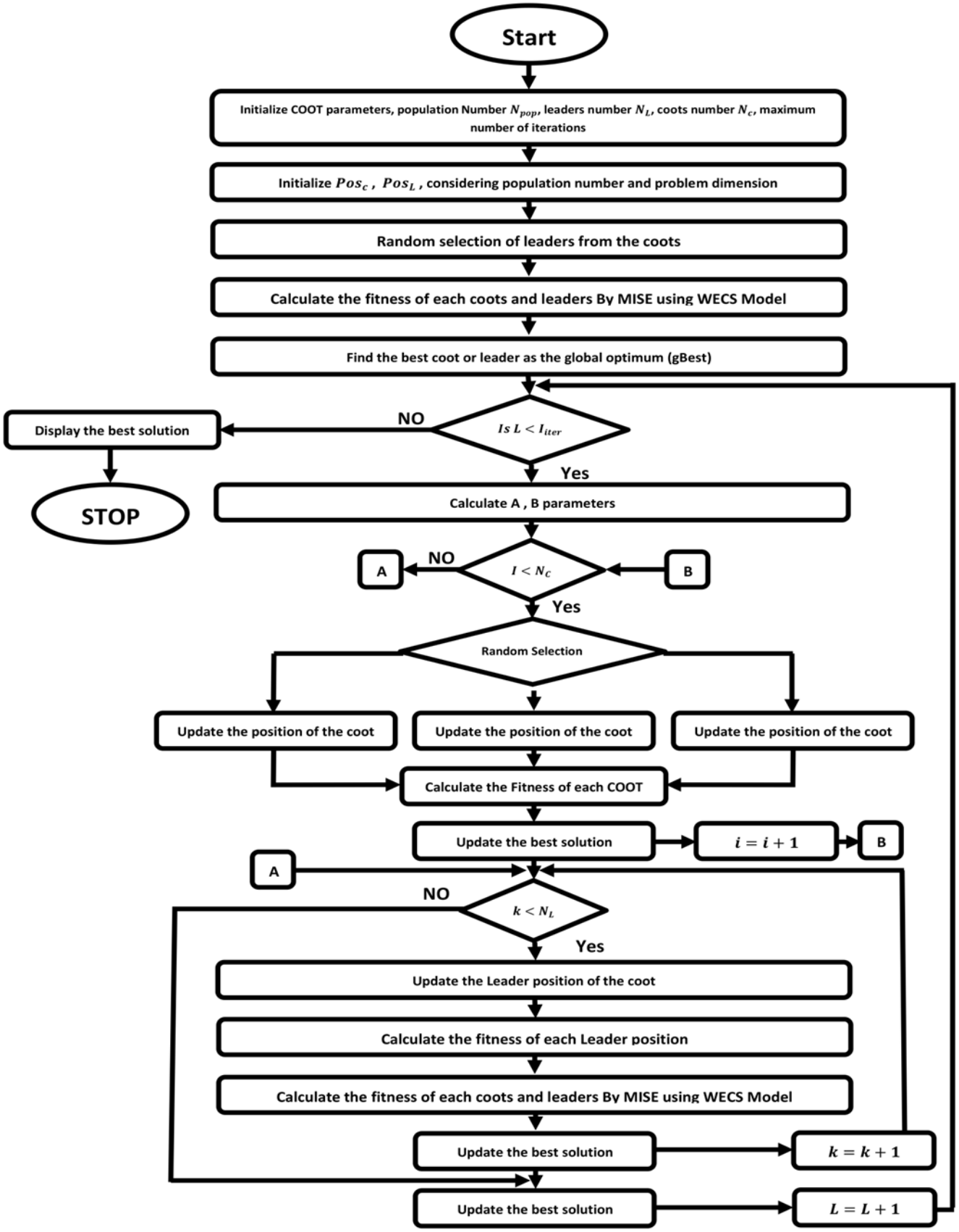


Figure III. 25 Flowchart of the COOT Optimization Algorithm approach for optimizing the Improved On-Off controller.

III. 5.3 Simulation Results

To evaluate the effectiveness of this work, the wind energy conversion system and the proposed control method were implemented in the MATLAB/Simulink environment, utilizing the WECS parameters provided in Table B.1 of Appendix B. Simulated tests were conducted using two different wind profiles.

III. 5.3.1 Low Turbulence Stochastic Wind Speed

In the initial stage, a low-turbulence stochastic wind model is utilized, as illustrated in Figure III.4. This model is employed for simulation to facilitate a more precise comparison between the results of the Improved On-Off controller and the COOT Improved On-Off Controller based on the Hysteresis Function for maximizing the power coefficient. Notably, this wind model, introduced by C. Nichita for simulation purposes [19], is thoroughly explained in Chapter I, Section 3.1.

The parameters T_f , K_f and β of the improved On-Off controller based Sign function and the COOT improved On–Off control based on Hysteresis function using low turbulence stochastic wind speed are presented in Table III.11.

Parameters	**Values**	
	Improved ON-OFF Control based sign function	COOT Improved On–Off Controller Based on Hysteresis Function for Power Coefficient Maximization
K_f	20	150
T_f	5	3
β	0.75	0.4

Table III. 11 Parameters of the Different Controllers using low turbulence stochastic wind speed.

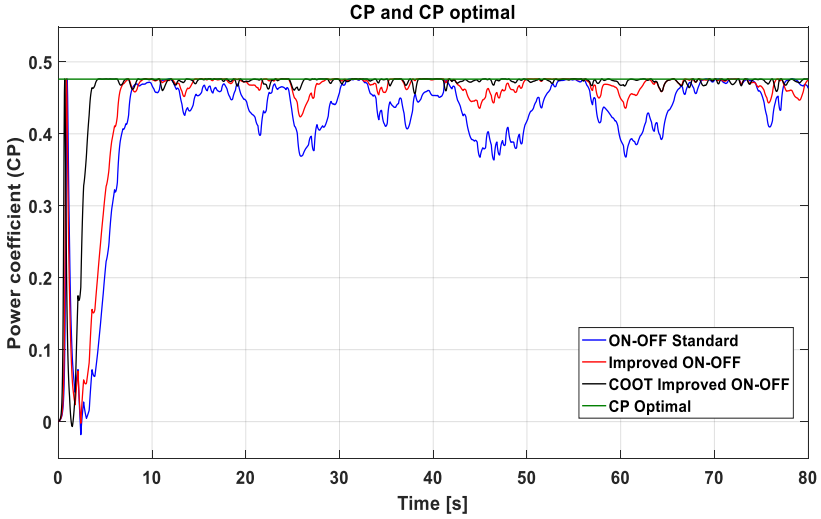


Figure III. 26 Power Coefficient (CP).

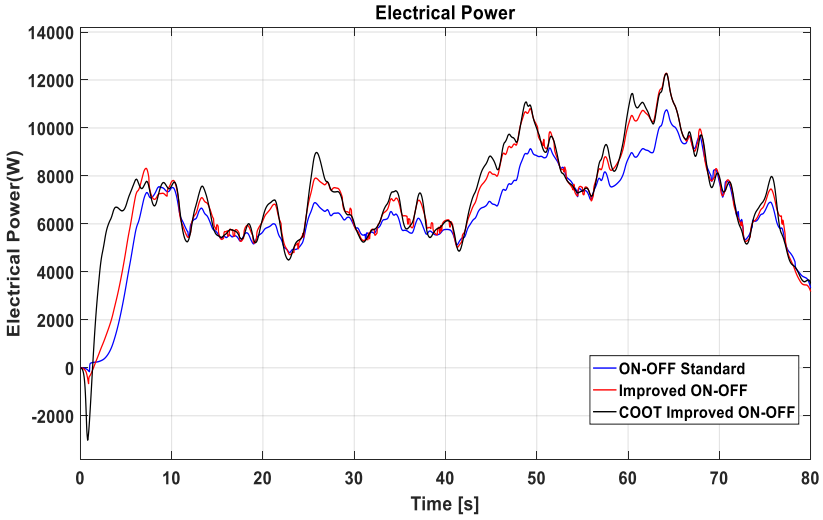


Figure III. 27 Electrical Power.

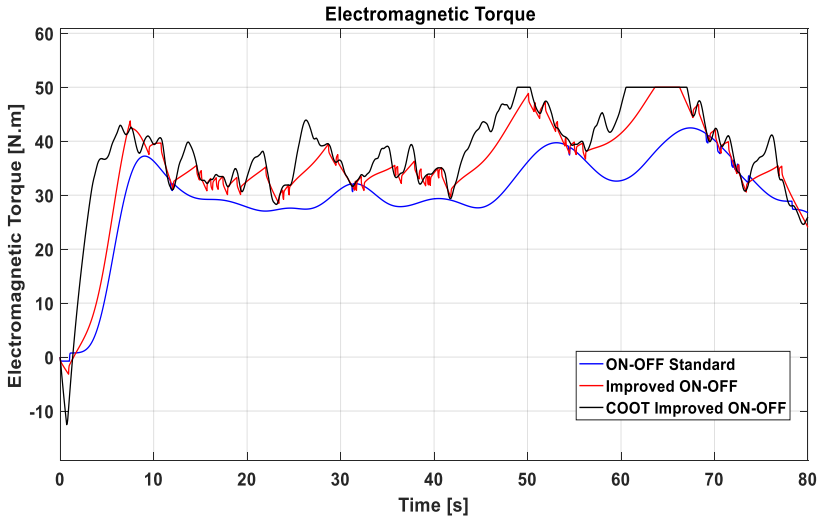


Figure III. 28 Electromagnetic Torque.

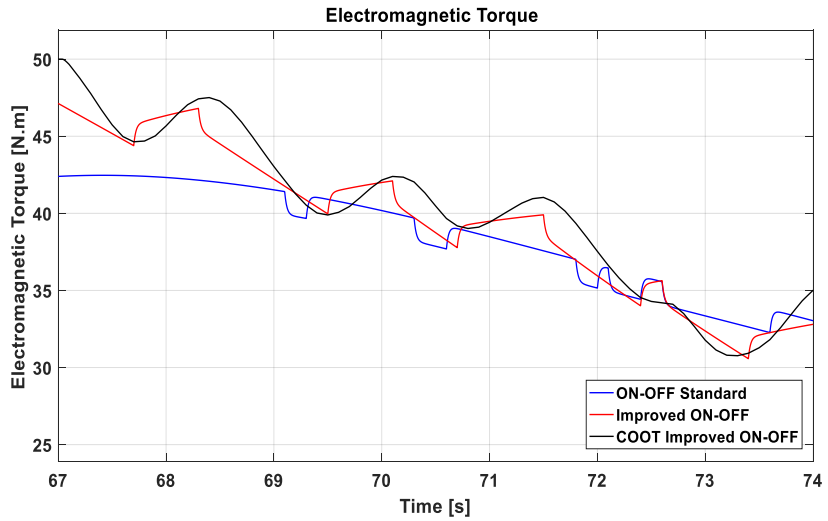


Figure III. 29 Electromagnetic Torque Zoom [67s-74s].

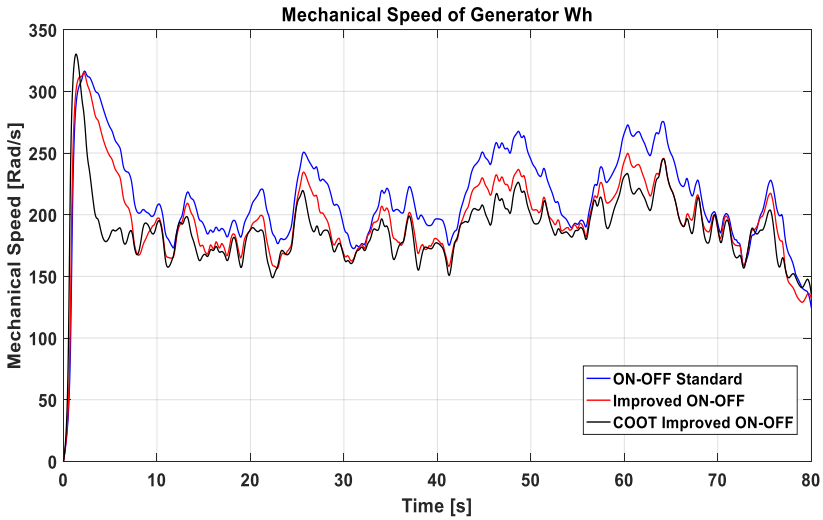


Figure III. 30 Mechanical Speed of Generator Ω_h .

The MPPT performance of the two controllers is presented in Figures III.26 through III.30. Figures III.26 and III.27 clearly demonstrate that the COOT Improved On-Off control based on the Hysteresis function is capable of extracting optimal wind energy, as it maintains the power coefficient closest to its optimum value (Cp=0.475), along with a steady and rapid mechanical rotational speed when compared to the improved On-Off controller (Figure III.30).

Regarding control forces, as depicted in Figures III.28 and III.29, the maximum electromagnetic torque reaches 50 N.m for both techniques, while the minimum value is approximately 24 N.m for the optimized Improved On-Off control based on the Hysteresis function. In Figure III.28, the torque ripple, caused by variations in the alternate control component, is significantly reduced when using the Hysteresis function, thereby lessening mechanical constraints.

These findings indicate that the proposed controller has successfully met certain performance criteria, particularly in its ability to efficiently track and generate maximum power output, fulfilling the requirements of producers.

III. 5.3.2 High Turbulence Stochastic Wind Speed

In this case, a high turbulent wind model is proposed to simulate the suggested controller in order to assess its resilience under various conditions (Figure III.10).

The parameters T_f , K_f and β of the improved On-Off controller based Sign function, and the COOT improved On–Off control based on Hysteresis function using high turbulence stochastic wind speed are presented in Table III.12.

Parameters	Values	
	Improved ON-OFF Control based Sign Function	COOT Improved On–Off Controller Based on Hysteresis Function for Power Coefficient Maximization
K_f	20	150
T_f	5	3
β	0.75	0.4

Table III. 12 Parameters Of The Different Controllers Using High Turbulence Stochastic Wind.

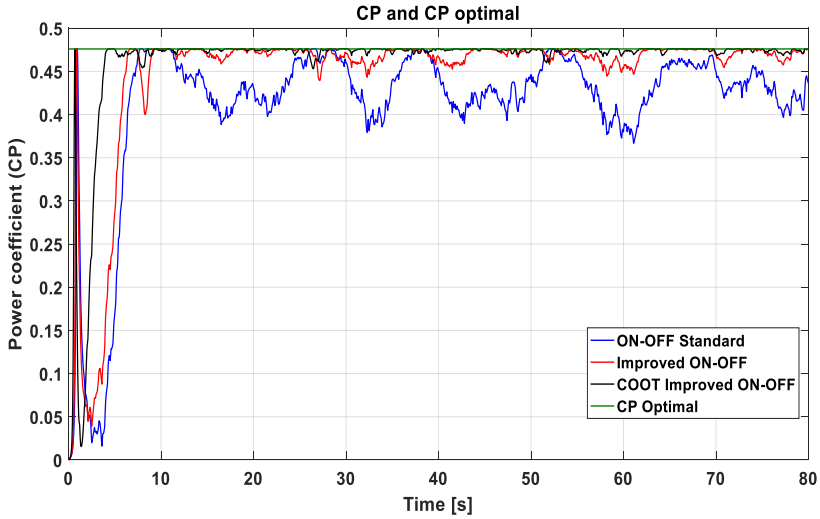


Figure III. 31 Power Coefficient (CP).

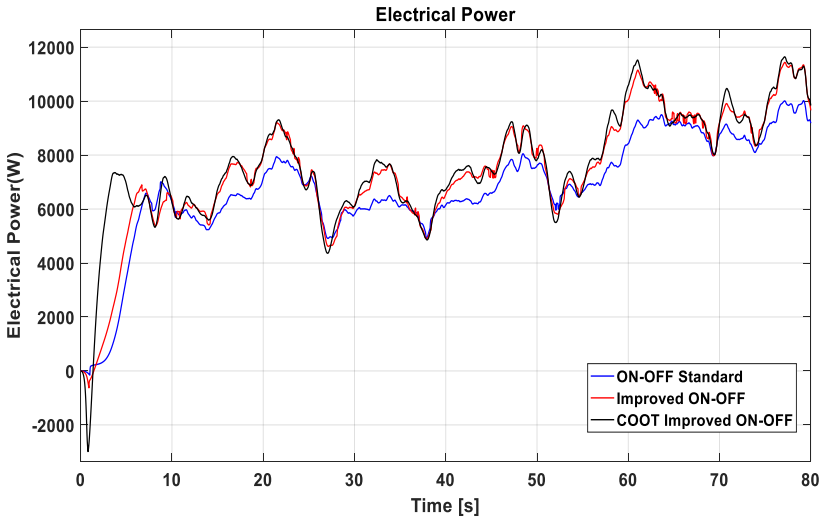


Figure III. 32 Electrical Power.

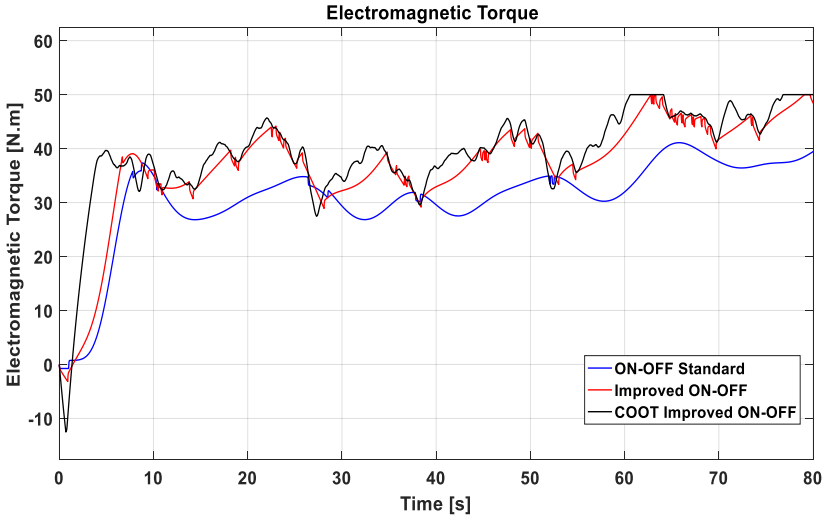


Figure III. 33 Electromagnetic Torque.

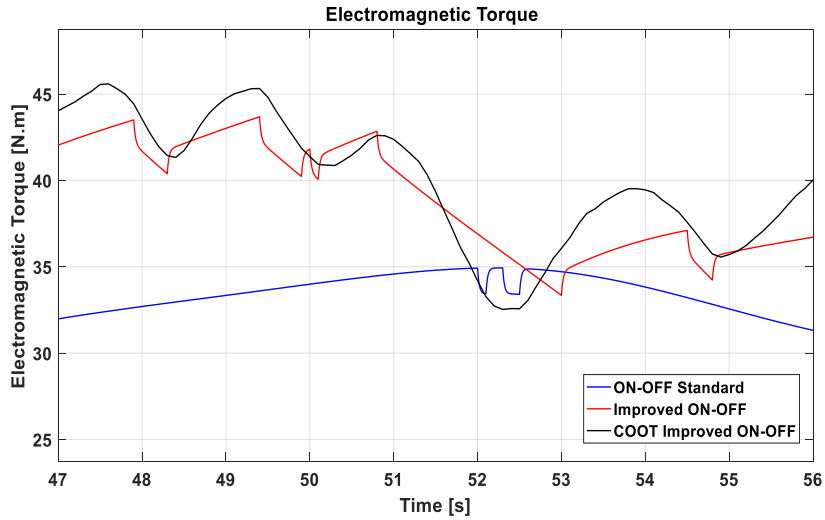


Figure III. 34 Electromagnetic Torque Zoom [47s-56s].

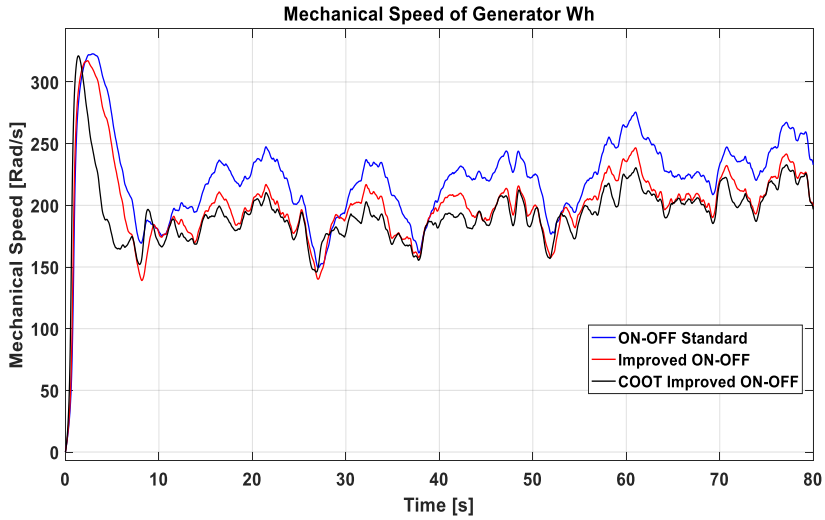


Figure III. 35 Mechanical Speed of Generator Ω_h .

Analyzing the results depicted in Figures III.31 and III.32 reveals that the outcomes achieved by the enhanced On-Off controller, which utilizes the Hysteresis function fine-tuned by the COOT

optimization algorithm, outperform those obtained with the improved On-Off controller based on the sign function, particularly in terms of maximum power point tracking efficiency.

The implementation of the improved On-Off controller, leveraging the Hysteresis function optimized by the COOT algorithm, effectively addresses the issue of chattering. Although the electromagnetic torque is higher compared to the improved On-Off controller based on the sign function (as shown in Figures III.33 and III.34), the proposed controller leads to a reduction in mechanical speed (as seen in Figure III.35).

These findings underscore the proposed controller's capability to deliver satisfactory performance across various wind speed conditions.

III. 6 Improved On-Off Control Based On Multi Objective PSO

Despite the effectiveness of the improved On-Off controller [6], testing revealed that the issue of chattering persisted. Consequently, it was determined that further performance enhancements were necessary, which could be achieved by adjusting certain controller parameters.

To address this, we employed the particle swarm optimization (PSO) algorithm to identify optimal values for the filtering time constant T_f, the gain K_f and β, with the goal of minimizing chattering and enhancing the performance of the improved On-Off control. Upon analyzing the results aimed at reducing the electromagnetic torque ripple (Figure III.35), we found that the chattering issue was completely resolved. However, this led to a significant shortfall in the required electric power, attributed to the power coefficient (CP) being lower than the optimal value needed [7].

Given the critical importance of increasing the electric power output, we decided to refocus our efforts on improving the power coefficient using the particle swarm optimization algorithm for the On-Off controller. This involved seeking the optimal values for the filtering time constant T_f, gain K_f, and β. By examining the results (Figure III.37), we observed a significant improvement in electric power output, with maximum power coefficient values achieved compared to the optimal power coefficient. However, despite the controller's effectiveness in maximizing power, an increase in electromagnetic torque ripple (i.e., the chattering problem) was also noted.

From previous experiments, we observed that targeting the maximization of the power coefficient (CP) alone had the unintended consequence of increasing electromagnetic torque ripple. Conversely, when focusing solely on reducing electromagnetic torque ripple, there was an undesirable reduction in the power coefficient.

To simultaneously optimize the power coefficient and reduce electromagnetic torque ripple, we decided to conduct a multi-objective experiment for this section of the chapter. To execute this experiment, we proposed a novel controller: the multi-objective particle swarm optimization (MOPSO) for the Improved On-Off controller.

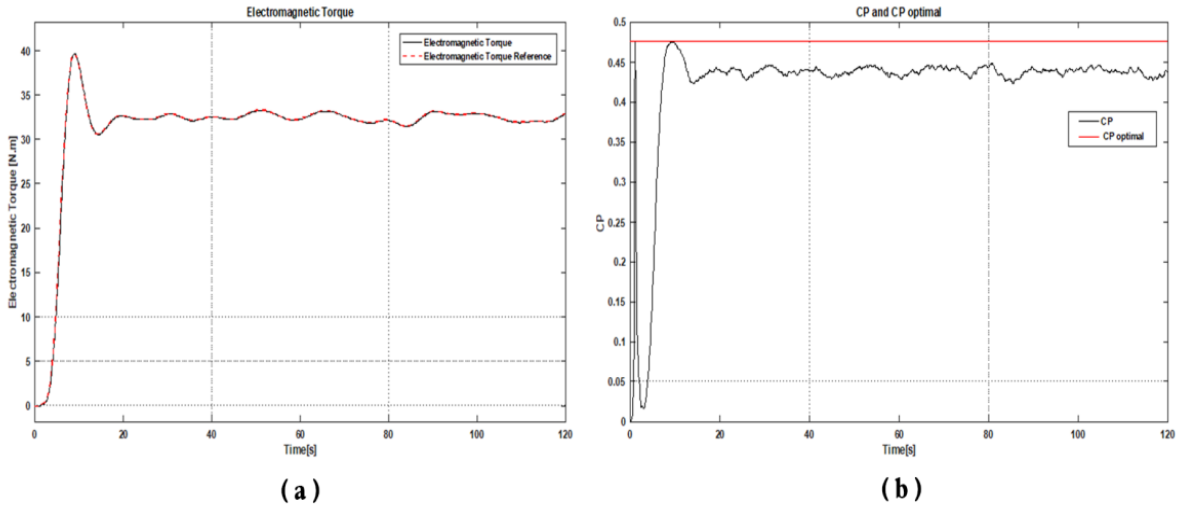


Figure III. 36 WECS responses (PSO Improved On-Off Controller for Electromagnetic Torque Ripple Minimization): (a) Electromagnetic Torque, (b) Power coefficient (CP).

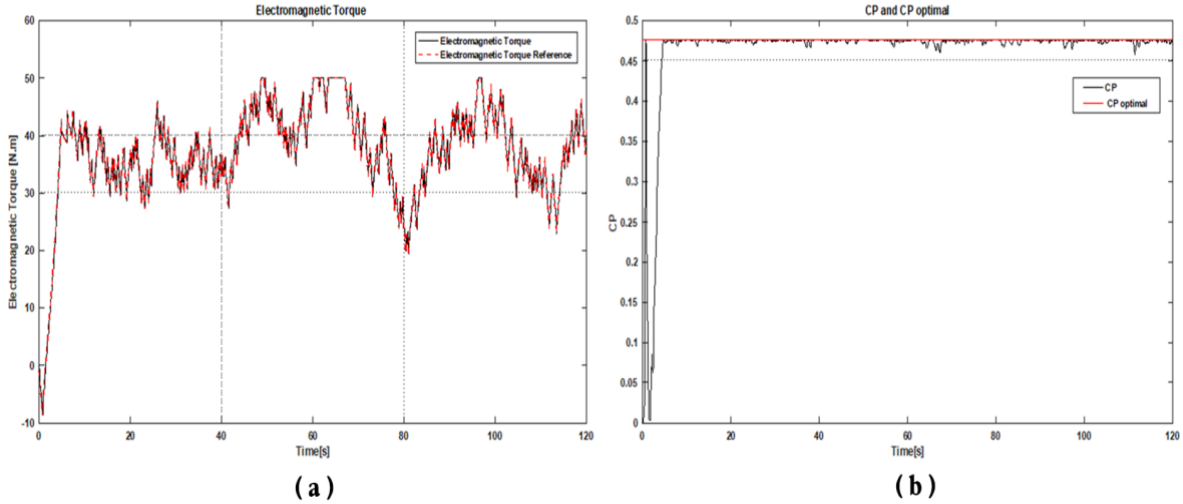


Figure III. 37 WECS responses (PSO Improved On-Off Controller for Power Coefficient Maximization): (a) Electromagnetic Torque, (b) Power coefficient (CP).

To address multiple targets using particle swarm algorithms, researchers employ various mathematical methods across different scientific fields to solve their problems [75,76]. One common approach involves combining multi-objective functions into a single objective. Consequently, multi-objective PSO results can be derived by applying a single-objective PSO using the following established mathematical equation [115,116,117]:

$$F_{err} = \sum_{i=1}^{Num} \left(l_i . F_{err}^{(i)} \right) \qquad \text{(III.22)}$$

Where Num is the number of the individual errors; $F_{err}^{(i)}$ is the value of the individual error corresponding to the objective i; and l_i is the weight factor with $\sum l_i = 1$. Finally, the set of parameters with the minimum error value can be selected as the optimal set.

In our controller we have two errors represented by $F_{err}^{(1)}$ and $F_{err}^{(2)}$ where we aim to maximize the power Coefficient value through $F_{err}^{(1)}$ and also we aim to minimize the electromagnetic torque ripple through $F_{err}^{(2)}$.

The maximization fitness function can be converted into a minimization fitness function by multiplying it by -1. Then both objectives can be minimized. When we have the Pareto front, we just have to transform the objective back so that it maximizes.

For multi-objective problems, the final error can be expressed as follows:

$$F_{err} = -l_1.F_{err}^{(1)} + l_2.F_{err}^{(2)} \qquad \text{(III.23)}$$

The multi-objective particle swarm optimization algorithm is used to search for the best parameters T_f, K_f and β of the Improved on-off controller as shown in (Figure III.38).

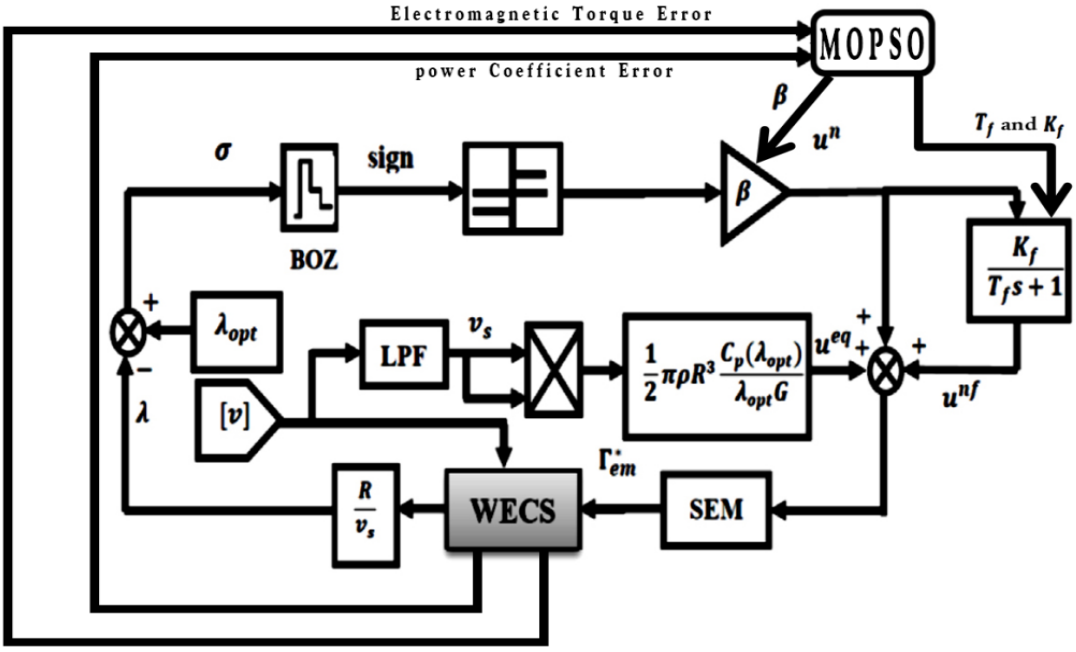


Figure III. 38 Multi Objective PSO Layout Diagram Block For Adjustment of Improved Controller Parameters.

To find a better solution in a minimum calculation time and precision, we calculate the best solution for each single objective, based on the minimization of a certain criterion (objective function) is the Mean integrated squared error calculated by the following equation:

$$\text{MISE} = \text{Fit} = \int \left(\text{e}(\text{t})^2 \right) \text{dt} \tag{III.24}$$

$$\text{Subject to} \quad \begin{cases} \beta_{min} \le \beta \le \beta_{max} \\ K_{fmin} \le K_f \le K_{fmax} \\ T_f \le T_f \le T_{fmax} \end{cases} \tag{III.25}$$

Where: $e_1(t) = CP_{optimal} - CP$ is the difference between the optimal Power Coefficient value and the output Power Coefficient value under improved On-Off control in $F_{err}^{(1)}$, which aims to maximize the Electric Power. And $e_2(t) = \Gamma_{em}^{*} - \Gamma_{em}$ is the difference between the electromagnetic torque reference value and the electromagnetic torque value under improved On-Off control in $F_{err}^{(2)}$ which aims to minimize the electromagnetic torque ripple.

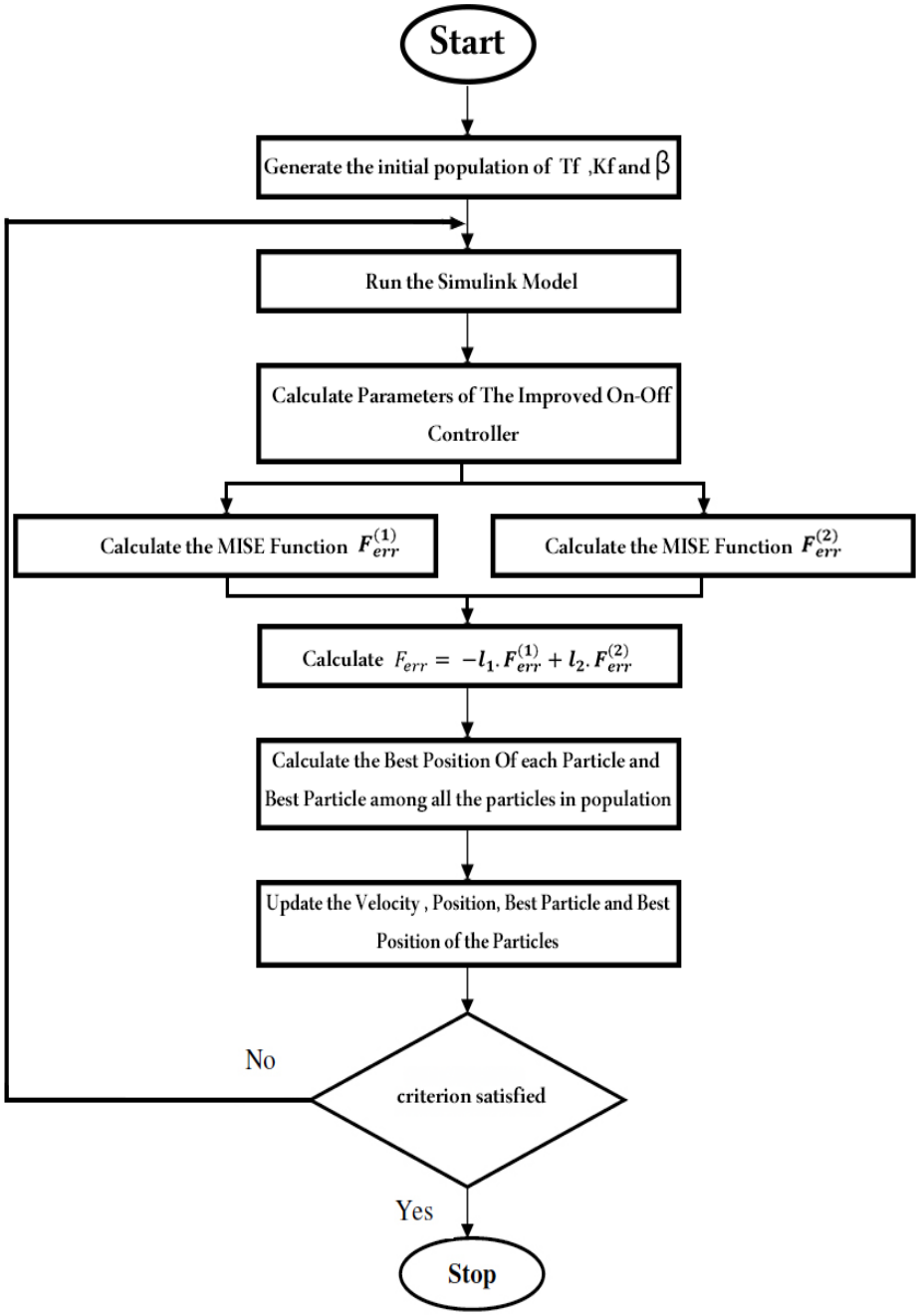


Figure III. 39 Flowchart of The MOPSO Approach For Optimizing The Improved On-Off Controller.

The MOPSO parameters used to find the optimum values of the improved On-Off Controller parameters are presented in Table III.13.

Parameters	Values
Number of Particles	10
Max Iteration	40
Weight Factor (l_i) of MOPSO	$l_1 = 0.5$ and $l_2 = 0.5$
Inertia Weight Factor (W) of PSO	0.9
Confidence Coefficient	$C_1 = 0.12$ and $C_2 = 1.2$

Table III. 13 MOPSO Parameters.

III. 6.1 Simulation Results

As with the previous experiments involving the proposed controllers, the wind energy conversion system and the suggested control strategy were implemented in the MATLAB/Simulink environment using the WECS parameters outlined in Table B.1 of Appendix B to evaluate this work. The simulations were conducted using two different wind profiles.

III. 6.1.1 Low Turbulence Stochastic Wind Speed

In the initial stage, and consistent with previous experiments, a low-turbulence stochastic wind model is employed, as shown in Figure III.4. This model is utilized for simulation to enable a more precise comparison of the results between the PSO Improved On-Off Controller for Electromagnetic Torque Ripple Minimization, the PSO Improved On-Off Controller for Power Coefficient Maximization, and the Multi-Objective PSO (MOPSO) Improved On-Off Controller for both Electromagnetic Torque Ripple Minimization and Power Coefficient Maximization. As discussed in earlier chapters, this wind model, introduced by C. Nichita for simulation purposes [19], is thoroughly detailed in Chapter 1, Section 3.1. The parameters T_f, K_f and β of the PSO Improved On-Off Controller for Electromagnetic Torque Ripple Minimization, the PSO Improved On-Off Controller for Power Coefficient Maximization, and the MOPSO Improved On–Off Control for Electromagnetic Torque Ripple Minimization and Power Coefficient Maximization using low turbulence stochastic wind speed are presented in Table III.14.

Parameters	Values		
	PSO Improved On-Off Controller for Power Coefficient Maximization	PSO Improved On-Off Controller for Electromagnetic Torque Ripple Minimization	Multi Objective PSO Improved ON-OFF Controller
K_f	300	1	510.0811
T_f	18.3489	2.6814	560.6600
β	1	0.100	0.1321

Table III. 14 Parameters of The Different Controllers Using Low Turbulence Stochastic Wind Speed.

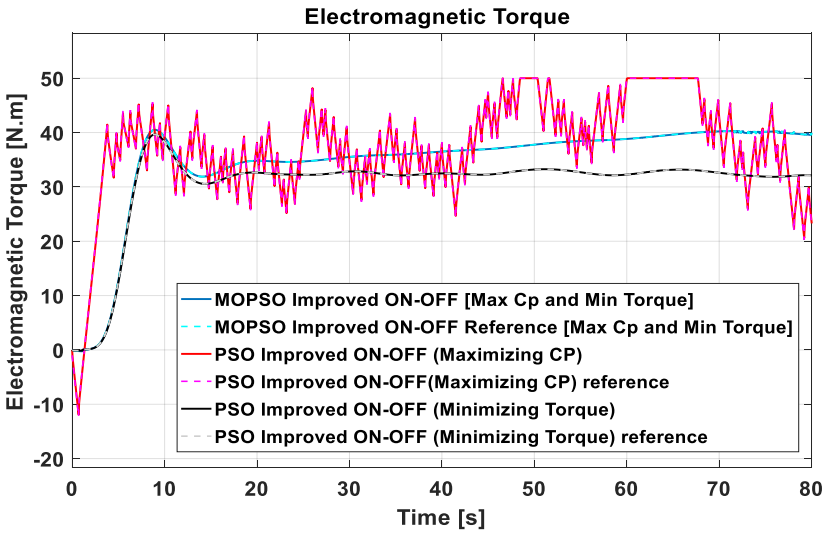


Figure III. 40 Electromagnetic Torque.

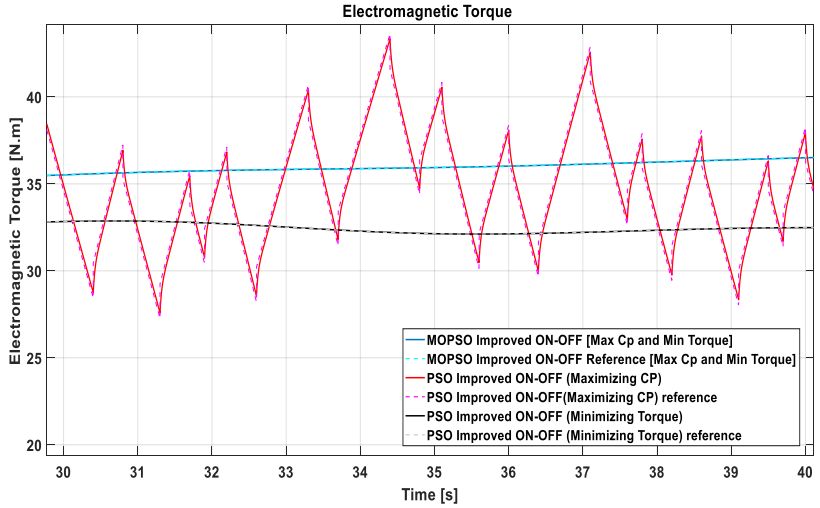


Figure III. 41 Electromagnetic Torque Zoom [30s-40s].

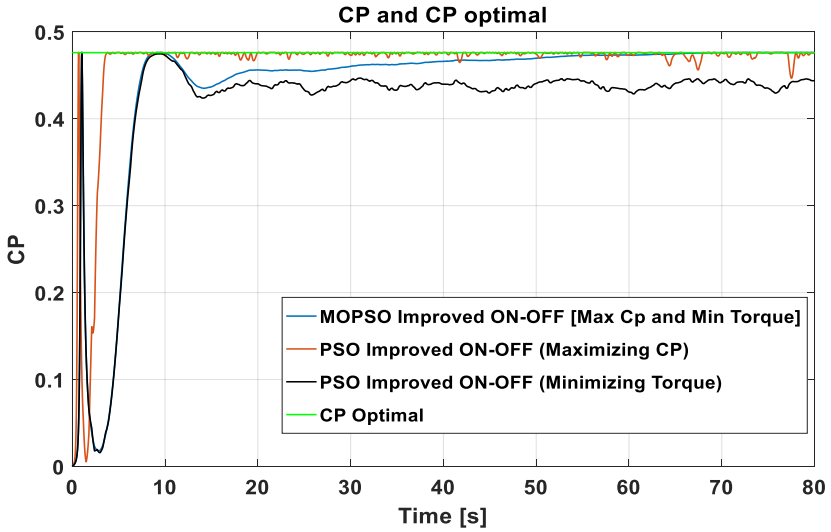


Figure III. 42 Power Coefficient (CP).

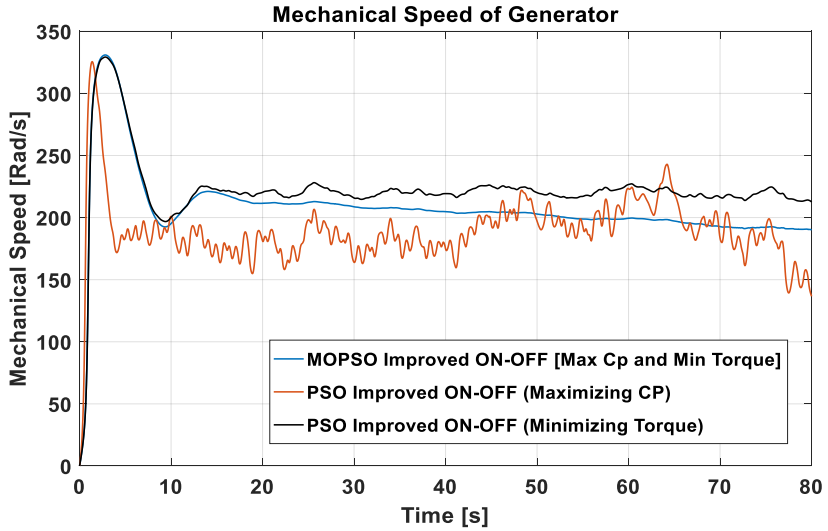


Figure III. 43 Mechanical Speed of Generator Ω_h .

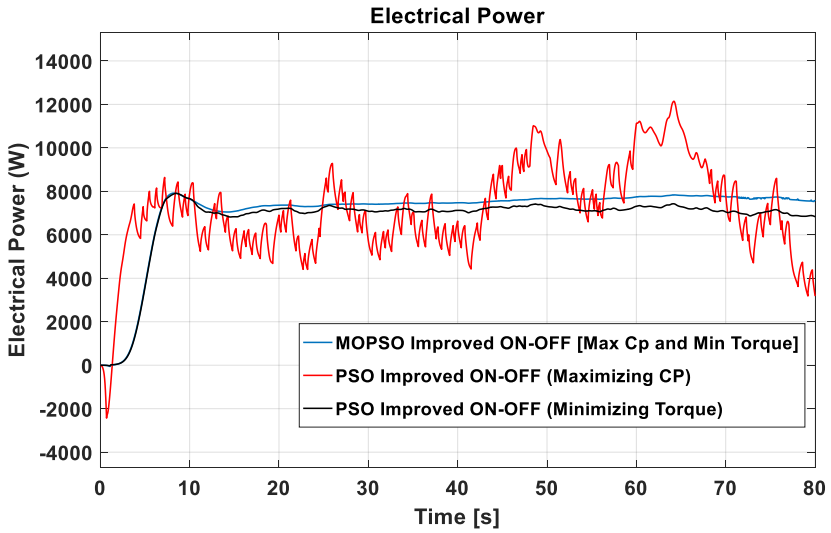


Figure III. 44 Electrical Power.

When analyzing the results derived from a low-turbulence stochastic wind profile, it becomes apparent that the Improved On-Off Controller optimized through MOPSO achieves a remarkable reduction in electromagnetic torque ripple—exceeding 95%—compared to its counterpart tuned by PSO for maximizing the power coefficient (CP). However, this reduction is marginally less effective than the performance achieved by the Improved On-Off Controller tuned by PSO for minimizing electromagnetic torque ripple (refer to Figures III.40 and III.41). The significant decrease in torque ripple with the MOPSO-tuned controller explains the enhanced mechanical stability and the smoother, vibration-free rotational speed observed, in contrast to the PSO-tuned controller aimed at CP maximization. This stability stems from the alleviation of mechanical loads on the drive shaft, primarily due to the elimination of the chattering phenomenon. Nonetheless, the optimal performance in this domain is attributed to the PSO-tuned controller designed specifically to minimize torque ripple (Figure III.43).

In terms of power coefficient (CP) and electrical power generation, the MOPSO-tuned controller demonstrates commendable performance, surpassing the PSO-tuned controller optimized for torque ripple minimization. However, the amount of power produced and the speed of attainment remain suboptimal when compared to the outcomes achieved by the PSO-tuned controller for CP maximization (Figures III.42 and III.44).

These findings highlight that the Improved On-Off Controller tuned via MOPSO offers a critical advantage by effectively mitigating the chattering phenomenon. This not only enhances the operational lifespan of the wind turbine but also facilitates the generation of substantial electrical energy.

III. 6.1.2 High Turbulence Stochastic Wind Speed

To assess the robustness of the proposed controller under varying conditions, it was crucial to evaluate its performance using a high-turbulence wind model, as depicted in Figure III.10.

The parameters T_f, K_f and β of PSO Improved On-Off Controller for Electromagnetic Torque Ripple Minimization, the PSO Improved On-Off Controller for Power Coefficient Maximization, and the MOPSO Improved On–Off Control for Electromagnetic Torque Ripple Minimization and Power Coefficient Maximization using High turbulence stochastic wind speed are presented in Table III.15.

Parameters	Values		
	PSO Improved On-Off Controller for Power Coefficient Maximization	PSO Improved On-Off Controller for Electromagnetic Torque Ripple Minimization	Multi Objective PSO Improved On–Off Controller
K_f	300	1	366.1590
T_f	35.9187	4.2987	466.7850
β	1	0.100	0.1488

Table III. 15 Parameters of The Different Controllers Using High Turbulence Stochastic Wind.

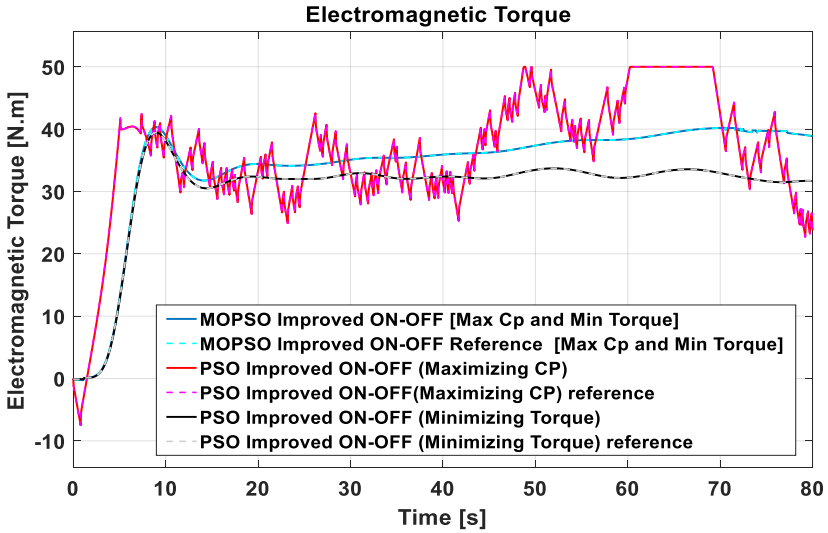


Figure III. 45 Electromagnetic Torque.

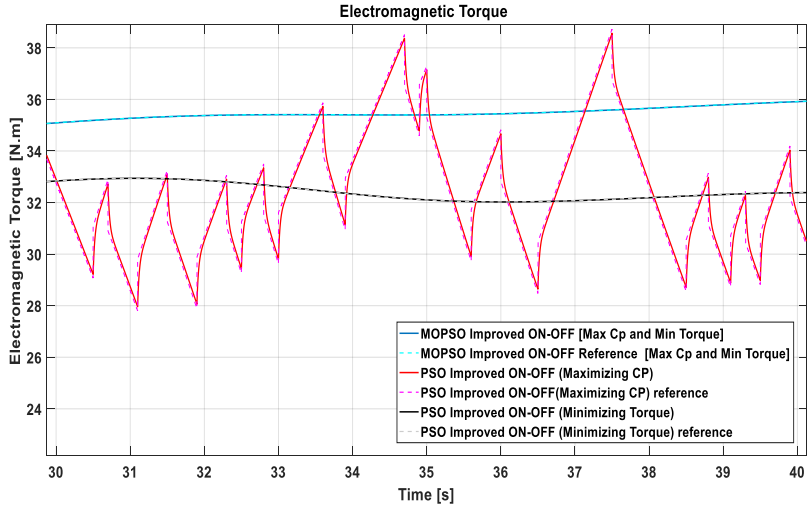


Figure III. 46 Electromagnetic Torque Zoom [30s-40s].

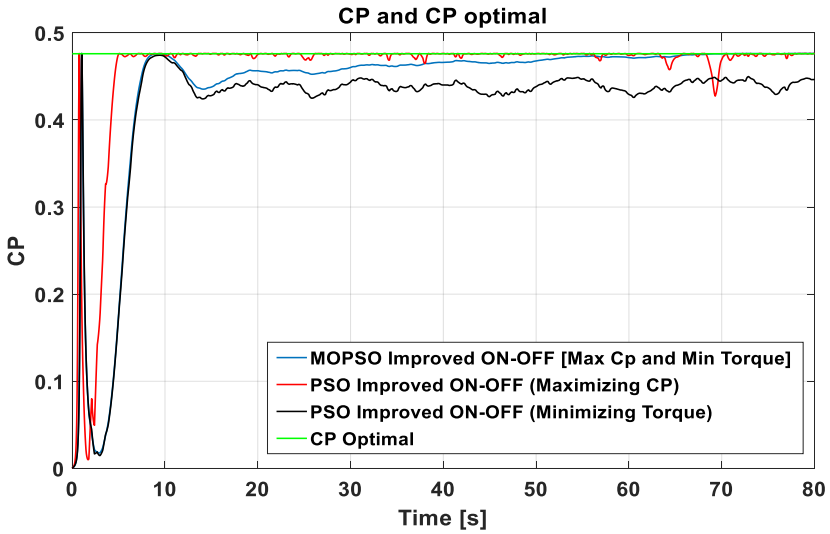


Figure III. 47 Power Coefficient (CP).

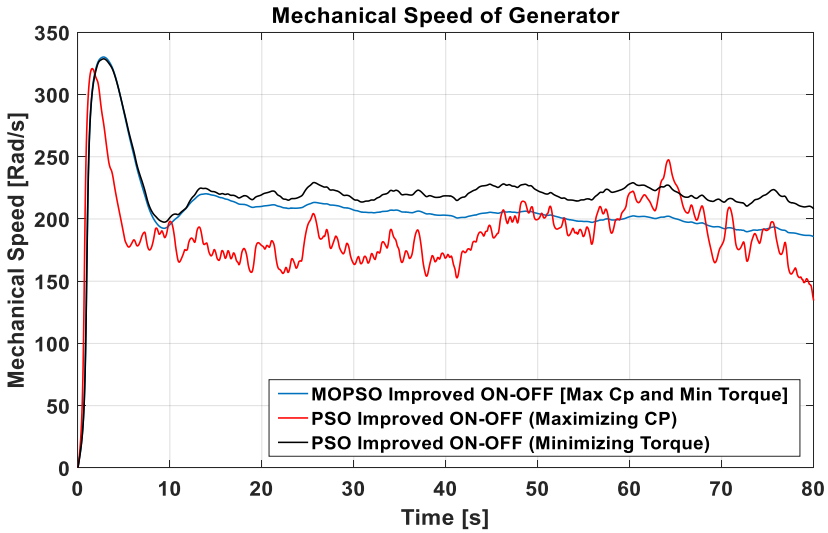


Figure III. 48 Mechanical Speed of Generator Ω_h .

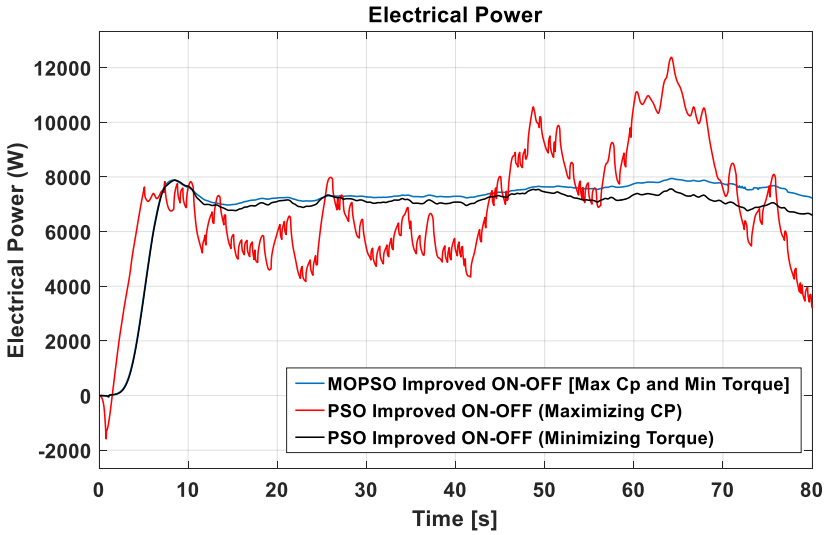


Figure III. 49 Electrical power.

A comparison of the curves in Figures III.45, III.46, and III.48 reveals that the Improved On-Off Controller tuned by MOPSO outperforms the one tuned by PSO for maximizing CP, particularly in addressing the chattering phenomenon. Nevertheless, its performance remains slightly inferior to that of the Improved On-Off Controller tuned by PSO for minimizing electromagnetic torque ripple.

Similarly, an examination of the curves in Figures III.47 and III.49 demonstrates that the MOPSO-tuned controller achieves better results than the PSO-tuned controller optimized for minimizing electromagnetic torque ripple, specifically in terms of maximizing electrical power output. However, these results still do not match the superior performance of the PSO-tuned controller for CP maximization.

Overall, these findings highlight the proposed controller's capability to deliver reliable and satisfactory performance under various wind speed conditions.

III.7 CONCLUSION

In conclusion, this chapter has explored various optimization strategies for enhancing the performance of an improved On-Off controller in a wind energy conversion system (WECS) equipped with a squirrel-cage induction generator (SCIG). Across the different methods applied—PSO, WOA, COOT, and MOPSO—the primary objectives were to reduce electromagnetic torque ripple, minimize chattering effects, and maximize power output.

The PSO-based approach demonstrated significant effectiveness in reducing chattering and extending the wind turbine's lifespan by limiting mechanical loads on the drive shaft. However, it introduced a new challenge by compromising the maximum power point tracking (MPPT) function, resulting in reduced power production. Similarly, the WOA-tuned controller showed favorable performance in reducing chattering and improving turbine longevity, but it also failed to fully maintain MPPT, leading to a decline in power generation.

The COOT optimization algorithm introduced an innovative improvement by incorporating a hysteresis function into the controller’s internal structure, which not only enhanced MPPT accuracy but also significantly mitigated the impact of chattering. The results indicated successful energy extraction and regulation, with reduced mechanical stress and power output fluctuations, pointing to the potential for real-world application.

Finally, the MOPSO-based controller achieved commendable results by optimizing the power coefficient, thereby maximizing electrical power production while also reducing chattering. Although the MOPSO approach reduced electromagnetic torque ripple by more than 95%, it did not eliminate it entirely, and a slight time delay and instability in maintaining maximum power output were observed. Despite these minor drawbacks, the improved On-Off controller tuned by MOPSO remains a promising solution, meeting the needs of producers with its ease of implementation and satisfactory performance.

Next chapter will focus on further refining these control strategies, particularly by leveraging the Frequency Separation Principle to fully address the identified issues and improve the overall efficiency and practical viability of wind energy conversion systems

CHAPTER IV: Advanced control structure based on the Principle of Frequency Separation of a Wind Energy Conversion System

IV. 1 Introduction

Building on the analysis in the preceding chapter, which explored various enhanced controllers utilizing Metaheuristic algorithms for both single and multi-objective optimization, fuzzy logic-based enhancements, and sliding mode controllers, it becomes evident that while notable performance gains have been realized, persistent issues such as continuous chattering and suboptimal maximum power point tracking (MPPT) remain unresolved challenges. In [10], researchers proposed a novel dual-loop control framework grounded in the frequency separation principle applied to wind turbine dynamics. This framework is specifically tailored for variable-speed wind turbines, with the primary aim of maximizing power generation while minimizing control efforts to alleviate mechanical stress on the drive train. The dual-loop architecture comprises two distinct control loops, each employing a specialized controller to address targeted challenges. The linear-quadratic Gaussian (LQG) controller [118,119] is deployed to mitigate the electromagnetic torque ripple, whereas a classical proportional-integral (PI) controller is utilized to enhance power conversion efficiency. The evaluation of this architecture demonstrated substantial improvements in wind turbine performance, characterized by enhanced power generation efficiency and reduced mechanical stress. These outcomes underscore the efficacy of control strategies based on the frequency separation principle. Nonetheless, further advancements remain achievable by refining the frequency separation methodology and evolving the control framework to attain even higher operational efficiency and reliability for wind turbines. Such progress promises transformative benefits for wind energy producers, addressing pivotal challenges in the renewable energy domain. This chapter introduces three innovative control strategies for wind turbines, all predicated on the frequency separation principle. This principle distinguishes between high-frequency and low-frequency components of wind dynamics, enabling the development of a sophisticated dual-loop control architecture. In the proposed framework, the high-frequency loop integrates various controllers: an LQR controller in the first approach and H∞ controllers in the second and third approaches. The low-frequency loop incorporates a fractional-order proportional-integral (FOPI) controller in the first and second approaches, while the third approach employs a filtered fractional-order proportional-integral (FOPIF) controller [12] optimized using the particle swarm optimization (PSO) algorithm (PSO-FOPIF). The overarching objective of these strategies is to mitigate electromagnetic torque ripple, commonly referred to as the vibration issue, while ensuring precise and efficient MPPT. By achieving these dual objectives, the proposed methodologies enhance the operational lifespan of wind turbines, reduce maintenance costs, and maximize energy yield. These advancements are anticipated to fulfill the expectations of both producers and investors within the renewable energy sector, presenting a significant leap toward addressing critical challenges in wind energy generation and utilization.

IV. 2 Control Problem Formulation

The proposed methodology is rooted in the frequency separation principle, which recognizes that the dynamics of wind energy conversion systems are governed by two distinct spectral ranges associated with wind speed components (I.6). The seasonal component, $\overline{v}$, defines the average operational point of the wind turbine, representing slow, low-frequency dynamics. In contrast, the turbulence component, $\Delta v(t)$, introduces high-frequency variations around this point. This principle advocates for the independent compensation of these two dynamics to enhance system performance. To implement this approach, advanced control strategies have been developed and rigorously evaluated. A Fractional-Order Proportional-Integral (FOPI) controller and a Filtered Fractional-Order Proportional-Integral Tuned by PSO (PSO-FOPIF) controller are designed to leverage the seasonal component. These controllers effectively drive and maintain the system at an operational point aligned with the Optimal Regime Characteristic (ORC). Concurrently, high-performance controllers, such as H∞ and Linear Quadratic Regulator (LQR), are tailored to the turbulence component, optimizing the system's behavior in the vicinity of the linearized operational point.

In summary, the outlined design process encompasses the following key steps:

Step 1. Acquire the wind speed, v, from the anemometer's output signal.

Step 2. Derive the seasonal wind speed, denoted as $\overline{v}$, by applying low-pass filtering to the signal v.

Step 3. Determine the turbulence component of the wind speed as $\Delta v = v - \overline{v}$.

Step 4. Send $\overline{v}$ to the low-frequency loop, detailed in Section IV.3.1, resulting in the steady-state control input, $\overline{T_{em}}$.

Step 5. Send Δv to the high-frequency loop, detailed in Section IV.3.2, generating the dynamic control input, ΔT_{em} .

Step 6. Obtain the total control input (electromagnetic torque), T_{em}, by summing the steady-state component and the dynamic component $T_{em} = \overline{T_{em}} + \Delta T_{em}$

Hence, the wind speed's two components need to operate independently within the two loops depicted in the proposed control structure, as illustrated in Figure IV.1.

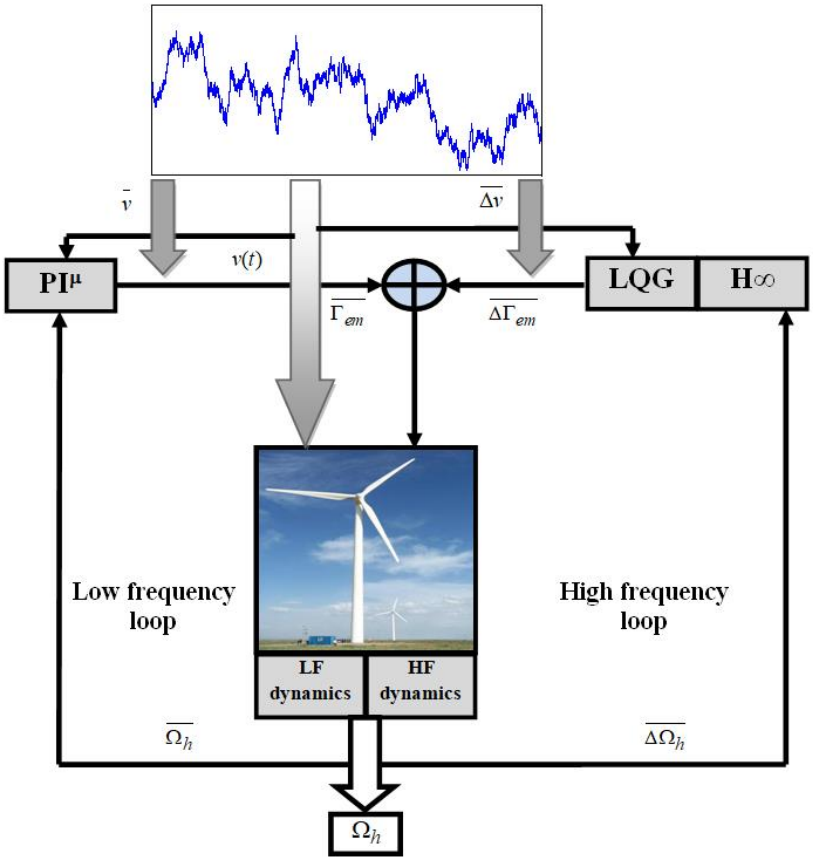


Figure IV. 1 Frequency Separation Principle.

IV. 2.1 Steady-state optimization: tracking the optimal point

An approach focused solely on maximizing energetic efficiency necessitates operating a wind turbine at variable speeds, ensuring that its operating point remains within the optimal regimes characteristic (ORC). This involves maintaining the Power Coefficient (C_P) , dependent on the tip speed ratio (λ) , at its maximum value, corresponding to the optimal value (λ_{opt} as illustrated in Fig. IV.2). Referred to as steady-state optimization, this is achieved by tracking the rotational speed corresponding to λ_{opt} , derived from equation (IV.1).

$$\Omega_{opt} = \frac{\overline{v}.\lambda_{opt}}{R} \qquad \text{(IV.1)}$$

Notably, the seasonal component of the wind speed, denoted as $\overline{v}$, plays a role in this relation, as it governs the slow variation of the operating point.

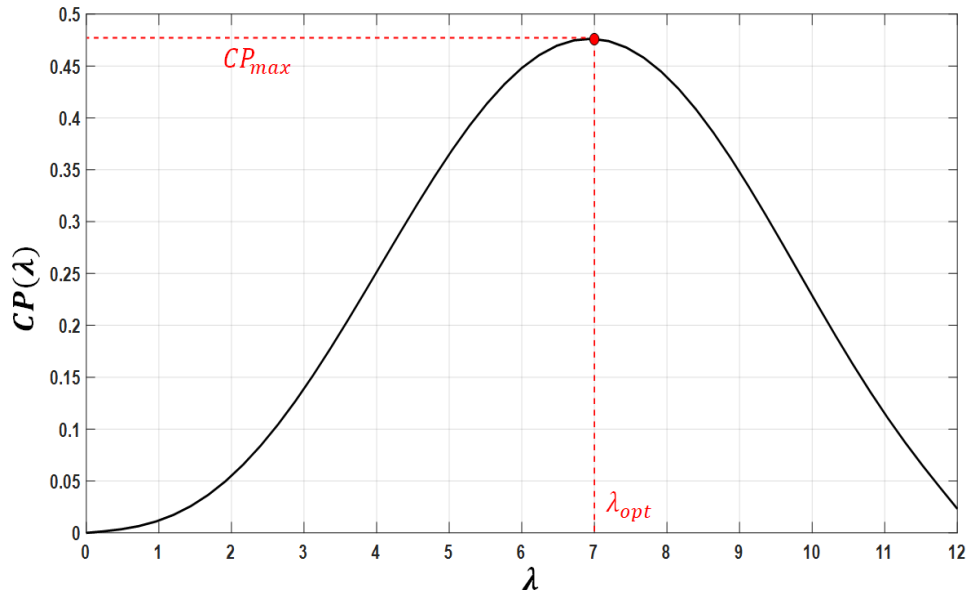


Figure IV. 2 The correlation between the power coefficient and the tip speed.

IV. 3 Optimal Control Structure Design Based on the Frequency Separation Principle

The design of the control structure is elaborated, beginning with its primary representation in Figure IV.1.

IV. 3.1 Crafting the design for the low-frequency loop

The optimization of the steady-state, also known as optimal operating point tracking, is accomplished through a low-frequency loop. This loop is influenced by the seasonal component $\bar{v}(t)$, which sets the operating point. Figure IV.3 illustrates the detailed scheme of this loop, which is further discussed below. The seasonal component, represented as $\bar{v}(t)$, is derived from the wind speed signal, $v(t)$, through the application of a low-pass filter. It is essential that the cutoff frequency of this filter does not surpass the bandwidth of the wind turbine. In [10], the authors used the filter output in relation (IV.1) to calculate the reference of a classical Proportional-Integral (PI) controller. This controller is responsible for generating the constant component of the electromagnetic torque, ensuring the attainment of the optimal "fixed" operating point on the C_P characteristic. Consequently, the parameter γ, which exhibits the highest variance, remains constant, thereby keeping the linear system (I.63) constant with respect to this parameter. In this study, a Fractional-Order Proportional-Integral (FOPI) controller and the Filtered Fractional-Order Proportional-Integral tuned by the Particle Swarm Optimization algorithm (PSO-FOPIF) controller are employed to achieve precise and efficient tracking of the optimal operating point along the C_P characteristic. The FOPI controller is used in the first and second proposed approaches, where it is determined using a pole placement procedure that relies on a

linearized model of the system to address the nonlinearities around a typical operating point. Additionally, the parameters of the PSO-FOPIF controller are tuned using the Particle Swarm Optimization (PSO) algorithm and are applied in the third proposed approach. Empirical methods, such as the Ziegler-Nichols method [120,121], can also be utilized. By leveraging the system's seasonal components, both controllers ensure the system operates consistently within the framework of the Optimal Regime Characteristic (ORC).

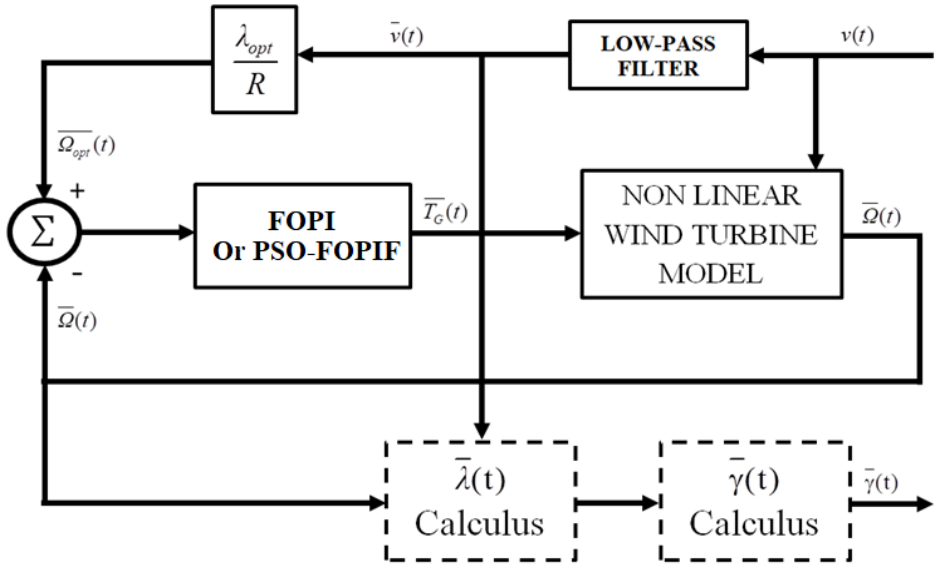
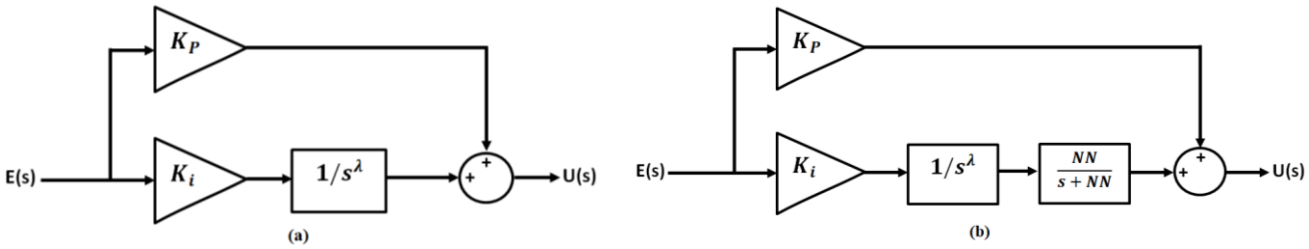


Figure IV. 3 Low-Frequency loop based on FOPI/PSO-FOPIF Controller.

Figure IV.4 illustrates the block diagram of the FOPI and FOPIF controllers, along with their respective transfer functions (IV.2 and IV.3).



$$G_{FOPI}(s)=\frac{U(s)}{E(s)}=K_P+\frac{K_i}{s^{\lambda}} \quad \text{(IV.2)}$$

$$G_{FOPI}(s)=\frac{U(s)}{E(s)}=K_P+\frac{K_i}{s^{\lambda}}.\frac{NN}{s+NN} \quad \text{(IV.3)}$$

Figure IV. 4 Block Diagram of the Controllers and Their Transfer Functions.
a: FOPI, b: FOPIF.

To optimize the performance of the FOPIF controller, the Particle Swarm Optimization (PSO) algorithm [13] is employed to determine the optimal values for the controller parameters $(K_P, K_i, \lambda, \mathrm{NN})$. Figure IV.5 illustrates the block diagram of the PSO-FOPIF controller.

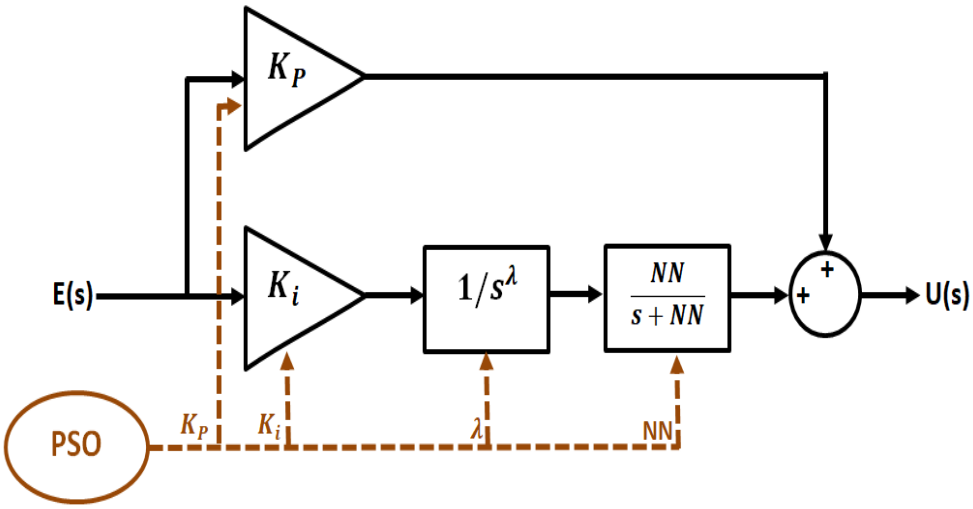


Figure IV. 5 Block Diagram of the PSO-FOPIF Controller.

IV. 3.2 The High-Frequency Loop Design

The high-frequency perturbation component operates within an optimal control loop (see Figure IV.6). In [10], researchers implemented a linear quadratic Gaussian (LQG) controller within this framework. This control loop generates the dynamic component of the electromagnetic torque, $\Delta T_{em}(t)$. In our study, we enhance the performance of this control loop [10] by replacing the LQG controller with an H∞ controller in the second and third proposed approaches, while retaining the LQR controller in the first approach. Our focus is on optimizing the design of the high-frequency loop, presenting the corresponding experimental results. The H∞ control method [11] is a robust control design approach aimed at developing controllers that maintain consistent performance in the presence of uncertainties and disturbances within the system. This methodology prioritizes robustness, ensuring stability and performance despite system uncertainties. Unlike some control design techniques that rely on time-domain analysis, H∞ control is rooted in the frequency domain. Designing an H∞ controller involves addressing a complex optimization problem to identify the controller that minimizes the H∞ norm for the closed-loop system. This task is typically achieved using numerical optimization techniques.

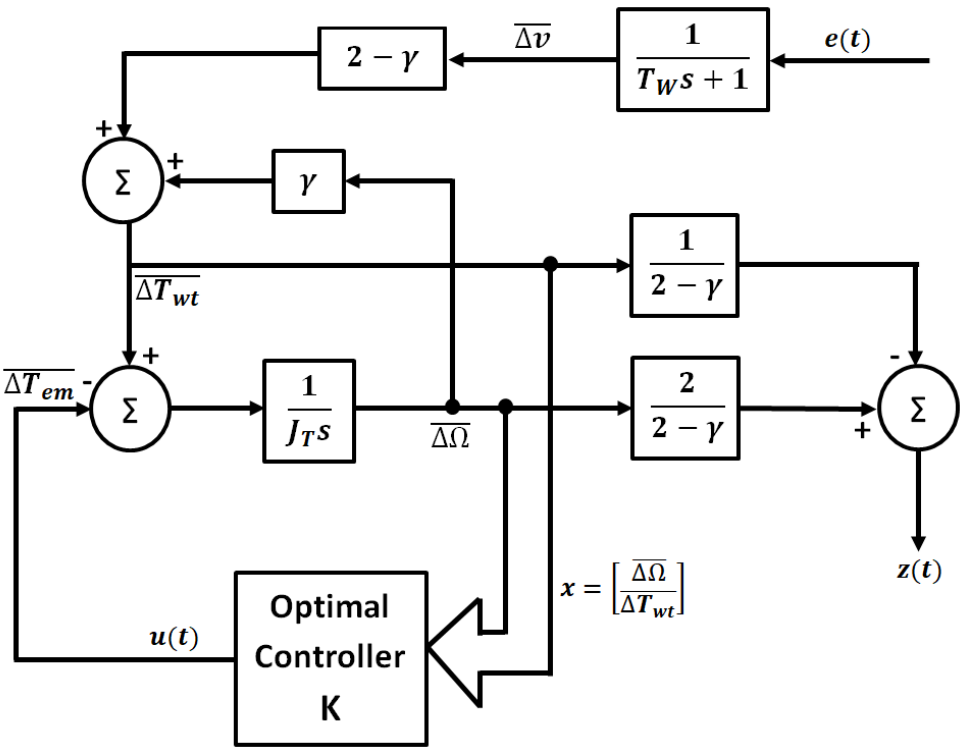


Figure IV. 6 The Optimal High-Frequency Loop.

IV. 3.2.1 The High-Frequency Loop Design based on the LQR Controller Approach

Most control strategies discussed in the literature, including those reviewed in previous chapters, focus exclusively on maximizing energy efficiency, often overlooking the adverse effects on system reliability caused by excessive control input effort. Despite its critical significance, the reliability aspect has only recently gained attention in the context of wind energy conversion system (WECS) control. Mechanical fatigue in the transmission system can be mitigated by minimizing the torque variation of the generator, $\Delta T_{em}(t)$,as highlighted by [122] and further elaborated by [52]. Leveraging the linear behavior of the system model near the optimal operating point, [52] formulated a joint optimization criterion to balance the competing objectives of maximizing energy conversion and minimizing torque fluctuations.

$$I = \underbrace{E\left\{\alpha(\lambda(t)-\lambda_{opt})^2\right\}}_{I_1} + \underbrace{E\left\{\Delta\Gamma_{em}^2(t)\right\}}_{I_2} \qquad \text{(IV.4)}$$

Here, $E\{.\}$ represents the statistical expectation operator. Consequently, the optimization problem is classified as a Linear Quadratic (LQ) formulation, as described by [96]. Operating around the optimal regime is achieved by minimizing only the first term of Equation (IV.4), I_1 , which prioritizes energy efficiency. However, this approach comes at the cost of significant torque variations, represented by I_2 . To balance these conflicting requirements, a positive weighting coefficient, α , is introduced, enabling adjustment of the trade-off between energy efficiency and system reliability.

IV. 3.2.1.1 Dynamic optimization—associated LQ problem

Due to the turbine's high inertia compared to wind speed variations, a control strategy solely based on steady-state optimization can lead to significant torque fluctuations at the generator shaft, potentially causing damage to mechanical subsystems, such as the gearbox. To address this issue, reliability considerations necessitate incorporating an optimization criterion represented by Equation (IV.4), where the second term emphasizes minimizing torque control variations. This approach, known as dynamic optimization, is formulated as a Linear Quadratic (LQ) optimization problem, as detailed below. As indicated by the performance index in Equation (IV.4), and considering the defined state model, the optimization problem involves balancing the reduction of variations in both the output and control input variables. The first term is expressed as a quadratic function of the state variable:

$$\begin{aligned} I_1 &= E\left\{\alpha\overline{\Delta\lambda}^2(t)\right\} \to \min \Leftrightarrow I_1 \\ I_1 &= E\left\{x^T(t)C_\alpha^T C_\alpha x(t)\right\} \to \min, \end{aligned} \tag{IV.5}$$

Where $C_\alpha = \sqrt{\alpha}C$.

The reliability constraint is solved by the control input variations' minimization (maximization of energy with minimization of control input—MEmci). The second component is defined as

$$I_2 = E\left\{\overline{\Delta T_{em}}^2(t)\right\} = E\left\{u^T(t)Nu(t)\right\} \to \min, \tag{IV.6}$$

Where $N = 1$ (the vector notation for $u(t)$ is used for formal conformity). Therefore, the global index is

$$I = E\left\{x^T(t)\left(C_\alpha^T C_\alpha\right)x(t) + u^T(t)Nu(t)\right\} \to \min. \tag{IV.7}$$

IV. 3.2.1.2 LQR design

The high-frequency turbulence component operates within an optimal control loop, as illustrated in Figure IV.6, governed by the performance criterion outlined in Equation (IV.7). This control loop generates the dynamic component of the electromagnetic torque, denoted as $\Delta T_{em}(t)$. This section focuses on the optimal design of the high-frequency control loop and its corresponding experimental validation. The optimization criterion expressed in Equation (IV.7) represents a Linear Quadratic (LQ) invariant stochastic optimization problem. The existence and uniqueness of the solution are ensured by a well-established set of conditions, which rely on specific structural properties of the controlled system [96]. In this context, these conditions are satisfied; however, their detailed justifications are omitted here for brevity. The unique optimal control input that minimizes the

criterion defined in Equation (IV.7) for the dynamic system described by Equations (I.63) and (I.65) is a full-state feedback control law of the form $u(t) = -Kx(t)$, where the feedback matrix K is determined as follows:

$$K = N^{-1}B^{T}S \tag{IV.8}$$

Where S is the unique, symmetric, and positive semi-defined matrix satisfying the Riccati algebraic matrix equation:

$$SA + A^{T}S + C_{\alpha}^{T}C_{\alpha} - SBN^{-1}B^{T}S = 0 \tag{IV.9}$$

The asymptotic stability of the closed-loop system—whose structure is presented in Figure IV.6 —described by

$$\dot{x}(t) = (A - BK)x(t) \tag{IV.10}$$

, is guaranteed.

Equation (IV.11) presents the values of matrices A and B.

$$A = \begin{bmatrix} 0 & 1.775568181818182 \\ -0,0466666044445274 & -1,82223478626271 \end{bmatrix}, B = \begin{bmatrix} -1,77556818181818 \\ 1,77556818181818 \end{bmatrix} \tag{IV.11}$$

As shown in Equation (IV.12), the values of the controller matrix K are:

$$K = \begin{bmatrix} 0,00400516179779231 & 0,736055969366667 \end{bmatrix} \tag{IV.12}$$

IV. 3.2.2 The High-Frequency Loop Design based on the H∞ Controller Approach

To address the challenges posed by the high inertia of wind turbines relative to wind speed variations, solely relying on steady-state optimization can lead to substantial torque fluctuations at the generator shaft, risking damage to mechanical subsystems, such as the gearbox. To enhance reliability, a dynamic optimization strategy becomes essential, one that simultaneously minimizes torque oscillations and ensures robust performance under disturbances. This requirement leads to the formulation of an H∞ control problem.

The control objective is formalized using an H∞ performance index, which aims to minimize the worst-case impact of disturbances on system performance. For a given state-space representation of the wind energy conversion system,

$$\begin{aligned}\dot{x}(t) &= Ax(t) + Bu(t) + Ew(t)\\ z(t) &= Cx(t) + Du(t)\end{aligned} \tag{IV.13}$$

Where:

$x(t)$ represents the state vector,

$u(t)$ is the control input,

$w(t)$ is the external disturbance,

$z(t)$ is the regulated output,

A, B, E, C *and* D are system matrices.

The H∞ control problem involves designing a control law:

$$u(t) = -Kx(t) \tag{IV.14}$$

such that the closed-loop system satisfies the performance criterion:

$$\left\| T_{w\to z}(s) \right\|_{\infty} < \gamma \tag{IV.15}$$

Where $T_{w\to z}(s)$ is the transfer function from the disturbance $w(t)$ to the regulated output $z(t)$, and γ is the performance bound. The H∞ norm of the transfer function is given by:

$$\left\| T_{w\to z}(s) \right\|_{\infty} = \sup_{\omega} \sigma_{max}\left(T_{w\to z}(j\omega) \right) \tag{IV.16}$$

Where σ_{max} denotes the maximum singular value, and $j\omega$ represents the frequency domain variable.

The optimization criterion is often expressed in a quadratic form. For example, the performance index J can be written as:

$$J = \int_0^{\infty} \left(x(t)^T Qx(t) + u(t)^T Ru(t) \right) dt \tag{IV.17}$$

Where Q and R are weighting matrices that penalize state deviations and control efforts, respectively. The inclusion of the H∞ norm constraint ensures robustness by minimizing the system's sensitivity to disturbances while balancing performance and control effort.

The resulting control gain K is obtained by solving a set of algebraic Riccati equations (AREs) derived from the system dynamics and the H∞ norm constraint. These equations ensure the stability and robustness of the closed-loop system:

$$A^T P + PA - \left(PB + C^T R^{-1} C\right) P + Q = 0 \tag{IV.18}$$

By applying the H∞ controller, the wind energy conversion system achieves a robust trade-off between maximizing energy capture, reducing mechanical stresses, and ensuring reliable operation under uncertain and varying environmental conditions.

IV. 3.2.2.1 H∞ design

The first step in controller design is to augment the system into a generalized plant $P(s)$, which combines the dynamics of the physical system, disturbances, weighting functions, and control objectives. This plant has inputs $[w;u]$ (disturbances and control) and outputs $[z;y]$ (regulated outputs and measured outputs):

$$\begin{aligned} \dot{x}(t) &= Ax(t) + B_1 w(t) + B_2 u(t) \\ z(t) &= C_1 x(t) + D_{11} w(t) + D_{12} u(t) \\ y(t) &= C_2 x(t) + D_{21} w(t) + D_{22} u(t) \end{aligned} \tag{IV.19}$$

Where $y(t)$ is the measured output used for feedback.

The wind turbine control system must mitigate excessive mechanical loads to preserve the durability and longevity of its components.

The general configuration for H∞ controller design is depicted in Figure IV.7 [123, 124], where $P(s)$ represents the augmented process and $K(s)$ denotes the controller.

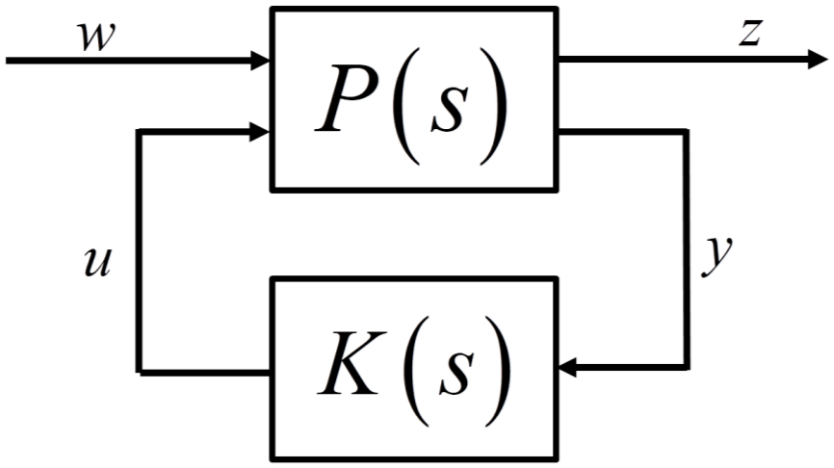


Figure IV. 7 General control configuration.

In the synthesis of robust controllers, weighting functions are applied to specific quantities that characterize the control system's behavior, namely the error e, the control input u, and the system output y. These weighting functions are typically associated with the sensitivity functions $\mathrm{S}(s)$, $\mathrm{R}(s)$, and $\mathrm{T}(s)$ [123,124].

The cost function, which characterizes the transfer from inputs w to outputs z, is represented as a linear fractional transformation $F_l(P,K)$:

$$T_{w\to z} = F_l(P,K) = P_{11} + P_{12}K\left(I - P_{22}K\right)^{-1}P_{21} \tag{IV.20}$$

The augmented process can also be expressed through input-state-output equations as presented in (IV.17).

If the nominal system $H(s)$ is defined by equations (I.63) and (I.65), the augmented process can be represented through a partitioned structure:

$$P(s) = \begin{bmatrix} P_{11}(s) & P_{12}(s) \\ P_{21}(s) & P_{22}(s) \end{bmatrix} = \begin{bmatrix} A & B_1 & B_2 \\ C_1 & D_{11} & D_{12} \\ C_2 & D_{21} & D_{22} \end{bmatrix} \tag{IV.21}$$

The synthesis problem for the H∞ controller is addressed by determining a controller, represented by the transfer matrix $K(s)$, that satisfies the control law outlined in equation (IV.14), given the augmented process. such that the H∞ norm of the cost function is minimized $min\left\|T_{w\to z}(s)\right\|_\infty$.

The H∞ norm of a system $H(s)$ is defined based on the singular values $\sigma_i\left(H(j\omega)\right)$, where $i = 1,2,\ldots,n$:

$$\|H\|_{\infty} = \sup_{\omega \in \mathrm{R}} \sigma_{max}\left(H(j\omega)\right) \tag{IV.22}$$

The performances of a closed-loop system can be specified by the following equations:

$$\left|S(j\omega)\right| \geq \varepsilon_1, \forall \omega \leq \omega_b ; \left|S(j\omega)\right| \leq M_s, \ \forall \omega > \omega_b \tag{IV.23}$$

Where ω_b is the bandwidth frequency and M_s is the peak limit of the sensitivity function.

The weighting function $W_1(s)$ is defined as:

$$W_1(s) = \frac{\frac{s}{M_s} + \omega_b}{s + \omega_b \varepsilon_1} \tag{IV.24}$$

In case of MIMO (Multiple Input Multiple Output) systems, the performance specifications are described by:

$$\sigma_i\left(S(j\omega)\right) \leq \sigma_{max}\left(S(j\omega)\right) \leq \left|W_1^{-1}(j\omega)\right| \tag{IV.25}$$

For Monovariable SISO (Single Input Single Output) systems, the previous equation becomes:

$$\left|S(j\omega)\right| \leq \left|W_1^{-1}(j\omega)\right| ; \left\|W_1^{-1}(j\omega) S(j\omega)\right\|_{\infty} \leq 1 \tag{IV.26}$$

Robust stability conditions can be expressed in the frequency range using the weighting functions $W_2(s), W_3(s)$ and the sensitivity matrices $\mathrm{R}(s)$, and $\mathrm{T}(s)$:

$$\sigma_{max}\left(R(j\omega)\right) \leq \left|W_2^{-1}(j\omega)\right| ; \sigma_{max}\left(T(j\omega)\right) \leq \left|W_3^{-1}(j\omega)\right| \tag{IV.27}$$

In case of additive disturbances $W_2(j\omega)$ acts as a filter on $\mathrm{R}(j\omega)$ and penalizes the command u. In case of multiplicative disturbances $W_3(j\omega)$ weights the complementary sensitivity $\mathrm{T}(j\omega)$, thus penalizing the output of the system.

The weighting functions $W_2(s)$ and $W_3(s)$ are defined by:

$$W_2(s) = \frac{s + \frac{\omega_{b0}}{M_u}}{\varepsilon_2 s + \omega_{b0}} ; W_3(s) = \frac{s + \frac{\omega_{c0}}{M_{\mathrm{T}}}}{\varepsilon_3 s + \omega_{c0}} \tag{IV.28}$$

With ω_{c0} the controller bandwidth, ω_{b0} the closed-loop bandwidth, M_u is the peak of $R(j\omega)$, M_T is the peak of $T(j\omega)$, and $\varepsilon_2, \varepsilon_3$ small values.

The H∞ controller can be obtained by using the Riccati equation approach or the LMIs (linear matrix inequalities) approach [123]. The optimal control problem is to check if a solution exists from the Riccati approach given in [125].

The process control system $H_P(s)$ weighted by the transfer function $W_1(s), W_2(s), W_3(s)$ is considered. The H∞ problem can be obtained by the *hinfsyn* method [126], using the following MATLAB commands:

$$\begin{aligned} &P = augw(H_P, W_1, W_2, W_3) \\ &[K, CL, GAM, INFO] = hinfsyn(P, nmeas, nu) \end{aligned} \tag{IV.29}$$

The sensitivity matrices satisfy the relations:

$$\begin{aligned} &\sigma_{max}\left(S(j\omega)\right) \le \gamma \sigma_{max}\left(W_1^{-1}(j\omega)\right) \\ &\sigma_{max}\left(T(j\omega)\right) \le \sigma_{max}\left(W_3^{-1}(j\omega)\right) \end{aligned} \tag{IV.30}$$

Equation (IV.31) presents the plant matrices used in the proposed controllers:

$$P = \begin{bmatrix} P_{11} & P_{12} \\ P_{21} & P_{22} \end{bmatrix} = \begin{bmatrix} A & B_1 & B_2 \\ C_1 & D_{11} & D_{12} \\ C_2 & D_{21} & D_{22} \end{bmatrix} \tag{IV.31}$$

With:

$$P_{11} = P_A = \begin{bmatrix} -10 & 0,443892045454545 & 0,0828597380051971 \\ 0 & -1,82223478626271 & -0,331438952020791 \\ 0 & 0,250 & 0 \end{bmatrix}, \quad P_{12} = P_B = \begin{bmatrix} 0,5 & 0 \\ 0 & 2 \\ 0 & 0 \end{bmatrix},$$

$$P_{21} = P_C = \begin{bmatrix} 0,461538461538461 & 0,0682910839160839 & 0,0127476520007996 \\ 0 & 0 & 0 \\ 0 & 0,887784090909091 & 0,165719476010394 \end{bmatrix},$$

$$P_{22} = P_D = \begin{bmatrix} 0,0769230769230769 & 0 \\ 0 & 1 \\ 1 & 0 \end{bmatrix}.$$

The controller, represented by the transfer matrix K(s) in Equation (IV.32), is designed to satisfy the control law given in Equation (IV.14).

$$K(s) = \left[\frac{\left(-5.309.10^5\right) s^2 - \left(9.675.10^5\right) s - 4.399.10^4}{s^3 + \left(3.143.10^5\right) s^2 + \left(3.157.10^6\right) s + 1.466.10^5} \right] \quad \text{(IV.32)}$$

IV. 4 Results and Discussion

As in the experiments detailed in previous chapters, simulations were conducted to assess the efficacy of control methods grounded in the frequency separation principle. These simulations were implemented in the MATLAB/Simulink environment, utilizing the wind energy conversion system along with the proposed control approach. For reference, the system parameters are summarized in Table B.1 of Appendix B. The evaluation employed two distinct wind profiles—representing low and high turbulence—generated based on the von Karman spectrum in compliance with International Electrotechnical Commission (IEC) standards. Additionally, the findings were validated using a real wind model captured with an anemometer in a controlled laboratory setup. To further examine the robustness of the proposed controllers, their performance was analyzed under varying internal system parameters, specifically by altering the total inertia of the high-speed shaft within the time interval [45s - 50s]. This investigation aimed to identify potential deviations from the results obtained under constant high-speed shaft inertia conditions.

IV. 4.1 Low turbulence stochastic wind speed

To enable a precise comparative analysis of the performance of FOPI and H∞ controllers based on the frequency separation principle, as well as FOPIF and H∞ controllers, FOPI and LQR controllers employing the same principle, and the Standard On-Off control method, a low-turbulence stochastic wind model is utilized. This wind model, depicted in Figure IV.8, was proposed by C. Nichita [19]. It generates a temporal wind profile by initially subjecting white noise to a transfer function derived from the Von Karman non-rational filter. The parameters of this filter are specifically calibrated to reflect the unique characteristics of the site and the associated wind dynamics, as illustrated in Figure IV.8. Notably, this model, introduced by C. Nichita for simulation purposes, is comprehensively explained in Chapter I, Section 3.1.

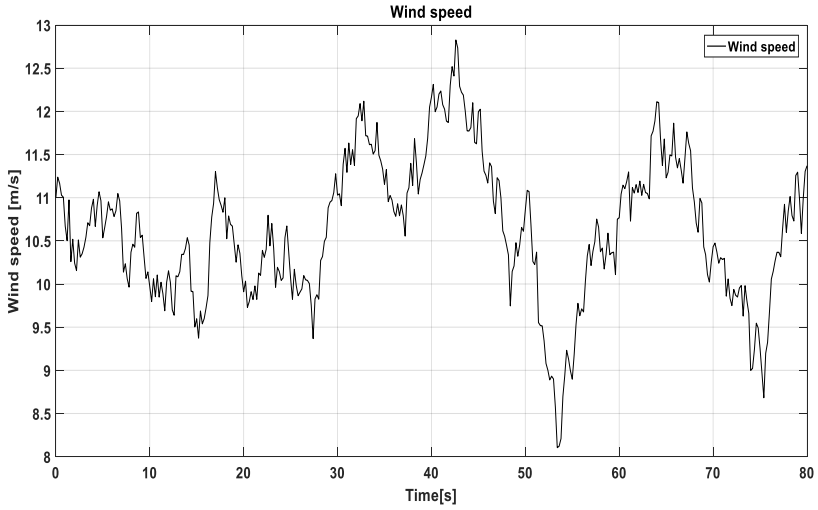


Figure IV. 8 Low turbulence stochastic wind speed.

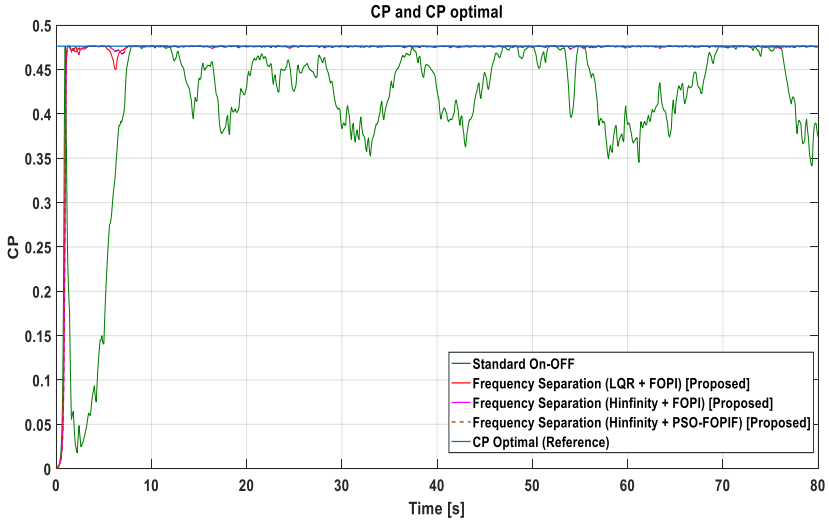


Figure IV. 9 Power Coefficient (CP).

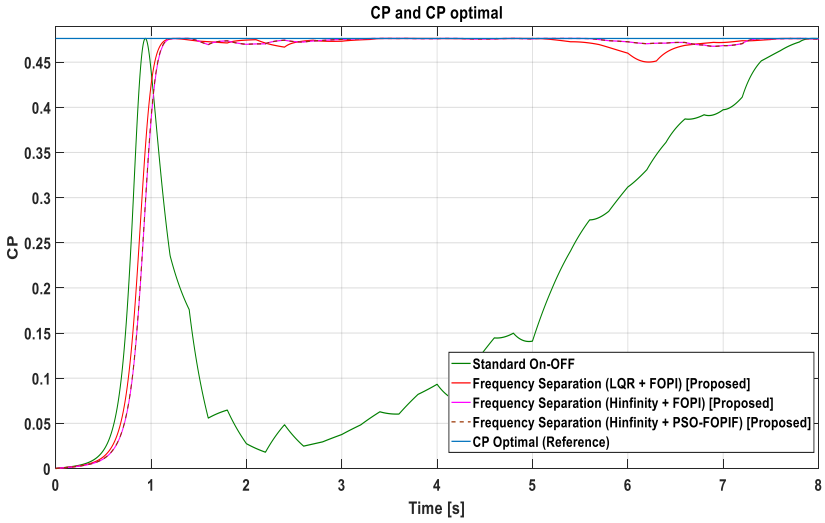


Figure IV. 10 Power Coefficient (CP) Zoom [0s-8s].

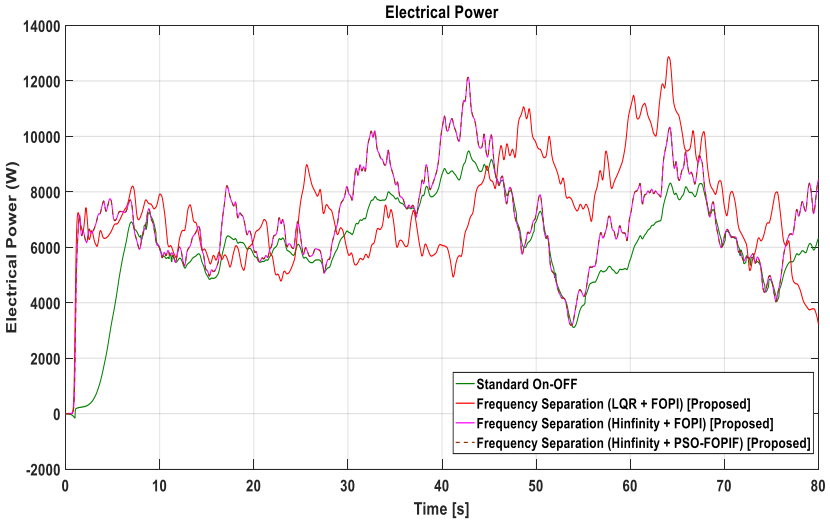


Figure IV. 11 Electrical Power.

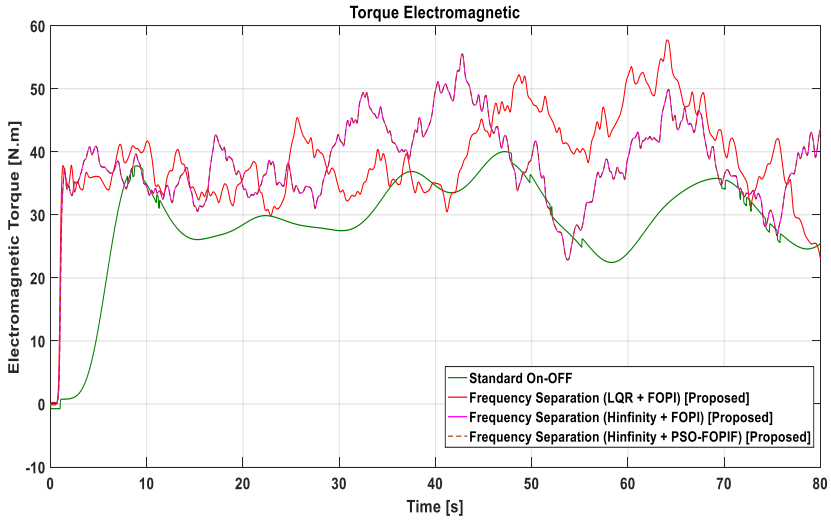


Figure IV. 12 Electromagnetic Torque.

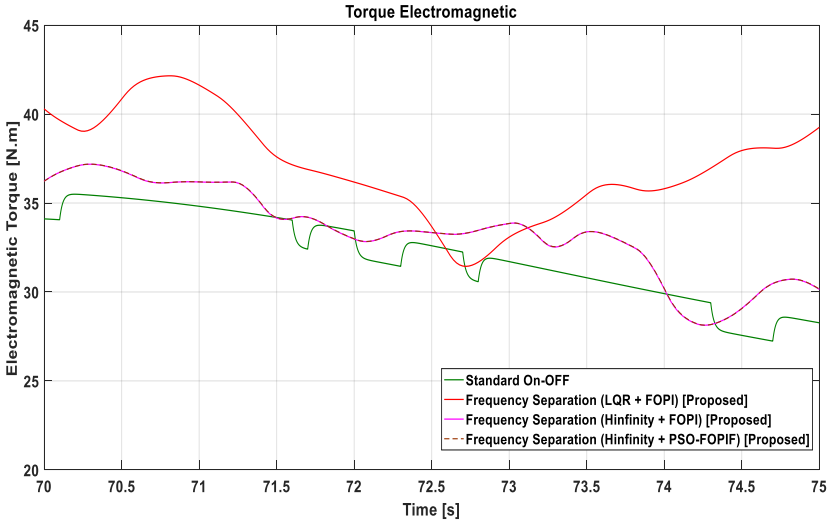


Figure IV. 13 Electromagnetic Torque Zoom [70s-75s].

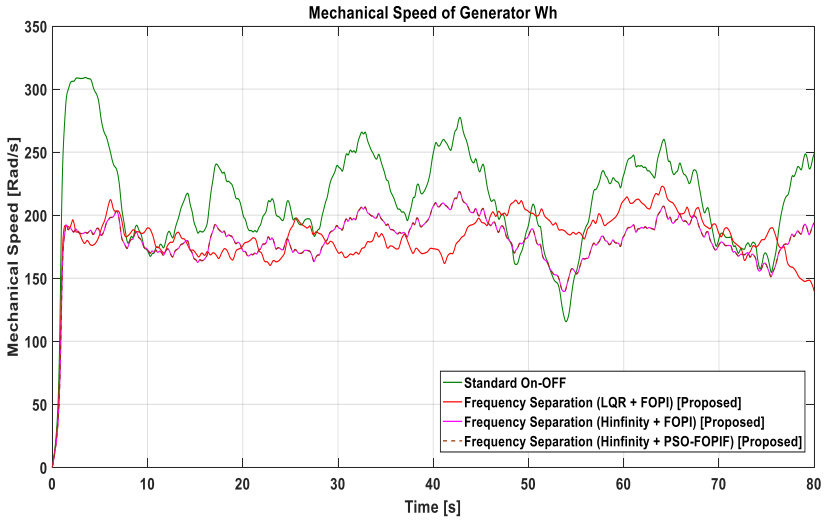


Figure IV. 14 Mechanical Speed of Generator ω_h .

A comparative analysis of the results obtained using a low-turbulence stochastic wind speed model (Figure IV.8) underscores the superior performance of the proposed control structures based on the frequency separation principle when compared to the standard on-off controller. These advanced structures, designed with various controllers, demonstrated consistent and reliable maximum power point tracking (MPPT) throughout the operational period. In contrast, the standard on-off controller struggled to maintain stable MPPT tracking. The evaluation of the power coefficient curve (Figure IV.9 and Figure IV.10) further validate these findings. Notably, the proposed control structure integrating H∞ and PSO-FOPIF controllers achieved slightly better performance than the configurations utilizing H∞ and FOPI controllers or LQR and FOPI controllers, as illustrated in Figure IV.8. This marginal yet critical improvement highlights the efficiency of the H∞ + PSO-FOPIF combination in optimizing energy capture. Figure IV.11 corroborates this by confirming the ability of the proposed controllers to generate maximum electrical power more effectively than the standard On-Off controller. Further insights from Figures IV.12, IV.13, and IV.14 reveal the robustness of the proposed control structures in addressing significant operational challenges. These controllers successfully mitigated electromagnetic torque ripple issues (Figures IV.12 and IV.13) and maintained generator speed stability within the designated range (Figure IV.14). By minimizing oscillations that could otherwise degrade the lifespan of wind energy conversion systems, the proposed controllers contribute to enhanced system durability. Conversely, the Standard On-Off controller failed to eliminate electromagnetic torque ripples (Figure IV.13) and was unable to stabilize the generator's mechanical speed (Figure IV.14). The results obtained from the low-turbulence stochastic wind model unequivocally demonstrate that the proposed control strategies not only achieve and sustain maximum power output but also extend the operational life of wind turbines. This dual advantage underscores the superiority of the proposed control structures, particularly under variable wind speed conditions, and solidifies their potential as a more effective alternative to conventional approaches.

To identify the most efficient control strategies under low-turbulence wind conditions, a comparative analysis has been conducted and summarized in Table IV.1. For enhanced visualization, the values illustrate key performance metrics, including the maximum electromagnetic torque $\left(T_{em_{\max}}\right)$, the standard deviation of the electromagnetic torque **(Std)**, the maximum power coefficient $\left(CP_{\max}\right)$, and energy efficiency $\eta_E\,(\%)$.

It is worth noting that energy efficiency η_E is expressed by the equation (IV.33):

$$\eta_E = \frac{P_{Capt}}{P_{opt}} = \frac{\int_{t0}^{tf} 0.5\pi R^2 v^3(t) CP(\lambda)\,dt}{\int_{t0}^{tf} 0.5\pi R^2 v^3(t) CP(\lambda_{opt})\,dt} \tag{IV.33}$$

Criteria / Method	$T_{em_{\max}}$	Std (T_{em})	$CP_{\max}$	Energy Efficiency $\eta_E\,(\%)$
Standard On-Off controller	40.0252	8.1894	0.4763	85.01
LQR + FOPI	57.7315	8.0814	0.4763	98.33
H∞ + FOPI	55.4998	7.6123	0.4763	98.19
H∞ + PSO-FOPIF	55.5040	7.6354	0.4763	98.16

Table IV. 1 Comparison of Different Control Strategies Under Low-Turbulence Wind Conditions.

The standard on-off controller exhibits the lowest maximum electromagnetic torque $\left(T_{em_{\max}}\right)$ (40.0252), indicating reduced torque stress on the system. In contrast, LQR + FOPI generates the highest maximum electromagnetic torque (57.7315), followed by H∞ + FOPI (55.4998) and H∞ + PSO-FOPIF (55.5040). All proposed controllers achieve a lower standard deviation of electromagnetic torque (Std) compared to the standard on-off controller (8.1894), with H∞ + FOPI achieving the lowest torque ripple (7.6123), indicating superior torque smoothness. These results demonstrate that the proposed controllers enhance dynamic stability and ensure smoother torque variations—key factors in reducing mechanical wear and extending system lifespan. Despite variations in electromagnetic torque and its standard deviation, all controllers achieve the same maximum power coefficient $\left(CP_{\max}\right)$ of 0.4763, This indicates that all controllers successfully tracked the maximum power value at a given moment in this particular scenario. Furthermore, an analysis of energy efficiency $\eta_E\,(\%)$ reveals that the proposed controllers achieve power extraction efficiencies exceeding 98%, significantly outperforming the standard on-off controller, which attains only 85%. These findings underscore the advantages of the proposed controllers in improving both energy efficiency and torque smoothness over the standard on-off approach.

IV. 4.2 High turbulence stochastic wind speed

We employed a high-turbulence wind model to simulate the proposed controllers, evaluating its robustness under different conditions (Figure IV.15).

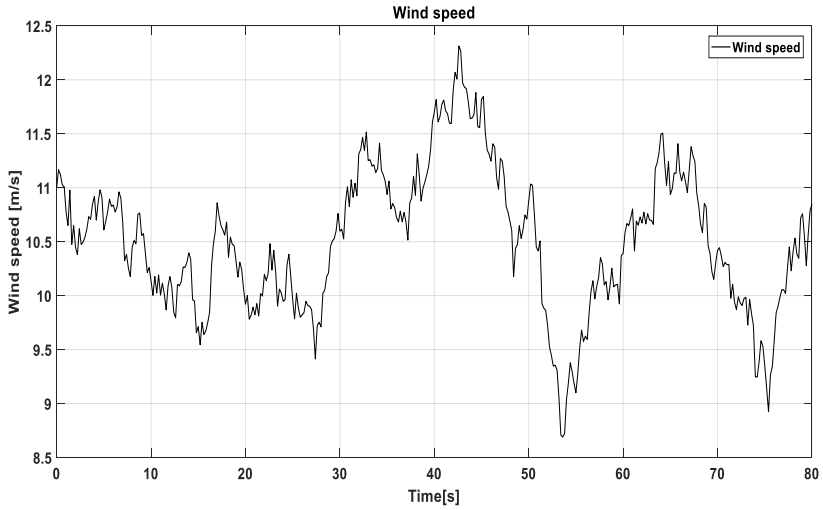


Figure IV. 15 High turbulence stochastic wind speed.

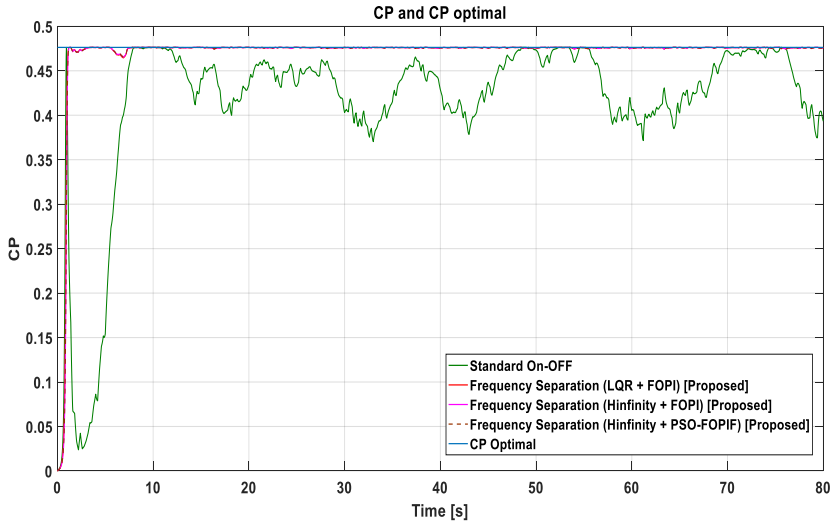


Figure IV. 16 Power Coefficient (CP).

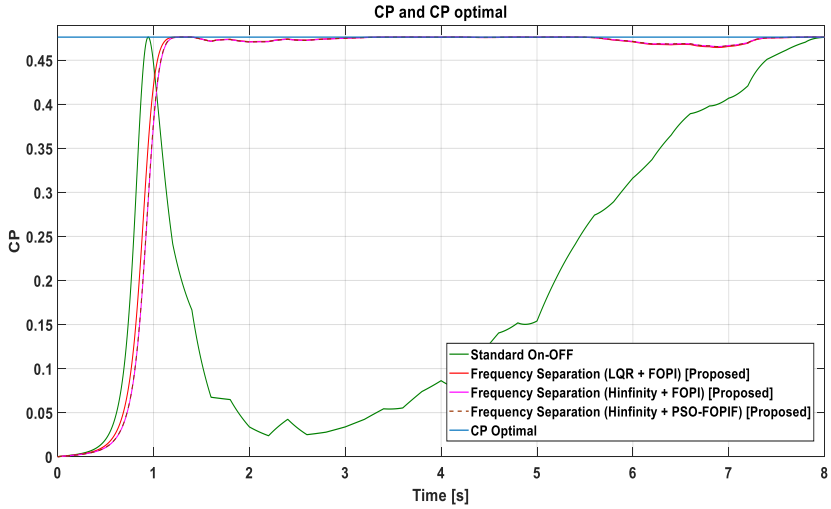


Figure IV. 17 Power coefficient (CP) Zoom [0s-8s].

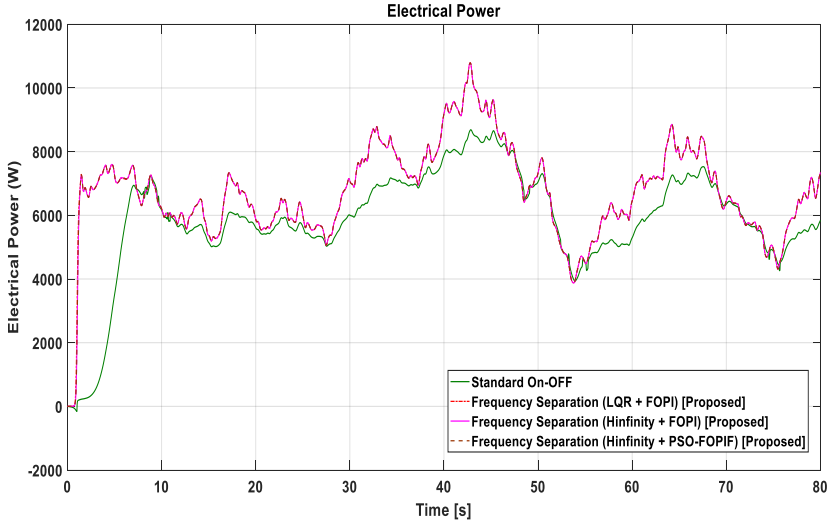


Figure IV. 18 Electrical Power.

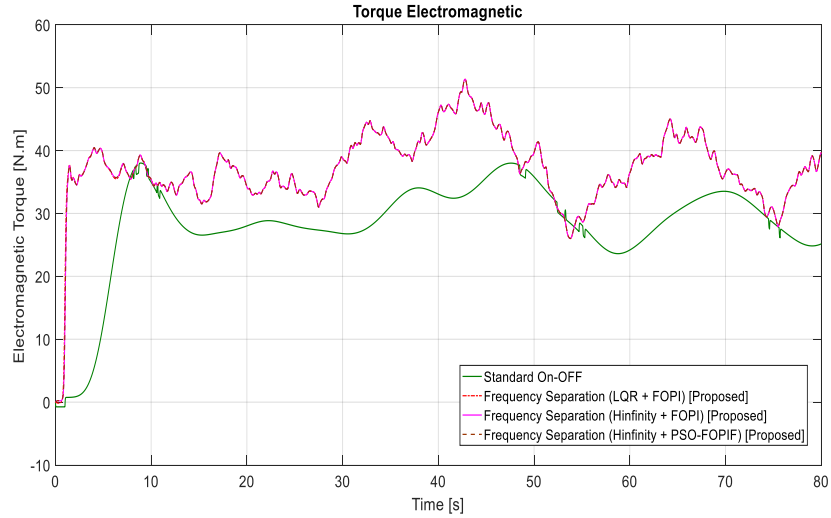


Figure IV. 19 Electromagnetic Torque.

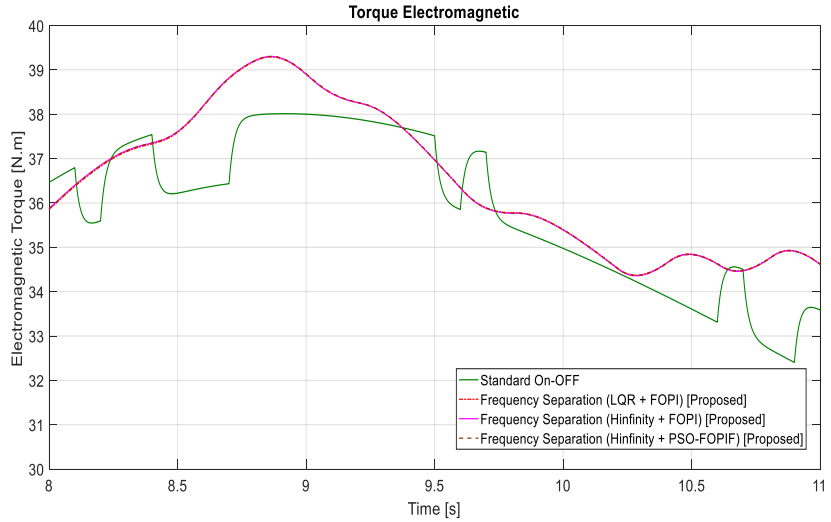


Figure IV. 20 Electromagnetic Torque Zoom [8s-11s].

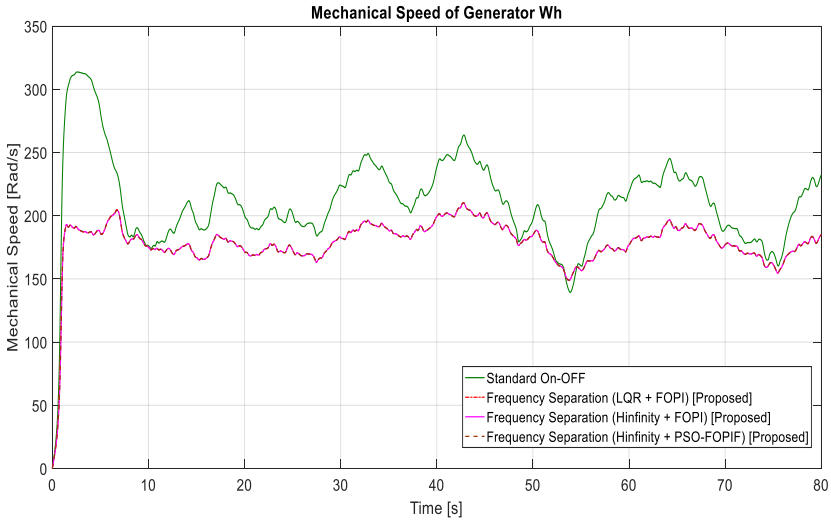


Figure IV. 21 Mechanical Speed of Generator ω_h .

The comparative analysis, based on results obtained using a high-turbulence stochastic wind speed model (Figure IV.15), highlights the superior performance of advanced control structures built on the frequency separation principle compared to the standard on-off controller. The proposed controllers demonstrated reliable and stable maximum power point tracking (MPPT), unlike the On-Off controller, which failed to sustain MPPT under similar conditions. The Power Coefficient curve (Figure IV.16) confirm the efficiency of these controllers. Among them, the configuration combining the frequency separation principle with H∞ and PSO-FOPIF controllers slightly outperformed others, including H∞ with FOPI and LQR with FOPI controllers, as shown in Figure IV.17. This underscores the effectiveness of the H∞ +PSO-FOPIF combination in maximizing energy capture. Furthermore, Figure IV.18 demonstrates that the proposed controllers consistently produced higher electrical power compared to the Standard On-Off controller. Figures IV.19, IV.20, and IV.21 further illustrate the advantages of the proposed control structures. They effectively mitigated electromagnetic torque ripple (Figures IV.19 and IV.20) and maintained generator speed stability within a defined range (Figure

IV.21). These improvements reduced operational oscillations that can compromise the lifespan of wind turbines. Conversely, the Standard On-Off controller failed to eliminate torque ripple (Figure IV.20) and could not stabilize the generator's speed within acceptable limits (Figure IV.21). This analysis unequivocally demonstrates the ability of the proposed controllers to achieve and sustain maximum power output while extending turbine service life. Tested under both low- and high-turbulence conditions, the controllers exhibited robustness and efficiency across variable wind profiles, as evidenced by the results, reaffirming their superiority over conventional methods.

To determine the most efficient control strategies under high-turbulence wind conditions, a comparative analysis has been conducted and summarized in Table IV.2. For better visualization, the Values depict key performance metrics, including the maximum electromagnetic torque $\left(T_{em_{\max}}\right)$, the standard deviation of the electromagnetic torque **(Std),** the maximum power coefficient $\left(CP_{\max}\right)$, and energy efficiency $\eta_E\,(\%)$.

Criteria / Method	$T_{em_{\max}}$	Std (T_{em})	$CP_{\max}$	Energy Efficiency $\eta_E\,(\%)$
Standard On-Off controller	38.0120	7.7163	0.4763	85.88
LQR + FOPI	51.3290	6.5899	0.4763	98.18
H∞ + FOPI	51.3300	6.6492	0.4763	98.12
H∞ + PSO-FOPIF	51.3356	6.6503	0.4763	98.12

Table IV. 2 Comparison of Different Control Strategies Under High-Turbulence Wind Conditions.

The proposed controllers demonstrate a significant improvement in both energy efficiency and torque smoothness compared to the standard on-off controller. While all controllers achieve the same maximum power coefficient $\left(CP_{\max}\right)$ of 0.4763—confirming their ability to track the optimal power extraction point under the given conditions—their impact on electromagnetic torque and energy efficiency varies. In terms of torque performance, the standard on-off controller exhibits the lowest maximum electromagnetic torque $\left(T_{em_{\max}}\right)$ (38.0120), indicating reduced torque stress on the system. However, it also has the highest standard deviation of electromagnetic torque **(Std)** (7.7163), leading to increased torque ripple. Conversely, the proposed controllers yield higher maximum electromagnetic torque values, with H∞ + PSO-FOPIF reaching the highest (51.3356), followed by H∞ + FOPI (51.3300) and LQR + FOPI (51.3290). Despite these higher torque peaks, all proposed controllers achieve smoother torque variations, with LQR + FOPI exhibiting the lowest torque ripple (6.5899). This enhancement in torque smoothness contributes to greater dynamic stability, reduced

mechanical wear, and an extended system lifespan. Furthermore, an analysis of energy efficiency reveals that the proposed controllers significantly outperform the standard on-off approach. While the standard controller achieves an efficiency $\eta_E\,(\%)$ of only 85.88%, the proposed controllers surpass 98%, ensuring superior power extraction. These results underscore the advantages of the proposed control strategies in optimizing both energy efficiency and system durability over conventional methods.

IV. 4.3 Real Wind Model (Natural Wind Intensity Curve)

To validate the performance of the proposed controllers in a practical setting, a real wind model (Figure IV.23) was employed, measured using an anemometer in a controlled laboratory environment. (Figure IV.22) illustrates a segment of our laboratory experiment, where an anemometer is positioned opposite a suitable laboratory antenna outlet. The recorded data allowed us to derive the natural wind intensity curve, which was utilized in our current investigation. It's important to mention that the experiment to measure natural wind intensity was conducted at the Renewable Energy Laboratory within the College of Engineering at the University of Sharjah in the United Arab Emirates.



Figure IV. 22 Extracting the natural wind intensity curve using an anemometer [The Renewable Energy Laboratory at the College of Engineering at the University of Sharjah].

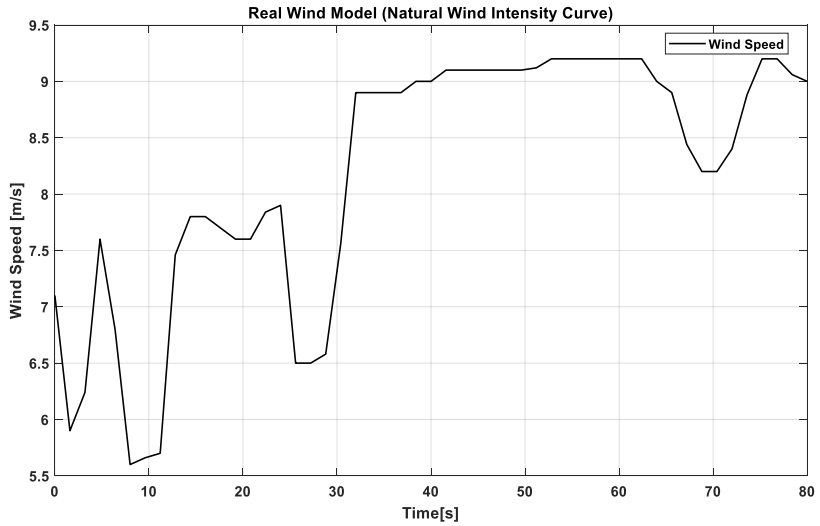


Figure IV. 23 Real Wind Model (Natural Wind Intensity Curve).

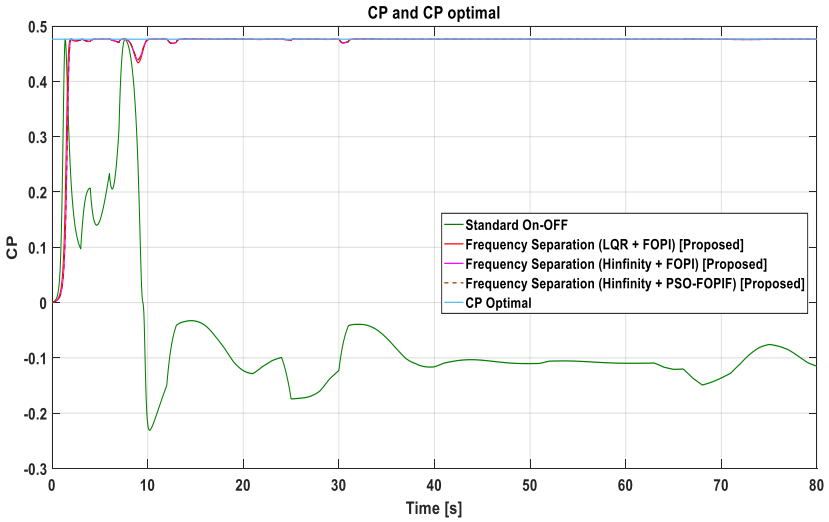


Figure IV. 24 Power Coefficient (CP).

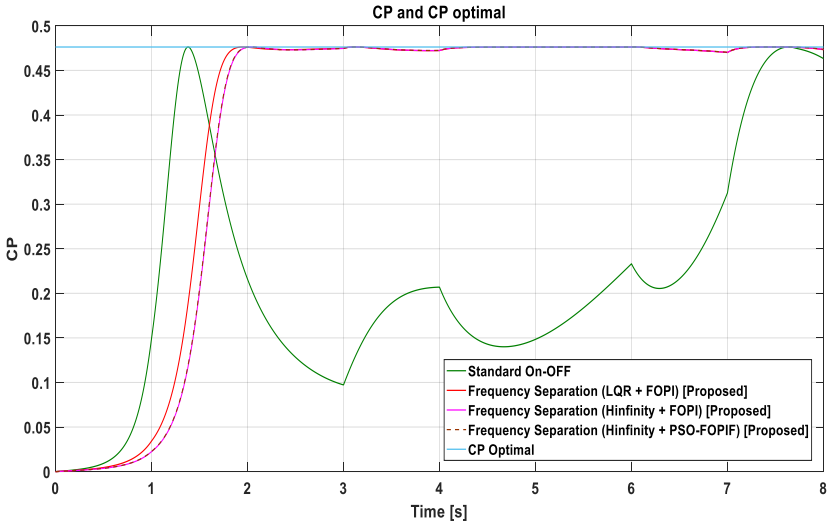


Figure IV. 25 Power coefficient (CP) Zoom [0s-8s].

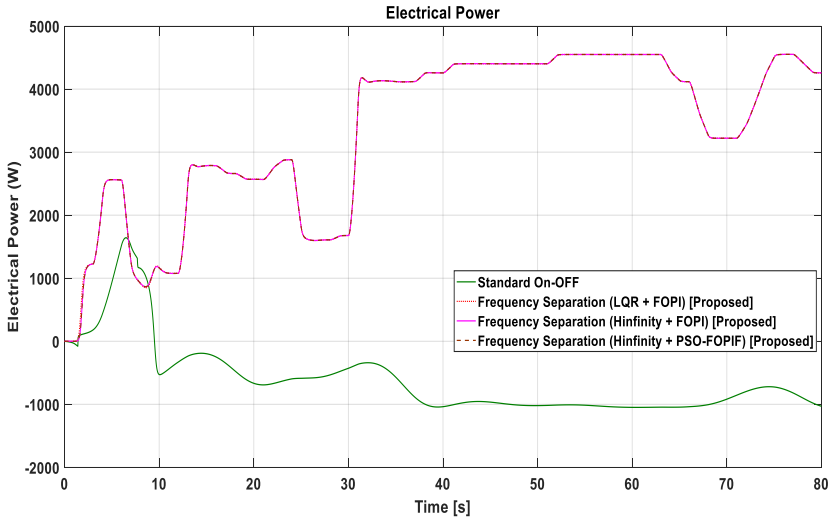


Figure IV. 26 Electrical Power.

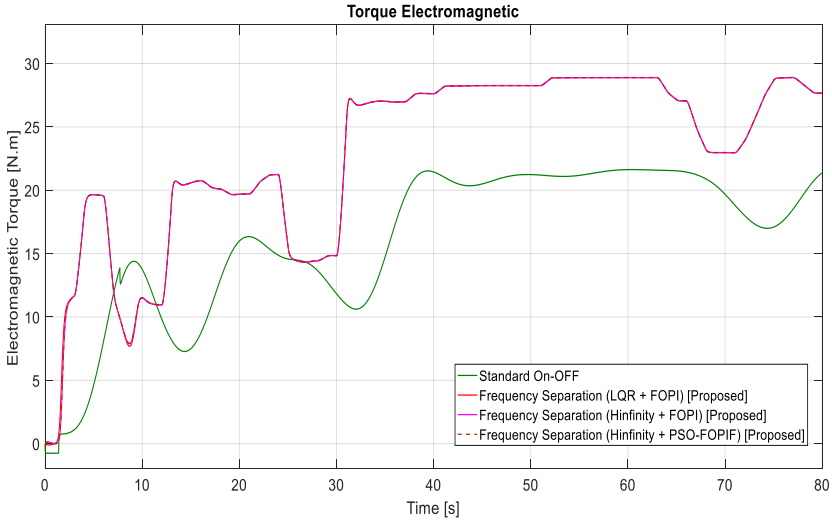


Figure IV. 27 Electromagnetic Torque.

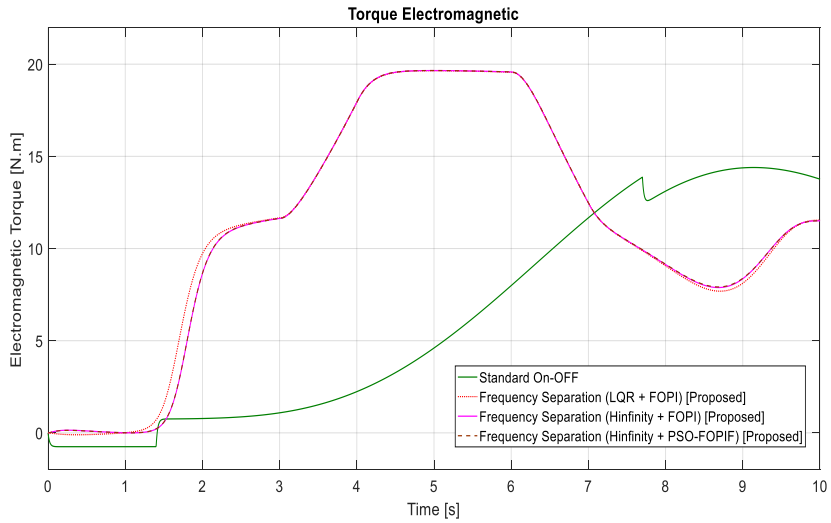


Figure IV. 28 Electromagnetic Torque Zoom [0s-10s].

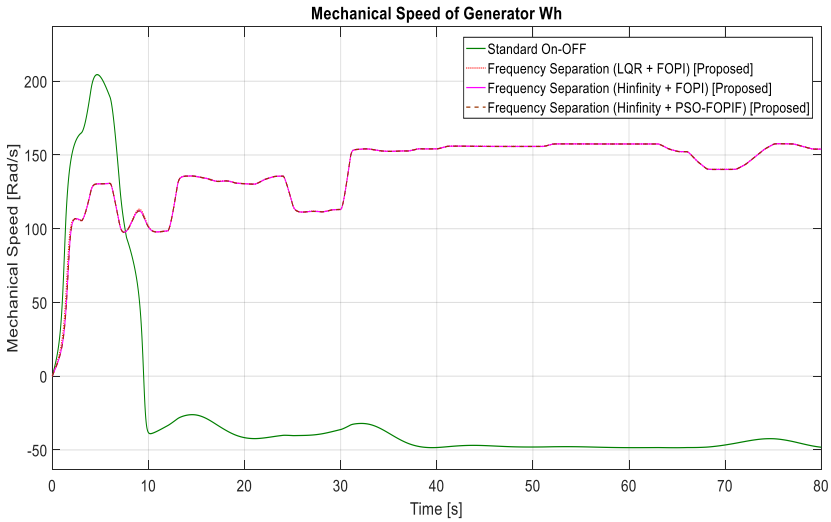


Figure IV. 29 Mechanical Speed of Generator ω_h .

A comparative analysis of the results obtained using a real wind model measured via an anemometer in a controlled laboratory environment highlights the exceptional performance of the proposed control structures based on the frequency separation principle. These structures, designed with various controllers, demonstrated reliable maximum power point tracking (MPPT), even under low wind speed conditions. Unlike the Standard On-Off controller, which consistently failed to maintain MPPT when the wind speed dropped to low levels (e.g., 5.5 m/s), the proposed controllers retained their MPPT capability. Furthermore, despite subsequent increases in wind speed, the Standard On-Off controller could not recover its MPPT functionality, as illustrated in Figure IV.24. An evaluation of the power coefficient curve (Figure IV.24), reveals that the proposed controller utilizing the frequency separation principle with LQR and FOPI controllers achieved slightly superior performance compared to its counterparts based on H∞ and FOPI controllers or H∞ and PSO-FOPIF controllers, as shown in Figure IV.25. This nuanced advantage underscores the effectiveness of the LQR + FOPI combination in maximizing power efficiency. Further analysis of Figures IV.27, IV.28, and IV.29 demonstrates that all proposed control structures successfully addressed key operational challenges. They effectively mitigated the issue of electromagnetic torque ripple (Figures IV.27 and IV.28) and maintained generator speed stability within a defined range (Figure IV.29). This robust performance significantly reduces oscillations that adversely impact the lifespan of wind energy conversion systems, thereby enhancing their longevity. In stark contrast, the Standard On-Off controller failed to eliminate electromagnetic torque ripples (Figures IV.27 and IV.28) and could not stabilize the generator's mechanical speed (Figure IV.29). These findings, derived from both real and natural wind models, unequivocally establish the efficacy of the proposed controllers in achieving and maintaining maximum power output while simultaneously extending the operational life of wind turbines. This dual benefit underscores the superiority of the proposed control structures over conventional methods, particularly under variable wind speed conditions.

To determine the most effective control strategies under a real wind model, a comparative analysis was conducted and summarized in Table IV.3. For clearer visualization, the table presents key performance metrics, including the maximum electromagnetic torque $\left(T_{em_{\max}}\right)$, the standard deviation of the electromagnetic torque **(Std)**, the maximum power coefficient $\left(CP_{\max}\right)$, and energy efficiency $\eta_E\,(\%)$.

Criteria / Method	$T_{em_{\max}}$	Std (T_{em})	$CP_{\max}$	Energy Efficiency $\eta_E\,(\%)$
Standard On-Off controller	21.6302	5.8456	0.4763	-17.90
LQR + FOPI	28.8951	6.8701	0.4763	98.99
H∞ + FOPI	28.8949	6.9168	0.4763	98.92
H∞ + PSO-FOPIF	28.8984	6.9211	0.4763	98.91

Table IV. 3 Comparison of Different Control Strategies Under Real Wind Model.

Energy efficiency $\eta_E\,(\%)$ analysis reveals a significant advantage of the proposed controllers, which achieve an energy extraction efficiency exceeding 98%, whereas the standard on-off controller suffers a substantial energy deficit of -17.9%. This highlights the superior energy harvesting capability of the proposed methods compared to the conventional approach. Regarding electromagnetic torque performance, the standard on-off controller exhibits the lowest maximum electromagnetic torque $\left(T_{em_{\max}}\right)$ (21.6302), indicating minimal torque stress on the system. In contrast, the H∞ + PSO-FOPIF controller generates the highest maximum electromagnetic torque (28.8984), followed by the LQR + FOPI controller (28.8951) and the H∞ + FOPI controller (28.8949). Despite these differences, all controllers achieve a similar electromagnetic torque standard deviation **(Std)**. Notably, the standard on-off controller achieves the lowest torque ripple (5.8456), reflecting superior torque smoothness. Additionally, all controllers successfully track the maximum power point in this wind scenario, achieving the same peak power coefficient $\left(CP_{\max}\right)$ (0.4763). However, while the standard on-off controller excels in reducing torque ripple, its poor energy extraction performance renders it ineffective in a real wind environment. In contrast, the proposed controllers balance both energy efficiency and torque smoothness, confirming their superiority over the standard on-off approach.

IV. 4.4 Robustness Test

After demonstrating the efficacy of the frequency separation-based control method through various proposed controllers—namely, Frequency Separation (LQR + FOPI), Frequency Separation (H∞ + FOPI), and Frequency Separation (H∞ + PSO-FOPIF)—under different wind conditions, this section delves into evaluating their robustness. The investigation focuses on assessing the controllers' performance under varying internal system parameters, specifically by altering the total inertia of the

high-speed shaft within the time interval [45s–50s]. This analysis aims to highlight potential deviations in results compared to scenarios where the total inertia of the high-speed shaft remains constant. The mathematical representation of the total inertia is provided in Equation (IV.34) [127–128].

$$J_T = \frac{J_{wt} + J_l}{G^2 + J_h} + J_g \tag{IV.34}$$

Where: J_h , J_l are inertias rendered respectively in HSS (the High Speed Shaft) and LSS (the Low Speed Shaft). J_{wt}, J_g Are respectively the inertias of the Turbine Rotor and the Electric Generator. The values of the inertias parameters are displayed in Table IV.4.

Parameters	Values
High Speed Shaft Inertia	$J_h = 0.005$
Low Speed Shaft Inertia	$J_l = 0.02$
Turbine Rotor Inertia	$J_{wt} = 3$
Electric Generator Inertia	$J_g = 0.01$

Table IV. 4 The Values of The Inertias Parameters.

Figure IV.30 depicts the variations applied to the total inertia of the high-speed shaft during the testing interval.

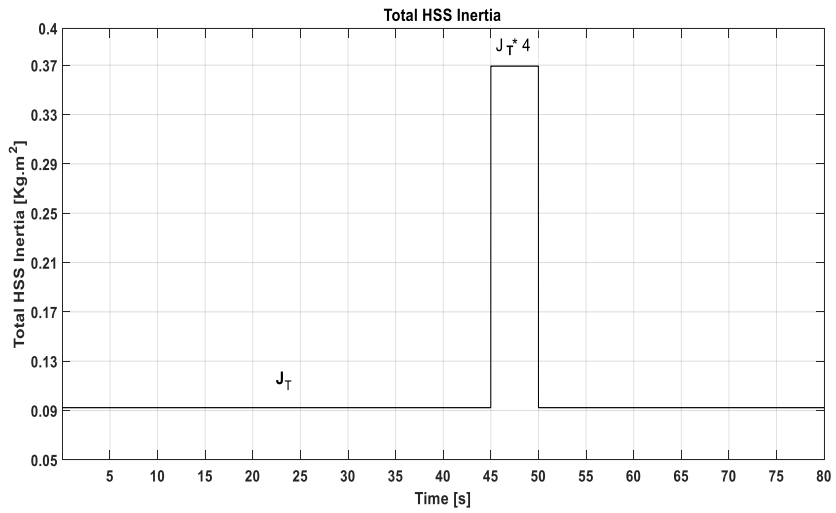


Figure IV. 30 Total High Speed Shaft Inertia.

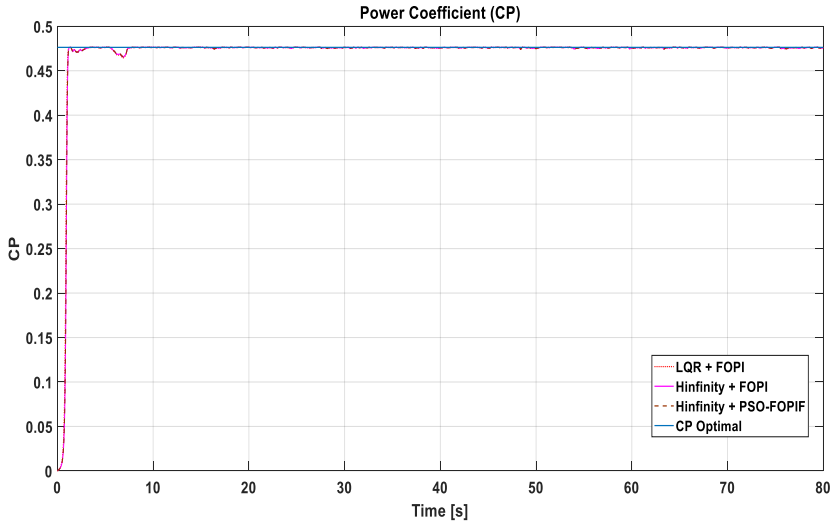


Figure IV. 31 Power coefficient (CP).

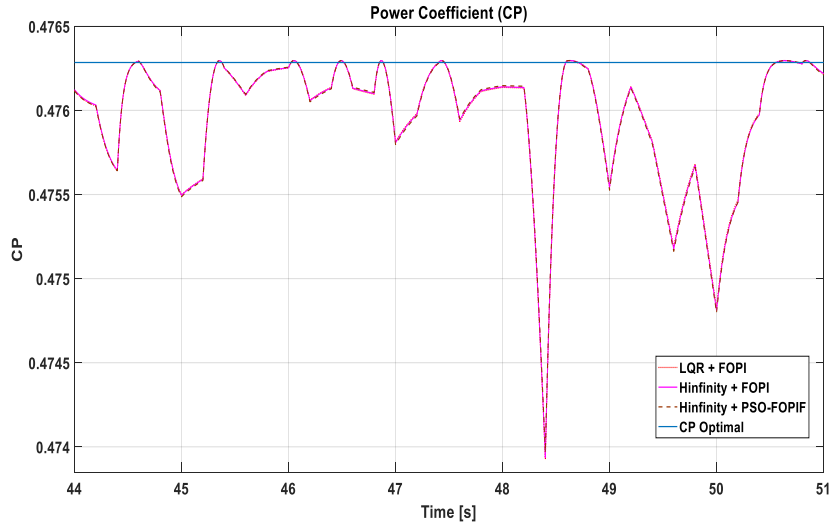


Figure IV. 32 Power coefficient (CP) Zoom [44s-51s].

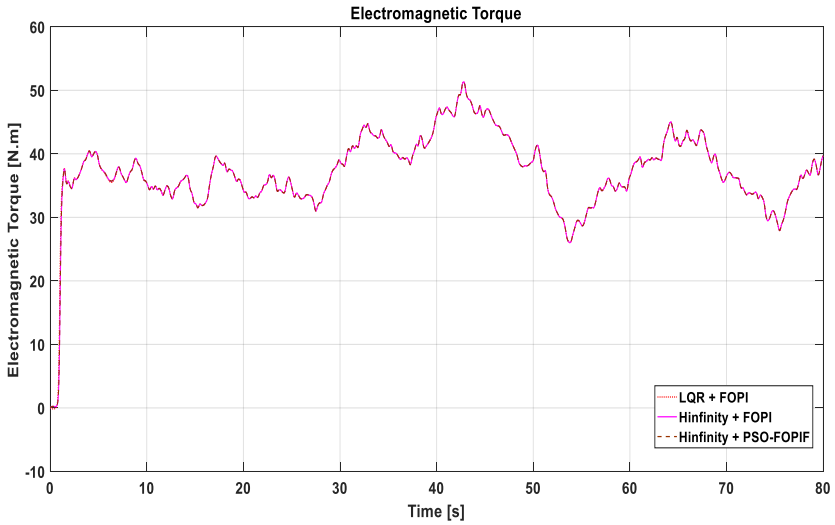


Figure IV. 33 Electromagnetic Torque.

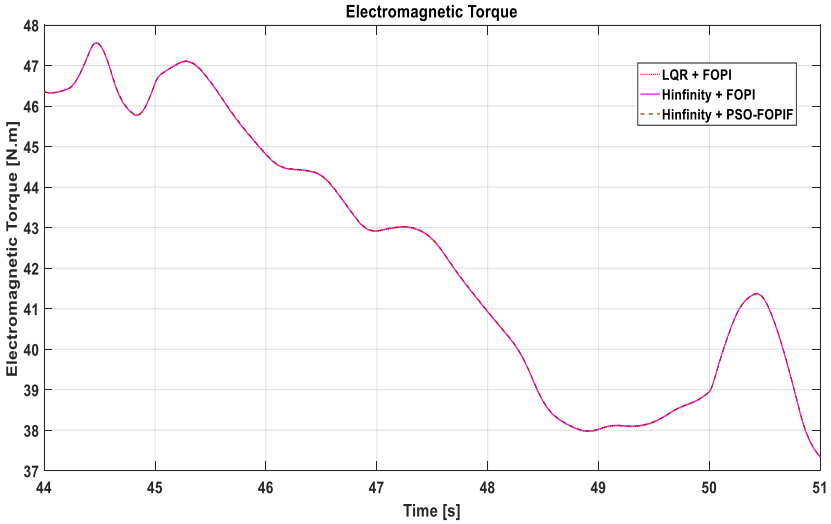


Figure IV. 34 Electromagnetic Torque Zoom [44s-51s].

The analysis of the results demonstrates that the proposed controllers—Frequency Separation (LQR + FOPI), Frequency Separation (H∞ + FOPI), and Frequency Separation (H∞ + PSO-FOPIF)—exhibited remarkable robustness, even under substantial variations in the total inertia of the high-speed shaft. This is particularly evident in the curves presented in (Figure IV.33) and (Figure IV.34), which illustrate the controllers' consistent ability to suppress electromagnetic torque ripples, even when the total inertia was tripled from its nominal value during the interval between 45 and 50 seconds. Additionally, the comparative analysis of the curves in (Figure IV.31) and (Figure IV.32) underscores the controllers' superior performance in tracking the maximum power point, further affirming their robustness and adaptability under demanding operational conditions.

To determine the most effective control strategies Under Varying Internal System Parameters, a comparative analysis was conducted and summarized in Table IV.5. For clearer visualization, the table presents key performance metrics, including the maximum electromagnetic torque $\left(T_{em_{\max}}\right)$, the standard deviation of the electromagnetic torque (Std), the maximum power coefficient $\left(CP_{\max}\right)$, and energy efficiency $\eta_E\,(\%)$.

Criteria / Method	$T_{em_{\max}}$	Std (T_{em})	$CP_{\max}$	Energy Efficiency $\eta_E\,(\%)$
LQR + FOPI	51.3290	6.6174	0.4763	98.35
H∞ + FOPI	51.3300	6.6766	0.4763	98.28
H∞ + PSO-FOPIF	51.3344	6.6665	0.4763	98.30

Table IV. 5 Comparison of Different Control Strategies Under Varying Internal System Parameters.

After analyzing the simulation results of the proposed controllers under various internal system parameters, the energy efficiency analysis reveals a significant advantage for the proposed methods,

with energy extraction efficiencies $\eta_E(\%)$ exceeding 98%. This highlights the superior energy harvesting capabilities of the proposed controllers. In terms of electromagnetic torque performance, the H∞ + PSO-FOPIF controller generates the highest maximum electromagnetic torque $\left(T_{em_{\max}}\right)$ (51.3344), followed by the H∞ + FOPI controller (51.3300) and the LQR + FOPI controller (51.3290). Despite these variations in maximum torque, all controllers exhibit similar electromagnetic torque standard deviation **(Std)**. Notably, the LQR + FOPI controller stands out by achieving the lowest torque ripple (6.6174), reflecting its superior torque smoothness. Furthermore, all controllers successfully track the maximum power point, achieving the same peak power coefficient $\left(CP_{\max}\right)$ of 0.4763. Despite variations in internal system parameters, the proposed controllers demonstrate a balanced performance, maintaining both high energy efficiency and smooth torque, confirming their robustness across different conditions.

IV.5 CONCLUSION

This chapter has presented a comprehensive evaluation of control strategies grounded in the frequency separation principle, demonstrating their efficacy through extensive simulations and real-world scenarios. By integrating advanced controller configurations—LQR + FOPI, H∞ + FOPI, and H∞ + PSO-FOPIF—these strategies have consistently showcased robust and efficient performance in addressing the critical challenges inherent to wind energy conversion systems. Under varying turbulence levels and realistic wind conditions, the proposed controllers achieved precise maximum power point tracking, effectively mitigated electromagnetic torque ripples, and ensured stable generator speed operation. These outcomes are instrumental not only in optimizing energy capture but also in significantly extending the operational lifespan of wind turbines, thereby reducing maintenance costs and enhancing overall economic feasibility. The comparative analyses further illuminated the unique strengths of each configuration. The H∞ + PSO-FOPIF controller demonstrated exceptional adaptability under fluctuating wind speed conditions, while the LQR + FOPI approach excelled in scenarios involving real wind profiles, highlighting the tailored advantages of these strategies. These findings emphasize the versatility and robustness of the proposed dual-loop control architectures across diverse operational environments, outperforming the standard on-off controller, which exhibited considerable limitations in maintaining performance consistency under similar conditions. Additionally, the capacity of these control strategies to suppress electromagnetic torque ripples, even amidst significant variations in system parameters such as high-speed shaft inertia, underscores their resilience and adaptability. This robustness ensures sustained performance in dynamic and unpredictable environments, further establishing the proposed methodologies as a reliable and

advanced alternative to conventional control approaches. In conclusion, the proposed frequency separation-based control strategies mark a significant advancement in wind energy technology. By addressing critical operational challenges, these strategies not only enhance energy efficiency and system durability but also align with the evolving technical and economic demands of renewable energy systems. By meeting the expectations of stakeholders, these innovative solutions contribute to a more sustainable and economically viable future for wind energy conversion systems, paving the way for further advancements in the field.

General Conclusions and Future Work

1. General Conclusions

The profound and multifaceted contributions of this PhD thesis to the field of wind energy conversion systems (WECS) underscore the importance of advancing control strategies to meet the escalating global demand for renewable energy. This research embarked on addressing critical challenges in harnessing wind energy, focusing on maximizing energy efficiency, reducing mechanical stress, and improving the economic feasibility of wind energy technologies. By systematically tackling the intricacies of modeling, control, and optimization in WECS, this work has laid a robust foundation for the development of innovative solutions tailored to the dynamic and non-linear nature of wind energy systems.

The thesis began with a comprehensive modeling of the wind energy conversion chain, establishing a rigorous analytical framework that detailed the aerodynamics of wind turbines, the drive train dynamics, and the operational characteristics of squirrel cage induction generators. This groundwork facilitated a deeper understanding of the non-linear behavior inherent in WECS and provided a basis for employing linearization techniques to enable advanced control designs. These initial efforts set the stage for exploring a diverse range of control strategies aimed at tracking the maximum power point (MPPT) and optimizing energy extraction from variable wind resources.

The exploration of MPPT strategies revealed the inherent trade-offs in WECS control: achieving maximum energy production often comes at the cost of increased mechanical wear and reduced turbine lifespan, while mitigating these effects can lead to diminished energy efficiency. Through a systematic analysis of traditional and enhanced controllers, including standard on-off, and fuzzy logic-based variants, the research identified key limitations, such as chattering and electromagnetic torque ripple, that necessitated further refinement. By incorporating advanced concepts such as sliding mode control and metaheuristic optimization algorithms—specifically PSO, WOA, COOT, and MOPSO—this thesis demonstrated significant improvements in controller performance, addressing the dual objectives of energy maximization and mechanical stress minimization.

A pivotal innovation in this research lies in the development and application of the frequency separation principle. By distinguishing between the high-frequency dynamics induced by turbulent wind and the low-frequency dynamics stemming from gradual wind variations, the proposed dual-loop control architectures enabled precise and adaptive responses to fluctuating operational conditions. The integration of advanced control configurations, including H∞ and Fractional-Order Proportional-Integral (FOPI) controllers, further enhanced the robustness and reliability of WECS. Particularly

noteworthy is the H∞ + PSO-FOPIF controller, which exhibited exceptional adaptability and performance under diverse wind conditions, addressing both energy capture efficiency and the mitigation of electromagnetic torque ripple.

The findings of this research underscore the critical role of optimization and advanced control techniques in advancing the sustainability of wind energy. By enhancing the operational durability of wind turbines and reducing maintenance costs, the proposed methodologies align with the economic and technical imperatives of renewable energy systems. Moreover, the contributions of this thesis extend beyond immediate technical advancements, offering a scalable and adaptable framework that can accommodate future innovations in wind energy technologies.

In conclusion, the proposed control strategies in this thesis, represent a significant step forward in the quest for efficient, reliable, and economically viable wind energy conversion systems. By addressing the dual challenges of energy efficiency and system resilience, this work not only contributes to the ongoing evolution of wind energy technologies but also supports the broader transition toward a sustainable and renewable energy future. The proposed solutions and insights provide a valuable foundation for further research and development, paving the way for the continued advancement of wind energy systems to meet the growing demands of a greener global economy.

2. Futures Works

The results presented in our work have demonstrated the effectiveness and robustness of the proposed approaches. Nonetheless, the work as a whole can be pursued mainly through perspectives that can contribute to better industrial and economic performance. Among the possible avenues of work we consider:

- All the control strategies developed in this work presuppose knowledge of wind speed. However, we know that wind speed is difficult to measure. So, for future work, we can consider implementing a robust and optimal wind speed estimator that will be generalized from conventional estimators, which assume that the wind turbine is operating at optimal power for a given wind speed.
- In the future, we propose to incorporate other heuristic algorithms into the control strategy based on frequency separation. We intend to work on more complex multi-objective problems to further improve the limits of our methods. Implementing these control approaches on real-world wind turbine installations is one of the most challenging future developments of this work.

- Consequently, in future work, we suggest to focus on the network part of the power conversion system by proposing approaches and solutions for the machine-side converter controller, dividing it into low-frequency and high-frequency loops.
- For low-power Wind Energy Conversion Systems (WECS), performance requirements are often minimal, focusing on power limitation at rated levels and energy optimization, perhaps establishing an energy-reliability optimization criterion. A multitude of wind facilities are integrated into hybrid renewable energy conversion systems, presenting distinct control challenges. To achieve effective solutions regarding the structure and control strategy of these systems, experimental examination under reproducible settings is essential. The creation of laboratory test rigs utilizing electromechanical WECS simulators is evidently significant in this perspective.

Implementing these control strategies in actual wind turbine installations is a last target to be considered for the future development of this work.

References

[1] Manwell, James F., Jon G. McGowan, and Anthony L. Rogers. Wind energy explained: theory, design and application. John Wiley & Sons, 2010.

[2] The World Wind Energy Association, Half-year Report 2024. https://wwindea.org/ss-uploads/media/2024/12/1733138465-eddec6e3-1aec-41d4-922f-d651ade895b6.pdf

[3] GWEC, GLOBAL WIND REPORT 2024, https://img.saurenergy.com/2024/05/gwr-2024_digital-version_final-1-compressed.pdf

[4] Kahla, Sami, et al. Maximum power extraction framework using robust fractional-order feedback linearization control and GM-CPSO for PMSG-based WECS. Wind Engineering. 2020;45 (4):1040-1054. doi:10.1177/0309524X20948263

[5] F. Zhang, H. Lan, F. Qiao, X. Sun and S. Sun, "On-off control of wind turbine for maximum wind power point tracking," 2012 Proceedings of International Conference on Modelling, Identification and Control, Wuhan, China, 2012, pp. 963-968.

[6] Brahmi, O., Bouchemha, A., Kahla, S. (2024). Improved On–Off Control for Electromagnetic Torque Ripple Minimization of Wind Energy Conversion System. In: Ziani, S., Chadli, M., Bououden, S., Zelinka, I. (eds) Proceedings of the 5th International Conference on Electrical Engineering and Control Applications–Volume 2. ICEECA 2022. Lecture Notes in Electrical Engineering, vol 1224. Springer, Singapore. https://doi.org/10.1007/978-981-97-4776-4_20

[7] Oussama, Brahmi, Bouchemha Amel, and Kahla Sami. Electromagnetic Torque Ripple Attenuation of WECS using an Improved On–Off Control based on PSO. AIJR Abstracts (2024): pp. 74-76.

[8] Brahmi O, Bouchemha A, Kahla S. New optimal robust control for maximum power point tracking and electromagnetic torque ripple minimization of wind energy conversion system. Wind Engineering. 2024;49 (2):356-374. doi:10.1177/0309524X241268908

[9] F. Xu, J. Zhang and M. Cheng, "Analysis of double objectives control for wind power generation system with frequency separation," 2011 4th International Conference on Electric Utility Deregulation and Restructuring and Power Technologies (DRPT), Weihai, China, 2011, pp. 1366-1371, doi: 10.1109/DRPT.2011.5994109

[10] Munteanu, Iulian, et al. Optimization of variable speed wind power systems based on a LQG approach, Control Engineering Practice, Vol. 13, Issue 7, 2005, pp. 903-912, ISSN 0967-0661, https://doi.org/10.1016/j.conengprac.2004.10.013

[11] Petersen, Ian R., Valery A. Ugrinovskii, and Andrey V. Savkin. Robust control design using H-∞ methods. Book Springer Science & Business Media, 2012, https://doi.org/10.1007/978-1-4471-0447-6

[12] Ayas, Mustafa Sinasi, and Erdinc Sahin, FOPID controller with fractional filter for an automatic voltage regulator, Computers & Electrical Engineering, Vol. 90, 2021, 106895, ISSN 0045-7906, https://doi.org/10.1016/j.compeleceng.2020.106895

[13] Kennedy, James, and Russell Eberhart., Particle swarm optimization, Proceedings of ICNN'95 - International Conference on Neural Networks, Perth, WA, Australia, 1995, pp. 1942-1948 vol.4, https://doi.org/10.1109/ICNN.1995.488968

[14] Naruei, Iraj, and Farshid Keynia. A new optimization method based on COOT bird natural life model, Expert Systems with Applications, Vol. 183, 2021,115352, ISSN 0957-4174, https://doi.org/10.1016/j.eswa.2021.115352

[15] Mostafa, Reham R., et al. "Enhanced COOT optimization algorithm for Dimensionality Reduction," 2022 Fifth International Conference of Women in Data Science at Prince Sultan University (WiDS PSU), Riyadh, Saudi Arabia, 2022, pp. 43-48, https://doi.org/10.1109/WiDS-PSU54548.2022.00020

[16] Mirjalili, Seyedali, and Andrew Lewis. The Whale Optimization Algorithm,Advances in Engineering Software, Vol. 95, 2016,pp.51-67, ISSN 0965-9978, https://doi.org/10.1016/j.advengsoft.2016.01.008

[17] Quarton, D.C. (1998), The evolution of wind turbine design analysis—a twenty year progress review. Wind Energ., 1: 5-24. https://doi.org/10.1002/(SICI)1099-1824(199804)1:1+<5::AID-WE1>3.0.CO;2-I

[18] Tong, Wei. Wind power generation and wind turbine design. Book WIT press, 2010. ISBN 978-1-84564-205-1 , eISBN 978-1-84564-388-1

[19] Nichita, Cristian, et al., "Large band simulation of the wind speed for real time wind turbine simulators," in IEEE Transactions on Energy Conversion, vol. 17, no. 4, pp. 523-529, Dec. 2002, https://doi.org/10.1109/TEC.2002.805216

[20] Struggl, Stephan, Viktor Berbyuk, and Håkan Johansson. "Review on wind turbines with focus on drive train system dynamics." Wind Energy 18.4 (2015): 567-590.

[21] Peeters, Joris. "Simulation of dynamic drive train loads in a wind turbine." Katholieke Universiteit Leuven (2006), https://doi.org/10.1002/we.1721

[22] Burton, Tony, et al. Wind energy handbook. John Wiley & Sons, 2011. Print ISBN: 9780470699751, Online ISBN:9781119992714, https://doi.org/10.1002/9781119992714

[23] Hansen, Martin. O. L. (2008). Aerodynamics of Wind Turbines: second edition. (2ed.) Earthscan Publisher.

[24] International Electrotechnical Commission (IEC). (2019). IEC 61400-1: Wind Turbines - Part 1: Design Requirements.

[25] Ackermann, Thomas, Wind power in power systems. John Wiley & Sons LTd, 2012 ISBN: 978-0-470-97416-2.

[26] Bianchi, Fernando D., Hernan De Battista, and Ricardo J. Mantz. Wind turbine control systems: principles, modelling and gain scheduling design. Springer Science & Business Media, 2007. https://doi.org/10.1007/1-84628-493-7

[27] Weibull, Waloddi. "A statistical distribution function of wide applicability." Journal of applied mechanics (1951).

[28] Abdullah, Majid A., et al. A review of maximum power point tracking algorithms for wind energy systems, Renewable and Sustainable Energy Reviews, Vol. 16, Issue 5, 2012, pp.3220-3227, ISSN 1364-0321, https://doi.org/10.1016/j.rser.2012.02.016

[29] Lianjun Zhang, Jeffrey H Gove, Chuangmin Liu, and William B Leak. 2001. A finite mixture of two Weibull distributions for modeling the diameter distributions of rotated-sigmoid, uneven-aged stands. Canadian Journal of Forest Research. 31(9): 1654-1659. https://doi.org/10.1139/x01-086

[30] Guenoupkati, A., Salami, A. A., Bokovi, Y., Koussetou, P. X., & Ouedraogo, S. (2023). Estimating mixture hybrid Weibull distribution parameters for wind energy application using Bayesian approach. International Journal of Renewable Energy Development, 12(5), 902-912. https://doi.org/10.14710/ijred.2023.54452

[31] Welfonder, E., R. Neifer, and M. Spanner. Development and experimental identification of dynamic models for wind turbines, Control Engineering Practice, Vol. 5, Issue 1, 1997, pp.63-73, ISSN 0967-0661, https://doi.org/10.1016/S0967-0661(96)00208-0

[32] Burton, T., Sharpe, D., Jenkins, N., & Bossanyi, E. (2001). Wind energy handbook,. Wiley and Sons Ltd., New York

[33] Rogez, Vincent. "Modélisation simplifiée de sources de production décentralisée pour des études de dynamique des réseaux. Application à l'intégration d'une production éolienne dans un réseau de distribution insulaire." Thèse de Doctorat, Génie Electrique: Université d'Artois, Béthune (2004).

[34] Bianchi, Fernando D., Hernan De Battista, and Ricardo J. Mantz. Wind turbine control systems: principles, modelling and gain scheduling design. Springer Science & Business Media, 2006. https://doi.org/10.1007/1-84628-493-7

[35] Hansen, Martin. Aerodynamics of wind turbines. Routledge, 2015.

[36] Betz, A. (1920) Das Maximum der theoretisch möglichen Ausnützung des Windes durch Windmotoren. Zeitschrift für das gesamte Turbinenwesen, 26, 307-309. (In German)

[37] Biswas, S.; Chen, J.S.-J. Power Coefficient for Large Wind Turbines Considering Wind Gradient Along Height. Energies 2025, 18, 740. https://doi.org/10.3390/en18030740

[38] Nejad, A. R., et al.. (2022). Wind turbine drivetrains: State-of-the-art technologies and future

development trends. Wind Energy Science, 7, 387-411. https://doi.org/10.5194/wes-7-387-2022

[39] ASADI, SAEED. Wind Turbine Drive Train System Dynamics: Multibody Dynamic Modelling and Global Sensitivity Analysis. PhD. Thesis, Department of Mechanics and Maritime Sciences, Sweden, 2018.

[40] Al-Bahadly, I. H. (Ed.). (2011). Wind Turbines. InTech. https://doi.org/10.5772/643

[41] Gawarkiewicz, Rafał, Filip Wasilczuk, and Michał Wasilczuk. "Drivetrain of a Wind Turbine." Machine Dynamics Research 39.2 (2016).

[42] Chen, Zhe, . Wind turbine drive train systems, Editor(s): John D. Sørensen, Jens N. Sørensen, In Woodhead Publishing Series in Energy, Wind Energy Systems, Woodhead Publishing, 2011, pp. 208-246, ISBN 9781845695804, https://doi.org/10.1533/9780857090638.2.208

[43] Hansen, Anca D., and Gabriele Michalke. "Multi-pole permanent magnet synchronous generator wind turbines' grid support capability in uninterrupted operation during grid faults." IET Renewable Power Generation 3.3 (2009): 333-348. https://doi.org/10.1049/iet-rpg.2008.0055

[44] Muljadi, E., et al. "Power quality aspects in a wind power plant," 2006 IEEE Power Engineering Society General Meeting, Montreal, QC, Canada, 2006, pp. 8 pp.-, https://doi.org/10.1109/PES.2006.1709244

[45] Pena, Ruben, J. C. Clare, and G. M. Asher. "Doubly fed induction generator using back-to-back PWM converters and its application to variable-speed wind-energy generation." IEE Proceedings-Electric power applications Vol. 143, Issue 3 (1996): 231-241. https://doi.org/10.1049/ip-epa:19960288

[46] Tavner, Peter J. Offshore Wind Turbines-Reliability, Availability & Maintenance. Institution of Engineering and Technology (IET), 2012.

[47] Sørensen, Poul Ejnar, et al. "Simulation of interaction between wind farm and power system." (2002). Denmark. Forskningscenter Risoe. Risoe-R No. 1281(EN)

[48] Thomsen, Kenneth, and Poul Sørensen. " Fatigue loads for wind turbines operating in wakes, Journal of Wind Engineering and Industrial Aerodynamics, Vol.80, Issues 1–2, 1999, pp. 121-136, ISSN 0167-6105, https://doi.org/10.1016/S0167-6105(98)00194-9

[49] Munteanu, Iulian, et al. "Energy-Reliability Optimization of Wind Energy Conversion Systems by Sliding Mode Control," in IEEE Transactions on Energy Conversion, vol. 23, no. 3, pp. 975-985, Sept. 2008, https://doi.org/10.1109/TEC.2008.917102

[50] Kahla, Sami, et al. Robust Fuzzy On–Off Synthesis Controller for Maximum Power Point Tracking of Wind Energy Conversion. Trans. Electr. Electron. Mater. 19, 146–156 (2018). https://doi.org/10.1007/s42341-018-0017-9

[51] Pande, Jayshree, and Paresh Nasikkar. A Maximum Power Point Tracking Technique for a Wind Power System Based on the Trapezoidal Rule. Energies 2023, 16, 2799. https://doi.org/10.3390/en16062799

[52] Ekelund, Thommy. "Modeling and linear quadratic optimal control of wind turbines." Doktorsavhandlingar vid Chalmers Tekniska Hogskola. 1997. (1997).

[53] Munteanu, Iulian, et al. Optimal control of wind energy systems: towards a global approach. Vol. 22. London: Springer, 2008. https://doi.org/10.1007/978-1-84800-080-3

[54] KAHLA, SAMI. Modélisation et commande d'un système éolien. These de Doctorat, university of Guelma, 2018.

[55] Hannan, M.A.; Al-Shetwi, A.Q.; Mollik, M.S.; Ker, P.J.; Mannan, M.; Mansor, M.; Al-Masri, H.M.K.; Mahlia, T.M.I. Wind Energy Conversions, Controls, and Applications: A Review for Sustainable Technologies and Directions. Sustainability 2023, 15, 3986. https://doi.org/10.3390/su15053986

[56] F. A. Farret, L. L. Pfitscher and D. P. Bernardon, "An heuristic algorithm for sensorless power maximization applied to small asynchronous wind turbogenerators," ISIE'2000. Proceedings of the 2000 IEEE International Symposium on Industrial Electronics (Cat. No.00TH8543), Cholula, Puebla, Mexico, 2000, pp. 179-184 vol.1, https://doi.org/10.1109/ISIE.2000.930508

[57] K. Belmokhtar, M.L. Doumbia, K. Agbossou, Novel fuzzy logic based sensorless maximum power point tracking strategy for wind turbine systems driven DFIG (doubly-fed induction generator), Energy,Volume 76,2014, Pages 679-693, ISSN 0360-5442, https://doi.org/10.1016/j.energy.2014.08.066

[58] Bhattacharjee, Chayan, and Binoy Krishna Roy. "Advanced fuzzy power extraction control of wind energy conversion system for power quality improvement in a grid tied hybrid generation system." IET Generation, Transmission & Distribution 10.5 (2016): 1179-1189, https://doi.org/10.1049/iet-gtd.2015.0769

[59] M. Nasiri, J. Milimonfared, S.H. Fathi, Modeling, analysis and comparison of TSR and OTC methods for MPPT and power smoothing in permanent magnet synchronous generator-based wind turbines, Energy Conversion and Management, Volume 86, 2014, Pages 892-900, ISSN 0196-8904, https://doi.org/10.1016/j.enconman.2014.06.055

[60] Zebraoui, Otmane, and Mostafa Bouzi. "Comparative study of different MPPT methods for wind energy conversion system." IOP Conference Series: Earth and Environmental Science. Vol. 161. No. 1. IOP Publishing, 2018. https://doi.org/10.1088/1755-1315/161/1/012023

[61] M. Vivert, G. Collaguazo, F. Naranjo and I. Quinde, "Perturbe and Observe MPPT algorithm with integral actions," 2021 IEEE 5th Colombian Conference on Automatic Control (CCAC), Ibague, Colombia, 2021, pp. 174-179, https://doi.org/10.1109/CCAC51819.2021.9633269

[62] Selman, Bart, and Carla P. Gomes. "Hill-climbing search." Encyclopedia of cognitive science 81.333-335 (2006): 10. https://doi.org/10.1002/0470018860.s00015

[63] C. Lee, "Fuzzy logic in control systems: fuzzy logic controller. I," in *IEEE Transactions on Systems, Man, and Cybernetics*, vol. 20, no. 2, pp. 404-418, March-April 1990, https://doi.org/10.1109/21.52551

[64] Mirjalili, Seyedali, and Seyedali Mirjalili. "Genetic algorithm." Evolutionary algorithms and neural networks: theory and applications (2019): 43-55. https://doi.org/10.1007/978-3-319-93025-1

[65] Hui, Joanne, and Alireza Bakhshai. "A fast and effective control algorithm for maximum power point tracking in wind energy systems." (2008). https://api.semanticscholar.org/CorpusID:18429144

[66] Heier, Siegfried. Grid integration of wind energy: onshore and offshore conversion systems. John Wiley & Sons 2014, ISBN: 9781119962946, ISBN:9781118703274, https://doi.org/10.1002/9781118703274

[67] Boukhezzar, Boubekeur, Houria Siguerdidjane, and M. Maureen Hand. Nonlinear control of variable-speed wind turbines for generator torque limiting and power optimization. J. Sol. Energy Eng. Nov 2006, 128(4): 516-530, https://doi.org/10.1115/1.2356496

[68] E. Muljadi and C. P. Butterfield, "Pitch-controlled variable-speed wind turbine generation," in IEEE Transactions on Industry Applications, vol. 37, no. 1, pp. 240-246, Jan.-Feb. 2001, https://doi.org/10.1109/28.903156

[69] B. Beltran, M. E. H. Benbouzid and T. Ahmed-Ali, "High-order sliding mode control of a DFIG-based Wind Turbine for power maximization and grid fault tolerance," 2009 IEEE International Electric Machines and Drives Conference, Miami, FL, USA, 2009, pp. 183-189, https://doi.org/10.1109/IEMDC.2009.5075203

[70] O. Erdinc, M. Uzunoglu, Optimum design of hybrid renewable energy systems: Overview of different approaches, Renewable and Sustainable Energy Reviews, Volume 16, Issue 3, 2012, Pages 1412-1425, ISSN 1364-0321, https://doi.org/10.1016/j.rser.2011.11.011

[71] Pranupa S, A T Sriram, S Nagaraja Rao, Wind energy conversion system using perturb & observe-based maximum power point approach interfaced with T-type three-level inverter connected to grid, Clean Energy, Volume 6, Issue 4, August 2022, Pages 534–549, https://doi.org/10.1093/ce/zkac034

[72] T. Esram and P. L. Chapman, "Comparison of Photovoltaic Array Maximum Power Point Tracking Techniques," in IEEE Transactions on Energy Conversion, vol. 22, no. 2, pp. 439-449, June 2007, https://doi.org/10.1109/TEC.2006.874230

[73] Li, H., and Zhe Chen. "Overview of different wind generator systems and their comparisons." IET Renewable power generation 2.2 (2008): 123-138. https://doi.org/10.1049/iet-rpg:20070044

[74] A. Rolan, A. Luna, G. Vazquez, D. Aguilar and G. Azevedo, "Modeling of a variable speed wind turbine with a Permanent Magnet Synchronous Generator," 2009 IEEE International Symposium on Industrial Electronics, Seoul, Korea (South), 2009, pp. 734-739, https://doi.org/10.1109/ISIE.2009.5218120

[75] C. A. C. Coello, G. T. Pulido and M. S. Lechuga, "Handling multiple objectives with particle swarm optimization," in IEEE Transactions on Evolutionary Computation, vol. 8, no. 3, pp. 256-279, June 2004, https://doi.org/10.1109/TEVC.2004.826067

[76] Sierra, Margarita Reyes, and Carlos A. Coello Coello. "Improving PSO-based multi-objective optimization using crowding, mutation and ∈-dominance." International conference on evolutionary multi-criterion optimization. Berlin, Heidelberg: Springer Berlin Heidelberg, 2005. https://doi.org/10.1007/978-3-540-31880-4_35

[77] Chen, J.; Chen, J. On Reducing the Shaft Torque Ripple of Small-to-Medium-Scale Wind Energy Conversion Systems Using Multi-Pulse Autotransformer Rectifier. Energies 2018, 11, 379. https://doi.org/10.3390/en11020379

[78] Erfort G, von Backström TW, Venter G. Reduction in the torque ripple of a vertical axis wind turbine through foil pitching optimization. Wind Engineering. 2019;44(2):115-124. https://doi.org/10.1177/0309524X19836711

[79] Kahla, Sami, et al. "Maximum power point tracking of wind energy conversion system using multi-objective grey wolf optimization of fuzzy-sliding mode controller." International Journal of Renewable Energy Research 7.2 (2017): 926-936. https://doi.org/10.20508/ijrer.v7i2.6125.g7073

[80] Hannachi M, Elbeji O, Benhamed M, Sbita L. Comparison between ABC and ACO: Tunning of On-Off MPPT for wind systems. Wind Engineering. 2021;45(6):1601-1612. https://doi.org/10.1177/0309524X21995113

[81] Hannachi M, Elbeji O, Benhamed M, Sbita L. Comparative study of four MPPT for a wind power system. Wind Engineering. 2021;45(6):1613-1622. https://doi.org/10.1177/0309524X21995946

[82] T. D. Gupta, K. Chaudhary, R. M. Elavarasan, R. K. Saket, I. Khan and E. Hossain, "Design Modification in Single-Tooth Winding Double-Stator Switched Reluctance Motor for Torque Ripple Mitigation," in IEEE Access, vol. 9, pp. 19078-19096, 2021, https://doi.org/10.1109/ACCESS.2021.3052828

[83] Abdel-Raheem Youssef, Ahmed I.M. Ali, Mahmoud S.R. Saeed, Essam E.M. Mohamed, Advanced multi-sector P&O maximum power point tracking technique for wind energy conversion system, International Journal of Electrical Power & Energy Systems, Volume 107, 2019, Pages 89-97, ISSN 0142-0615, https://doi.org/10.1016/j.ijepes.2018.10.034

[84] Khan, M., Raza, M. A., Faheem, M., Sarang, S. A., Panhwar, M., & Jumani, T. A. (2024). Conventional and artificial intelligence based maximum power point tracking techniques for efficient solar power generation. Engineering Reports, 6(12), e12963. https://doi.org/10.1002/eng2.12963

[85] Neda Mahmod Mohammad Altwallbah, Mohd Amran Mohd Radzi, Norhafiz Azis, Suhaidi Shafie, Muhammad Ammirrul Atiqi Mohd Zainuri, New perturb and observe algorithm based on trapezoidal rule: Uniform and partial shading conditions, Energy Conversion and Management, Volume 264, 2022, 115738, ISSN 0196-8904, https://doi.org/10.1016/j.enconman.2022.115738

[86] Q. Mei, M. Shan, L. Liu and J. M. Guerrero, "A Novel Improved Variable Step-Size Incremental-Resistance MPPT Method for PV Systems," in IEEE Transactions on Industrial Electronics, vol. 58, no. 6, pp. 2427-2434, June 2011, https://doi.org/10.1109/TIE.2010.2064275

[87] Y. Xia, K. H. Ahmed and B. W. Williams, "A New Maximum Power Point Tracking Technique for Permanent Magnet Synchronous Generator Based Wind Energy Conversion System," in IEEE Transactions on Power Electronics, vol. 26, no. 12, pp. 3609-3620, Dec. 2011, https://doi.org/10.1109/TPEL.2011.2162251

[88] S.M. Tripathi, A.N. Tiwari, Deependra Singh, Grid-integrated permanent magnet synchronous generator based wind energy conversion systems: A technology review, Renewable and Sustainable Energy Reviews, Volume 51, 2015, Pages 1288-1305, ISSN 1364-0321, https://doi.org/10.1016/j.rser.2015.06.060

[89] Z. M. Dalala, Z. U. Zahid, W. Yu, Y. Cho and J. -S. Lai, "Design and Analysis of an MPPT Technique for Small-Scale Wind Energy Conversion Systems," in IEEE Transactions on Energy Conversion, vol. 28, no. 3, pp. 756-767, Sept. 2013, https://doi.org/10.1109/TEC.2013.2259627

[90] Hui Li, K. L. Shi and P. G. McLaren, "Neural-network-based sensorless maximum wind energy capture with compensated power coefficient," in IEEE Transactions on Industry Applications, vol. 41, no. 6, pp. 1548-1556, Nov.-Dec. 2005, https://doi.org/10.1109/TIA.2005.858282

[91] Pande, J.; Nasikkar, P.; Kotecha, K.; Varadarajan, V. A Review of Maximum Power Point Tracking Algorithms for Wind Energy Conversion Systems. J. Mar. Sci. Eng. 2021, 9, 1187. https://doi.org/10.3390/jmse9111187

[92] Iulian Munteanu, Antoneta Iuliana Bratcu, Laurenţiu Frangu, Nonlinear Control for Stationary Optimization of Wind Power Systems, IFAC Proceedings Volumes, Volume 37, Issue 19, 2004, Pages 195-200, ISSN 1474-6670, https://doi.org/10.1016/S1474-6670(17)30682-1

[93] MUNTEANU, Iulian. "Using a nonlinear controller to optimize a variable speed wind power system." Journal of Electrical Engineering 6.4 (2006): 8-8.

[94] Yashar Mousavi, Geraint Bevan, Ibrahim Beklan Kucukdemiral, Afef Fekih, Sliding mode control of wind energy conversion systems: Trends and applications, Renewable and Sustainable Energy Reviews, Volume 167, 2022, 112734, ISSN 1364-0321, https://doi.org/10.1016/j.rser.2022.112734

[95] Shtessel, Yuri, et al. Sliding mode control and observation. Vol. 10. New York: Springer New York, 2014. https://doi.org/10.1007/978-0-8176-4893-0

[96] Levine, William S. "The control handbook." CRC Handbook (1996).

[97] Itkis, Uri. "Control systems of variable structure, A Halsted press book. Edition, illustrated. Publisher, Wiley, 1976.

[98] J. Y. Hung, W. Gao and J. C. Hung, "Variable structure control: a survey," in IEEE Transactions on Industrial Electronics, vol. 40, no. 1, pp. 2-22, Feb. 1993, https://doi.org/10.1109/41.184817

[99] Edwards, Christopher, and Sarah Spurgeon. Sliding mode control: theory and applications. CRC press, 1998.

[100] Sastry, Shankar, and Shankar Sastry. "Lyapunov stability theory." Nonlinear systems: analysis, stability, and control (1999): 182-234. https://doi.org/10.1007/978-1-4757-3108-8_5

[101] Desalegn B, Gebeyehu D, Tamirat B. Wind energy conversion technologies and engineering approaches to enhancing wind power generation: A review. Heliyon. 2022 Oct 26;8(11):e11263. https://doi.org/10.1016/j.heliyon.2022.e11263 . PMID: 36345520; PMCID: PMC9636551 .

[102] DeCarlo, R. A. "Variable structure sliding-mode controller design." Control Handbook (1996).

[103] K. D. Young, V. I. Utkin and U. Ozguner, "A control engineer's guide to sliding mode control," in IEEE Transactions on Control Systems Technology, vol. 7, no. 3, pp. 328-342, May 1999, https://doi.org/10.1109/87.761053

[104] Metropolis, N., & Ulam, S. (1949). The Monte Carlo Method. Journal of the American Statistical Association, 44(247), 335–341. https://doi.org/10.1080/01621459.1949.10483310

[105] Kirkpatrick, S., C. Gelatt, and M. Vecchi. "Simulated annealing, sa." (1982).

[106] Holland, J. H. (1992). Genetic Algorithms. Scientific American, 267(1), 66–73. http://www.jstor.org/stable/24939139

[107] L.B. Booker, D.E. Goldberg, J.H. Holland, Classifier systems and genetic algorithms, Artificial Intelligence, Volume 40, Issues 1–3, 1989, Pages 235-282, ISSN 0004-3702, https://doi.org/10.1016/0004-3702(89)90050-7

[108] M. Dorigo and G. Di Caro, "Ant colony optimization: a new meta-heuristic," Proceedings of the 1999 Congress on Evolutionary Computation-CEC99 (Cat. No. 99TH8406), Washington, DC, USA, 1999, pp. 1470-1477 Vol. 2, https://doi.org/10.1109/CEC.1999.782657

[109] Storn, R., Price, K. Differential Evolution – A Simple and Efficient Heuristic for global Optimization over Continuous Spaces. Journal of Global Optimization 11, 341–359 (1997). https://doi.org/10.1023/A:1008202821328

[110] Zong Woo Geem, Joong Hoon Kim, Loganathan GV. A New Heuristic Optimization Algorithm: Harmony Search. SIMULATION. 2001;76(2):60-68. https://doi.org/10.1177/003754970107600201

[111] Yang, XS. (2009). Firefly Algorithms for Multimodal Optimization. In: Watanabe, O., Zeugmann, T. (eds) Stochastic Algorithms: Foundations and Applications. SAGA 2009. Lecture Notes in Computer Science, vol 5792. Springer, Berlin, Heidelberg. https://doi.org/10.1007/978-3-642-04944-6_14

[112] Yang, XS. (2010). A New Metaheuristic Bat-Inspired Algorithm. In: González, J.R., Pelta, D.A., Cruz, C., Terrazas, G., Krasnogor, N. (eds) Nature Inspired Cooperative Strategies for Optimization (NICSO 2010). Studies in Computational Intelligence, vol 284. Springer, Berlin, Heidelberg. https://doi.org/10.1007/978-3-642-12538-6_6

[113] A. Bouchemha, O. Brahmi, S. Kahla and C. Ghenai, "Enhanced On-Off Control for Wind Energy Conversion System Electromagnetic Torque Ripple Minimization based on Whale Optimization Algorithm," 2024 IEEE 4th International Maghreb Meeting of the Conference on Sciences and Techniques of Automatic Control and Computer Engineering (MI-STA), Tripoli, Libya, 2024, pp. 170-175, https://doi.org/10.1109/MI-STA61267.2024.10599571

[114] Malgorzata Peszynska, Ralph E. Showalter, Approximation of hysteresis functional, Journal of Computational and Applied Mathematics, Volume 389, 2021, 113356, ISSN 0377-0427, https://doi.org/10.1016/j.cam.2020.113356

[115] Yin, Zhen-Yu, et al. "Optimization techniques for identifying soil parameters in geotechnical engineering: Comparative study and enhancement." International Journal for Numerical and Analytical Methods in Geomechanics 42.1 (2018): 70-94. https://doi.org/10.1002/nag.2714

[116] M. Raissi, P. Perdikaris, G.E. Karniadakis, Physics-informed neural networks: A deep learning framework for solving forward and inverse problems involving nonlinear partial differential equations, Journal of Computational Physics, Volume 378, 2019, Pages 686-707, ISSN 0021-9991, https://doi.org/10.1016/j.jcp.2018.10.045

[117] Papon, Aurélie, et al. "Single-and multi-objective genetic algorithm optimization for identifying soil parameters." International Journal for Numerical and Analytical Methods in Geomechanics 36.5 (2012): 597-618. https://doi.org/10.1002/nag.1019

[118] Xingjia Yao, Changchun Guo, Zuoxia Xing, Yan Li, Shu Liu and Xiaodong Wang, "Pitch regulated LQG controller design for variable speed wind turbine," 2009 International Conference on

Mechatronics and Automation, Changchun, 2009, pp. 845-849, . https://doi.org/10.1109/ICMA.2009.5246272

[119] X. Yao, S. Liu, G. Shan, Z. Xing, C. Guo and C. Yi, "LQG Controller for a Variable Speed Pitch Regulated Wind Turbine," 2009 International Conference on Intelligent Human-Machine Systems and Cybernetics, Hangzhou, China, 2009, pp. 210-213, https://doi.org/10.1109/IHMSC.2009.176

[120] B. Boukhezzar, L. Lupu, H. Siguerdidjane, M. Hand, Multivariable control strategy for variable speed, variable pitch wind turbines, Renewable Energy, Volume 32, Issue 8, 2007, Pages 1273-1287, ISSN 0960-1481, https://doi.org/10.1016/j.renene.2006.06.010

[121] Hang, Chang C., Karl Johan Åström, and Weng Khuen Ho. "Refinements of the Ziegler–Nichols tuning formula." IEE Proceedings D (Control Theory and Applications). Vol. 138. No. 2. IET Digital Library, 1991. https://doi.org/10.1049/ip-d.1991.0015

[122] Novak, Peter, and Thommy Ekelund. "Modeling, Identification and Control of a Variable-Speed HAWT." Proc of the 5th European Wind Energy Association Conference, Thessaloniki, Greece. 1994.

[123] J. Doyle, "Robust and optimal control," *Proceedings of 35th IEEE Conference on Decision and Control*, Kobe, Japan, 1996, pp. 1595-1598 vol.2, https://doi.org/10.1109/CDC.1996.572756

[124] Zhou, Kemin, and John Comstock Doyle. Essentials of robust control. Vol. 104. Upper Saddle River, NJ: Prentice hall, 1998. https://cir.nii.ac.jp/crid/1130282268725855744

[125] Dullerud, Geir E., and Fernando Paganini. A course in robust control theory: a convex approach. Vol. 36. Springer Science & Business Media, 2013. https://doi.org/10.1007/978-1-4757-3290-0

[126] Balas, Gary, et al. "Robust control toolbox 3." The Mathworks, Inc., Natick, MA (2005).

[127] SARIBATIR, B. M., & SEZER, M. E. (1987). Modelling and control of a wind energy conversion system. International Journal of Control, 46(1), 327–343. https://doi.org/10.1080/00207178708933901

[128] Tang, Chun, et al. "Dynamic wind turbine output power reduction under varying wind speed conditions due to inertia." Wind Energy 16.4 (2013): 561-573. https://doi.org/10.1002/we.1507

[129] J. Chen, T. Lin, C. Wen and Y. Song, "Design of a Unified Power Controller for Variable-Speed Fixed-Pitch Wind Energy Conversion System," in IEEE Transactions on Industrial Electronics, vol. 63, no. 8, pp. 4899-4908, Aug. 2016, https://doi.org/10.1109/TIE.2016.2547365

[130] Ahmed, S., et al. "A Novel Maximum Power Point Tracking Algorithm for Wind Energy Conversion System." Engineering Letters 27.4 (2019).

[131] S. M. R. Kazmi, H. Goto, H. -J. Guo and O. Ichinokura, "A Novel Algorithm for Fast and Efficient Speed-Sensorless Maximum Power Point Tracking in Wind Energy Conversion Systems," in IEEE Transactions on Industrial Electronics, vol. 58, no. 1, pp. 29-36, Jan. 2011, https://doi.org/10.1109/TIE.2010.2044732

[132] Mohammad Junaid Khan, An AIAPO MPPT controller based real time adaptive maximum power point tracking technique for wind turbine system, ISA Transactions, Volume 123, 2022, Pages 492-504, ISSN 0019-0578, https://doi.org/10.1016/j.isatra.2021.06.008

[133] Chaicharoenaudomrung, Koson, et al. "Maximum Power Point Tracking for Stand-Alone Wind Energy Conversion System Using FLC-P&O Method." IEEJ Transactions on Electrical and Electronic Engineering 15.12 (2020): 1723-1733. https://doi.org/10.1002/tee.23246

[134] Khan, M. J., Mathew, L., Alotaibi, M. A., Malik, H., & Nassar, M. E. (2022). Fuzzy-Logic-Based Comparative Analysis of Different Maximum Power Point Tracking Controllers for Hybrid Renewal Energy Systems. Mathematics, 10(3), 529. https://doi.org/10.3390/math10030529

[135] Azzouz, S., Messalti, S., Harrag, A. (2019). A novel hybrid MPPT controller using (P&O)-neural networks for variable speed wind turbine based on DFIG. Modelling, Measurement and Control A, Vol. 92, No. 1, pp. 23-29. https://doi.org/10.18280/mmc_a.920104

[136] Wang, Jiannan, and Waseem Azam. "Natural resource scarcity, fossil fuel energy consumption, and total greenhouse gas emissions in top emitting countries." Geoscience frontiers 15.2 (2024): 101757. https://doi.org/10.1016/j.gsf.2023.101757

[137] Jeffreys, Harold. "On the relation between wind and distribution of pressure." Proceedings of the Royal Society of London. Series A, Containing Papers of a Mathematical and Physical Character 96.676 (1919): 233-249. https://doi.org/10.1098/rspa.1919.0050

Scientific Production

International journal articles

1. **Brahmi O**, Bouchemha A, Kahla S. New optimal robust control for maximum power point tracking and electromagnetic torque ripple minimization of wind energy conversion system. Wind Engineering. 2024;0(0). doi:10.1177/0309524X241268908
2. **Brahmi, Oussama**; Bouchemha, Amel; Kahla, Sami; ,Wind Energy Conversion System Control: A Multi-Objective PSO Approach Based On Improved On–Off Control,J. Electrical Systems,20,2,170-188,2024,Engineering and Scientific Research Groups

International Conference Papers

1. **Brahmi, O.**, Bouchemha, A., Kahla, S. (2024). Improved On–Off Control for Electromagnetic Torque Ripple Minimization of Wind Energy Conversion System. In: Ziani, S., Chadli, M., Bououden, S., Zelinka, I. (eds) Proceedings of the 5th International Conference on Electrical Engineering and Control Applications–Volume 2. ICEECA 2022. Lecture Notes in Electrical Engineering, vol 1224. Springer, Singapore. https://doi.org/10.1007/978-981-97-4776-4_20
2. **Oussama, B**., Amel, B., & Sami, K. (2024). Electromagnetic Torque Ripple Attenuation of WECS using an Improved On–Off Control based on PSO. AIJR Abstracts, 74-76.
3. A. Bouchemha, **O. Brahmi**, S. Kahla and C. Ghenai, "Enhanced On-Off Control for Wind Energy Conversion System Electromagnetic Torque Ripple Minimization based on Whale Optimization Algorithm," *2024 IEEE 4th International Maghreb Meeting of the Conference on Sciences and Techniques of Automatic Control and Computer Engineering (MI-STA)*, Tripoli, Libya, 2024, pp. 170-175, doi: 10.1109/MI-STA61267.2024.10599571.
4. **O. Brahmi**, A. Bouchemha and S. Kahla, "Enhanced Fuzzy On–Off Control for Maximum Power Point Tracking of Wind Energy Conversion System," *First International Congress Focused on Renewable Energies and Energy Systems (ICREPS 2024)*, Naama, Algeria, 2024.

National Conference Papers

1. **O. Brahmi**, A. Bouchemha and S. Kahla, "On-Off Control based on Whale Optimization Algorithm for Electromagnetic Torque Ripple Minimization of WECS," *National Conference on Artificial Intelligence: From Theory to Practice (NCAI'2023)*, Tebessa , Algeria,2023.
2. **O. Brahmi**, A. Bouchemha and S. Kahla, "Standard On-Off Control based on Sine Cosine Algorithm for Electromagnetic Torque Ripple Minimization of WECS," *National Conference on Computational Systems and Applications (NCCSA'2024)*, Khemis Miliana , Algeria, 2024.
3. **O. Brahmi**, A. Bouchemha and S. Kahla, "Analyzing the Efficiency: A Comparative Study of Sliding Mode Control vs. Standard On-Off Control for Wind Energy Conversion Systems (WECS)," *First National Conference on Advances in Telecommunications, Electronics and Computer Engineering (ATECE'24)*, Khenchela , Algeria,2024.

Appendix A

The parameters for the low-turbulence stochastic wind speed model used in the simulation are outlined in Table A.1.

Parameters	Values
m_1	0.4
m_2	0.25
L_f	195
$V\left(m/s\right)$	11
$T_s\left(\mathrm{s}\right)$	1
κ_σ	0.14

Table A. 1 Parameters of The Low Turbulence Stochastic Wind Speed

The simulation parameters for the high-turbulence stochastic wind speed model are detailed in Table A.2.

Parameters	Values
m_1	0.4
m_2	0.25
L_f	500
$\mathrm{V}\left(\mathrm{m/s}\right)$	11
$T_s\left(\mathrm{s}\right)$	1
κ_σ	0.25

Table A. 2 Parameters of The High Turbulence Stochastic Wind Speed.

Here, $\left(m_1, m_2\right)$ represents Nichita parameters, L_f is the wind turbulence length scale, V is the average wind speed, which varies based on the wind's intensity (weak, medium, or strong), T_s is the sampling period, and κ_σ is the turbulence intensity.

Appendix B

Table B.1 presents the parameters of the wind energy conversion system used consistently across all simulation sections of this thesis, conducted within the MATLAB/Simulink environment.

Turbine rotor	**Drive train**	**SCIG**
Blade length: $R = 2.5$ m	*Multiplier ratio:* $G = 6.25$ $J_1 = 3.6$ kg.m^2 *Efficiency :* $\eta = 0.95$	$p = 2$ $Rs = 1.265\Omega$ $Rr = 1.43\Omega$ $Lm = 0.1397H$ $Ls = 0.1452H$ $Lr = 0.1452H$, $\omega_s = 157\ rad/s$ $\Gamma_{em\max} = 50$ Nm $Vs = 220\ V$

Table B. 1 Parameters of The Low-Power Rigid-Drive-Train SCIG-Based WECS.

Biography



Oussama BRAHMI was born in Tebessa, (Algeria), on June 15, 1995. He received his Master's degree in Electrotechnical Engineering from Tebessa University in 2020. He is currently a PhD candidate at TEBESSA University (Algeria). His research interests include power energy conversion systems, Meta heuristic optimization and power electronics.

Email: oussama.brahmi@univ-tebessa.dz
Google Scholar: https://scholar.google.com/citations?user=FILhlFMAAAAJ&hl=ar&oi=ao
Researchgate: https://www.researchgate.net/profile/Oussama-Brahmi
ORCID: https://orcid.org/0000-0002-8396-5312
LinkedIn: https://www.linkedin.com/in/oussama-brahmi-b09861174/